Stockholm University

# Searches for exotic stable massive particles with the ATLAS experiment

Christian Ohm

CERN-THESIS-2011-151
04/11/2011

Doctoral Thesis in Physics at Stockholm University, Sweden 2011

Christian Ohm

---

# Searches for exotic stable massive particles with the ATLAS experiment


Department of Physics
Stockholm University
2011

Doctoral Dissertation 2011
Fysikum
Stockholm University
Roslagstullsbacken 21
106 91 Stockholm


ISBN 978-91-7447-341-4
Printed by Universitetsservice US AB, Stockholm 2011

## Abstract

This thesis presents two signature-based searches for exotic long-lived particles using experimental data collected by the ATLAS experiment at the Large Hadron Collider (LHC) at CERN. At the LHC, proton-proton collisions take place at the world-record center-of-mass energy of 7 TeV and luminosities of up to $3 \times 10^{33}$ cm$^{-2}$s$^{-1}$. New physics has long been anticipated at the LHC and in this thesis two searches for hitherto unobserved particles are presented.

Long-lived heavy hadrons have been predicted by models of supersymmetry, and these were the target of the first physics analysis. Using measurements of timing and energy loss, a search for so-called *R*-hadrons was performed. No excess was observed in the data, and new lower limits were established on the masses of meta-stable supersymmetric particles with color charge: $m_{\tilde{g}} > 562$-$586$ GeV (depending on choice of scattering model), $m_{\tilde{t}} > 309$ GeV and $m_{\tilde{b}} > 294$ GeV. These constraints are the most stringent limits published to date.

In addition, a "blue-sky" search was made for objects possessing high electric charge. Ionization energy loss measurements were combined with variables describing the shape of electromagnetic showers to separate the sought signal from background processes. No event in the experimental data passed the selection and the results are in agreement with a background-only hypothesis. Upper limits between 1-12 pb were computed for the production cross sections of particles with electric charge $6e < q < 17e$ and mass $200 < m < 1000$ GeV. This is the first dedicated search for such particles at the LHC.

Finally, a system designed to monitor the LHC beams and timing signals based on beam pick-up detectors is described together with results from early LHC operation.

# Contents

# Acknowledgments

Research in experimental particle physics today relies heavily on collaboration, and none of the work presented in this thesis would have been possible without the help and previous work of many colleagues.

First and foremost, I would like to thank my supervisor David Milstead. Despite the occasional uncertainty regarding his physical whereabouts due to constant travel, I have always felt like this self-proclaimed "international man of mystery" is close-by and accessible. Furthermore, I am truly amazed both by his inspiring enthusiasm for physics and knowledge in the field, as well as his eating habits and remarkable metabolism. All jokes aside, we have fought side by side and worked hard together, had a lot of fun and I consider you a good friend. You've taught me much more than I thought I could grasp, and put up with my stubbornness. I'll really miss working this closely with you. Many thanks also to my second supervisor Torbjörn Moa who always helped out when I needed it. Thanks for everything from careful feedback on notes to sailing adventures. In particular, your constructive criticism received in response to drafts of various chapters during the last few weeks have been crucial to finalizing this thesis.

I have worked very closely with Rasmus Mackeprang, Morten Dam Jørgensen, Esben Klinkby, Troels Petersen, Philippe Mermod and my Stockholm colleagues Marianne Johansen and Sten Hellman developing the searches analyses for meta-stable exotic particles. I really appreciate our relationships and relaxed working environment, and I thoroughly enjoyed analyzing the first LHC collision data together!

I would like to thank the entire elementary particle physics group at Stockholm University for the open, friendly and supportive atmosphere. I would like to thank Sten Hellman for always letting me bounce my ideas off him and for trying to poke holes in them, Jörgen Sjölin, Sara Strandberg and Christophe Clément for very useful discussions about several aspects of analysis methods. During the time when we shared an office at CERN, Christophe also managed to dispense invaluable advice both regarding tile dimensions as well as design prospects for accelerators for felines. Many thanks to Barbro Åsman, Bengt Lund-Jensen, Christian Bohm, Erik Johansson and Kerstin Jon-And for sharing your experience in the field and helping with strategic advice when I needed it. My fellow PhD students – coming into the group would not have been the same without Marianne, Elin, Björn, Henrik, Gustav, Thomas and Henrik, and leaving it wouldn't be the same without Kattis, Karl, Maja, Olle, Pawel, Matthias and Marcel. Thanks also to Karl-Johan Grahn for our exchange of ideas and tricks (and for helping out keeping

track of Dave). I'd like to thank Aras Papadelis and Johan Lundberg for wisdoms about `const`-ness and statistics, but also for wearing grillz with me at a Wu-Tang concert, sharing near-death experiences in Kattis' car, Oktoberfest memories, von Trier movie nights, smoke machines and rants. Johan also provided crucial feedback on large portions of this thesis, so in the event that anyone would find it an enjoyable read, I'm indebted to him. I've grown some much appreciated friendships with several members of our group, many of which I know will stay strong even if we don't work together.

I am deeply grateful to Thilo Pauly (and the rest of the CERN ATLAS Level-1 Central Trigger group) for introducing me to high-energy physics and ATLAS - it was exciting to see our little baby perform when the first LHC beams reached ATLAS! Alexander Solodkov, Guillaume Unal and Zachary Marshall provided much appreciated help when developing the Tile time-of-flight method and learning to run GEANT4 simulation. Wolfgang Liebig taught me many useful things about ATLAS software development which I am truly grateful for. Claudia Gemme, Leonardo Rossi and Thijs Cornelissen provided crucial help in getting the most out of the $dE/dx$ measurement from the Pixel detector. Paul de Jong, George Redlinger, Pascal Pralavorio, Paul Jackson and the members of the editorial board helped us push the $R$-hadron search forward and provided very important feedback. Many thanks also to Matt W. Moore for the cover art and Dr. Li for finding the perfect quote for Part III.

On a more personal note, I am very thankful for my friends in Geneva. In particular, major shout-outs are in order for my roommates the last year, Seth and Travis. Kerstin, Toyoko, Eddie, Louise, Mark, Jack, Gabe, Sara, Brian, David, Ben, Pelle, Anna, Gustav, Chris, Sami, Dean, Abdi, Zach, Jimmy D, EKO Eddie, all members and extended family of CCW and A.W.E.S.O.M.E., and the CERN basketball team: Genf City wouldn't have been the same without you and I hope we'll stay in touch even when we're spread out across the world. Unfortunately, living in Geneva for most of my PhD meant that I could not spend as much time as I would like with my family and friends in Sweden. Jag vill rikta ett speciellt tack till mina närmaste vänner Kalle, Emad, Johan, Anna, Amanda, Kattis, Marie, Arvid, Wasa, Paulina, Erik, Mårten, Mackan, Anders – jag uppskattar verkligen er vänskap. Sist, men viktigast av allt, vill jag tacka min familj och släkt, ni betyder allt för mig. Vår gemenskap i "storfamiljen" är anledningen till att Stockholm alltid kommer vara en fast punkt för mig - tack för att ni finns.

Christian

# Preface

In the field of experimental particle physics, properties of fundamental particles are measured and theories describing the smallest constituents of matter and their interactions are tested with the aim to advance our understanding of our universe. The Standard Model of particle physics is a quantum field theory which has withstood extensive experimental tests and can predict fundamental processes in nature with an incredible accuracy. However, there are phenomena in nature which it cannot explain, and there is reason to believe there is new physics to be discovered at the TeV scale.

The Large Hadron Collider (LHC) at the CERN laboratory located on the Franco-Swiss border outside Geneva has entered its operational phase and started to provide experimental data for particle physics research. The LHC is currently producing proton-proton collisions with the world-record center-of-mass energy of 7 TeV at an instantaneous luminosity of up to $3 \times 10^{33}$ cm$^{-2}$s$^{-1}$. The ATLAS experiment is a general-purpose detector designed to make precision measurements of fundamental quantities and search for new physics phenomena by studying the processes that take place in these collisions.

This thesis presents two of the first published searches for new physics at the LHC, and documents published contributions to the ATLAS experiment of a more technical nature.

## About this thesis

The ATLAS experiment is designed to exploit the full discovery potential of the LHC and search for physics not previously observed in nature. To facilitate this, ATLAS comprises a number of sub-detectors which together identify particles and measure their properties and kinematics. Protons are collided head-on at the center of ATLAS every 25 ns which, combined with the sheer physical dimensions of the ATLAS detector, means particles from three consecutive collisions can co-exist in the detector at any given time. In order to accurately reconstruct the processes taking place in the collisions, the signals from the final state particles must be aligned in time with nanosecond precision. The published work presented in this thesis is divided into two areas, with timing as a recurring theme.

Firstly, two of the first published searches for new physics at the LHC are presented. Paper I describes a search for long-lived supersymmetric color multiplets, exploiting calorimeter time-of-flight and specific ionization energy loss in the inner tracking detector. Paper II presents a search for meta-stable heavily ionizing particles, where the

cluster shape in the electromagnetic calorimeter and ionization energy loss in a straw-based tracking detector are the main observables.

Secondly, timing is used to monitor the LHC beams and the synchronization signals that control the data taking in ATLAS. Work done in ATLAS on a beam pick-up based monitoring system and a beam-related input signal to the Level-1 trigger system is described in Papers III and IV. These papers provide an overview of the so-called BPTX[1)] system and its use in ATLAS, and present results from the very first period of LHC operation. Details pertaining to Papers I and II are presented in Parts III and IV, respectively.

This thesis is intended to be read as follows. Part I describes the motivation for the LHC and the experimental research program of the ATLAS experiment. The Standard Model (SM) of particle physics is briefly described, along with its shortcomings. Proposed theoretical extensions involving supersymmetry and extra dimensions are also given a cursory review. Finally, one class of particles predicted in several theories of beyond-SM physics, so-called Stable Massive Particles (SMPs) are described, and their expected interactions and resulting phenomenology are reviewed. The reader is given the required background knowledge about the experimental facilities in Part II. An overview of the LHC is followed by a description of the accelerator complex at CERN, and details about how the proton beams are formed. A review of the ATLAS experiment is then presented, with emphasis on the sub-detectors relevant to the work presented in this thesis. For the search analysis described in Paper I, the author played the leading role and made several crucial contributions. This article documents a signature-driven search inspired by models of supersymmetry featuring long-lived states. Details of in-depth studies not disseminated in the publication are given in Part III. Similarly, Part IV presents details relevant to the author's contributions to Paper II, which describes a search for exotic highly ionizing particles. Parts III and IV are to a large extent based on internally peer-reviewed supporting documentation to which the author of this thesis made considerable contributions, as outlined in the section "The author's contribution" below.

In Papers III and IV the work is already described to an appropriate depth, and therefore no additional supporting material is included in this thesis. For more details about the purpose, design and implementation of the BPTX system, Ref. [1] can be consulted.

The attached papers are:

Paper I: ATLAS Collaboration, *Search for stable hadronising squarks and gluinos with the ATLAS experiment at the LHC*, Phys. Lett. B 701:1-19, 2011, hep-ex/1103.1984.

Paper II: ATLAS Collaboration, *Search for massive long-lived highly ionising particles with the ATLAS detector at the LHC*, Phys. Lett. B 698, 353-370, 2011, hep-ex/1102.0459.

Paper III: C. Ohm, T. Pauly, *The ATLAS beam pick-up based timing system*, Nucl. Instrum. Meth. A 623:558-560, 2010, hep-ex/0905.3648.

[1)] BPTX is a loose acronym referring to the Beam Pick-up Timing system for the eXperiments.

Paper IV: C. Ohm, T. Pauly, *The software of the ATLAS beam pick-up based LHC monitoring system*, J. Phys. Conf. Ser. 219:022040, 2010, hep-ex/0909.5378.

This thesis follows the convention commonly employed in the experimental HEP community to use so-called natural units where $c = h/2\pi = 1$, where $c$ is the speed of light and $h$ is the Planck constant. Consequently, masses and momenta are given in GeV rather than GeV/$c^2$ and GeV/$c$, respectively.

## The author's contribution

I started my PhD studies at Stockholm University under the supervision of David Milstead and Torbjörn Moa in January 2008, and I immediately started working on searches for stable massive particles (SMPs). By surveying the sensitivity of various ATLAS subdetectors to delayed signals, I sought new prospective discriminators for slow-moving particles. I contributed to the development of Monte Carlo samples of various SMP signal samples, including event generator steering, configuration of extensions of the GEANT4 simulation package, and improvements concerning how timing and truth information is treated in the simulation.

In the period leading up to the first LHC operation with beam in September 2008, I continued working on the beam pick-up system I had developed when writing my master's thesis as a CERN technical student. I designed user interfaces for the monitoring applications and helped integrate the system with the computing infrastructure in the underground counting room and ATLAS control room. I served as the beam timing expert in the ATLAS control room when the first LHC beam reached ATLAS. The beam pick-up system proved crucial, both for its monitoring capabilities and as input to the Level-1 trigger system. In the week of single-beam operation that followed, the data analyzed and presented in Papers III and IV were collected.

When the LHC suffered delays during 2009, my focus shifted back to preparing for physics analysis and developing search strategies for SMPs using Monte Carlo simulations. I led the development of methods for measuring time-of-flight using the ATLAS calorimeters which is described in detail in a reviewed and approved internal ATLAS note [2]. I took a leading role when designing the search which resulted in Paper I, based primarily on the calorimeter time-of-flight method and $dE/dx$ measurements from the inner tracker. I also led the development of the data format used for the analysis. Using the full 2010 collision dataset the search was performed and the paper was accepted for publication in the beginning of 2011. Throughout the analysis I was the main analyst, did nearly all the technical work, made all the plots in the paper and nearly all of the ones in the supporting documents. I helped edit the paper, do extra checks during the review process and push the work through the approval process.

The work which led to Paper II was performed in parallel with the work described above. Though my primary focus was on Paper I, I contributed significantly to signal Monte Carlo simulation software (event generation and GEANT4 simulations) and helped

define the search strategy. I was one of two analysts that produced the final event yield tables for the results, and reproduced all figures in the paper and almost all from the supporting note as a cross-check.

In addition to the work related to the attached papers, I have made contributions to topics which are not described in this thesis. I initiated the process to create a new data analysis format dedicated to searches for long-lived particles, and together with Nick Barlow (Cambridge) implemented the needed software. We now maintain this data format and eight different searches for new physics in ATLAS depend on it for their analyses. Among the more technical contributions is the design and development of a suite of software tools for tagging cosmic muons in collision events or finding slow-moving exotic particles. I helped design the framework for transparently collecting timing data from various sub-detectors associated with reconstructed tracks, and implemented interface classes, the calorimeter-specific timing tool and a few event data model classes. Using these techniques I contributed to the first W/Z measurements in ATLAS by cleaning out contamination of muons from cosmic rays in the candidate events. I am also responsible for the distributed storage resources for the ATLAS Supersymmetry Working Group.

Since I spent most of my PhD at CERN, I had the opportunity to also contribute to the operation of the ATLAS detector. I have served as trigger shifter in the control room, and 24-hour on-call expert for the Level-1 Calorimeter trigger system. Among the detector-related activities are also contributions to the timing calibration of the Tile calorimeter in order to optimize its performance for the time-of-flight measurements used in Paper I.

I have presented results on behalf of ATLAS at eight international conferences and workshops, on topics related to both the detector and physics analyses.

Finally, I have been involved in an outreach project that aims to design an exercise that allows undergraduate students to analyze real ATLAS data and determine the mass and lifetime of the $K_s^0$ meson. I made improvements to the event display software, developed a series of cuts for distilling a set of events with visible $K_s^0$ decays, and produced the datasets.

# Part I

# Motivation for the Large Hadron Collider

*"Your theory is crazy, but it's not crazy enough to be true."*

– Niels Bohr, 1885-1962

# 1 The Standard Model

## 1.1 Overview

The Standard Model (SM) of particle physics is a quantum field theory that attempts to describe the elementary particles that make up the matter in our universe and the forces that govern their interactions. First the particle content is reviewed and then a description is given of the three fundamental forces of nature the theory purports to model. Unless explicitly stated otherwise the information about the SM in this chapter has been extracted from references [3] and [4].

### 1.1.1 Elementary particles

The visible matter in our universe is dominantly made up of protons, neutrons and electrons, the first two comprising up and down valence quarks. Together with the electron neutrino, these particles make up the first of three generations of spin-1/2 fermions in the SM. Each generation consists of two quarks possessing both electric and color charge, an electrically charged lepton and an electrically neutral lepton. The charged leptons are collectively denoted $\ell^-$. Table 1.1 lists the names and some of the properties of the particles contained in the SM.

All of the matter particles also have antiparticles differing by the sign of their charges, effectively nearly doubling the number of particles. The antiparticles are denoted by the same symbols as the particles but with a bar added over it, or in the case of the charged leptons and some hadrons, by changing the sign of the electric charge.

In the SM, the ways in which the fundamental particles can interact are modeled via exchanges of integer-spin bosons. The electromagnetic and strong forces are mediated by the massless photons and gluons, respectively. The weak force has two massive mediator particles, the $W^{\pm}$ and the $Z^0$.

The final particle is the Higgs boson which is the only particle predicted by the SM that has not been discovered experimentally. This particle is a consequence of postulating a new doublet of complex scalar fields needed in the theory to give mass to the $W^{\pm}$ and $Z^0$ bosons, as required by experimental results. The discovery or exclusion of the Higgs boson is one of the primary motivations for building the Large Hadron Collider.

| Type | Name | Symbol | Mass (MeV) | Electric charge ($e$) |
|---|---|---|---|---|
| Quarks | up | $u$ | 2.3 | +2/3 |
| (spin=1/2) | down | $d$ | 6 | -1/3 |
| | strange | $s$ | 95 | -1/3 |
| | charm | $c$ | 1250 | +2/3 |
| | bottom | $b$ | 4200 | -1/3 |
| | top | $t$ | $172.6 \times 10^3$ | +2/3 |
| Leptons | electron | $e$ | 0.511 | -1 |
| (spin=1/2) | electron neutrino | $\nu_e$ | $< 0.003$ | 0 |
| | muon | $\mu$ | 105.7 | -1 |
| | muon neutrino | $\nu_\mu$ | $< 0.19$ | 0 |
| | tau | $\tau$ | 1777.0 | -1 |
| | tau neutrino | $\nu_\tau$ | $< 18.2$ | 0 |
| Gauge bosons | photon | $\gamma$ | 0 | 0 |
| (spin=1) | gluon | $g$ | 0 | 0 |
| | $W$ | $W^\pm$ | $80.4 \times 10^3$ | $\pm 1$ |
| | $Z$ | $Z^0$ | $91.2 \times 10^3$ | 0 |
| Higgs boson | Higgs | $H$ | $> 114 \times 10^3$ | 0 |
| (spin=0) | | | | |

Table 1.1: The elementary particles of the Standard Model. The electric charges are given as a multiple of the elementary charge $e$.

### 1.1.2 Fundamental interactions

Three of the four fundamental forces of nature listed in Table 1.2 are described by the SM. The relative strengths quoted should be interpreted as loose approximations since the coupling of a force is not well-defined and depends on the energy scale of the interaction. Quantitatively, this can be understood as a consequence of so-called renormalization. Renormalization is a common name for techniques used to remove divergences in calculations, e.g. by redefining measurable quantities such that they effectively absorb the infinities. For example, virtual photons emitted and reabsorbed by an electron renders its mass and energy infinite in calculations, but if the mass is redefined to include the virtual particle corrections and set to the measured mass, the problem is avoided.

#### The electromagnetic interaction

The electromagnetic force is mediated by the photon ($\gamma$) and couples to all particles with electric charge. The theory that describes this interaction is called quantum electrodynamics (QED) and is one of the most accurate theories of physics ever constructed, withstanding experimental tests to a precision of better than 10 parts per billion. As an example,

| Name | Mediator | | Relative strength | Flavor conserving |
|---|---|---|---|---|
| Strong | gluon | ($g$) | 10 | Yes |
| Electromagnetic | photon | ($\gamma$) | $10^{-2}$ | Yes |
| Weak | $W$, $Z$ | ($W^{\pm}$, $Z^0$) | $10^{-13}$ | No |
| Gravity | graviton | ($G$) | $10^{-42}$ | - |

Table 1.2: The fundamental interactions of nature. The strong, electromagnetic and weak interactions are described by the SM, but gravity is not. Values taken from [3].

consider the electron magnetic moment, $\boldsymbol{\mu}$, given by

$$\boldsymbol{\mu} = -\frac{g}{2}\mu_B \frac{\mathbf{S}}{\hbar/2}, \tag{1.1}$$

where $\mu_B = e\hbar/2m$, $\mathbf{S}$ is the spin and $g$ is the so-called $g$-factor which deviates from the value 2 owing to vacuum fluctuations. Measurements and theoretical predictions for $(g-2)/2$ are given below, and show that the QED sector of the SM is able to reproduce extremely precise experimental data.

Theory: $(1159652153.5 \pm 28.0) \times 10^{-12}$ [5]
Experiment: $(1159652180.73 \pm 0.28) \times 10^{-12}$ [6]

### The strong interaction

The strong force is responsible for holding the quarks together in hadrons, e.g. the nucleons in atomic nuclei, and is described by the theory of quantum chromodynamics (QCD). The quarks in Table 1.1 are said to be of different *flavor*. The quarks are called *color triplets* referring to the fact that they carry one of three so-called *color charges*: red, green or blue. Just as electric charge, the color charge is inverted for antiparticles, thus the antiquarks carry *anticolor* and are referred to as *color antitriplets*. The mediator of the strong force, the gluon ($g$), is special since it itself carries color charge and is therefore also affected by the strong force. A massless gluon carries one color and one anticolor charge, and belongs to a so-called *color octet* of gluons.

While the strengths of other forces diminish with increasing distance, the strong interaction is very weak at distances comparable to the size of a hadron.Free quarks have not been observed [7] and it appears that they must be bound with other quarks in color neutral hadrons. This phenomenon, for which there is currently no theoretical justification, is called *color confinement*. A phenomenological explanation for this phenomenon is that the energy required to separate two quarks increases with distance, and at some point it is energetically favorable to produce a quark-antiquark pair from the vacuum. The process will repeat until the momenta separating the quarks have been transformed into a shower of hadrons, within the context of experiment commonly called a *jet*. Composite particles formed from quarks are called hadrons and come in two categories: baryons which are formed from three quarks, and mesons which are bound quark-antiquark pairs.

### The weak interaction

As described above, both the electromagnetic and strong forces have massless mediators. The weak interaction, however, has several mediator particles with high masses, effectively limiting its range. The $Z^0$ and $W^{\pm}$ bosons mediate the neutral and charged weak currents, respectively. The weak force couples to all the fundamental fermions of the SM, including the neutrinos. The weak interaction is the only force in the SM that breaks parity and only couples to left-handed particles, i.e. those that have spin and momentum of opposite direction. Another unique feature of the weak interaction is apparent in the beta decay of the neutron,

$$n \rightarrow p + e^- + \bar{\nu}_e. \tag{1.2}$$

In this process, one of the $d$-quarks in the neutron decays into an $u$-quark and a $W^-$, which immediately decays to an electron and an electron antineutrino,

$$d \rightarrow u + W^- \rightarrow u + e^- + \bar{\nu}_e, \tag{1.3}$$

as illustrated in Figure 1.1. The weak force is the only SM interaction that permits changing the flavor of a quark.

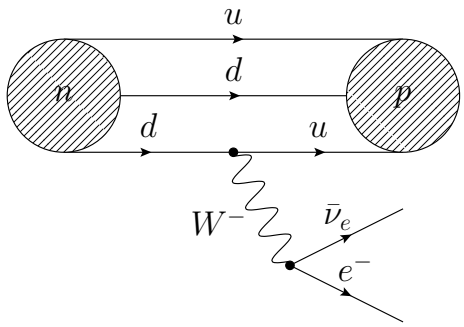


Figure 1.1: The neutron decays through the weak interaction.

The weakness of the weak force effectively increases the lifetime of all particles relying on it for their decay processes, like for example the charged pion ($\pi^+$) and hadrons containing a strange quark (e.g. $K_s^0$).

The electromagnetic and weak interactions have successfully been described as different manifestations of the same fundamental interaction and combined into a common electroweak interaction. This body of fundamental theoretical work is called *electroweak unification*.

## 1.2 Problems with the Standard Model

Despite the success in describing and predicting the physical processes observed in experiment, there are strong arguments as to why the SM cannot be the final theory of nature. In

this section a brief overview will be given of a few selected shortcomings of the SM and why it is believed to only be a low-energy approximation of a more fundamental theory.

The SM, by construction, does not attempt to describe the force of gravity. Despite being apparent in our daily lives, gravity is extremely weak on the scale of fundamental particles, compared to the strong and electroweak interactions. For this reason, its direct effects in experimental high-energy physics research will remain negligible in the foreseeable future. Attempts to develop a consistent theory of quantum gravity that can extend the SM have so far been unsuccessful. The effects of quantum gravity will become significant at high enough energies, and this scale is by many regarded as a maximum cut-off energy for when the SM can no longer be valid. A first-order approximation of when this must happen unless new physics is present, is the Planck scale. The Compton wavelength $\lambda_c = h/m$ is approximately the scale at which quantum effects start to play a significant role in how a particle behaves. A mass confined to a radius smaller than the Schwarzschild radius $r_s = 2Gm$ will collapse and form a black hole. Setting $\lambda_c = r_s$ gives an approximate expression for the Planck mass,

$$m_P = h/2G \approx 1.22 \times 10^{19} \text{ GeV}, \tag{1.4}$$

where $h$ and $G$ are the Planck and gravitational constants, respectively.

From cosmological observations of the movements of galaxies it has been inferred that the matter we can see constitutes only $\sim$17% of the mass in the universe. The rest of the mass is believed to be made up of *dark matter* [8]. Dark matter has not been detected through electromagnetic or strong interactions, and the presently favored interpretation is that it is composed of so-called weakly interacting massive particles (WIMPs) possessing zero electric charge with a mass around the TeV scale. Until fairly recently, neutrinos were considered excellent DM candidates, much due to their "undisputed virtue of being known to exist" [9]. However, they are not abundant enough to be the dominant component of dark matter [8]. Since the SM does not provide any candidate particles which could explain the dark matter, it is implied that it does not give a complete picture of the particle content of our universe. Dark energy, which makes up 74% of the energy in the universe, and which is thought to be responsible for the continued acceleration of the universe is even less well understood than dark matter [10].

The lack of observation of the Higgs boson can also be regarded as a weakness of the SM. From direct experimental searches for the Higgs boson at LEP, the lower mass limit is 114 GeV [11], and the combined data of the CDF and DØ experiments at the Tevatron have excluded the range $158 < m_H < 175$ GeV, with a 95% confidence level [12]. Recent results from the ATLAS [13] and CMS [14] collaborations at the LHC exclude a SM Higgs boson in the mass ranges 155-210 GeV and 290-400 GeV, and 149-206 GeV and 300-440 GeV, respectively. The SM does not predict the mass of the Higgs boson but, through precision measurements of other parameters, indirect constraints can be determined. The masses of the $W$ and $Z$ bosons have been measured with tremendous precision, corresponding to relative errors of 0.03% and 0.002%, respectively[1)]. Assuming

[1)] $m_W = 80.399 \pm 0.023$ GeV, $m_Z = 91.1876 \pm 0.0021$ GeV [6]

the SM Higgs boson is not accompanied by beyond-SM physics, electroweak precision measurements like these put constraints on the loop corrections caused by the Higgs boson, and thereby also its mass. From a combined fit including the masses of the weak bosons and the top quark, a fit of the unknown parameters in the SM can be made, indirectly excluding $m_H \gtrsim 200$ GeV [15, 16, 17]. Respecting the indirect mass limits for this hypothetical Higgs particle then leaves the window $114 < m_H \lesssim 150$ GeV.

From the theoretical side, another indication of the incompleteness of the SM is the so-called fine tuning problem. Following renormalization, the physical Higgs mass squared can be regarded as the quadratic sum of a so-called *bare mass* and contributions from quantum corrections,

$$m_H^2 = (m_H^2)_0 + \frac{kg^2\Lambda^2}{16\pi^2}, \tag{1.5}$$

where $(m_H)_0$ is the bare mass, a fundamental parameter of the theory. Here $g$ is an electroweak coupling and $k$ is a constant which can be calculated. The second term corresponds to a one-loop correction involving virtual particles, e.g. the top quark as depicted in Figure 1.2. The quantity $\Lambda$ corresponds to the scale up to which these processes are

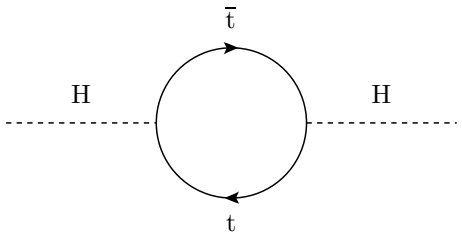


Figure 1.2: Feynman diagram of the first-order correction to the Higgs mass, featuring a $t\bar{t}$ loop.

calculated. This scale is chosen to be the cut-off scale above which the SM is no longer valid, often chosen to be the Planck scale. Requiring $m_H \sim 100$ GeV then means that there has to be an "unnatural" tuning or cancellation between two nominally uncorrelated terms which can have values up to $10^{19}$ [6]. This reasoning relies on the Planck scale to be the scale for new physics processes, and that no new physics is lurking around the electroweak scale or in what would be a vast 16 orders of magnitude desert of nothingness. This problem is often referred to as the *hierarchy problem* since it is a consequence of the disparity between the strenghts of the electroweak and gravitational forces. It is considered by many to be one of the primary reasons to look for new physics at the TeV scale. However, it is a purely theoretical problem, and this author, being an experimentalist, does not think he is entitled to an opinion about what values nature has chosen for its constants.

Finally, the neutrinos are massless in the SM, but measurements of neutrino oscillations [18] indicate that the neutrinos have non-zero masses. These could however be incorporated into the SM without introducing any major tensions [6].

# 2 Physics beyond the Standard Model

In this chapter, a brief overview of the motivation, features and phenomenology of two examples of Beyond the Standard Model (BSM) theories are presented. This is followed by a potential experimental signature that would allow direct detection of new states in a detector.

## 2.1 Supersymmetry

### 2.1.1 Overview

By postulating that all SM particles have partner particles, differing only in spin, theories of supersymmetry (SUSY) attempt to solve several problems of the SM [19, 20, 21]. For every SM fermion, a supersymmetric partner boson is added, and vice versa. Much like the concept of antimatter added partner particles only differing in the sign of their charges, supersymmetry doubles the number of fundamental particles. However, unlike antimatter, the supersymmetric partners have not been observed experimentally. This indicates that if supersymmetry exists, the supersymmetric particles have masses different from their corresponding SM particles, implying supersymmetry is a broken symmetry.

The nomenclature is to add an s to the beginning of the SM fermion names, and -ino to the end of SM boson names. The new particles are denoted by the same symbols as their SM partners, but crowned with a tilde. For example, the SUSY partner of the tau is the stau, denoted $\tilde{\tau}^-$ and the partner of the gluon is the gluino, denoted $\tilde{g}$.

Among the attractive features of SUSY is that it can provide a dark matter candidate. In supersymmetry, a new quantum number called $R$-parity is added,

$$P_R = (-1)^{2s+3B+L}. \tag{2.1}$$

$R$-parity is a multiplicative quantum number, and all SUSY particles have $P_R = -1$ while SM particles has the value $P_R = 1$. As a consequence, if $R$-parity is fully conserved, a supersymmetric particle must always decay to at least one other supersymmetric particle, and they must always be produced in pairs. This results in the requirement that the lightest supersymmetric particle (LSP) must be absolutely stable, making it a possible candidate for dark matter. Examples of SUSY particles that do not couple to the strong

or electromagnetic interactions and could serve as WIMP dark matter candidates include the neutralino ($\tilde{\chi}^0$) and gravitino ($\tilde{G}$) [8].

There are also several purely theoretical motivations for SUSY. As an example, it enables the approximate unification of the coupling constants of the electromagnetic, weak and strong interactions at high energies. It is also theoretically appealing with SUSY at the TeV scale since it could keep the fine-tuning of the Higgs mass and the hierarchy problem described in Section 1.2 at an "acceptable" level by providing internal loop diagrams that largely cancel the contributions from quantum effects.

### 2.1.2 Phenomenology

The Minimal Supersymmetric Standard Model (MSSM) is the most general supersymmetric extension of the SM [19]. With $\sim$100 free parameters the MSSM can accommodate several types of experimental signatures. The phenomenology of models and points in parameter space are determined in part by the mass hierarchies and the resulting LSP and next-to-lightest supersymmetric particle (NLSP). It is a general feature of the models that the production of SUSY particles results in long cascade decays with several promptly decaying intermediate states. Therefore, the typical search channels at hadron colliders involve high-$p_{\mathrm{T}}$ jets and leptons, often with high multiplicities. In the case of $R$-parity conserving SUSY with a dark matter candidate LSP, the signature can also feature so-called *missing transverse momentum*, commonly referred to as *missing transverse energy* and denoted by $E_{\mathrm{T}}^{\mathrm{miss}}$. $E_{\mathrm{T}}^{\mathrm{miss}}$ is calculated by combining the projections of the momenta of the reconstructed particles in the plane transverse to the beam line. The failure to measure the momentum of the LSP will cause an imbalance, something that can also happen in SM processes involving neutrino production.

## 2.2 Theories of Extra Dimensions

There are several theories involving additional spatial dimensions. In Universal Extra Dimentions (UED) scenarios, the fields describing the matter and force carriers of the SM can propagate in these extra dimensions. Analogously to $R$-parity in SUSY, a new discrete conserved Kaluza-Klein ($KK$) quantum number will give rise to a phenomenology yielding new stable states, and thereby potential dark matter candidates [22]. Additional motivations for theories of extra dimensions include explanations as to why gravity is so weak, and a lowered Planck scale [23].

In terms of experimental signatures, UED can look similar to SUSY and feature long decay chains giving final states with $E_{\mathrm{T}}^{\mathrm{miss}}$, high multiplicities of high-$p_{\mathrm{T}}$ jets and leptons [24].

## 2.3 Stable Massive Particles and their interactions

Most theories of BSM physics have a multitude of free parameters. Depending on what point nature has chosen (if any) in parameter space, the resulting phenomenology can be very different. Both frameworks discussed in the previous section feature regions in parameter space where stable[1)] massive particles (SMPs) exist. For example, such particles appear in both *R*-parity conserving [25, 26, 27, 28, 29, 30, 31] and violating [32, 33, 34] SUSY.

SMPs often offer striking experimental signatures with very little or no SM background. For this reason, searches for SMPs have always been performed when a new energy regime is opened up for experimental exploration.

This section reviews what mechanisms can cause a particle to be long-lived, and gives a few examples of SMPs predicted in the literature along with a summary of limits from collider experiments. Finally, an overview of their expected interactions and resulting phenomenologies are presented.

### 2.3.1 Suppressed decays

New unknown particles could be long-lived due to the same mechanisms that render some SM particles to have non-negligible lifetimes [35].

1. A new conserved quantum number, like the example with *R*-parity explained in Section 2, would cause the lightest particle carrying it to be long-lived. In the SM, this is the case for the proton which is the lightest hadron carrying baryon number, and the electron which is the particle with the lowest mass carrying electric charge.

2. If the effective coupling through which the decay occurs is suppressed, this can cause a long lifetime. A good SM example of this is the muon which decays through a weak interaction as shown in Figure 2.1.

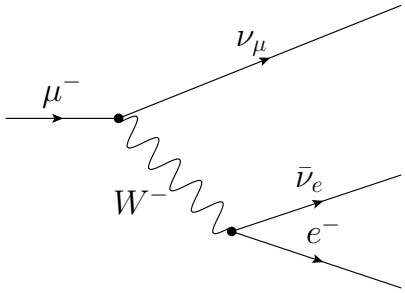


Figure 2.1: Decay diagram of a muon, governed by the weak interaction.

[1)] In this thesis, the word stable is used for particles with decay lengths $\gtrsim$ the size of a typical collider experiment.

3. If the mass difference between the particle and its combined decay products is small, the lack of available phase space for the decay products results in an extended lifetime. An example of a well-known decay for which this is true is the neutron decaying to an electron, proton and antineutrino.

### 2.3.2 Types of stable massive particles

Several types of stable massive particles have been envisaged through phenomenological studies. The details of their expected experimental signatures vary [7]. In this section three kinds of SMPs are considered, covering the signatures relevant to the work presented in this thesis.

#### Charged lepton-like stable massive particles

In for example SUSY, models exist that predict electrically charged lepton-like particles. One example of such a model is Gauge-Mediated Supersymmetry Breaking (GMSB) [20] which can feature one or (possibly several nearly mass-degenerate) meta-stable NLSP sleptons ($\tilde{\ell}$). In this scenario, the slepton would be long-lived due to the small difference between its mass and that of the LSP, the gravitino ($\tilde{G}$).

#### Hadron-like stable massive particles

A long-lived particle possessing color charge is expected to hadronize to form a color singlet hadron, due to the color confinement mechanism described in Section 1.1.2. A stable massive particle with color charge can therefore give rise to several long-lived hadronic states, which within SUSY are called $R$-hadrons[2)]. As an example, in scenarios based on Split SUSY [21] the separation of the mass scales of the gauginos and the scalars can result in long-lived gluinos. Figure 2.2 shows the gluino decay diagram which is heavily suppressed due to the internal line corresponding to a $\tilde{q}$ with $m_{\tilde{q}} \gg m_{\tilde{g}}$.

In the fragmentation process of long-lived exotic color triplets and octets, the parton will acquire a light quark system. The electric charge of the resulting hadron will depend on its quark contents. A stable color octet, $C_8$, here exemplified by the gluino ($\tilde{g}$), can form meson states with a quark-antiquark pair, $C_8q\bar{q}$ and (anti)baryon states together with three quarks, $(C_8\bar{q}\bar{q}\bar{q})C_8qqq$. Similarly, a color triplet, $C_3$, e.g. a stop quark, $\tilde{t}$, can form mesons ($C_3\bar{q}$) and baryons ($C_3qq$) [7, 36, 37, 38, 39].

Table 2.1 presents results from the hadronization of a stable $\tilde{g}$ and $\tilde{t}$ as predicted by Monte Carlo simulations using the PYTHIA [40] and HERWIG [41] event generators. Following the hadronization, mesonic states are expected to dominate. Though HERWIG does not support the $\tilde{g}g$ and baryonic states, it should be noted that the fraction of electrically charged gluino-based $R$-hadrons produced by both generators is approximately the same (45%). For production of long-lived squarks the expected fraction of electrically charged

[2)] While the term $R$-hadron refers to the $R$-parity in SUSY, the discussions about stable color charged particles and their phenomenology apply to other scenarios as well, e.g. $KK$-excited gluons in UED.

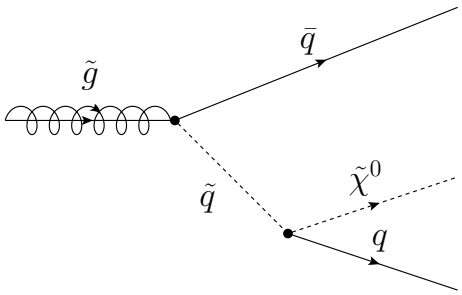


Figure 2.2: The decay diagram for the gluino, heavily suppressed in Split SUSY scenarios due to the internal squark line and $m_{\tilde{q}} \gg m_{\tilde{g}}$. The similarity with the decay of the muon depicted in Figure 2.1 is striking.

states following hadronization is predicted by PYTHIA to be slightly higher (60%).

#### Highly ionizing particles

The observation of a exotic massive long-lived particle possessing a large electric charge $|q| \gg e$, where $e$ is the elementary charge, would represent striking evidence for physics beyond the Standard Model. Since the energy loss due to ionization is proportional to $q^2$, we here classify them as highly ionizing particles (HIPs). Examples of putative particles with high electric charge which can give rise to HIP signatures include $Q$-balls [42], stable micro black-hole remnants [43] and so-called dyons, i.e. particles with magnetic charge [44].

Dyons such as magnetic monopoles have been proposed and would also suffer considerable ionization energy losses. The existence of a magnetic monopole is considered to be appealing from a theoretical standpoint since it could explain electric charge quantization [45, 46].

In contrast to the lepton-like and hadron-like SMPs described above and motivated by e.g. SUSY scenarios, calculations for the production of HIPs are problematic. Their large electromagnetic coupling of prevents a perturbative approach [6], and therefore no reliable calculations exist so far for their production. As a consequence, results of searches for HIPs in which no signal is observed are best presented as cross section limits rather than mass limits.

### 2.3.3 Existing limits

Table 2.3.3 lists the published collider-based limits for lepton-like and hadron-like SMPs previous to the results presented in this thesis. Searches for $R$-hadrons at earlier colliders were typically based on either the possibility of a highly ionizing particle in an inner tracking system (LEP) [47, 48, 49] or a slow-moving muon-like object (Tevatron) [50, 51, 52, 53, 54]. The latter limits rely on an assumption that the $R$-hadron is electrically charged when it leaves the calorimeters and enters the muon detectors. However, as will

| $R$-hadron | PYTHIA Fraction (%) | HERWIG Fraction (%) |
|---|---|---|
| $R^{+}_{\tilde{g}u\bar{d}}$, $R^{-}_{\tilde{g}d\bar{u}}$ | 34.2 | 28.2 |
| $R^{0}_{\tilde{g}u\bar{u}}$, $R^{0}_{\tilde{g}d\bar{d}}$ | 34.2 | 28.2 |
| $R^{+}_{\tilde{g}u\bar{s}}$, $R^{-}_{\tilde{g}s\bar{u}}$ | 9.7 | 17.5 |
| $R^{0}_{\tilde{g}d\bar{s}}$, $R^{0}_{\tilde{g}s\bar{d}}$, $R^{0}_{\tilde{g}s\bar{s}}$ | 10.4 | 26.1 |
| $R^{0}_{\tilde{g}g}$ | 9.9 | — |
| $R^{++}_{\tilde{g}}$, $R^{--}_{\tilde{g}}$ (anti)baryons | 0.1 | — |
| $R^{+}_{\tilde{g}}$, $R^{-}_{\tilde{g}}$ (anti)baryons | 0.8 | — |
| $R^{0}_{\tilde{g}}$ (anti)baryons | 0.7 | — |

(a)

| $R$-hadron | Fraction (%) |
|---|---|
| $R^{+}_{\tilde{t}\bar{d}}$ | 39.6 |
| $R^{0}_{\tilde{t}\bar{u}}$ | 39.6 |
| $R^{+}_{\tilde{t}\bar{s}}$ | 11.8 |
| $R^{++}_{\tilde{t}}$ baryons | 0.8 |
| $R^{+}_{\tilde{t}}$ baryons | 6.7 |
| $R^{0}_{\tilde{t}}$ baryons | 1.5 |

(b)

Table 2.1: Example predictions from PYTHIA and HERWIG of the fractions of different species of $R$-hadrons following the hadronization of a gluino (a) and a stop quark (b). Table taken from [7].

be described below, the hadronic scattering in the dense calorimeter material and the mass hierarchy of the possible states can render the $R$-hadron dominantly electrically neutral in the muon spectrometer. Such an effect would be expected for $R$-hadrons formed from sbottom-like squarks; the situation for gluino-based $R$-hadrons is unclear. The most conservative mass limits for different types of $R$-hadrons are therefore 300-400 GeV for gluinos [39, 55, 56], 92 GeV for sbottoms [7] and 249 GeV for stops [54]. A discovery window at low masses is therefore open at the LHC for low-luminosity searches as seen in recent papers matching the results from the Tevatron [56, 57]. In addition to the limits published before the work presented in this thesis, there are also new limits on long-lived

gluinos and sleptons based on a signature in the muon spectrometer in ATLAS [58] as well as recent preliminary results from CMS that exclude stable gluinos with $m < 899$ GeV, and stop quarks with $m < 620$ GeV [59].

| $\sqrt{s}$ ( GeV) | Collisions | Experiment | Particle | Mass limit ( GeV) | Ref. |
|---|---|---|---|---|---|
| 1960 | $p\bar{p}$ | CDF | Squark | $m_{\tilde{t}} > 249$ | [60] |
| 1800 | $p\bar{p}$ | CDF | $4^{th}$ gen. quark | $m_{t'} > 220, m_{b'} > 190$ | [50] |
| 130-209 | $e^+e^-$ | OPAL | Heavy leptons | $m_{l'} > 102$ | [61] |
| 133-208 | $e^+e^-$ | L3 | Heavy leptons | $m_{l'} > 103$ | [62] |
| 91.2-209 | $e^+e^-$ | ALEPH | Squark | $m_{\tilde{t}} > 95, m_{\tilde{b}} > 92$ | [47] |
| 130-183 | $e^+e^-$ | DELPHI | Squark | $m_{\tilde{t}} > 80, m_{\tilde{b}} > 40$ | [48] |
| 130-183 | $e^+e^-$ | DELPHI | Free squark | $m_{\tilde{t}} > 84$ | [48] |
| 7000 | $pp$ | CMS | Squark | $m_{\tilde{t}} > 202$ | [56] |
| 91.2 | $e^+e^-$ | ALEPH | Gluino | $m_{\tilde{g}} > 27$ | [47] |
| 91.2 | $e^+e^-$ | DELPHI | Gluino | $m_{\tilde{g}} > 18$ | [49] |
| 7000 | $pp$ | CMS | Gluino ($\mu$-like signature) | $m_{\tilde{g}} > 311$ | [56] |
| 7000 | $pp$ | CMS | Gluino (no muon track) | $m_{\tilde{g}} > 398$ | [56] |
| 189-209 | $e^+e^-$ | ALEPH | Slepton | $m_{\tilde{\tau}} > 97, m_{\tilde{\mu}} > 97$ | [63] |
| 130-208 | $e^+e^-$ | DELPHI | Slepton | $m_{\tilde{\tau}} > 98, m_{\tilde{\mu}} > 98$ | [64] |
| 189-209 | $e^+e^-$ | OPAL | Slepton | $m_{\tilde{\tau}} > 98, m_{\tilde{\mu}} > 98$ | [65] |
| 1960 | $p\bar{p}$ | D0 | Chargino | $m_{\tilde{\chi}^\pm} > 206$ | [51] |
| 189-209 | $e^+e^-$ | ALEPH | Chargino | $m_{\chi^\pm} > 101$ | [66] |
| 130-189 | $e^+e^-$ | DELPHI | Chargino | $m_{\chi^\pm} > 93$ | [67] |
| 189 | $e^+e^-$ | L3 | Chargino | $m_{\chi^\pm} > 94$ | [68] |

Table 2.2: A list of experimental mass limits on lepton-like and hadron-like stable massive particles from collider experiments [7], completed with limits from [51, 56, 60].

The lack of firm theoretical descriptions of the production mechanisms for HIPs makes it difficult to predict how kinematics and cross sections are affected by center-of-mass energy and particle type. It also complicates meaningful comparisons between limits established at different colliders. Several dedicated experiments have been performed and a few are mentioned here as examples. The MODAL experiment installed in the empty intersection point I5 at LEP-1 quoted sensitivity to HIPs with electric charge of up to $|240e|$ [69]. Searches using passive detectors in the OPAL cavern resulted in competitive limits for Dirac monopoles, exluding production cross sections above 3 nb for $m < 45$ GeV and magnetic charge in the range $0.9g_D$-$3.6g_D$, where $g_D$ is the fundamental Dirac unit of magnetic charge [70]. A summary of limits from searches for highly charged particles and magnetic monopoles can be found in [7].

SMPs have also been sought in ordinary matter. If strictly stable particles were produced in the early universe they could be bound in the matter around us. Searches for e.g. heavy hadrons have therefore been performed in e.g. meteorites [71], nuclear isotopes [72], and water [73], but without any evidence for signal. These searches are complementary to the searches conducted at collider experiments since they offer a competitive reach in mass, at the price of a very limited sensitivity to SMPs with finite lifetimes.

Finally, observervations of an SMP at a collider experiment could possibly have pro-

found implications for cosmology. For example, any SMPs produced at a collider would also have been produced in the early universe and possibly affected the evolution of the universe. Requirements on the relic density sets an upper limit on the mass of an absolutely stable gluino around a few TeV [7, 26], though mechanisms have been proposed to relax such limits [26]. An excessively long-lived but decaying gluino ($\tau_{\tilde{g}} > 100$ s) is also constrained since it would affect the delicate balance of light elements and compromise Big Bang nucleosynthesis [74]. In conclusion, there are no solid cosmological constraints on SMPs in the regions of $m$-$\tau$ space accessible at TeV-scale colliders [7].

### 2.3.4 Interactions with matter

The experimental signatures of SMPs depend on which ways, and to what extent, the SMP interacts with the detector. In the following the expected interactions for the types of SMPs described above are reviewed.

Both the lepton-like and hadron-like SMPs are expected to give rise to penetrating signatures in a detector. In contrast, HIPs are expected to undergo dramatic ionization energy losses when traversing matter which could, depending on the kinematics, result in their stopping inside the detector volume. At modern collider experiments, all classes of SMPs discussed here are expected to be produced with momenta comparable to their mass, resulting in a speed $\beta = v/c$ significantly lower than unity.

It should be noted that also a small fraction of lepton-like and hadron-like SMPs can come to a stop inside the detector, leading to out-of-time decays when there are no collisions in the detector. This signature falls outside the scope of this thesis, but has been covered by other studies [57, 75, 76].

#### Electromagnetic energy losses

Models of electromagnetic energy loss for charged particles passing through matter are well-established [77, 4] and predict that SMPs possessing a non-zero electric charge $q$ will lose energy through ionization. The magnitude of the energy loss per unit length traversed in a material is determined by the function describing its *stopping power*, often denoted $-dE/dx$. For a given material, this function depends on the velocity $v$ of the particle, as seen in Figure 2.3. Muons constitute the primary background in searches for penetrating SMPs [78] although, by exploiting the difference in $-dE/dx$ at a given momentum, SMPs can be distinguished from the SM backgrounds.

Like SMPs with moderate electric charge, HIPs with high mass would not lose energy through bremsstrahlung, and unless they are hadron-like they would also not undergo hadronic interactions. Therefore, HIPs are not expected to produce extended showers in the calorimeters but deposit large amounts of energy through ionization in a narrow area along their trajectory. To first order the ionization energy loss of particles with high electric charge is described by the Bethe-Bloch equation and scales with $q^2$. The ionization energy losses suffered by a Dirac monopole are expected be similar to those for a particle with electric charge $q = 137e/2$ [7], i.e. approximately 4700 times higher than for an

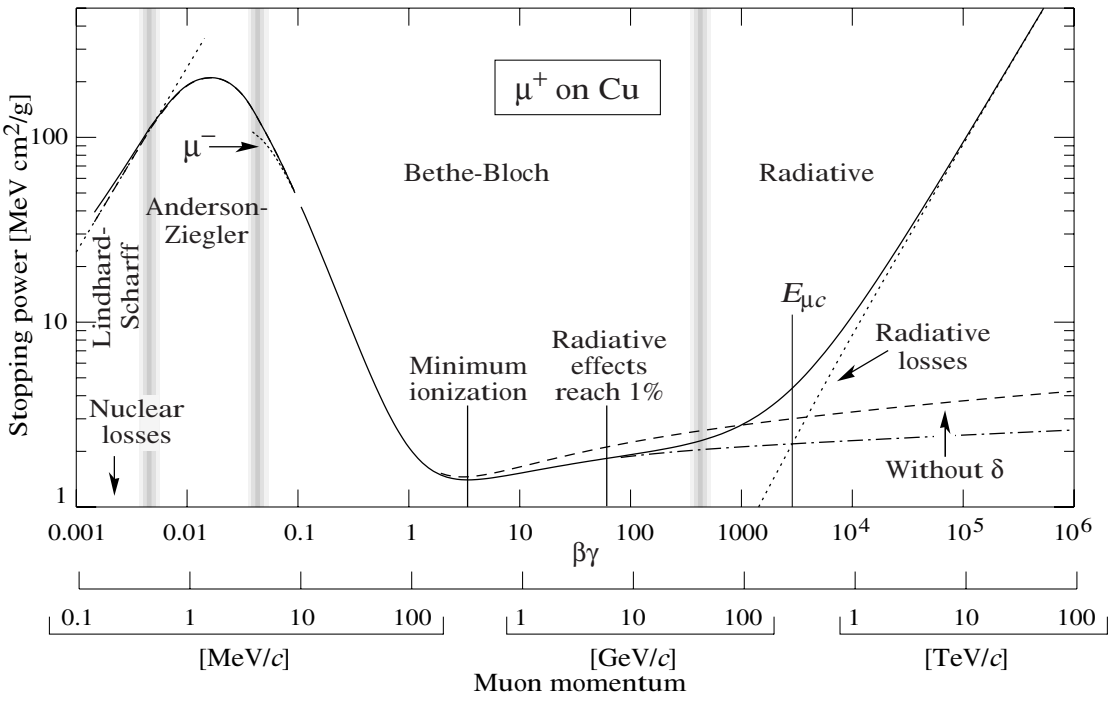


Figure 2.3: Stopping power, often denoted $-dE/dx$, for antimuons traversing Cu as a function of $\beta\gamma = \beta/\sqrt{1-\beta^2}$, where $\beta = v/c$, and the momentum $p$ [4].

identical particle with charge $e$. Depending on the kinematic range and charge of interest, different SM particles constitute the dominating background, but due to the spectacular characteristics of the expected energy losses, signal and background can be separated quite well.

It is also worth noting that the trajectory of a magnetically charged particle through a magnetic field will be deflected along the field lines rather than orthogonally, as for electrically charged particles.

### Hadronic processes

Here a brief summary is given of studies of how exotic hadrons containing one heavy parton are expected to interact with matter. For more details the main references [36, 37, 38, 39] should be consulted.

It can be reliably assumed that the massive parton will not interact and can be considered a spectator in these processes. This is due to the per-parton scattering cross section being proportional to $1/m^2$, effectively rendering it negligible for the heavy parton. The light quarks bound in the hadron can interact with matter, e.g. detector material if produced in a collider experiment. However, due to its high mass, the heavy parton carries

almost all the momentum of the composite particle, limiting the kinetic energy it can lose due to scattering of its lighter constituents with matter. Owing to the limited kinetic energy of the light quark system, the scattering of squark-based *R*-hadrons can be described by techniques used to model low energy hadron-hadron processes [39, 79]. The cross sections for these processes are not likely to differ by orders of magnitude compared to those of proton-proton and pion-proton interactions. Because of these features, a hadronic SMP is not expected to cause high-energy hadronic showers to the same extent as SM hadrons when passing through a typical collider experiment.

This penetrating, muon-like experimental signature can however be complicated by the peculiar nature of some of the hadronic processes. As an example, consider a $\tilde{g}$-based *R*-hadron $\tilde{g}d\bar{d}$ interacting with a proton, as shown in the leftmost diagram of Figure 2.4. The illustrated process features charge exchange via inelastic scattering, causing an electrically neutral *R*-hadron to acquire charge. The middle diagram shows a similar process by which a neutral meson state is transformed into a charged baryon state. As a final example, the illustration on the right in Figure 2.4 shows the formation of a nuclear resonance with double electric charge. However, the production of these resonant states in scattering are expected to be supressed [37].

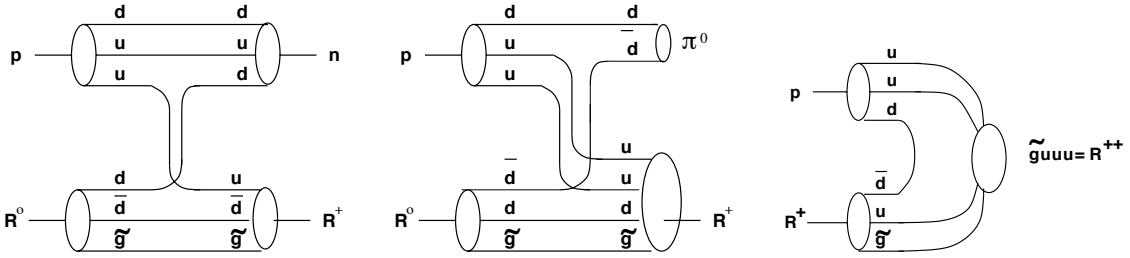


Figure 2.4: Diagrams adopted from [7] showing scattering processes involving *R*-hadrons interacting with neutrons and protons.

Through these processes, spectacular detector signatures with virtually no SM background can arise for hadronic SMPs. Current general-purpose detectors at hadron colliders are composed of three main parts, moving outwards from the collision point: an inner tracking detector, calorimeters, and a muon spectrometer (see Chapter 4). The momenta of charged particles are measured both in the inner tracker and the muon spectrometer, with the dense calorimeters measuring the energy deposited in between. The signature of a particle that undergoes charge exchange when passing through the calorimeters could therefore have a track in only one of the tracking detectors. Through multiple interactions, e.g. of the types illustrated in Figure 2.4, the propagating hadron can have positive charge in the inner tracker and negative charge in the muon spectrometer, resulting in tracks bending in opposite directions.

The processes in which *R*-mesons convert to *R*-baryons are exothermic and would thus be expected to take place while the reverse processes would be kinematically disfavored. The baryon-to-meson processes would suffer a further suppression due to the need for

the $R$-baryon to interact with a meson or antibaryon state in order for it to lose its baryon number [37]. It could therefore be expected that $R$-hadrons containing squarks or gluinos, which would likely be dominantly produced as mesonic states in the hadronization process [7, 80], would leave the calorimeter system as baryonic states. $R$-hadrons formed from antisquarks are not expected to form long-lived antibaryon states but $\bar{\tilde{q}}q$ states. However, if this meson state oscillates into its antiparticle, $\tilde{q}\bar{q}$, this would then be likely to form a stable $\tilde{q}qq$ baryon state in subsequent hadronic scattering processes. The mass spectra for squark-based $R$-hadrons can be inferred from heavy SM quark (i.e. charm, bottom) mass hierarchies [7, 27, 37] as the mass hierarchies of heavy quark hadrons and heavy squark hadrons have negligible spin-dependence [27]. This implies that the lightest baryonic state to which squark-based $R$-hadrons would eventually convert and decay is $\tilde{q}ud$, the supersymmetric analog to the $\Lambda_c \equiv cud^+$ and $\Lambda_b \equiv bud^0$ states. For a down-type squark such as the sbottom quark, the dominating state after passage through the calorimeters would be electrically neutral, rendering a search based on the muon spectrometer ineffective [39]. For a stable stop quark, a significant fraction is expected to be charged. For the case of a stable gluino it is not possible to directly infer the lightest baryon state from known particle spectra.

A number of scattering models have been proposed, and in this work the so-called *generic* [37, 38], *regge* [39, 79], and *intermediate* [55] are considered and reviewed below. In common for all of them is that they share a central picture of a non-interacting heavy parton.

**The generic model**

This model is based on few assumptions and allows a wide range of signatures in the detector. It allows all possible 2-to-2 and 2-to-3 processes, with individual processes weighted according to phase space factors. It assumes a cross section which does not depend on energy. It therefore represents an inclusive approach though it is not based on any dynamical theory. It assumes that baryonic $R$-hadron states are degenerate and thus do not all decay down to a lowest-mass state. Among the allowed signatures are sign-flipping of the electric charge and the formation of doubly charged states.

**The intermediate model**

The intermediate model is only applicable to stable gluinos. It employs the exact same scattering model as the generic model. However, it assumes a gluino $R$-hadron mass spectrum which is based on recent bag model calculations [81, 82, 83, 55].

**The Regge model**

The Regge model assumes a cross section derived from low-energy hadron scattering and makes calculates energy losses using the triple Regge formalism [84, 85]. This model was developed for squark-based $R$-hadrons and later extended to include a treatment of gluinos.

Compared to the ionization energy loss which is continuous, the energy lost through hadronic processes is stochastic in nature. Based on asymptotic values of scattering cross section measurements for SM hadrons scattering off nucleons, the per-parton cross section can be approximated to 12 mb [37]. A hadron-like SMP is therefore expected to undergo hadronic scattering $\mathcal{O}(10)$ times when passing through a modern general-purpose detector, which means the final charge state can to very good approximation be considered decoupled from the initial one. Since the cross section for hadronic interactions is modeled to be proportional to the number of light quarks in the hadron, some conclusions can be drawn regarding the magnitude of the energy depositions for various colored particles. A color octet and triplet will almost immediately form baryon states when interacting with the detector, resulting in hadrons with three and two interacting light constituents, respectively ($C_8qqq$ and $C_3qq$). For the antitriplet, a meson final state, $\bar{C}_3q$, is more likely due to the lack of antimatter in the detector material, suppressing the formation of an antibaryon state. Even if an antibaryon state would be formed, it would immediately annihilate with the normal matter in the detector. In case of observation, the relative magnitude of the energy depositions of the SMPs in the same event could therefore shed some light on the nature of the stable parton. To further distinguish between these cases the track charge distributions can be studied. In the case of pair production of an exotic long-lived color octet or down-type triplet, both hadrons resulting from the hadronization could have the same charge, something that could not happen for an up-type color triplet unless fractionally charged hadrons or pentaquarks are considered.

# Part II

# Experimental facilities

*"The true method of knowledge is experiment."*

– William Blake, 1757-1827

# 3 The Large Hadron Collider

## 3.1 Overview

The Large Hadron Collider (LHC) [86] is a proton-proton collider at the CERN laboratory outside of Geneva, Switzerland. The machine is installed inside a 27 km long underground tunnel and designed to collide protons[1)] at the unprecedented center-of-mass energy of 14 TeV at a luminosity of $10^{34}$ cm$^{-2}$s$^{-1}$. Figure 3.1 shows an illustration of the area around the French-Swiss border near Lac Léman where the LHC is built, and the locations of the four major experiments that will study the collisions it produces: ALICE [87], ATLAS [88], CMS [89] and LHCb [90]. Using superconducting NbTi cables cooled to approximately 1.9 K by superfluid He, the LHC magnets produce a field of over 8 T in order to bend the trajectory of the particles circulating inside the accelerator. In addition to the 1232 dipole magnets bending the beams into orbit, the LHC has many multipole magnets used to focus the beams close to the collision points, and extensive beam instrumentation for diagnostics and control of the beams.

In September 2008, the LHC successfully circulated its first proton bunches, enabling several of the LHC experiments to study their first beam-related data. Due to a severe technical malfunction the accelerator was taken out of operation after only one week, before collisions were achieved, and intense investigations and consolidation work followed. The first $pp$ collisions were finally recorded by ATLAS on November 23, 2009, and throughout 2010 the luminosity quickly increased. For the 2010 run relevant to the results in this thesis, the center-of-mass energy was 7 TeV. Figure 3.2 shows the cross sections for various physics processes in proton-(anti)proton collisions as a function of center-of-mass energy. When operating with the nominal design parameters, the inelastic proton-proton cross section of 80 mb at the LHC will result in a total rate of approximately $10^9$ inelastic proton-proton collisions per second.

ATLAS and CMS are general-purpose detectors designed to survey the new energy regime made accessible for particle physics research by the LHC. LHCb will primarily study *CP*-violation through rare decays of hadrons containing *b*-quarks. Finally, ALICE is optimized to study heavy-ion collisions in search for new states of matter in extreme energy densities, such as a color-deconfined state which is often referred to as a *quark-gluon plasma* [92]. The four papers attached to this thesis describe work carried out as a member of the ATLAS collaboration, and an overview of the ATLAS detector is therefore

[1)] The LHC will also collide $Pb^{82+}$ ions.

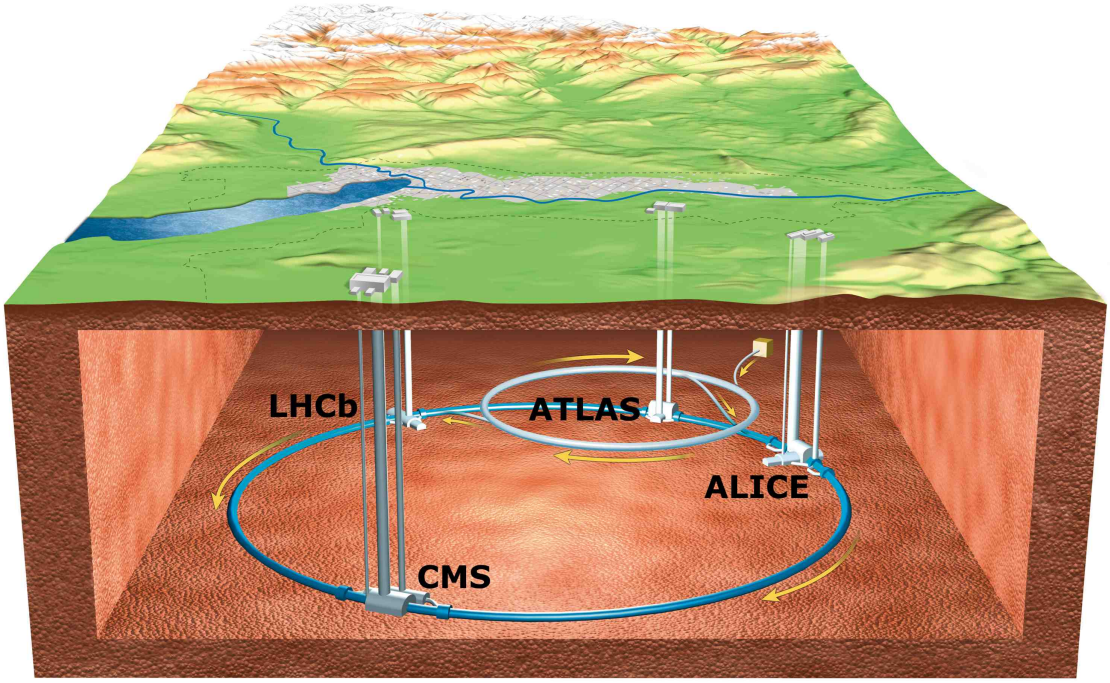


Figure 3.1: The 27 km long Large Hadron Collider and the four major experiments: ALICE, ATLAS, CMS and LHCb.

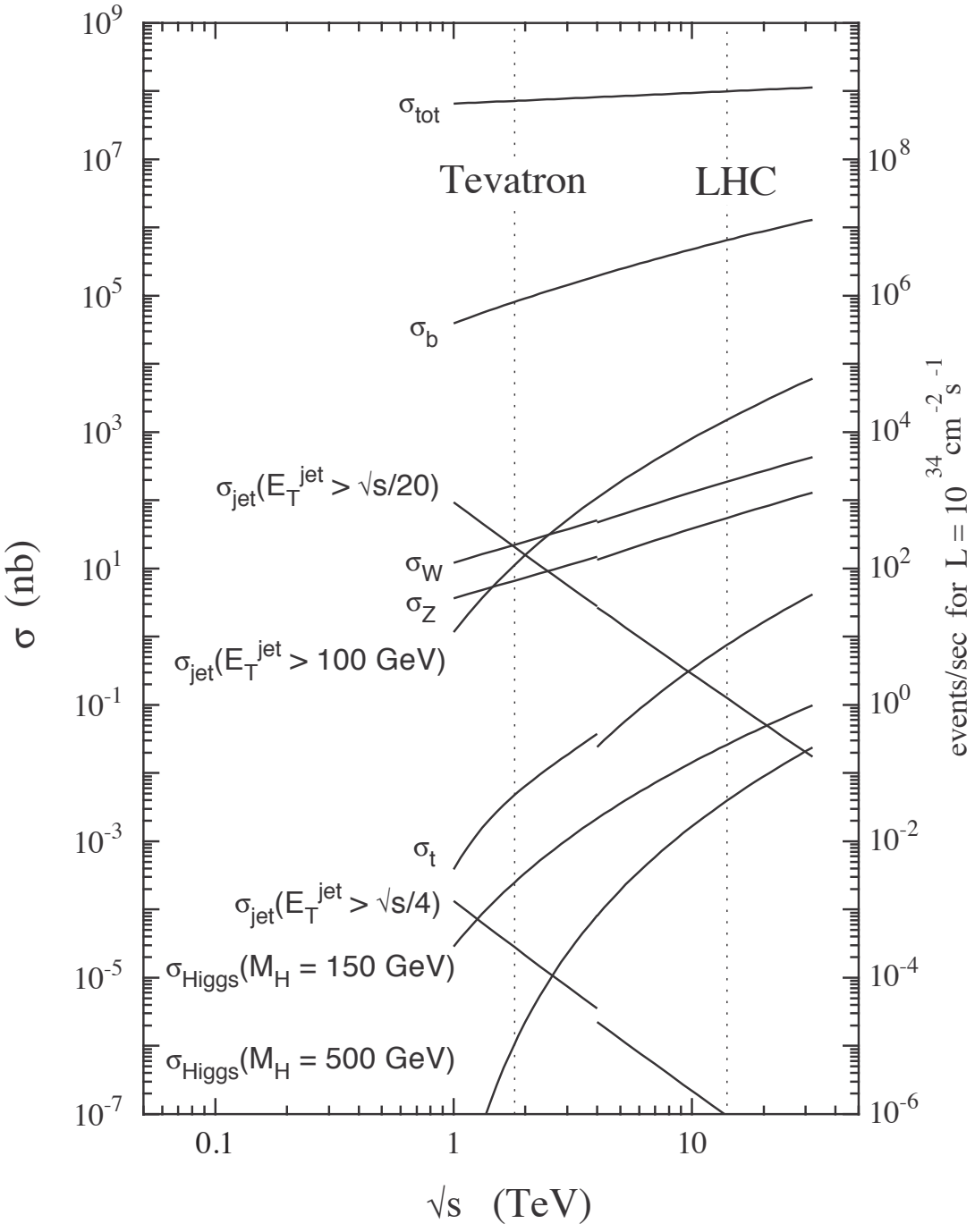


Figure 3.2: Cross sections for important processes in proton-(anti)proton collisions as a function of center-of-mass energy [91].

available in Chapter 4.

## 3.2 The proton beam

Before reaching the LHC, the particles are accelerated by a chain of accelerators that gradually increase the energy of the particles. Figure 3.3 shows the most important links in the chains for both proton and ion beam production. There are several foreseen filling schemes defined for the LHC, each designed for different modes of operation. For an in-depth description of all the filling schemes, the reader is referred to [93].

The protons start their journey to the LHC in the linear accelerator Linac2. This accelerator yields protons with an energy of 50 MeV which are then injected to the first circular accelerator of the chain, the *Proton Synchrotron Booster* (PSB). The *Proton Synchrotron* (PS) will then raise the energy from 1.4 GeV to 25 GeV. From the PS the bunched beam will be injected to the *Super Proton Synchrotron* (SPS) where the energy of the particles increases by a factor of almost 20 up to 450 GeV which is the injection energy of the LHC. More information about the CERN accelerators and their specifications are available in [94].

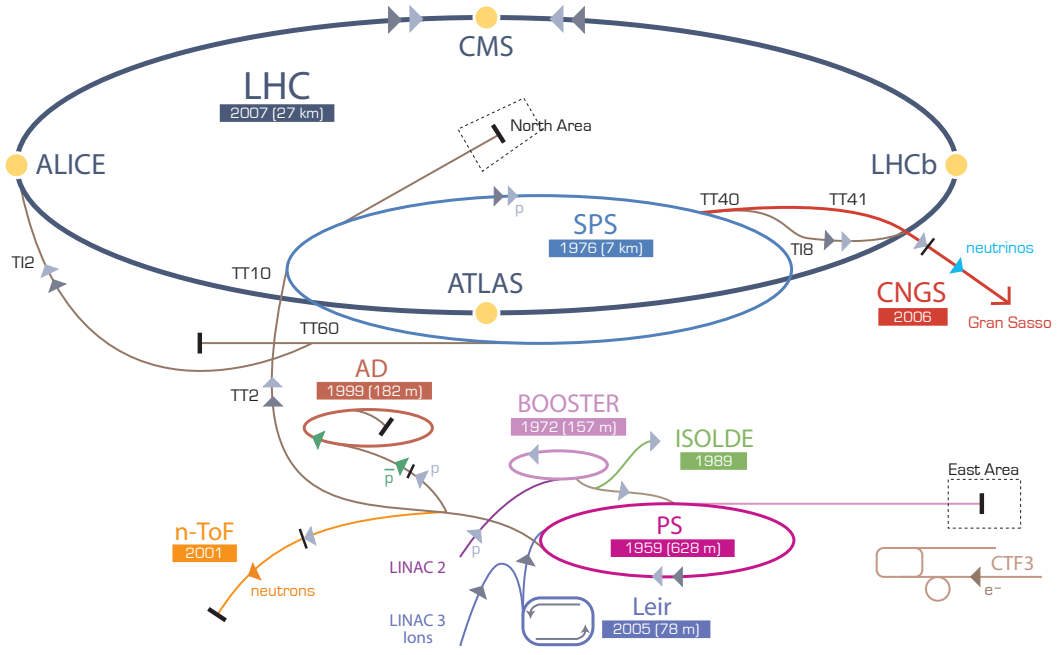


Figure 3.3: The beam production chain for the LHC at CERN.

Since the accelerators in the chain sequentially grow bigger in circumference, the storage rings can hold several fills of the previous link. For example, when building up

the “25 ns Physics Beam” the PS will have 72 bunches per fill. To fill up the SPS, there is an alternating pattern with two, three or four PS fills per SPS fill. The LHC is then filled up by 12 of these variable-length SPS fills. See Figure 3.4 for an illustrative schematic of how the LHC beam can be composed in terms of fills in the accelerators prior in the chain, which effectively defines the *bunch pattern*.

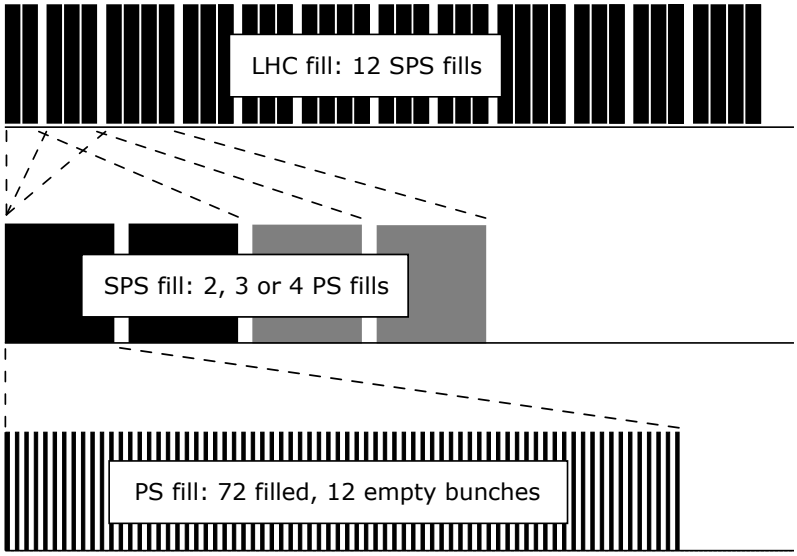


Figure 3.4: A schematic drawing of how the “25 ns Physics Beam” of the LHC is composed.

The bunch patterns of the two counter-rotating beams together determine when there will be collisions in the the center of the experiments. The radio frequency (RF) cavities of the LHC that capture, accelerate and store the beams operate at approximately 400 MHz. This results in 35640 potential wells in the RF field, so-called *RF buckets*, where it is energetically favorable for the bunches to be located in the beam. This corresponds to a spacing in time of only 2.5 ns, but only every tenth RF bucket is used, making the resulting bunch spacing 25 ns. The LHC therefore has 3564 possible locations where bunches can sit for each beam, resulting in 3564 *bunch crossings*. In the “25 ns Physics Beam” described in Figure 3.4, 2808 of these bunch locations are filled per beam. The structure of this beam can be described in terms of PS fills as

$$234 \quad 334 \quad 334 \quad 334$$

or in terms of empty ($e$) and filled ($b$) bunch locations

$$[2(72b+8e)+30e]+[3(72b+8e)+30e]+[4(72b+8e)+31e]+$$

$$3\{2[3(72b+8e)+30e]+[4(72b+8e)+31e]\}+80e=$$

$$=2808b+756e=3564$$

If something goes wrong during the filling of the LHC, bunches may sit in the wrong RF buckets, which could result in collisions occurring in the wrong place in the detectors and cause problems in their data acquisition systems. If the quality of the beam is insufficient, the beam is dumped and the LHC is refilled. The beam dumping is achieved by letting *kicker magnets* bend the beam out of the storage ring. The kicker magnets require at least a 3 μs window to ramp up the magnet currents. Because of this, all filling schemes need to have a long *abort gap* to allow the kicker magnets reach their full field strength. To fill up the LHC again takes about 4 minutes per beam.

# 4 The ATLAS experiment

As mentioned in the previous chapter, the LHC will provide $pp$ collisions at unprecedented center-of-mass energy at a high luminosity, and the ATLAS[1)] experiment is designed to exploit its full discovery potential. As a general-purpose detector, it comprises several sub-detectors, each contributing to identification and measurement of the properties of the particles produced in the high-energy collisions it will be exposed to. In this chapter an overview of the ATLAS detector will be given, with a slightly biased emphasis on the subsystems related to the work presented in the attached papers. For a complete description of the ATLAS detector the reader is referred to [88].

The ATLAS collaboration consists of approximately 3000 physicists, engineers, technicians and students from 174 institutes in 38 countries, which makes it one of the largest scientific collaborations ever formed. The ATLAS experiment is the result of over 20 years of design work, development, implementation, testing, commissioning and operation.

## 4.1 Overview

Shaped like a cylinder, built concentrically around the LHC beam pipe with a radius of 11 m and length of 44 m, the ATLAS detector weighs approximately 7000 tonnes. Figure 4.1 provides an overview of the experiment and its different sub-detectors. The sub-detectors can be grouped into three major systems: the Inner Detector (ID) [95], the calorimeters [96, 97], and the Muon Spectrometer (MS) [98].

In ATLAS, two coordinate systems are used, one cartesian and one polar, with a common origin in the nominal interaction point in the center of the detector. In the cartesian coordinate system the $x$-axis points towards the center of the LHC ring, and the $y$-axis points upwards, away from the center of the earth. The $z$-axis points along the beam axis, in the counter-clockwise direction if seen from above, thus forming a right-handed coordinate system. The polar coordinate shares this $z$-axis, the polar angle $\theta$ is defined as the angle from the beam axis and $\phi$ is the azimuthal angle, for which $\phi = 0$ is defined as the value along the positive $x$-axis. At colliders, the *pseudorapidity* $\eta = -\ln(\tan\theta/2)$ is often preferred instead of the polar angle $\theta$ since the particle flow is approximately uniform per unit in $\eta$. When discussing distances in pseudorapidity-azimuthal angle space, $\Delta R = \sqrt{\Delta\eta^2 + \Delta\phi^2}$ is often used. Finally, when transverse quantities such as $p_{\mathrm{T}}$, $E_{\mathrm{T}}$ and

[1)] ATLAS is an acronym for A Toroidal LHC ApparatuS.

$E_{\mathrm{T}}^{\mathrm{miss}}$ are discussed, the projections in the $x$-$y$ plane are implicitly alluded to.

## 4.2 Magnet system

In order to measure the momentum of high-$p_{\mathrm{T}}$ charged particles with sufficient precision, a strong magnetic field is required to bend their trajectory. ATLAS has two magnet systems, the solenoid and the toroid which produce intense magnetic fields in the ID and MS, respectively. The superconducting wires in both magnet systems need to be cooled down to $\sim$4.5 K.

### 4.2.1 The solenoid

The solenoid produces an axial field of $\sim$2 T that will bend the path of electrically charged particles in the ID volume in the $\phi$-direction. To minimize the material in front of the ATLAS calorimeters, the solenoid field is achieved with a single-layer coil of superconducting NbTi 1.2 mm diameter wire. The solenoid stretches 5.8 m along the $z$-axis and the inner and outer radii are 2.46 m and 2.56 m, respectively.

### 4.2.2 The toroid

The toroid field is achieved by leading currents through superconducting NbTiCu wire in eight coils in the barrel, symmetrically spaced in $\phi$, and two end-cap structures, produc-

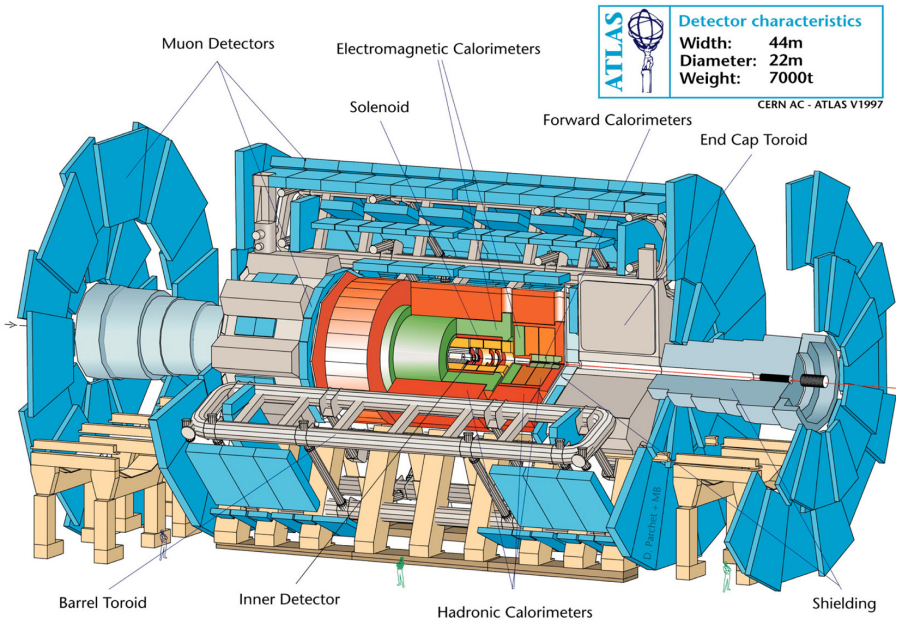


Figure 4.1: A cross-section of the ATLAS experiment showing the various sub-detectors.

ing fields of approximately 0.5 T and 1 T in the barrel and end-cap region, respectively. The inner and outer diameters of the barrel toroid magnet system are 9.4 m and 20.1 m, respectively, and the magnet system spans 25.3 m along the beam direction.

## 4.3 Inner Detector

At a hadron collider like the LHC, large multiplicities of charged particles are expected in every event. In order to measure the momentum of charged hadrons and leptons and to determine the location of primary and secondary vertices with satisfactory precision, the ATLAS ID is composed of three sub-detectors as shown in Figure 4.2. Combined, these three detectors offer hermetic tracking in the acceptance ($|\eta| < 2.5$) for tracks with $p_{\mathrm{T}}$ down to $\sim$0.5 GeV. The resolution depends on $\eta$ and $p_{\mathrm{T}}$, and ranges from 2% for 1 GeV tracks at $\eta = 0$ to 16% for tracks with $p_{\mathrm{T}} = 100$ GeV at $\eta = 2.4$ [99]. The efficiency for reconstructing muons with $p_{\mathrm{T}} > 5$ GeV is approximately 99%. For hadrons and electrons the efficiency is approximately 94% at $\eta = 0$ for the same $p_{\mathrm{T}}$ range but deteriorates with increasing $\eta$ down to approximately 80% for $\eta > 1.7$ due to the increased amount of material in the ID.

To facilitate a high efficiency while rejecting fake tracks caused by the electronics noise and beam-induced background, good spatial resolution is crucial in a high-occupancy environment. In addition, since all material between the interaction point and the calorimeters degrade the the resolution of the measured energy, inner tracking detectors have to be designed on a tight material budget. This trade-off between the number of space-points per charged particle in the inner tracker and the energy resolution achievable in the calorimeters, combined with requirements on radiation hardness to remain operational after years of exposure to the LHC, controlled the design choices of the ATLAS Inner Detector (ID).

### 4.3.1 The Pixel detector

With approximately 80 million read-out channels, the closest ones 50.5 mm from the center of the beam pipe, the silicon-based Pixel detector provides the most accurate position measurements in ATLAS. Typically, all tracks in the acceptance of the Pixels get three hits, each with an intrinsic accuracy in $R$-$\phi \times z$ of $10 \times 115$ µm in the barrel.

Since this thesis in concerned with the direct detection of particles expected to suffer anomalous energy losses in matter, it is worth noting that an energy deposition corresponding to 8.5 minimum ionizing particles (MIPs) or more can saturate the pixel sensors, resulting in a risk of losing hits. However, the charge released by a track crossing the Pixel detector is rarely contained within just one pixel [100]. This saturation effect is modeled correctly in the simulations of the Pixel detector.

### 4.3.2 The Semiconductor Tracker

The Semiconductor Tracker (SCT) is also based on silicon technology, but in the form of strips mounted with a 40 mrad stereo angle. A charged particle traversing the SCT will give up to eight hits, combining to form four space-point measurements, each with an intrinsic accuracy of $R$-$\phi \times z$ of $17 \times 580$ μm (barrel). The total number of channels in the SCT is 6.4 million. In the SCT, reconstructed hits are expected whenever a sensor is crossed by a charged particle, regardless the charge, and there is no risk of hits being lost due to saturation.

### 4.3.3 The Transition Radiation Tracker

The Transition Radiation Tracker (TRT) is composed of gas-filled straw tubes, with a total of 351 000 channels. The TRT straws only provide measurements in the bending plane, each with an intrinsic accuracy of 130 μm, but no measurements can be made along the straw direction ($\hat{z}$ in the barrel, $\hat{R}$ in the endcap). The TRT offers particle identification capabilities through benefiting from the transition radiation mechanism which results in higher-amplitude signals for particles at high $\beta = v/c$, allowing discrimination between electrons and charged hadrons.

In the front-end electronics of the TRT, the measured signals are discriminated against two thresholds, classifying the hits as low-threshold (LT) or high-threshold (HT) hits. There is no upper limit to the amount of ionization in a straw which will lead to a signal [101]. The lack of losses from saturation ensures that even the most ionizing particles will be detected in the TRT.

## 4.4 Calorimeters

ATLAS is equipped with several calorimeters based on different technologies, all of the non-compensating sampling type. There are five calorimeters in ATLAS: the Liquid Argon (LAr) electromagnetic (EM) barrel, the Tile hadronic barrel, the LAr EM end-cap, the LAr hadronic end-cap, and the LAr Forward calorimeter. Figure 4.3 depicts the entire calorimeter system, and indicates where the various calorimeters are installed. The primary purpose of the calorimeter system is to stop all particles (except muons and neutrinos) emanating from the interaction point and thereby measure their energy and position. While the hadronic calorimeters predominantly measure hadrons, the electromagnetic calorimeters measure electrons and photons and contribute to measuring the energy of hadrons in jets. Since many physics signals searched for at the LHC include $E_{\mathrm{T}}^{\mathrm{miss}}$, it is important to provide energy measurements over a large region in $\eta$. Combined, the ATLAS calorimeters cover $|\eta| < 4.9$, but with varying granularity in $\eta \times \phi$.

As input to the Level-1 Calorimeter trigger system (See Section 4.6.1), analog sums of the energies in so-called trigger towers of size $\sim 0.1 \times 0.1$ in $\eta \times \phi$, are formed. This is done since the Level-1 trigger operates at a very high rate, and therefore cannot handle full-granularity calorimeter data.

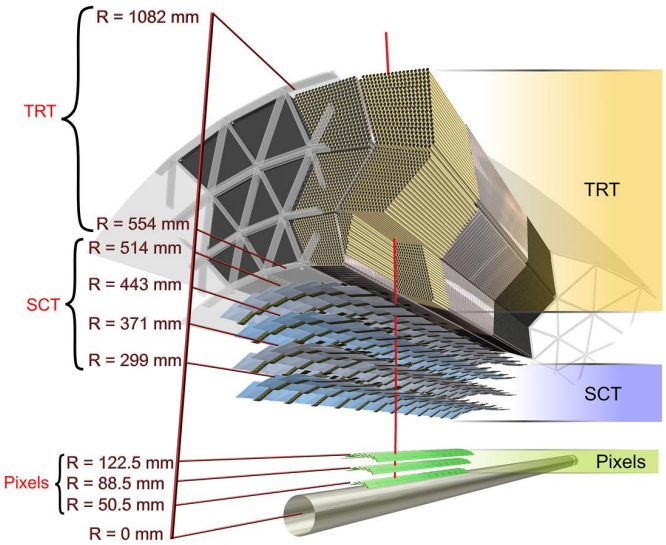


Figure 4.2: A cross-sectional illustration of the sub-detectors that constitute the Inner Detector, with radial distances from the center of the beam pipe to the various module layers.

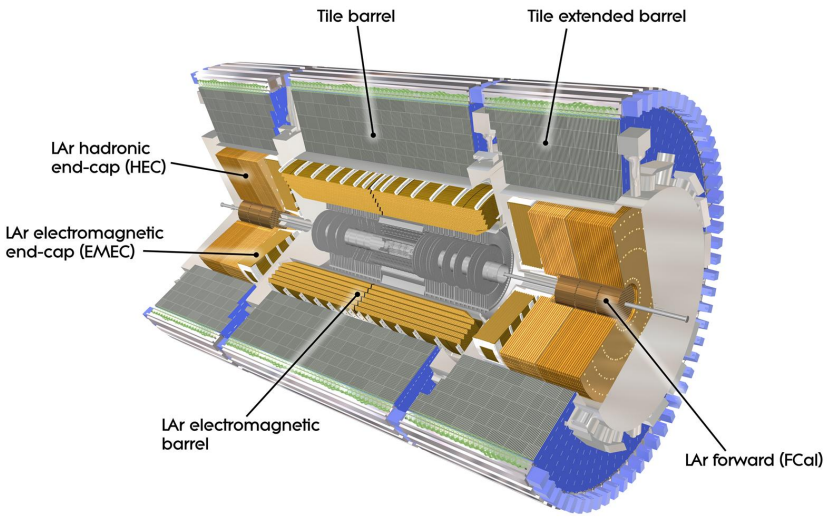


Figure 4.3: A cross-section illustration of the ATLAS calorimeter systems.

### 4.4.1 The LAr calorimeters

The LAr calorimeters use liquid argon as the active material, together with various metal absorbers. Charged particles that pass through the active material ionize the argon atoms, releasing ionization electrons which are collected as a current by applying an electric field of 10 kV/cm on average [102, 103]. The visible energy is scaled by the sampling fraction to obtain the true deposited energy in both the active material and the absorber.

The LAr-based electromagnetic barrel (EMB) calorimeter covers $|\eta| < 1.475$. The inner and outer radii are 1.4 and 2 m, respectively, and the LAr barrel calorimeter covers 6.4 m along the $z$-axis. As illustrated in Figure 4.4, the barrel offers a fine segmentation in all sampling layers, especially in the second layer where it corresponds to $0.025 \times 0.0245$ in $\eta \times \phi$. The high granularity allows detailed measurements of the shapes of the electromagnetic showers from e.g. photons and electrons.

The electromagnetic end-cap (EMEC) calorimeter comprises two wheel-like structures, covering $1.375 < \eta < 2.5$ and $2.5 < \eta < 3.2$. The LAr forward calorimeter (FCAL) consists of three cylindrical structures placed in sequence along the beam pipe and covers $3.1 < \eta < 4.9$. The first cylinder is used for measurements of electromagnetic energy losses while the two remaining layers are used for hadronic calorimetry.

The hadronic end-cap (HEC) calorimeter, much like the EMEC, consists of two concentric wheels per side, with a total coverage in pseudorapidity of $1.5 < \eta < 3.2$.

The energy resolution $\sigma_E$ for the EMB depends on the measured energy and is described by two terms,

$$\frac{\sigma_E}{E} = \frac{a}{\sqrt{E}} \oplus b, \tag{4.1}$$

where the constants have been determined to $a = 10.1 \pm 0.1\%\text{GeV}^{1/2}$ and $b = 0.17 \pm 0.04\%$ [104].

### 4.4.2 The Tile calorimeter

The Tile calorimeter is a sampling calorimeter which uses iron as passive material and plastic scintillators as active layers. It is divided into four partitions, two of which constitute the mechanically distinct long barrel, and two extended barrel partitions. Each partition consists of 64 modules divided in equal azimuthal angle ($\phi$) intervals. Figure 4.5 shows how a long barrel module and an extended barrel module are divided into cells in a plane parallel to the beam axis. The sampling layers are denoted *A*, *BC* and *D*, and have a granularity in $\eta \times \phi$ of $0.1 \times 0.1$ in the two innermost layers, and $0.2 \times 0.1$ in the outermost. Figure 4.6 illustrates how the alternating layers of scintillating plastic and iron are configured, and shows the wavelength-shifting fibers used to guide the light to the photomultiplier tubes (PMTs) near the digitizer electronics.Two linear PMT outputs are digitized for each channel, differing in gain by a factor of 64.

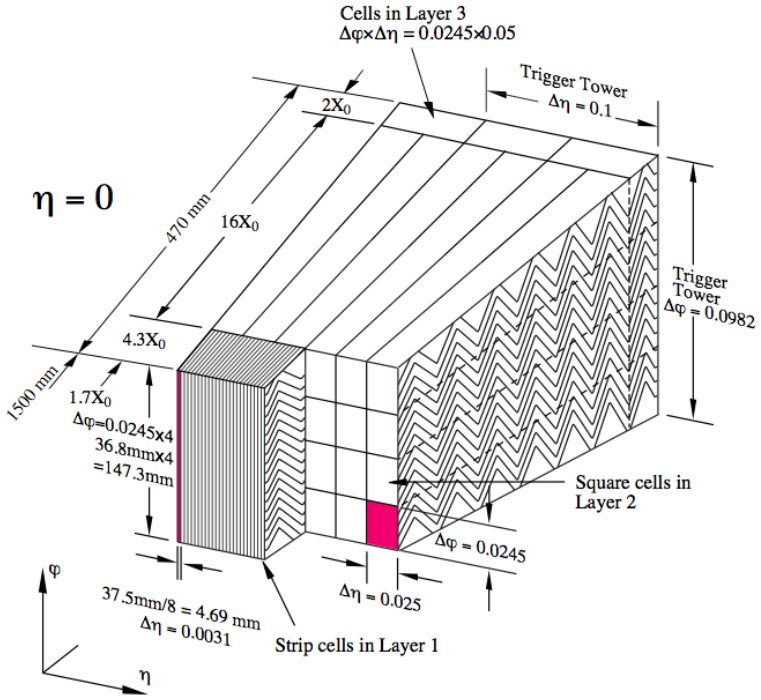


Figure 4.4: An illustration showing the cell segmentation of the LAr electromagnetic barrel calorimeter [88].

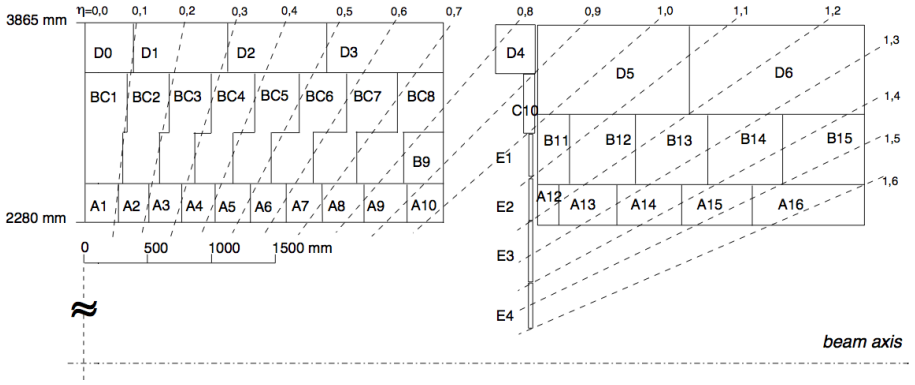


Figure 4.5: An illustration showing how the Tile calorimeter is partitioned and how the cells are arranged [88].

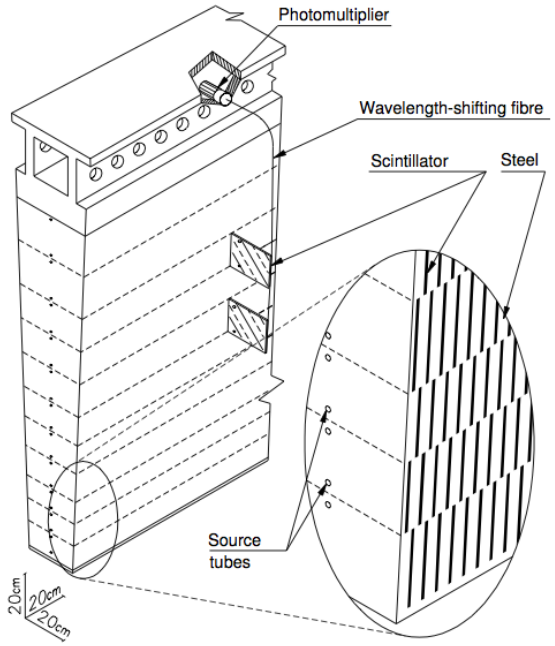


Figure 4.6: A schematic drawing of a module in the Tile calorimeter [88].

## 4.5 Muon Spectrometer

The outermost of the ATLAS sub-detectors is the Muon Spectrometer (MS). The requirement to accurately measure the curvature of high-$p_{\mathrm{T}}$ tracks dictates the size of the MS and thereby also the dimensions of ATLAS. The ATLAS muon spectrometer is composed of several types of muon detectors, which together cover $|\eta| < 2.7$. The ATLAS muon system is designed to determine the momentum accurately for muons with $3 < p_{\mathrm{T}} < 1000$ GeV [99]. The sub-detectors of the MS are immersed in the magnetic

field from the toroid magnet discussed in Section 4.2. The muon system is equipped with fast Resistive Plate Chambers (RPC) ($|\eta| < 1.05$) and Thin Gap Chambers (TGC) ($1.05 < |\eta| < 2.4$) for use in the Level-1 trigger system. For precision measurements, the Monitored Drift Tubes (MDT) ($|\eta| < 2.7$) and Cathode Strip Chambers (CSC) ($2.0 < |\eta| < 2.7$, only in the innermost station) have been installed.

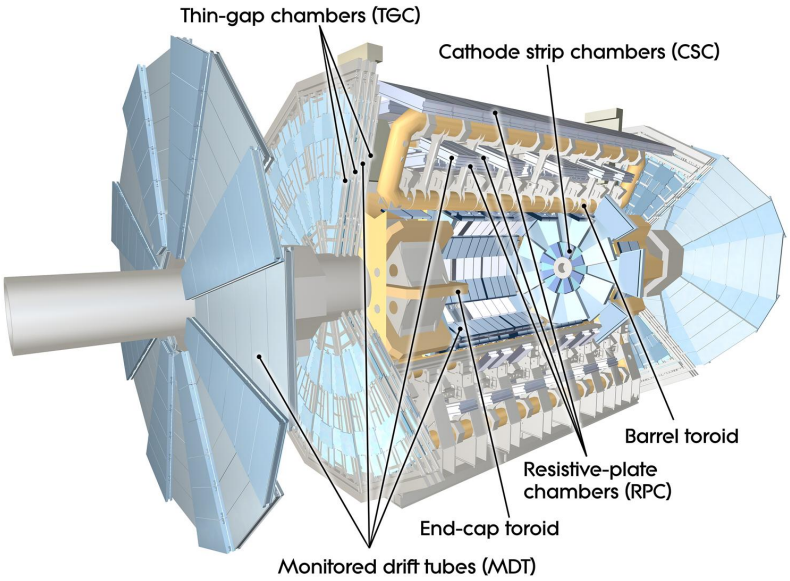


Figure 4.7: A cross-section illustration of the sub-detectors of the Muon Spectrometer.

## 4.6 Trigger and data acquisition systems

### 4.6.1 Trigger system

At nominal LHC running, bunches of protons will collide inside ATLAS every 25 ns. Neither the data acquisition system nor the resources for doing offline analysis are capable of handling such amounts of data. Therefore, a trigger system is required to select only the most interesting events to be written to disk and analyzed further offline. Luckily, the measurements of the dominant processes occurring in the collisions are not limited by statistics and therefore the majority of them can be discarded.

In general, the rare processes of primary interest to ATLAS are characterized by large momentum transfer in the hard process, resulting in jets and/or leptons with large transverse momentum ($p_{\mathrm{T}}$), and/or missing transverse energy ($E_{\mathrm{T}}^{\mathrm{miss}}$). The ATLAS trigger system is implemented in three layers, sequentially refining the selection of the events to be recorded for offline analysis. For a schematic overview of the trigger system, see Figure 4.8.

### First level trigger

Implemented in fast custom electronics boards, the Level-1 trigger has to decide quickly if the event is interesting for further analysis. Because of the size of the pipeline memories that store the data, this decision has to be taken in a very short time. Including the time it takes for the signals to travel through the cables from the detectors in the ATLAS cavern to the counting room, the Level-1 trigger system has to make a decision in 2 μs. In order to do this, it uses a subset of the data from the calorimeters and muon detectors. By quickly examining a reduced-granularity representation of each event, searching it for high-$p_{\mathrm{T}}$ muons, electrons/photons, jets and $\tau$-lepton candidates and determining an approximate eventwise jet-energy sum and $E_{\mathrm{T}}^{\mathrm{miss}}$, the decision is taken to keep it for further scrutiny in the high-level trigger, or reject it. A schematic illustration of the parts that make up the Level-1 trigger is available in Figure 4.9.

The electronics modules that implement the logic of the Level-1 calorimeter trigger (L1Calo) run a set of algorithms on so-called *trigger towers*, analog sums of the calorimeter signals in $\Delta\eta\times\Delta\phi = 0.1\times0.1$ regions, to look for high-$p_{\mathrm{T}}$ object candidates. The Level-1 muon trigger (L1Muon) implements similar logics and estimates the $p_{\mathrm{T}}$ of muon candidates by approximating the curvature of the trajectory of the muon between the stations in the muon spectrometer. Both L1Calo and L1Muon report the multiplicities of identified candidates over various threshold values to the Central Trigger Processor (CTP), which takes the Level-1 trigger decision. Upon a Level-1 Accept (L1A), the locations of so-called *Regions of Interest* (RoI) are reported to the RoI builder.

Due to limitations in the detector read-out systems, the Level-1 trigger system has to reduce the event rate to a maximum of 75 kHz, effectively making the Level-1 rejection factor $\sim$500.

### The High-Level Trigger

The high-level trigger (HLT) is implemented entirely in software, and runs on off-the-shelf computers and networking technology. In contrast to the Level-1 trigger which has to process the events sequentially, the HLT operates asynchronously and processes many events in parallel.

The Level-2 Trigger refines the event selection further by studying the full-resolution data, but to save bandwidth between the detector read-out electronics and the computing farm running the HLT algorithms, it only retrieves the data in the areas defined by the RoIs provided by Level-1. In addition to the muon spectrometer and calorimeter information available at Level-1, information recorded by the inner tracking detector is also used. Level-2 makes a decision in about 10 ms and rejects about 95% of the events accepted by Level-1, yielding an input event rate of about 3.5 kHz to the third level in the trigger system where the final decision is taken.

The third level of the trigger system is called the Event Filter (EF). At this stage, the complete data from all sub-detectors are gathered and the events are reconstructed using algorithms similar to those run in the offline reconstruction. The final selection based on

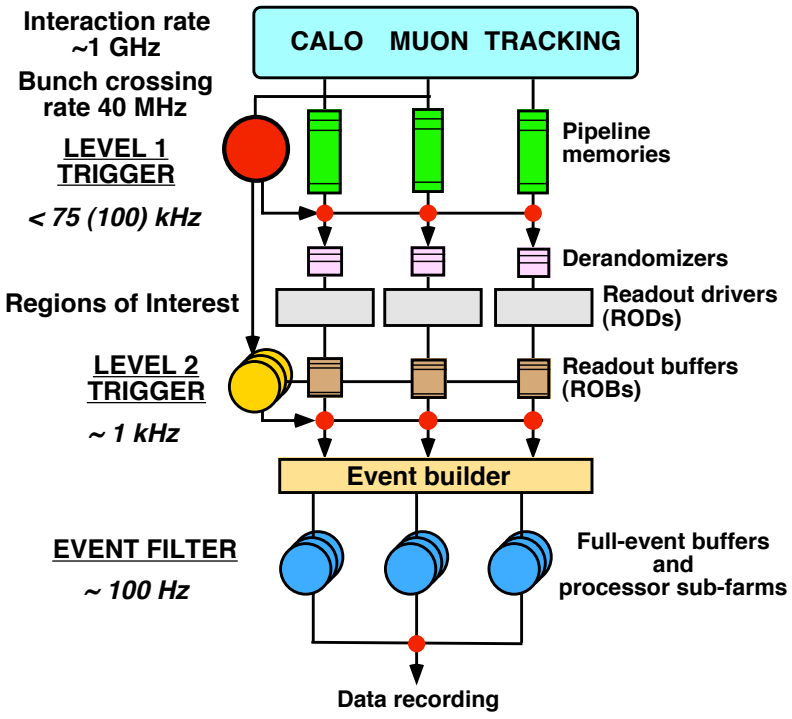


Figure 4.8: An overview of the trigger system for ATLAS [105].

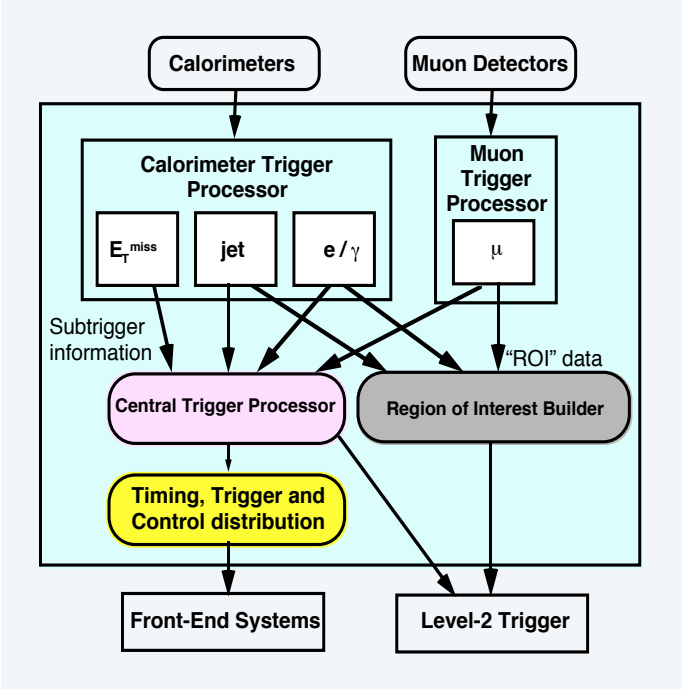


Figure 4.9: Schematic of the Level-1 Trigger.

these carefully reconstructed physics objects accepts on average one of ten events.

In total, the Level-2 trigger uses approximately 500 computing nodes, the EF uses 1800 nodes, and an additional 100 nodes are used for event building. The total rejection factor is $10^7$ for the trigger system, resulting in a nominal output rate of 100 events per second to be stored for offline analysis[2)].

### 4.6.2 Data Acquisition system

While the Level-1 trigger forms its decision whether or not to keep an event, the sub-detector data are stored in on-detector pipeline memories. Upon a L1A, the data are read out by the sub-detector-specific read-out drivers (RODs) which formats the digitized signals before sending it to the read-out buffers (ROBs) of the read-out system (ROS) of the Data Acquisition (DAQ) system. The Level-2 trigger then retrieves the detector data in the RoIs pointed out by the Level-1 trigger, and takes a decision based on them. If the event is accepted, the read-out system holding the full data sends them on to the event building (EB) system before further filtering in the EF. Depending on what triggers the events pass, they get sorted into different *trigger streams*. There are three major trigger streams for physics analysis in ATLAS, `Egamma`, `JetTauEtmiss` and `Muons`. There are also additional streams for e.g. partially reconstructed calibration events and a `debug` stream for events that were forcefully accepted due to time-out problems in the HLT.

### 4.6.3 Timing at ATLAS

If a L1A is issued by the Level-1 CTP, the read-out is done from the on-detector memory buffers using only the time as a reference. As a consequence of the high bunch crossing frequency of the LHC and the sheer physical dimensions of ATLAS, particles produced in up to three consecutive collisions can co-exist in the ATLAS detector volume at any given time. In order to ensure that the data read out from the various subsystems are associated with the correct bunch crossings, careful calibration of the timing is essential. Upon a L1A signal, the Level-1 trigger system tags the recorded data with identifiers so that they can be read out asynchronously by the HLT [106]. The reference for all timing in ATLAS are the beam-synchronous timing signals received from the LHC machine. The sub-detector electronics therefore rely on a stable phase relationship between the clock signal and the time of the collisions. Unexpected changes to this phase could cause degraded reconstruction of detector signals, sub-optimal resolution or system instabilities. The beam monitoring system based on electrostatic beam pick-up detectors described in Papers III and IV was designed to monitor this phase relationship. A more complete description of the design of this system and its purpose is available in [1].

[2)] For parts of the 2010-2011 data taking, the trigger was configured to accept events at up to 400 Hz.

### 4.6.4 Clock signal distribution chain

Transmission of LHC timing signals to ATLAS

Clock signals derived from the accelerating RF cavities of the LHC are transmitted to the experiments to keep them synchronized with the accelerator. The signals are distributed to the experiments from the RF transmitters at SR4 through optical fibers as illustrated in Figure 4.10. Temperature fluctuations affect properties of the fiber which result in a phase change for the carried signals. This phase change can give seasonal drifts of a few nanoseconds, and diurnal drifts of up to 200 ps [107]. In addition, other unforeseen problems could arise in the clock distribution chain causing similar phase shifts that would cause problems even in a perfectly timed-in ATLAS experiment. Since ATLAS relies on a stable phase relationship between the clock signal that drives the data acquisition electronics and the collisions taking place in the center of the detector, this phase must be monitored to guarantee the quality and integrity of the data recorded by the sub-detectors.

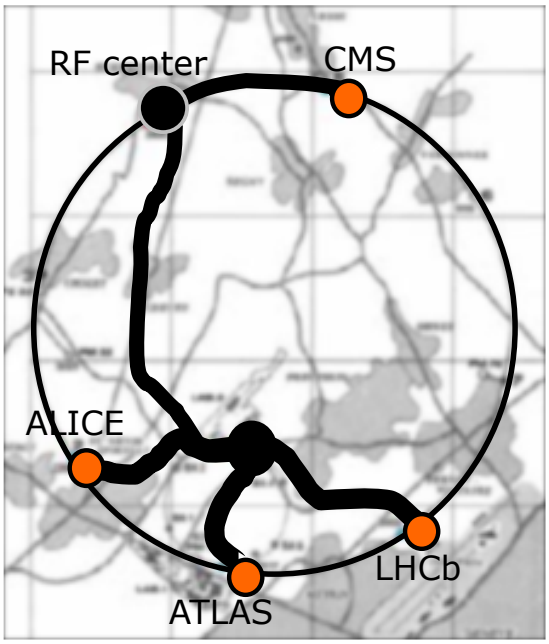


Figure 4.10: The timing signals are transmitted to the experiments through fibers.

# Part III

# Details for Paper I:

# Search for stable hadronising squarks and gluinos with the ATLAS experiment at the LHC

*"...be a little slow, be a little late."*

– Avon Barksdale

# About Part III

Exotic stable massive particles could provide the first signal of new physics. Since SMPs offer spectacular experimental signatures with virtually no physics backgrounds, searches for them are important ingredients of the early physics programs at colliders. The following chapters contain additional studies related to the search presented in Paper I. While the presentation of this material does not rely on the reader previously having read the paper itself, perusing the concise presentation found there could be useful before diving into the details given here.

In this work, the first limits from the ATLAS experiment on the production of hadronic SMPs are presented. Although the search is sensitive to a number of different models of new physics, the results are presented in the context of SUSY models predicting the existence of $R$-hadrons [81].

Much preparatory work has been performed in assessing the potential of ATLAS of observing and quantifying the properties of SMPs [2, 78, 108, 109, 110, 111, 112], and the techniques used to obtain the results in Paper I rely on and extend this body of work.

Chapter 5 reviews the expected detector response in ATLAS for $R$-hadrons, with special emphasis on two dedicated discriminators used to separate the sought signal particles from SM background processes. The simulated physics processes used in the search are then described. The event and candidate preselection is presented in Chapter 6, along with studies of efficiency for selecting signal processes. The method used to extract an estimate of the expected background is described in Chapter 7 and studies of the effects of systematic uncertainties are presented in Chapter 8. In Chapter 9 the final selections are defined and the final event yields and background estimates are determined. After investigating the effects of various systematic uncertainties, the chapter is concluded by summarizing the results.

# 5 Expected detector response for $R$-hadrons in ATLAS

Understanding the detector signatures expected for signal and background processes is crucial to designing an efficient search analysis. This chapter details the expected response of $R$-hadrons in ATLAS. After a brief overview, the two main observables used to discriminate signal from background are carefully described. The chapter is concluded with an account of how the sought physics processes and their backgrounds are simulated.

## 5.1 Overview

As shown in Table 2.1, roughly half of the produced $R$-hadrons are expected to be charged following hadronization. Since the hadronic interactions which can affect the charge predominantly happen in the denser parts of the detector, i.e. the calorimeters, normal tracking efficiencies are expected in the ID for the initially charged states. The Pixel detector offers detailed measurements of the deposited energy per unit length in the silicon, $dE/dx$, and is taken advantage of to separate the slow-moving signal particles from the relativistic background particles. This technique and its performance is covered in great detail in Section 5.2. In the SCT, hit efficiency and tracking performance similar to that for muons is expected. Also from the detector response from the straws in the TRT variables related to the ionization energy loss can be extracted. These techniques, though very promising during the development phase of the analysis, were not used for the final results of Paper I and will not be covered in this thesis.

In the ATLAS calorimeters, the hadronic interactions described in Section 2.3.4 are expected in addition to the ionization energy loss for electrically charged states. When traversing the ATLAS sub-detectors, $\mathcal{O}(10)$ potentially charge-altering hadronic interactions are expected, and the absolute majority of these would occur in the dense calorimeters. Since the $R$-hadrons are not expected to shower, typical energy losses are roughly compatible with those expected from MIPs. In the Tile calorimeter (see Section 4.4.2), the timing resolution of MIP-like energy depositions is approximately 1 ns, making it possible to measure the time-of-flight for particles that traverse it. Details pertaining to these methods are described in Section 5.3. As discussed in Section 2.3, many species of $R$-hadrons are expected to become (and then remain) baryons after only a few hadronic interactions. This will most likely happen in the dense calorimeters.

In the Muon Spectrometer (MS), a charged R-hadron is expected to be reconstructed with good efficiency as long as it is not too slow. Since the MS is the outermost part of ATLAS, slow particles would leave particularly late signals there compared to those from particles with $\beta = 1$. Both the RPC and MDT detectors offer good timing performance and dedicated reconstruction algorithms have been developed to benefit from this and identify slow particles [112]. However, if the baryon state with the lowest mass is electrically neutral, which is likely for stable $\tilde{b}$ and certainly possible for stable $\tilde{g}$ scenarios, signatures with tracks in the MS could be severely suppressed due to the scattering effects described in Section 2.3. Due to this uncertainty regarding the fraction $R$-hadrons possessing electric charge in the MS, the efficiency of a search relying on a signal there could be severely compromised. To avoid this, the search presented here is *MS-agnostic* – it does not require any signals there and is in fact indifferent to whether or not the MS even exists. Choosing an approach that only requires signals in the ID and calorimeters also extends the sensitivity of the search to SMPs with shorter lifetimes, i.e. that decay while traversing ATLAS.

## 5.2 Energy loss in the Pixel detector

The specific ionization energy loss, $dE/dx$, measured by the Pixel detector [100] plays an important role in the search presented in Paper I. In this section a technical description of the measurement is given and the performance for separating SM particles of different masses at low momentum is demonstrated. Finally the potential for identifying slow-moving signal particles is illustrated and a method for calculating the particle mass based on the $dE/dx$ and a track momentum measurement is derived.

### 5.2.1 Charge collection pixel sensors

For every triggered event, the read-out electronics of the Pixel detector [113] provide an array of hits in the detector. This data contains the physical coordinates and the Time-over-Threshold (ToT) value associated with each hit. The ToT value is calculated by subtracting the time of the trailing edge (TE) from the time of the leading edge (LE). The threshold is defined by a voltage discriminator.

The ToT is calibrated such that a MIP traversing a Pixel detector module perpendicular to its surface has a value of 30 bunch crossings, i.e. $30 \times 25 = 750$ ns. A signal exceeding 255 bunch crossings, i.e. equivalent to 8.5 MIPs or more, is set to overflow. This limitation does not affect this work since the explored kinematic region results in an expected charge corresponding to a ToT below this value. Studies with controlled charge injection into the Pixel detector have shown a good linear relationship between charge deposition and Time-over-Threshold (ToT) response.

The energy deposited by a particle crossing the Pixel detector is rarely confined to a single pixel sensor. Neighboring sensors are therefore clustered together. The charge of a cluster is calculated by summing the pixel charges after calibration corrections. A

set of quality requirements applied to the clusters help ensure a sensible estimate of the deposited energy. Approximately 91% of the clusters pass these requirements and are considered *good*. The energy deposited in the silicon depends on the length of the track in the sensor. By factoring out the traversed distance in the detector, a path-length compensated measurement of the specific energy loss is calculated, in the following referred to as Pixel $dE/dx$.

### 5.2.2 Extraction of $dE/dx$

The Pixel $dE/dx$ measurement is performed in several steps. One cluster per traversed layer in the Pixel detector is expected for a given track, typically resulting in 2-6 clusters. Since the energy deposited in each follows the asymmetric Landau distribution [114], a truncated mean is calculated to avoid bias due to fluctuations in the deposited energy per cluster. In the event a track has five or more good clusters, the two with the highest energy are discarded, in other cases only the most energetic cluster is ignored in the calculation. The Pixel $dE/dx$ value achieved through this procedure is then calibrated such that a MIP deposits 1.24 MeVg$^{-1}$cm$^2$, as measured in dedicated studies [6].

The calibration has been validated using low-$p$ tracks in data recorded with a minimum-bias trigger. Figure 5.1 illustrates the measured Pixel $dE/dx$ as a function of the momentum $p$ multiplied by the charge $q$ for ID tracks with three good clusters in the range $|p| < 2.5$ GeV. Several bands are visible and since the ionization energy loss to first order only depends on the speed of the particle, the bands can be identified as coming from particles with different masses, i.e. from the inside moving out: $\pi^{\pm}$, $K^{\pm}$ and $p/\bar{p}$. The faint band only visible for positively charged tracks corresponds to deuterons. Fits to the most probable values are shown for $\pi^{\pm}$ (black), $K^{\pm}$ (gray) and $p/\bar{p}$ (blue) are superimposed.

Figure 5.2 shows the expected specific energy loss as a function of momentum for tracks in simulated events with $R$-hadrons containing gluinos of mass 100, 200 and 500 GeV. Since the resolution of the reconstructed momentum degrades with momentum, the bands grow thicker with mass. The small band at lower momenta around the MIP value (Pixel $dE/dx \approx 1.2$ MeVg$^{-1}$cm$^2$) corresponds to SM particles also produced in the simulated events.

The distributions of measured Pixel $dE/dx$ in data are shown in Figure 5.3. The spectra are centered around the MIP value. Overlaid are the predictions of simulations of background processes and the predicted spectra for $R$-hadrons of masses 100, 300 and 500 GeV (Section 5.4 contains details about the simulated samples). Throughout this part, whenever several background processes are shown in a plot they are stacked as in Figure 5.3. The figure shows fair agreement between the observed spectrum and the prediction for background processes, and a good separation between the signal and background/data distributions. The spectra for the high-mass signal scenarios extend into the high Pixel $dE/dx$ region. The spectra were produced for candidate tracks fulfilling the preselection criteria listed in Section 6.2.

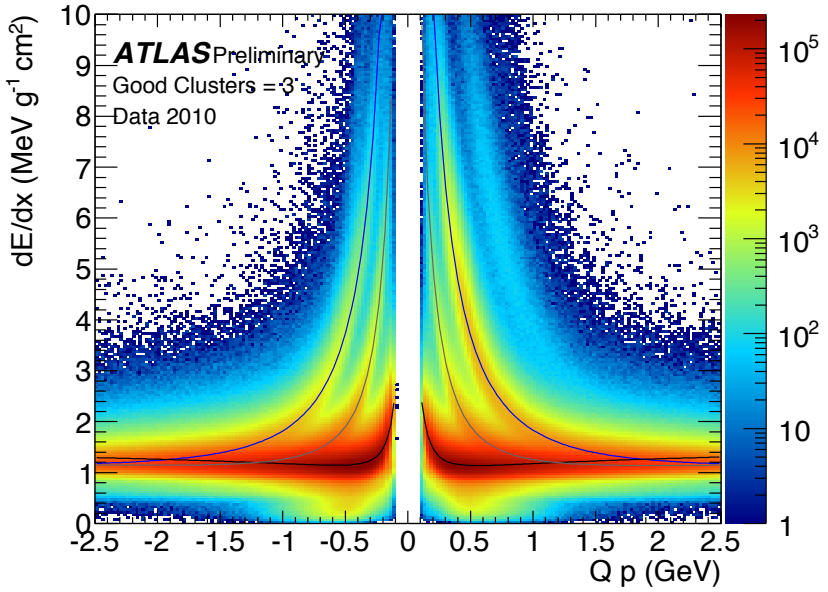


Figure 5.1: Measured Pixel $dE/dx$ versus signed momentum for tracks with three good clusters.

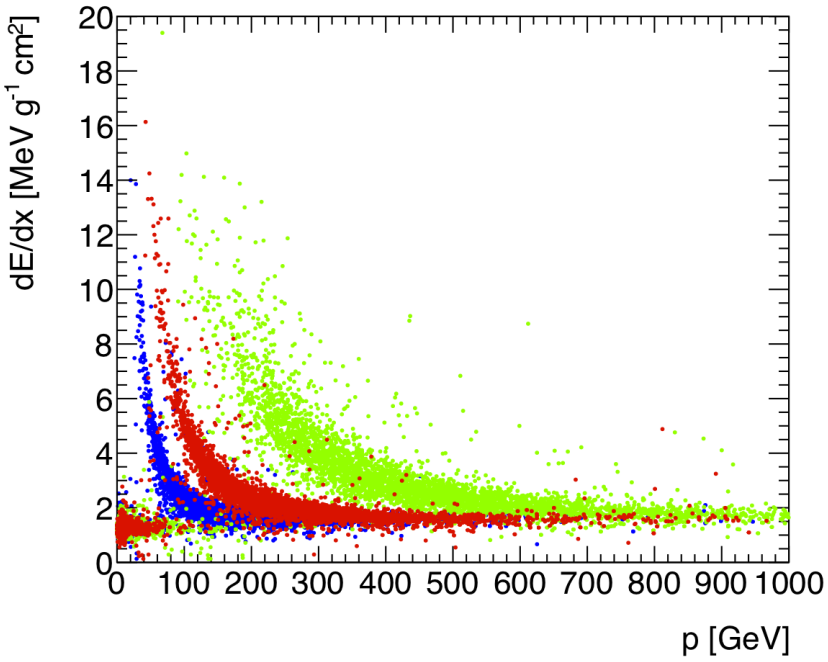


Figure 5.2: Predicted values of $dE/dx$ versus reconstructed momentum for tracks in simulated events with gluino $R$-hadrons with mass 100 GeV (blue), 200 GeV (red) and 500 GeV (green).

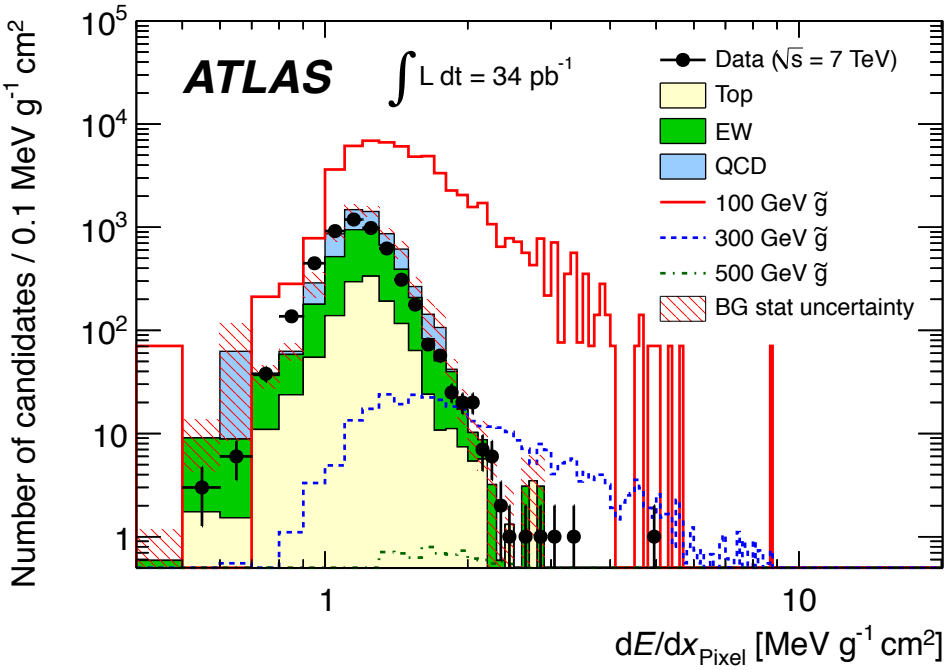


Figure 5.3: Distributions of Pixel $dE/dx$ from data and simulations of background and signal processes.

### 5.2.3 Mass estimation using the $dE/dx$ method

Since the $dE/dx$ to a good approximation only depends on the speed of the particle, the measurement of the first provide information about the latter. As seen in Figure 5.1, the relation between $p = m\beta\gamma$ and Pixel $dE/dx$ is invertible for values of $dE/dx$ significantly larger than the expected value for a MIP. By using SM particles with low masses, the relationship between $dE/dx$ and $\beta\gamma$ can be determined quantitatively. Once this relationship is established, a $dE/dx$ measurement for a given track can together with the measured momentum give an estimate for the mass $m$ of the particle,

$$m = \frac{p}{\beta\gamma}. \tag{5.1}$$

Mathematically, the full Bethe-Bloch equation is not analytically invertible, which leaves the options of either using a simplified and invertible expression, or employing more computationally intense numerical inversion. For the purposes of particle identification discussed here, the region of interest is $0.2 \lesssim \beta\gamma \lesssim 1.5$. The lower bound is due to pixel sensor charge saturation and the upper bound is due to lack of separation between signal and background. The most probable $dE/dx$ value, denoted $\mathscr{M}_{dE/dx}$, can in this region be described by a simplified 5-parameter Bethe-Bloch equation:

$$\mathscr{M}_{dE/dx}(\beta) = \frac{p_1}{\beta^{p_3}} \ln(1 + (p_2\beta\gamma)^{p_5}) - p_4. \tag{5.2}$$

The agreement between this expression and the most probable energy loss for simulated pion, kaon and proton tracks is shown in Figure 5.4.

Due to the discrete nature of the truncation employed in the $dE/dx$ calculation in Section 5.2.2, tracks with two, three and four or more good clusters will give slightly different distributions of Pixel $dE/dx$. By determining values for the parameters $p_i$ for these three groups of tracks separately, the lost precision due to smearing is minimized. Since the response is known to be slightly different for positively and negatively charged particles, each of the three groups are subdivided into two, giving a total of six sets of parameter values are extracted from low-$p_{\mathrm{T}}$ hadron tracks.

Applying the extracted parameters for the $dE/dx$–$\beta\gamma$ relationship in equation (5.2) to an independent sample of low-$p_{\mathrm{T}}$ tracks, equation (5.1) can be used to calculate the masses of the SM hadrons in a closure test. The results are shown for kaons and protons in Table 5.1 and indicates that the method can estimate the masses with a resolution of approximately 10-15%. This is an important result since it implies that the method is applicable also to heavier particles at higher $p_{\mathrm{T}}$, i.e. the sought signal.

The low-mass SM particles allows monitoring of the calibration and the stability of the pixel mass measurement over time. Results showing the stability of the measured proton mass is available in Appendix B.

There is one minor complication when extrapolating to the high-mass signal region for the search. In the ATLAS tracking algorithms, all charged particle tracks are reconstructed

| $n_{GC}$ | $q$ | $m_K$[GeV] | $\Delta m_K$[GeV] | $\sigma_K^{avg}$[GeV] | $m_p$[GeV] | $\Delta m_p$[GeV] | $\sigma_p^{avg}$[GeV] |
|---|---|---|---|---|---|---|---|
| 2 | + | 0.499 | 0.005 | 0.098 | 0.938 | -0.000 | 0.125 |
| 3 | + | 0.492 | -0.002 | 0.078 | 0.939 | 0.001 | 0.109 |
| $\geq 4$ | + | 0.490 | -0.004 | 0.065 | 0.934 | -0.004 | 0.101 |
| 2 | − | 0.503 | 0.010 | 0.099 | 0.943 | 0.005 | 0.147 |
| 3 | − | 0.500 | 0.007 | 0.071 | 0.943 | 0.005 | 0.107 |
| $\geq 4$ | − | 0.504 | 0.010 | 0.076 | 0.939 | 0.001 | 0.100 |

Table 5.1: Fitted peak and width values for the $K$ and proton mass peaks as obtained from approximately $12 \times 10^6$ data events. The errors on the fitted peak values range from 1 to 3 MeV.

assuming that their energy loss in the detector material is that of a pion. The measured momentum is therefore underestimated by a few percent for tracks for kaons and protons with momenta below 1 GeV. The parameters of equation (5.2) are therefore derived using a somewhat distorted $p$ distribution, leading an overestimation of the $R$-hadron masses by a few percent [100]. However, since the relative width of the measurement is not affected, it has negligible consequences on the results of this analysis, as will be explained in Chapter 9.

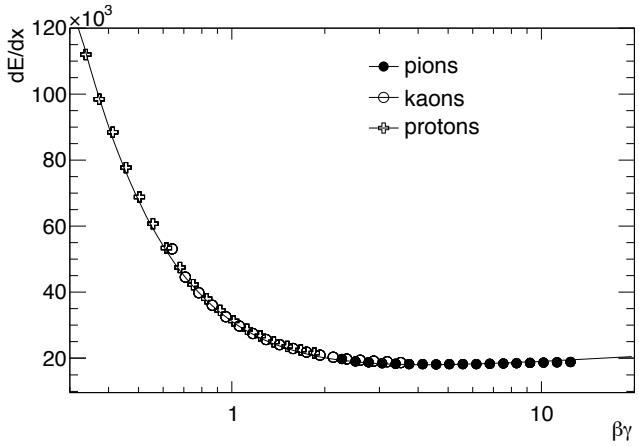


Figure 5.4: Distribution of the most probable value of the $dE/dx$ distribution for pions, kaons and protons fitted with the simplified Bethe-Bloch function in equation (5.2). The unit on the y-axis is $\mathrm{MeVg^{-1}cm^2}$.

## 5.3 Time of flight in the Tile calorimeter

The hadronic Tile calorimeter described in Section 4.4.2 offers sufficiently good timing measurements of energy depositions to enable Time-of-Flight (ToF) measurements for particles that traverse it. Since no slow-moving high-$p_{\mathrm{T}}$ particles with a penetrating detector signature exists in the SM, a ToF measurement is a powerful discriminant in a search for a signal with this signature. This section provides technical details of the Tile ToF technique and explains how estimates of the speed of a particle, $\beta_{\mathrm{Tile}}$, and its mass, $m_{\mathrm{Tile}}$, can be calculated. The performance of these observables is then demonstrated in experimental data and simulated physics processes.

### 5.3.1 Detector signal processing and reconstruction

For each Tile calorimeter channel, the energy and time is reconstructed by analyzing seven digital sample points $S_i$, spaced by 25 ns. The expected amplitude values for the sample points can be calculated by the function

$$S_i = Ag(t_i - t_0) + P, \tag{5.3}$$

where $A$ is the amplitude, $g(t)$ is the normalized pulse shape function shown in Figure 5.5, $P$ is the pedestal value and $t_0$ the time of the peak of the signal relative to a reference time defined by the time of the trigger. For optimal performance, a fit method can be used to extract the amplitude, time and pedestal values from the digital samples. Due to tight time constraints during online operation, the optimal filtering method used in the Tile

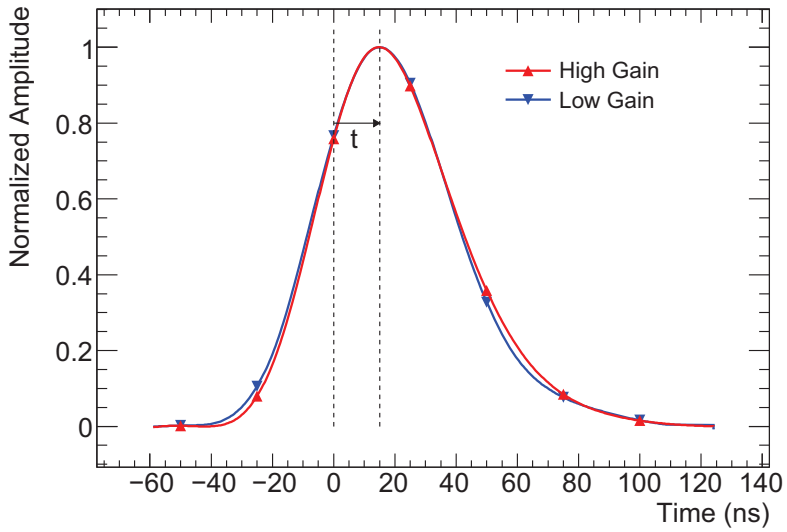


Figure 5.5: A schematic illustration of the sampled signal from a Tile calorimeter channel and the fitted pulse shape function.

calorimeter [115] has been implemented in the read-out driver electronics. This method computes values of $A$, $t$ and $P$ online, using linear combinations of the digital samples using the coefficients $a_i$, $b_i$, $c_i$ in equations (5.4)-(5.7).

$$A = \sum_{i=1}^{7} a_i S_i \tag{5.4}$$

$$At = \sum_{i=1}^{7} b_i S_i \tag{5.5}$$

$$t = \frac{At}{A} = \frac{\sum_{i=1}^{7} b_i S_i}{\sum_{i=1}^{7} a_i S_i} \tag{5.6}$$

$$P = \sum_{i=1}^{7} c_i S_i \tag{5.7}$$

The constants have been optimized to minimize the effects of noise, stemming from both read-out electronics and pile-up (see Section 5.4.1), on the resolution.

ATLAS employs the convention for timing measurements that signals left by a particle produced in the triggered collision and traveling at the speed of light ($\beta = 1$) is assigned $t_0 = 0$. The reconstruction method described above is designed to yield the best possible energy resolution around $t_0 = 0$, at the price of a slightly degraded resolution for out-of-time energy depositions.

To properly deal with large values of $t_0$, which would be expected for a delayed particle, an iterative version is available. In the iterative version, the obtained value of $t_0$ is used to select another set of coefficients optimized for signals that are shifted in time which are applied to the sample points. This is repeated until convergence is achieved, i.e. when the fit is good enough. Studies performed with real cosmic data events show that optimal filtering with iterations is able to reconstruct the time within 0.1 ns of the value one would obtain by performing a full fit to the sample points, even for very large time values (tens of ns) [116].

During high-luminosity running, the high event rate and limited computing resources requires running the optimal filtering algorithm online without iterations. Despite this the signal reconstruction still performs well and the measured time for signals that arrive approximately 10 ns late are expected to be accurate to approximately 5%, i.e. sufficiently accurate for the range of delays relevant to this search. For the full 2010 dataset used in the analyses in this thesis, it was possible to operate Tile with the iterative signal reconstruction algorithm. In the MC, however, the non-iterative version of the signal reconstruction algorithm was used to compute the energies and times for energy deposits in Tile. This should lead to conservative timing performance in the MC.

### 5.3.2 Tile timing performance

The Tile timing performance has been studied with the internal laser calibration system [117], test beam data [110] and cosmic rays [118] before LHC collisions. During

early LHC running timing calibrations and timing resolution measurements were performed during various types of single-beam running. Since the effect of noise on the detector signal reconstruction is larger for low-amplitude signals, the timing resolution depends on the energy scale of the deposit [110]. A cell time resolution of approximately 1 ns has been measured for cell energies greater than $\sim$1 GeV. For details regarding corrections and calibrations of the cell times, as well as smearing applied to the simulated signal (and background) samples in the analysis, the reader is referred to Appendix 5.3.3.

It is now straightforward to qualitatively demonstrate the usefulness of Tile in searches for SMPs. A particle traversing Tile typically crosses cells in three layers. The radial position of the centers of the innermost and outermost cells in the long (extended) barrel varies roughly between 2.5-3.7 m (2.5-3.5 m). The difference in time of flight between a relativistic particle and a SMP ($\Delta t_{ToF}$) depends on the speed ($\beta$) and $\eta$ of the particles, as shown in Table 5.2.

| $\eta$ | $\beta$ | $\Delta t_{TOF}$ (ns) (inner) | $\Delta t_{TOF}$ (ns) (outer) |
|---|---|---|---|
| 0 | 0.95 | 0.42 | 0.65 |
| | 0.8 | 2.04 | 3.11 |
| | 0.6 | 5.44 | 8.29 |
| 1.3 | 0.95 | 0.85 | 1.20 |
| | 0.8 | 4.02 | 5.72 |
| | 0.6 | 10.7 | 15.2 |

Table 5.2: Values of $\Delta_{ToF}$ at the innermost and outermost cells for SMPs produced with various values of $\eta$ and $\beta$.

For SMPs and relativistic particles produced with $\eta = 0$, the difference in time-of-flight varies between approximately 0.4 and 5.4 ns, depending on cell position and the speed of the particle. SMPs could be identified using measurements of cell timing if their energy depositions are large enough to correspond to a cell timing resolution of less than $\Delta t_{ToF}$. The distributions of total Tile calorimeter cell energy for SMP candidates in data passing the preselection described in Section 6.2 is shown in Figure 5.6. Also shown are background predictions, stacked in the same way as in Figure 5.3. The agreement between simulations and experimental data is more than sufficient for the search done here. Predictions for signal scenarios with $R$-hadrons of mass 100, 300 and 500 GeV are also shown; the distribution extends to larger values of cell energy than seen in data and predicted by background simulations. In conclusion, energies of $\mathcal{O}$(1 GeV) per cell are expected for hadron-like SMPs, the corresponding to a timing resolution of approximately 1 ns. Thus, from the values of $\Delta t_{ToF}$ in Table 5.2, it is possible to discriminate between slow-moving SMPs produced over a range in $\eta$ and $\beta$ and SM backgrounds using Tile timing measurements.

### 5.3.3 Calibration and smearing of the Tile timing measurements

Since the drifts in the LHC clock signal described in Section 4.6.4 affect the Tile ToF measurements directly, high-precision timing measurements from the BPTX system [119] were used to correct for these. In addition, the Tile cell time spectra in data and MC were aligned by studying $Z \to \mu\mu$ events and adjusting the cell times such that the cell time spectra for the cells crossed by the muons are centered at $t = 0$. For the data, a shift of 600 ps was added to all Tile cell times, and for the MC 160 ps was subtracted to align the muon energy deposits at $t = 0$ ns. Partly owing to perfect timing alignment, the intrinsic cell time resolution for MIP-like energies is better in the MC compared to what is observed in the data. To improve the description of the background MC, a smearing was applied to the simulated values by adding random times $\sim N(0, 1.42)$ ns. By correcting and smearing the cell times in the MC signal samples in same way, a more realistic timing performance is achieved. Figure 5.7 shows the corrected spectra of reconstructed times in the Tile cells crossed by the candidates surviving the preselection described in Section 6.2, for experimental data as well as background and a few selected signal Monte Carlo samples.

### 5.3.4 Determination of $\beta_{\text{Tile}}$

By combining the distance $d_{\text{cell}}$ from the IP to the cell providing the energy deposition and its measured time, it is possible to calculate an estimate of the speed of a particle. Equation (5.8) provides an expression for the reconstructed speed from a cell ($\beta_{\text{cell}}$) as a function of reconstructed cell time ($t_{\text{reco}}$).

$$\beta_{\text{cell}} = \frac{v}{c} = \frac{d_{\text{cell}}}{t_{\text{true}} c} = \frac{d_{\text{cell}}}{(t_{\text{reco}} + \frac{d_{\text{cell}}}{c})c} = \frac{1}{\frac{t_{\text{reco}} c}{d_{\text{cell}}} + 1} \tag{5.8}$$

Since the $\Delta t_{ToF}$ measurements in different cells are independent, corresponding $\beta_{\text{cell}}$ values can be combined to form a measurement with higher precision for a given track. To benefit from the improved cell time resolution for larger energy depositions, the combined speed measurement $\beta_{\text{Tile}}$ is calculated as a weighted average as given in equation (5.9).

$$\beta_{\text{Tile}} = \frac{\sum_{i=0}^{n} w_i \beta_i}{\sum_{i=0}^{n} w_i} \tag{5.9}$$

In this equation $n$ is the number of cells and the weight for the speed measurement of cell $i$ is a function of its measured energy, $w_i \equiv w(E_i) = E_i$. Several other weighting functions were investigated but found to not significantly improve the resolution [2]. To calculate $\beta_{\text{Tile}}$, a minimum cell energy is required such that energy depositions with poor timing resolution do not contaminate the measurement. In this work, a cell energy threshold of 500 MeV was chosen, making sure cells measuring low-energy depositions due to noise are severely suppressed in the timing measurements.

The distributions of measured $\beta_{\text{Tile}}$ in data are shown in Figure 5.8. The spectra for data and background processes are centered around $\beta \sim 1$. Following the corrections and

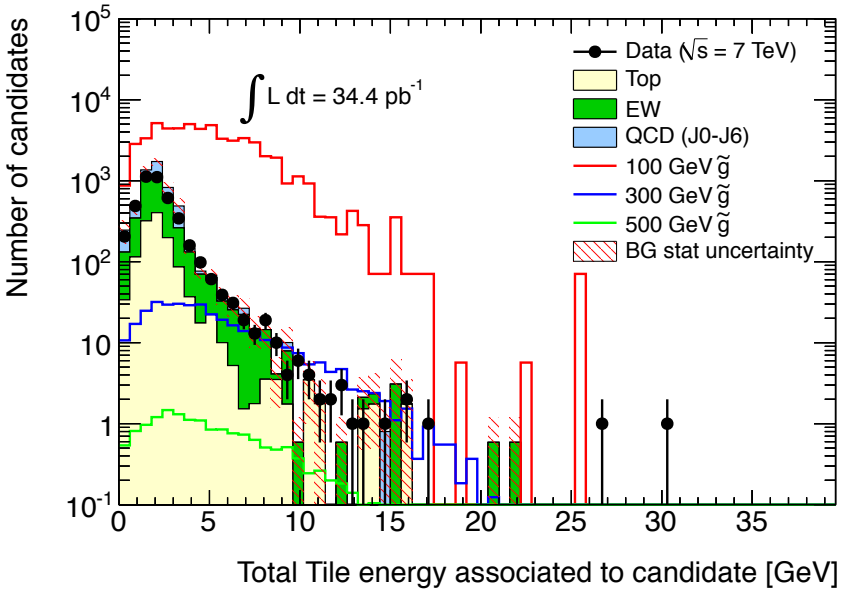


Figure 5.6: Distributions of the total Tile energy associated with selected candidates in data and simulations of background and signal processes.

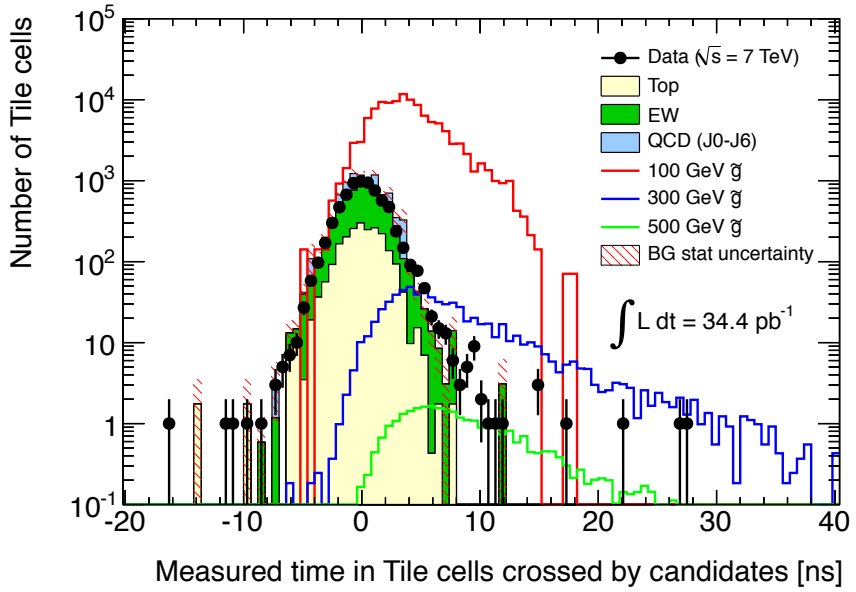


Figure 5.7: Times measured by Tile cells crossed by the extrapolated tracks of candidates. An energy deposition of 500 MeV was required from the cells.

smearing of the cell time spectra, the simulated backgrounds provide a fair description of the bulk of the data but do not reproduce the tails sufficiently. Also shown are the predicted $\beta_{\text{Tile}}$ spectra for gluino *R*-hadrons of masses 100, 300 and 500 GeV. As expected, these distributions dominantly occupy the low $\beta$ region ($\beta < 0.8$). The distributions shown in Figure 5.8 were produced for candidates fulfilling the preselection criteria listed in Section 6.2. The large number of entries for the background MC in the bin close to $\beta = 1.6$ is caused by one single QCD event with a weight of approximately 53. The tails at high and low $\beta_{\text{Tile}}$ for the background MC are entirely due to resolution effects since no slow particles exist in these processes.

### 5.3.5 Mass estimation using $\beta_{\text{Tile}}$

For candidates with $\beta_{\text{Tile}} < 1$, the candidate mass can be evaluated using the momentum and speed of the particle according to $m = p/\beta\gamma$, as described in Section 5.2.3. When calculating a mass in this way, the candidates with superluminal measured $\beta_{\text{Tile}}$ yield a complex mass. Since this is a search for slow-moving particles, these candidates are discarded when imposing requirements on the reconstructed mass in the analysis. The predicted reconstructed mass spectra for *R*-hadrons of various masses and heavy partons are given in Figure 5.9.

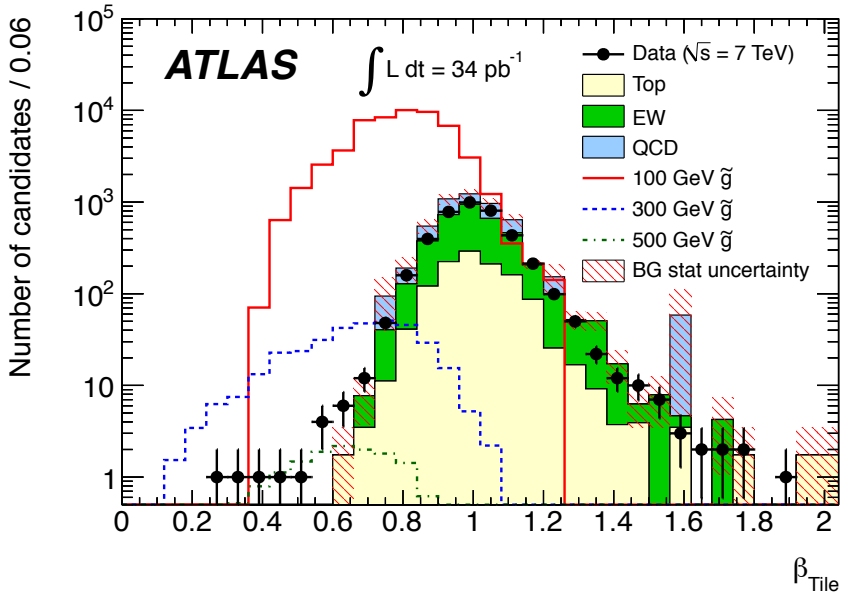


Figure 5.8: Distributions of $\beta$ from data and simulations of background processes and signal.

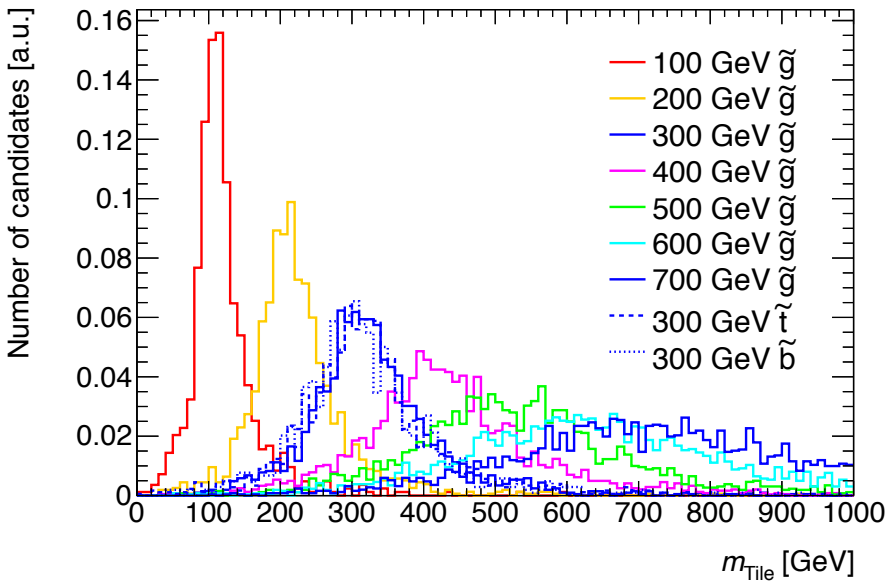


Figure 5.9: Reconstructed masses using the momentum measurement of the inner detector and $\beta_{\text{Tile}}$. In order to reconstruct a mass based on the Tile measurements, a $\beta$ of less than 1 is required.

## 5.4 Simulation of signal and background processes

To reliably estimate how well SMPs can be found with ATLAS, it is important to understand in great detail what the sought processes and their expected backgrounds look like in the detector. For these purposes, simulations are paramount. This section first describes the way simulated Monte Carlo (MC) samples are produced in ATLAS generally. Specific details are then given for the signal and relevant SM processes used to produce the results in Paper I. As argued earlier in this text, several plausible scenarios are available for the signal processes and their resulting detector signatures. Special attention is paid to factors affecting the performance of the discriminators used in the search, the Pixel $dE/dx$ and $\beta_{\text{Tile}}$ measurements.

### 5.4.1 Monte Carlo sample production

In ATLAS, the production of fully simulated Monte Carlo (MC) samples is divided into four distinct steps. Figure 5.10 depicts the steps and the data formats exchanged between the components.

In the *event generation* the hard physics process is generated using MC generators and calculations are performed resulting in the kinematics of the final state particles. This first step does not in any way depend on a detector, but only on the description of the colliding particles, such the center of mass energy, type of particle and their parton distribution functions (PDFs). Examples of program packages that perform event generation are PYTHIA [40], HERWIG [41] and MC@NLO [120].

The *detector simulation* takes the final state particles calculated by the event generator and propagates them through the detector material. By stepwise calculating the interactions between the particles and the matter they traverse, a record of *hits*, i.e. energy depositions in the detector, is built up. This step relies heavily on the modeling of the detector geometry, operating conditions such as high-voltage levels, temperatures, calibration and alignment. In ATLAS, the full detector simulation is almost exclusively done using GEANT4 [121]. Technically, particles are assigned physics processes which describe their interactions with matter, and it is these that determine the calculated interactions as their passage through matter is simulated.

In the *digitization* step, the hits calculated by the detector simulation step are converted to detector read-out signals. This step also depends on detector conditions, threshold settings, etc. The parts of the trigger system which are implemented in hardware are emulated here. In this step, *pile-up* effects are taken into account. Pile-up is a common name for instrumental effects due to interference in the detector signals between additional proton-proton collisions. At the nominal LHC luminosity, approximately 25 $pp$ collisions are expected per bunch crossing. The effects from these additional collisions are called *in-time pile-up* and include e.g. contributions to the overall detector activity and and increased charged track multiplicities. Since the detector signals are longer than the distance between consecutively filled bunch crossings in time, they are affected by earlier collisions as well, and these effects are called *out-of-time pile-up*. Collectively the

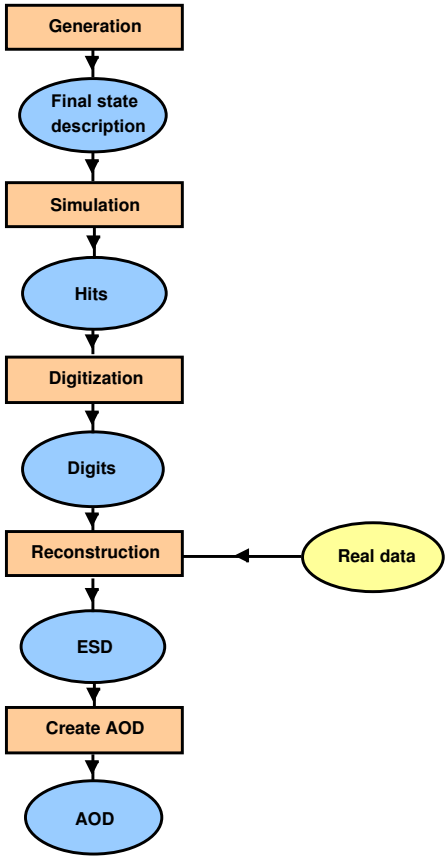


Figure 5.10: The full chain of steps for producing simulated MC samples and reconstructing experimental data in ATLAS.

two types of pile-up affects several physics observables and must therefore be described correctly by the simulated physics processes. Technically this is done e.g. by taking hits from simulated low-energy $pp$ collisions and adding these to the hits from the main physics signal, and the sum is used as input to the digitization. The output is returned in a format called *digits* which is similar to the data read out from the actual detector.

Finally, the *reconstruction* step processes the simulated detector signals and calculates e.g. measured hits and drift circles in tracking detectors and energy depositions in calorimeter cells. These low-level objects are then used as input to higher-level reconstruction algorithms that reconstruct e.g. track segments and calorimeter clusters. Ultimately, calibrated physics objects such as jets, electrons, muons, taus, $E_{\mathrm{T}}^{\mathrm{miss}}$ and vertices are constructed. The same reconstruction algorithms runs on simulated detector signals as on the real ones read out from the detector. The output of the reconstruction is saved in two formats: the complete Event Summary Data (ESD) and the more light-weight Analysis Object Data (AOD).

Monte Carlo simulations were used primarily to determine the resolution and efficiency of reconstructing the *R*-hadron signal together with associated systematic uncertainties on the quantities used in the event selection and limit calculations. As described in Chapter 7, the predicted backgrounds were estimated using data. However, samples of background processes were used to optimize *R*-hadron selections and to demonstrate the robustness of the data-driven background approach. In addition to the Monte Carlo simulations, next-to-leading order perturbative QCD calculations were also used to predict the cross sections of *R*-hadron production.

### 5.4.2 Background processes

Following the description of the interactions for *R*-hadrons in matter, it can be concluded that a penetrating signature can be expected, with high-$p_{\mathrm{T}}$ tracks and associated MIP-like energy depositions in the calorimeter. Due to the uncertainties related to the *R*-hadron signals in the MS, the search described in this part does not rely on any signal in this part of ATLAS. In the SM, the dominating source of this type of signature are high-$p_{\mathrm{T}}$ muons, e.g. from the decay of weak bosons. To understand the processes which contribute to the candidates measured in data, simulated samples of an assortment of SM processes that could give rise to this signature was used. Table 5.3 lists SM physics processes giving rise to high-$p_{\mathrm{T}}$ muons. The number of events, cross section and resulting integrated luminosity is listed for each process. The cross sections for the QCD and electroweak processes were calculated at leading order, but the ones for processes involving top quark(s) are based on next-to-leading order calculations.

In the following, the processes are (unless explicitly stated otherwise) scaled to the luminosity of the data by their cross sections and grouped into *QCD*, *EW* and *Top*, according to the grouping in the table.

### 5.4.3 *R*-hadron signal processes

The PYTHIA package [40] was used to generate direct pair production of gluinos, stops and sbottoms. The string hadronisation model [122], incorporating customized hadronisation routines [7] for *R*-hadrons, was used to produce final states containing *R*-hadrons. The simulation of *R*-hadron interactions in matter was handled by special GEANT4 routines based on different scattering models [38, 39, 55].

#### Electromagnetic interactions in matter

As mentioned in 2.3, phenomenological models of electromagnetic energy loss in matter for particles possessing moderate amounts of electric charge are well established, and have been implemented in GEANT4 [121].

| Sample | No. events | $\sigma$ (nb) | $\mathscr{L}(\text{pb}^{-1})$ |
|---|---|---|---|
| QCD: PYTHIA jet production | | | |
| $8 < p_{\text{T}} < 17$ GeV | 1400000 | 9860000 | 0.000142 |
| $17 < p_{\text{T}} < 35$ GeV | 1400000 | 678000 | 0.00206 |
| $35 < p_{\text{T}} < 70$ GeV | 1400000 | 41000 | 0.0342 |
| $70 < p_{\text{T}} < 140$ GeV | 1400000 | 2200 | 0.638 |
| $140 < p_{\text{T}} < 280$ GeV | 1400000 | 87.8 | 15.9 |
| $280 < p_{\text{T}} < 560$ GeV | 100000 | 2.33 | 42.9 |
| $560 < p_{\text{T}} < 1120$ GeV | 10000 | 0.0336 | 297 |
| EW: PYTHIA | | | |
| $W \to \mu\nu$ | 100000 | 8.94 | 11.2 |
| $W \to \tau\nu$ | 100000 | 8.94 | 11.2 |
| $Z \to \mu\mu$ | 50000 | 0.856 | 58.4 |
| $Z \to \mu\mu$ | 50000 | 0.854 | 58.5 |
| Top: MC@NLO | | | |
| $t\bar{t} \to \ell + X$ | 10000 | 0.144 | 69.4 |
| $Wt$ | 1999 | 0.0146 | 137 |
| $t \to \mu\nu + X$ ($s$-channel) | 2000 | 0.000468 | 4270 |
| $t \to \tau\nu + X$ ($s$-channel) | 1998 | 0.000470 | 4250 |
| $t \to \mu\nu + X$ ($t$-channel) | 2000 | 0.00718 | 279 |
| $t \to \tau\nu + X$ ($t$-channel) | 1998 | 0.00713 | 280 |

Table 5.3: MC samples for background processes used in the $R$-hadron search.

### Models of nuclear interactions in *R*-hadron scattering

The three scattering models described in Section 2.3.4 are available in GEANT4. Since the treatment of gluino-based *R*-hadrons suffers from large uncertainties, the generic model, which relies on a minimal set of underlying assumptions, was used to provide efficiencies and resolutions of gluino-based *R*-hadrons. Unless explicitely stated otherwise, all gluino results are based on the generic scattering model but results are also calculated for the intermediate and Regge models described in Section 2.3.4. These low-energy techniques and calculations of *R*-hadron masses can be more reliably applied to the treatment of squark-based *R*-hadrons. Therefore, the default choice of model for these particles is the Regge approach.

### Signal MC samples

Samples corresponding to the mass range for gluinos (squarks) to which this search is sensitive, i.e. 100-700 GeV (100-500 GeV) in steps of 100 GeV, were used.

For the gluino samples, a version using the generic scattering model was prepared for each of the mass points, and in addition versions using the intermediate and Regge models were prepared for the 100, 300, 500 and 700 GeV mass points. The hadronisation of gluino R-hadrons contains one parameter which is not fixed from first principles. The parameter represents the probability that a gluino will hadronize to a $\tilde{g}g$ "gluinoball" state, here denoted $p_{\tilde{g}g}$. This probability is by convention set to 10% in PYTHIA [7]. As this probability has a direct impact on the yield of any selection requiring an ID track, it is straightforward to interpret the results for other values of $p_{\tilde{g}g}$.

Signal scenarios featuring stable stop and sbottom squarks were prepared using the Regge-based scattering model, as prescribed above.

## 5.4.4 Next-to-leading order calculations of $\tilde{q}$ and $\tilde{g}$ production rates

The PROSPINO [123] program calculates, using perturbative QCD, the cross section for the pair production of heavy exotic colored particles to next-to-leading order accuracy. The cross sections, as functions of mass, are shown for pair production of gluinos and squarks in Figure 5.11. The renormalization scale was chosen to the be the gluino mass. The effects of varying up and down the renormalization scale by a factor of two are also shown. The calculations were made with the CTEQ6.6 [124] parton distribution function (PDF) set. All masses other than that of the sparticle which is being produced were set to a high value (10 TeV) to remain conservative [35, 55]. Given the aforementioned mass assumptions, the calculated gluino and squark cross sections are appropriate for Split SUSY [21, 30, 125, 80] and *R*-parity violating supersymmetry [32, 33, 34], hypotheses, respectively.

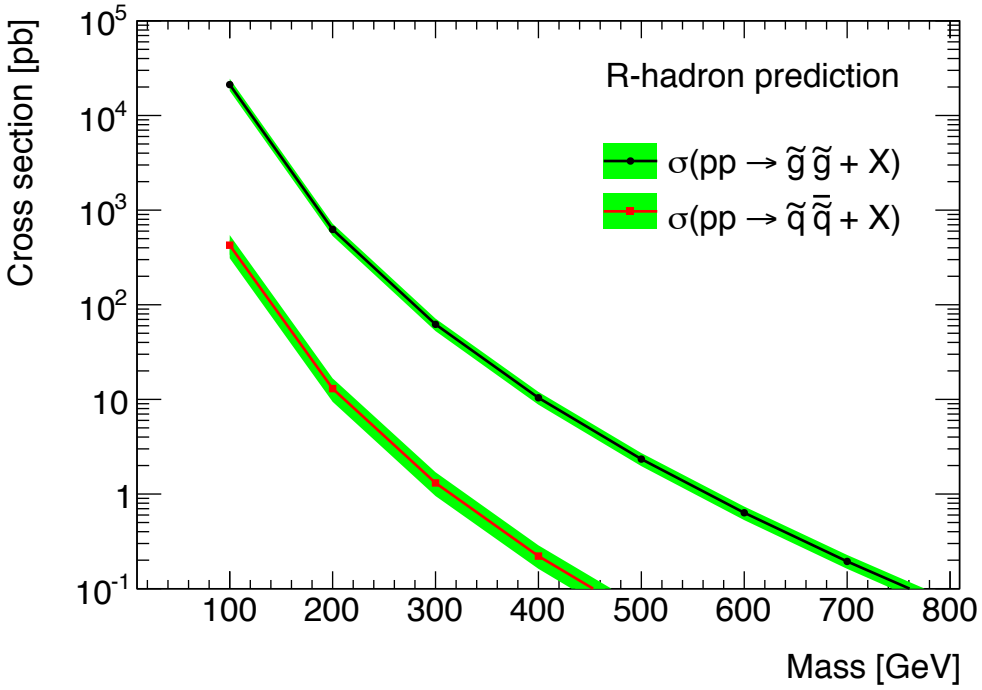


Figure 5.11: Predicted cross section for $pp \to \tilde{g}\tilde{g} + X$ and $pp \to \tilde{q}\bar{\tilde{q}} + X$ as calculated by the Prospino NLO program using CTEQ6.6 PDF set. The band corresponds to the effects of varying up and down the renormalization scale by a factor of two.

# 6 Event and candidate selection

## 6.1 Trigger

### 6.1.1 Choice of trigger

Triggering on the *R*-hadrons themselves can be difficult due to several reasons. As discussed in Section 4.6.1, ATLAS has a trigger system implemented in three levels, and only calorimeter and muon spectrometer information is available at the first level. Due to their limited energy depositions in the calorimeter, the *R*-hadrons themselves will not give rise to signatures that pass the jet, $e/\gamma$ or $\tau$ signatures with high efficiencies. In addition to the uncertainties related to the fraction of charged *R*-hadrons in the MS, first-level triggers based on this subsystem are currently sensitive to the delays expected for SMPs, though dedicated high-level triggers exist [112]. For the higher-mass scenarios a significant fraction of the *R*-hadrons are expected to be produced with $\beta \lesssim 0.5$. An event which gives rise to a trigger with a delay of approximately $0.5\text{BC} = 12.5$ ns or more runs the risk of triggering the following event, which means that sub-detectors with short read-out windows risk missing the data associated with the signal event. The first-level trigger has a dead time of several BCs between two consecutive triggers which further complicates triggering on late objects. Catching a signal event with a trigger in the following bunch crossing therefore also relies on a lack of in-time activity in the signal event.

As argued in Chapter 5, the scope of this analysis is to perform a muon spectrometer agnostic *R*-hadron search. This excludes the use of muon triggers. Instead the strong nature of the gluino and squark production mechanisms and their associated QCD radiation is exploited. The bulk of the production cross section comes from $gg$ fusion, where the initial state radiation[1)] frequently gives rise to energetic jets as illustrated in Figure 6.1. The modest energy depositions of the heavy objects themselves combined with the additional jet naturally give rise to missing transverse energy which can be triggered on already in the first-level trigger system.

The unprescaled jet signature triggers had a high energy threshold during the 2010 data taking, reaching the plateau of the efficiency curve at approximately 150 GeV. Since we would like to be sensitive to energies lower than this value, it is preferable to trigger on the QCD radiation jets indirectly with a $E_{\text{T}}^{\text{miss}}$ trigger which has a lower threshold. In

[1)] Final state radiation off the heavy colored particle is also expected, but to a much lesser extent than the dominating ISR radiation.

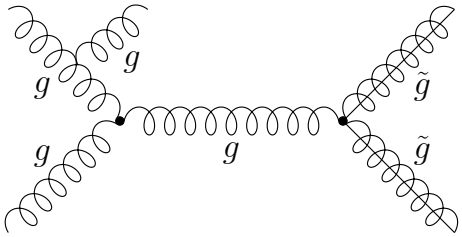


Figure 6.1: Feynman diagram showing the $gg \to \tilde{g}\tilde{g}$ process featuring QCD emission from one of the initial state gluons.

this search the so-called `xe40_noMu` trigger signature is used to collect the data sample. It starts with the Level-1 trigger `L1_XE25`, which calculates a crude estimate of $E_{\mathrm{T}}^{\mathrm{miss}}$ using analog sums of the energies in the cells in so-called trigger towers of size $\Delta\eta \times \Delta\phi = 0.1 \times 0.1$. If this estimated $E_{\mathrm{T}}^{\mathrm{miss}} > 25$ GeV the event passes. The signature then requires that the `EF_xe40_noMu` trigger is passed. At the EF level the trigger system can access individual cells and build clusters around those with high measured energy. By looping over all topological clusters without applying any calibration or correction [126], an estimate of the $E_{\mathrm{T}}^{\mathrm{miss}}$at the electromagnetic scale is calculated. The `noMu` suffix indicates that no corrections to the $E_{\mathrm{T}}^{\mathrm{miss}}$ based on reconstructed muons are applied. Events for which this higher-resolution estimate exceeds 40 GeV pass the trigger signature. Both the Level-1 and EF requirements rely only on calorimeter energy deposits to calculate the $E_{\mathrm{T}}^{\mathrm{miss}}$, and are thus entirely muon spectrometer agnostic. It gives a trigger efficiency which is approximately twice the one achieved with a jet trigger, and ranges from approximately 15% for a 100 GeV gluino scenario to 40% for a 600 GeV scenario.

### 6.1.2 $E_{\mathrm{T}}^{\mathrm{miss}}$ and jet $E_{\mathrm{T}}$ spectra and trigger turn-on curves for signal

The offline $E_{\mathrm{T}}^{\mathrm{miss}}$ based only on calorimeter clusters at the EM scale[2)], the so-called `MET_Topo` variable, and the $E_{\mathrm{T}}$ spectra of calibrated anti-$k_{\mathrm{t}}$ jets [127] for a selected set of R-hadron scenarios are shown in Figure 6.2, extracted before any cuts were made. The smaller number of entries in the first bin is due to summation effects in (a) and a jet reconstruction energy threshold of 7 GeV in (b). Both spectra fall exponentially with energy which means that it is large gains are to be expected from having a lower threshold in the trigger.

Figure 6.3 shows the turn-on curves for `L1_XE25` and `EF_xe40_noMu` with respect to the offline $E_{\mathrm{T}}^{\mathrm{miss}}$ variable called MET_Topo, based on calorimetry only. The turn-on curves can be approximated well by a single error function. Slightly flatter turn-ons are

[2)]The EM scale corresponds to the energy scale before any hadronic calibrations are applied to compensate for invisible energy in hadronic showers.

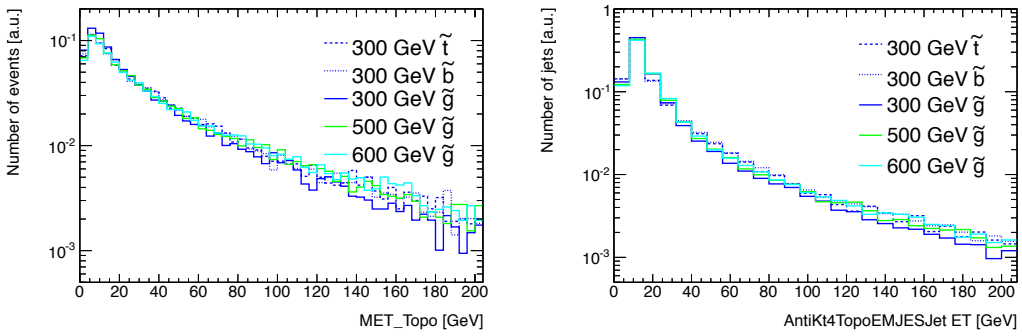


(a) (b)

Figure 6.2: The $E_{\mathrm{T}}^{\mathrm{miss}}$ based on topological calorimeter clusters at EM scale (a) and the $E_{\mathrm{T}}$ spectra for anti-$k_{\mathrm{t}}$ jets based on topological calorimeter clusters (b) for the 100, 300 and 500 GeV gluino samples.

observed for higher masses, due to degradation of the $E_{\mathrm{T}}^{\mathrm{miss}}$ resolution with increasing $\sum E_{\mathrm{T}}$.

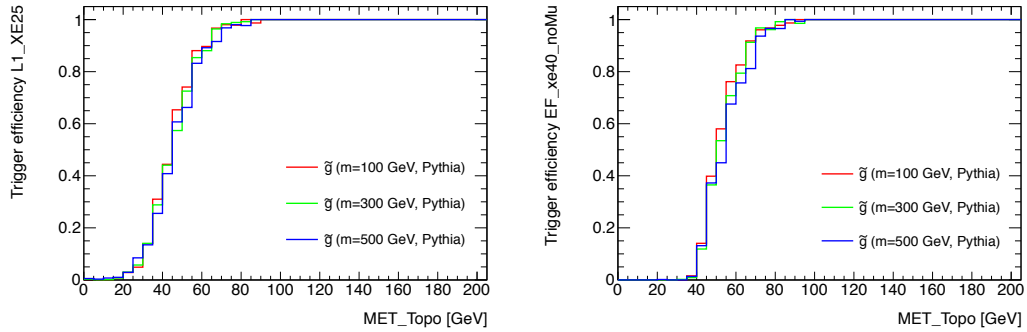


(a) (b)

Figure 6.3: Turn-on curves for L1_XE25 (a) and EF_xe40_noMu (b) as a function of offline $E_{\mathrm{T}}^{\mathrm{miss}}$ based only on topological calorimeter clusters at EM scale.

The spectra and behavior visualized in Figures 6.2a and 6.3 all have systematic uncertainties associated with them, and these are estimated in the following two sub-sections.

### 6.1.3 Determination of MET_Topo scale uncertainty

An uncertainty on the trigger efficiency arises from the lack of knowledge of how well the `MET_Topo` variable is modeled by the Monte Carlo. In the event topologies studied here the value of `MET_Topo` is dominated by contributions from one or possibly two relatively high-$p_{\mathrm{T}}$ jets, but has an additional softer component from the underlying event and

the electromagnetic and hadronic depositions of the *R*-hadrons. From tracker-aided $E/p$ studies [128] there exists an energy-dependent approximation of the scale uncertainty for individual clusters. The uncertainty ranges from approximately 20% for $p_{\mathrm{T}} = 500$ MeV, 10% around $p_{\mathrm{T}} = 1$ GeV and flattens out at around 5% for $p_{\mathrm{T}}$. These results were used to evaluate the uncertainty of the scale of the relevant $E_{\mathrm{T}}^{\mathrm{miss}}$ quantity for the signal processes considered in this search. To first verify that the $E_{\mathrm{T}}^{\mathrm{miss}}$ due to summed clusters, denoted `MET_cluster` is similar to the `MET_Topo`, Figure 6.4 was prepared. The distributions are fairly symmetric and centered close to zero, and the conclusion is drawn that there is little difference.

To get an estimate of the total `MET_Topo` scale uncertainty, each cluster was scaled according to its uncertainty, and all scaled clusters were summed to construct a scaled-shifted `MET_cluster`. The relative scale shifts expected for `MET_Topo` from varying the energies of the individual clusters by their scale uncertainties are shown in Figure 6.5. The effect on the trigger efficiency was then calculated by multiplying this scaled `MET_Topo` spectrum with the turn-on-curve, bin by bin. Table 6.1 shows the uncertainties in `MET_Topo` deduced from scaling the individual clusters, as well as its relative effect on the trigger efficiency for a few signal samples. The uncertainty on the trigger efficiency ranges from -12.6%/+13.4% to -7.1%/+7.1% for the 100 GeV and 700 GeV *R*-hadron samples, respectively.

| Sample | `MET_Topo` scaled up | Relative effect on trigger eff. | `MET_Topo` scaled down | Relative effect on trigger eff. |
|---|---|---|---|---|
| 100 GeV $\tilde{g}$ | +9.6% | +13.4% | -9.7% | -12.6% |
| 200 GeV $\tilde{g}$ | +9.2% | +9.9% | -9.4% | -10.8% |
| 300 GeV $\tilde{g}$ | +8.8% | +8.1% | -8.9% | -8.6% |
| 400 GeV $\tilde{g}$ | +8.7% | +7.6% | -8.8% | -8.1% |
| 500 GeV $\tilde{g}$ | +8.7% | +7.2% | -8.8% | -7.5% |
| 600 GeV $\tilde{g}$ | +8.7% | +7.0% | -8.8% | -7.1% |
| 700 GeV $\tilde{g}$ | +8.8% | +7.1% | -8.8% | -7.1% |
| 300 GeV $\tilde{t}$ | +9.0% | +7.8% | -9.1% | -8.4% |
| 300 GeV $\tilde{b}$ | +9.0% | +7.9% | -9.0% | -8.4% |

Table 6.1: Effect on overall MET_Topo scale by varying the scale of the individual clusters as described in text. Also shown is the resulting change in trigger efficiency.

Since most of the QCD radiation in these processes comes from the initial state, there is no reason to believe that the effects would depend on what sparticle is produced. To test this statement the 300 GeV mass point was evaluated for gluinos, stops and sbottoms and no significant discrepancies were observed.

The more primitive approach of just assuming a uniform 10% scale uncertainty to all signal samples was tested as well, and the resulting relative impact on the trigger efficiency can be seen in Table 6.2. The two techniques give very similar results.

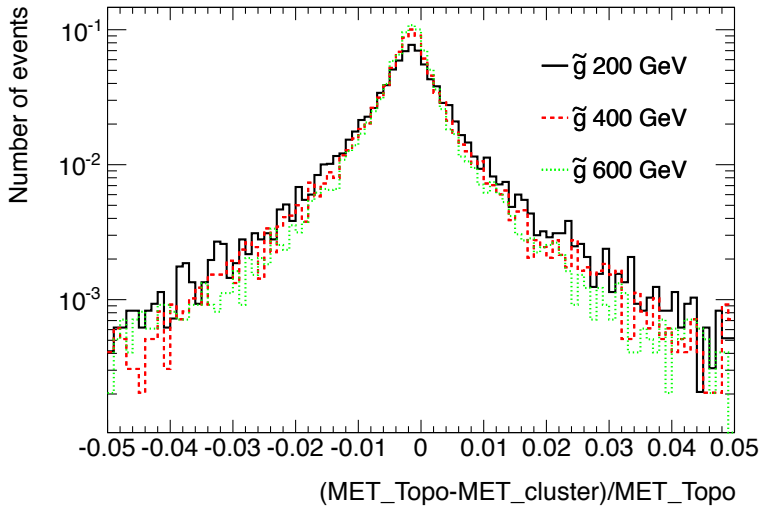


Figure 6.4: The relative difference between MET_Topo and manually recomputed $E_{\mathrm{T}}^{\mathrm{miss}}$ based on topological clusters at the EM scale.

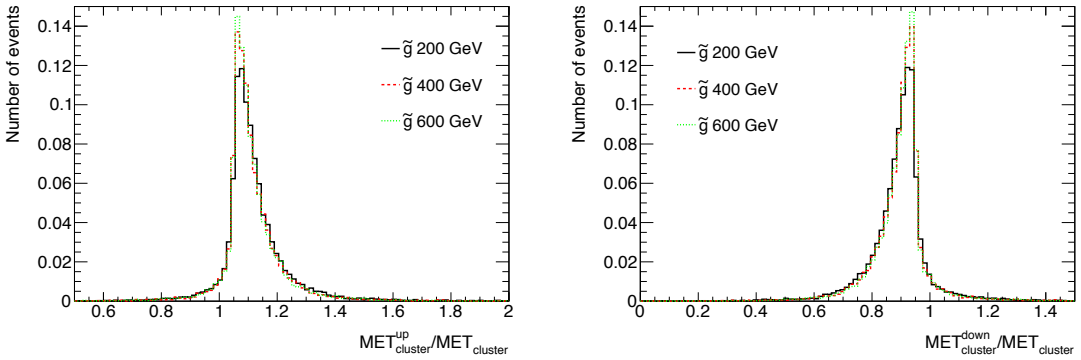


(a) (b)

Figure 6.5: The resulting relative scale shift of MET_Topo from varying the scale of the individual cluster energies (a) up and (b) down.

| $m$ (GeV) | 100 | 200 | 300 | 400 | 500 | 600 |
|---|---|---|---|---|---|---|
| **Gluino** | | | | | | |
| Scale +10% | +13.7% | +11.0% | +9.4% | +9.0% | +8.8% | +8.5% |
| Scale -10% | -13.6% | -11.7% | -9.9% | -9.6% | -9.2% | -8.9% |
| **Stop** | | | | | | |
| Scale +10% | +12.5% | +9.2% | +8.6% | +8.1% | +7.5% | - |
| Scale -10% | -12.7% | -9.8% | -9.2% | -8.8% | -8.2% | - |
| **Sbottom** | | | | | | |
| Scale +10% | +12.1% | +9.2% | +8.7% | +8.0% | +7.5% | - |
| Scale -10% | -12.5% | -9.9% | -9.3% | -8.6% | -8.1% | - |

Table 6.2: Change in trigger efficiency for gluino, stop and sbottom *R*-hadrons induced by variation in MET_Topo scale by 10%.

### 6.1.4 Trigger turn-on curve uncertainties

One way of estimating how uncertainties in the shape of the turn-on curve affect the total trigger efficiency is to vary the parameters of the fitted turn-on function within their uncertainties. By doing this and multiplying the resulting turn-on curve bin by bin with the expected $E_{\mathrm{T}}^{\mathrm{miss}}$ spectra for signal, the effect of these uncertainties on the trigger efficiency can be quantified. The relevant fit parameters are the effective threshold $B$ (the $E_{\mathrm{T}}^{\mathrm{miss}}$ value at 50% efficiency) and the resolution $C$ (standard deviation of the gaussian function that models the slope) in equation (6.1),

$$\varepsilon(E_{\mathrm{T}}^{\mathrm{miss}}) = \frac{A}{2}\left(1+\mathrm{erf}(\frac{E_{\mathrm{T}}^{\mathrm{miss}}-B}{\sqrt{2}C})\right), \tag{6.1}$$

where $A$ is the plateau value. This exercise was performed systematically for combinations of $1\sigma$ variations of the fit parameters. Table 6.3 shows the trigger efficiencies obtained for the 100 GeV and 500 GeV gluino signals. The same procedure was applied to the other *R*-hadron samples, with very similar results. The approximated systematic uncertainty due to the uncertainty in the fit parameters is therefore concluded to be $\pm 2\%$ in the trigger efficiency.

To compare the performance of the $E_{\mathrm{T}}^{\mathrm{miss}}$ trigger [129] in data and MC, turn-on curves for inclusive $W \to e\nu$ and $W \to \mu\nu$ samples were extracted for the `xe40_noMu` chain are shown in Figure 6.6. The turn-on curve for the $W \to e\nu$ process is sharper than the turn-on for $W \to \mu\nu$ and for *R*-hadrons, due to the superior energy resolution of the high-energy electron which is the dominant contribution to the measured energy imbalance. By contrast, the $W \to \mu\nu$ events firing this trigger are expected to do so due to additional jets since the $p_{\mathrm{T}}$ of muons is not taken into account in `xe40_noMu`. The energy resolution of jets is lower than for electrons, explaining the difference in the turn-on curves. The latter process therefore features an event topology very similar to the one expected for *R*-hadron signal scenarios, as can be seen in Figure 6.6.

| Efficiency (relative change) | $B-1\sigma$ | $B$ | $B+1\sigma$ |
|---|---|---|---|
| $R$-hadron, $m_{\tilde{g}} = 100$ GeV | | | |
| $C-1\sigma$ | 0.15559 (+1.2%) | 0.15331 (-0.3%) | 0.15109 (-1.8%) |
| $C$ | 0.15611 (+1.5%) | 0.15382 | 0.15157 (-1.5%) |
| $C+1\sigma$ | 0.15666 (+1.9%) | 0.15435 (+0.4%) | 0.15209 (-1.1%) |
| $R$-hadron, $m_{\tilde{g}} = 500$ GeV | | | |
| $C-1\sigma$ | 0.3910 (+0.7%) | 0.3877 (-0.1%) | 0.3844 (-1.0%) |
| $C$ | 0.3915 (+0.9%) | 0.3882 | 0.3849 (-0.8%) |
| $C+1\sigma$ | 0.3920 (+1.0%) | 0.3887 (+0.1%) | 0.3854 (-0.7%) |

Table 6.3: Efficiencies (and relative change with respect to the central values of the fit parameters) obtained by multiplying the fitted turn-on curve (for L1+EF) bin by bin with the MET spectrum, for the 100 GeV (top) and 500 GeV (top) gluino signal MC samples. Independent $1\sigma$ variations of the effective threshold ($B$) and the resolution ($C$) are shown.

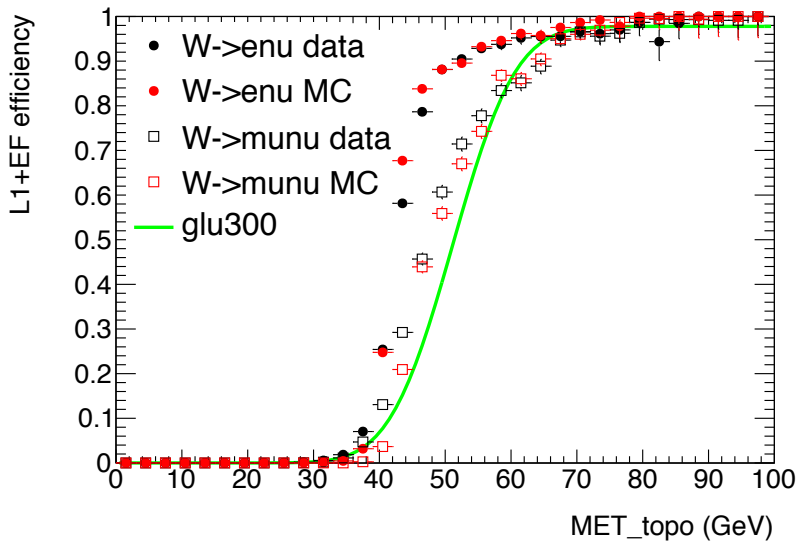


Figure 6.6: Turn-on curves for selected $W$ decays to electrons and muons in data and MC, as well as for a 300 GeV gluino sample.

By analyzing the binwise difference between the turn-on curves measured and predicted for the $W \to \mu\nu$ and $W \to e\nu$ processes, an estimate of the difference between turn-on performance in data and MC was extracted. In the turn-on region the difference was typically 4%. Adjusting the turn-on by this uncertainty and folding it with the signal MET_Topo spectrum (Figure 6.2) results in relative efficiency differences ranging from $\pm 3.0\%$ for $m_{\tilde{g}} = 500$ GeV to $\pm 5.2\%$ for $m_{\tilde{g}} = 100$ GeV. This difference is a maximum difference between the trigger performance in data and MC, and not a standard deviation. It is therefore not added in quadrature with the other errors.

## 6.2 Data selection

The experimental data used in this search were collected from July to October 2009 and correspond to an integrated luminosity of 34 pb$^{-1}$. Data from the `JetTauEtmiss` and `debug`[3)] trigger streams were used and selections were applied to discard data with poor quality due to detector problems. The initial event selection required the events to have passed one of several triggers considered in the analysis, including the final choice, the `xe40_noMu` trigger signature described in the previous section. It also demanded the presence of a reconstructed track with $p_{\mathrm{T}} > 10$ GeV and associated MIP-like calorimeter deposits, or a reconstructed muon. In the yield tables below, these requirements are referred to as *skimming*.

### 6.2.1 Signal candidate preselection

The SMP signature considered in this search features an ID track with associated calorimeter energy losses approximately compatible with those expected for a muon. A number of criteria were applied to select *R*-hadron candidates. Candidates are defined as offline muons reconstructed by the `CaloTag`, `CaloLikelihood` and/or `CaloMuonId` algorithms [78]. These algorithms are designed to tag actual muons using only ID tracks and calorimeter energy measurements and do not rely on any signals in the muon spectrometer. For the processing of the 2010 data used in this analysis, these algorithms were run with commissioning settings, accepting most extrapolated tracks with associated energy deposits falling in a rather large window around those expected for muons. This implies a high efficiency for selecting electrically charged *R*-hadrons. The efficiency of reconstructing *R*-hadrons in this way is shown in Figure 6.7 as a function of the particle speed, $\beta$, momentum, $p$, pseudorapidity, $\eta$, and azimuthal angle, $\phi$. The efficiency shown here is defined with respect to the true simulated *R*-hadrons which possess non-zero electrical charge following the hadronization. Around half of *R*-hadrons are produced as electrically neutral objects and this represents an irreducible, though well understood source of loss.

[3)] The debug stream contains events which the trigger system had trouble processing online. Since the considered signal could potentially cause trouble in the reconstruction, it was decided to examine these events as well.

Following this preselection, tighter subsystem-specific selections were imposed to ensure well-measured track kinematics, Pixel $dE/dx$ and $\beta_{\text{Tile}}$ for each candidate.

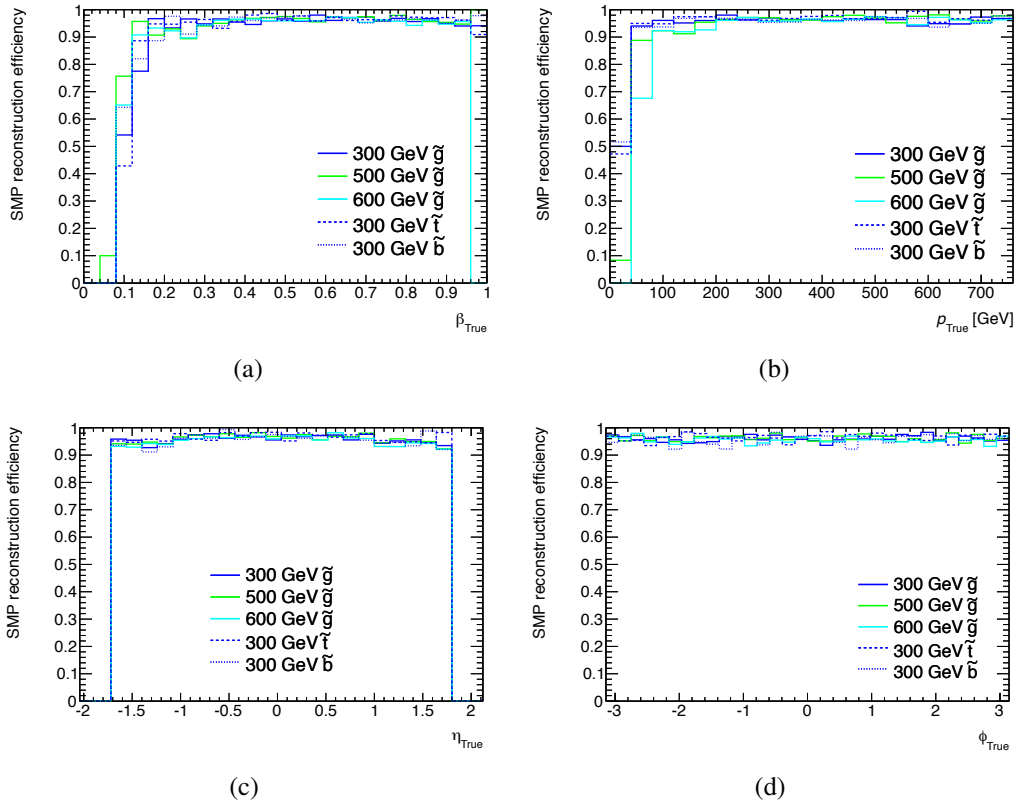


Figure 6.7: Predicted efficiency for reconstructing $R$-hadrons of different types and masses with a calorimeter+ID based muon algorithm, as a function of the particle speed $\beta$ (a), momentum $p$ (b), pseudorapidity $\eta$ (c) and azimuthal angle $\phi$ (d), given that the candidate possesses a non-zero electric charge after hadronisation.

A preselection of events containing $R$-hadron candidates was made according to the criteria listed below. The requirements can be grouped in two categories. Criteria *i-iii* reduce the risk of contaminating the data sample with events caused by non-collision backgrounds or poorly reconstructed objects stemming from instrumental effects. After this clean-up, criteria *iv-vi* were imposed in order to suppress backgrounds from physics processes involving real high-$p_{\text{T}}$ muons. The requirements are summarized in order below.

*i*) **Trigger** The event must have passed the `xe40_noMu` trigger signature, i.e. passed `L1_XE25` and `EF_xe40_noMu`.

*ii*) **Vertex cleaning** The event must have at least one reconstructed vertex with at least three associated tracks. This selection has an insignificant effect on the event yield.

*iii*) **Track quality** Requirements regarding the quality of the reconstructed track were then applied to the candidates, according to the recommendations prescribed by the muon reconstruction community in ATLAS. The requirements include at least two Pixel hits[4)], six SCT hits and six TRT, with the additional criterion that less than 90% of the TRT hits are *outliers*. Figure 6.8 shows the observed distributions of the number of pixel hits, SCT hits and TRT hits, compared with predictions for simulated background processes and a select set of *R*-hadron samples. The distributions shown in Figure 6.8 were made using all candidate tracks in events passing the trigger. In general, the data are described well by the simulated backgrounds, though the statistical uncertainties are large for the total background this early stage of the selection. The predicted hit multiplicities for *R*-hadrons broadly follow those observed in data, as expected from the discussion in Section 5.1.

*iv*) **Tile calorimeter acceptance** Only candidates satisfying $|\eta| < 1.7$ were considered since this search is geometrically limited by the acceptance of the Tile calorimeter.

*v*) **Distance to jet**. Strong processes leading to jet production are potentially a large source of background. In this case, the candidates will be found within a jet. A fundamental property of massive *R*-hadrons produced at LHC energies is that they would not fall within a reconstructed high-$E_T$ jet. Although the gluino pair-production processes superficially resembles a gluon-gluon production mechanism, owing to the mass of the gluinos, the *R*-hadron possesses $> 99\%$ of the energy of any jet which would be formed. It would thus appear isolated. To reduce backgrounds from strong processes, e.g. dijet production, a cut was imposed on the angular distance between a candidate and any anti-$k_{\mathrm{t}}$ jet [127] in the event with $E_{\mathrm{T}}$ >40 GeV at the EM scale. The quantity $\Delta R = \sqrt{(\Delta\eta)^2 + (\Delta\phi)^2}$ was considered, where $\Delta\eta$ and $\Delta\phi$ are the differences in azimuthal angle and pseudorapidity between the candidate and a jet. Distributions of $\Delta R$ as seen in data and predicted by background and signal simulations after preselection are shown in Figure 6.9. An approximate agreement between data and the background predictions is observed, consistent within the errors due to limited statistics for the low-$p_{\mathrm{T}}$ QCD samples. As expected, there is a peak at $\Delta R \sim 0$ corresponding to background candidates within jets. The *R*-hadron spectra dominantly correspond to $\Delta R > 0$ and consequently a distance-to-jet selection $\Delta R > 0.5$ was imposed.

*vi*) **Transverse momentum**. In Figure 6.10 the transverse momentum distribution is shown for data and compared with predictions from a number of background sources, after preselection and the $\Delta R$ cut described above. As can be seen, the simulated backgrounds reproduce the data very well both in shape and yield. Also shown are the predicted *R*-hadron spectra which are typically much harder than that of candidates

[4)]The recommended ID track selection only requires one Pixel hit, however two are needed later on in the analysis to ensure a well-measured Pixel $dE/dx$

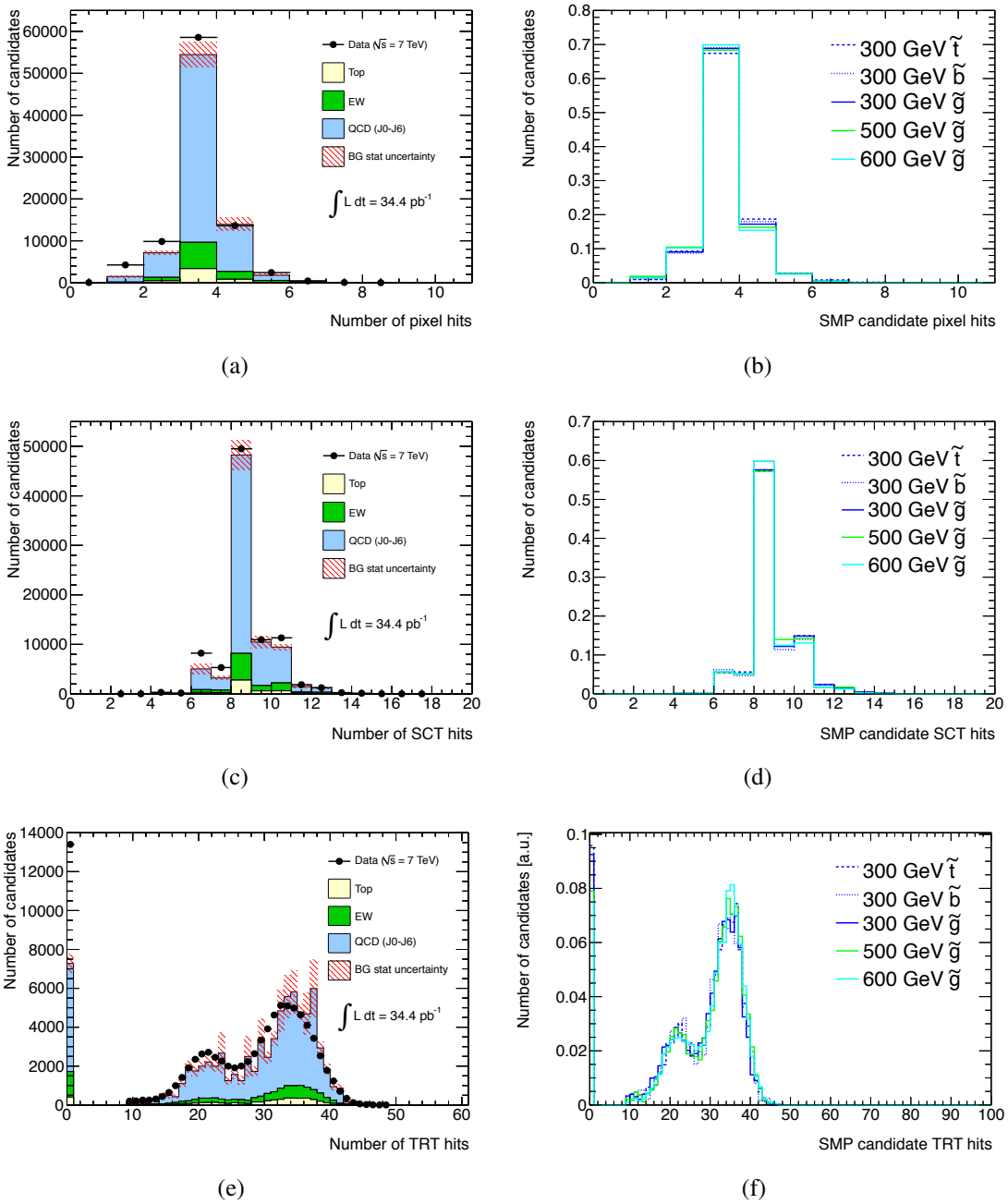


Figure 6.8: Distributions of the number of Pixel, SCT and TRT hits for candidates in data and from simulated background (left) and a selected set of *R*-hadron signal scenarios.

arising from background processes. Using $S/\sqrt{B}$ as the figure of merit, the cut was optimized to $p_{\mathrm{T}} > 50$ GeV.

The mass spectra from Pixel and Tile for candidates passing the preselection are shown in Figure 6.11. Tails extending up to several hundred GeV are seen for the individual measurements, which are predicted well by the background MC processes.

Given the redundancy inherent to using two subsystems which each provide a speed-sensitive measurement, the tails due to instrumental effects can be strongly suppressed by requiring that both subsystems observe a slow object. Figure 6.12 shows the two-dimensional distributions of $\beta_{\mathrm{Tile}}$ and Pixel $dE/dx$, for both data and signal. The power of using two mass estimates is illustrated by the lack of correlation in Figure 6.13 (a) in which the candidate masses evaluated using both Pixel $dE/dx$ and $\beta_{\mathrm{Tile}}$ is shown for data. Figure 6.13 (b) shows the same distribution for a 500 GeV gluino signal, where the two mass estimates give similar results. The diagonal shape of the two-dimensional mass distribution comes from the fact that they both use the same momentum measurement.

### 6.2.2 Event yield

In Table 6.4 the observed and expected event yields are summarized. The MC-based background predictions reproduce the observed data to with an accuracy of $\sim 20\%$. It should again be emphasized that the background simulations are used purely to aid the optimization of *R*-hadron selections and to reveal the composition of the observed backgrounds, but not for the final results. For example, the simulated background samples can shed some light on what type of particles pass the candidate selections, and this is shown in Appendix A. For the evaluation of the cross section and mass limits in Section 9.1, a purely data-driven background approach is used and this is described further in Chapter 7. To illustrate the power of imposing mass cuts on two subsystems, mass requirements are in the final line of the table. The "Mass preselection" line includes the requirement that the events passing has at least one candidate with mass estimates from both the Pixel detector and the Tile calorimeter. There is a significant drop in the background when imposing the mass requirement. This is due to the requirements of extracting valid mass estimates from both sub-systems. The Tile measurement requires a $\beta$ value below one (see Section 5.3.5), which in turns imposes cuts on the Tile cell energies. Also, the Pixel $dE/dx$ is only defined for tracks with two or more good clusters. To cut down background, the $m_{\mathrm{Pixel}} > 0$ GeV cut here also requires that Pixel $dE/dx > 1.8$ MeVg$^{-1}$cm$^2$.

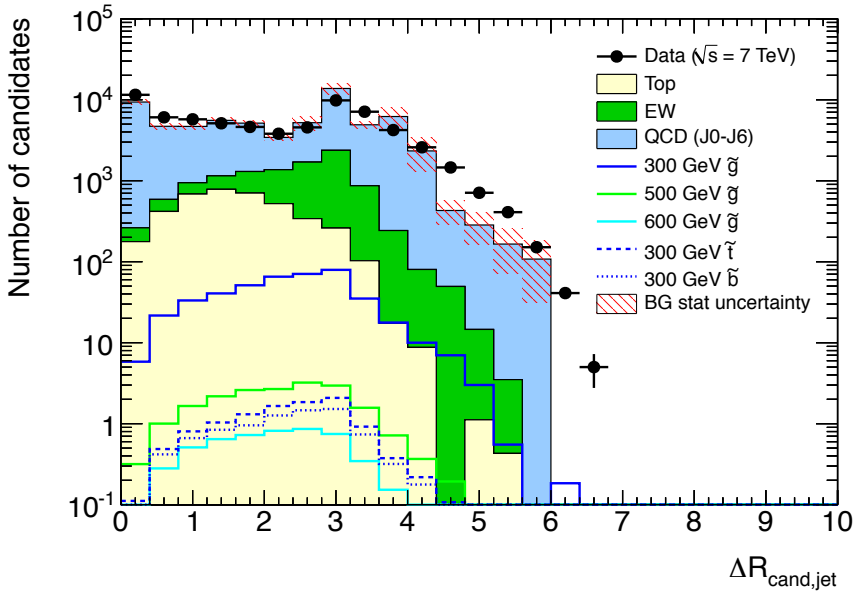


Figure 6.9: Distributions of $\Delta R = \sqrt{(\Delta\eta)^2 + (\Delta\phi)^2}$ after trigger, vertex and track cleaning and $|\eta < 1.7|$ has been required. Data and predicted spectra from a number of possible background sources are shown.

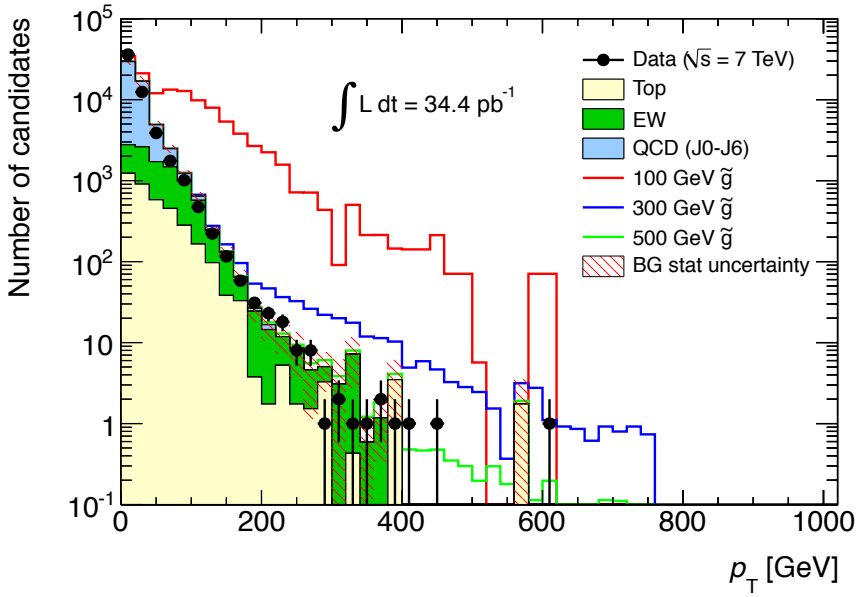


Figure 6.10: Distributions of transverse momentum after the $\Delta R_{SMP,jet} > 0.5$ requirement has been imposed. Data and predicted spectra from a number of possible background sources are shown, along with predictions for a few signal scenarios.

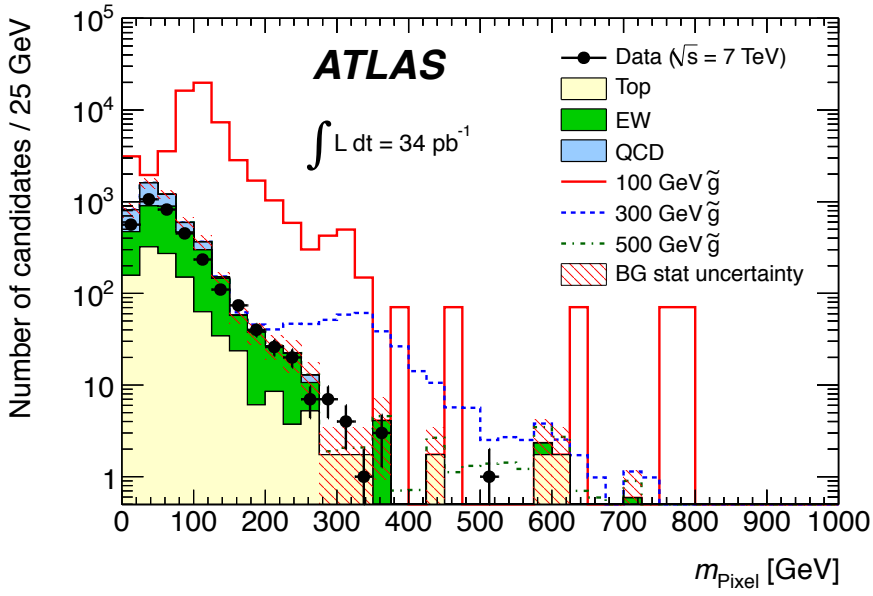


(a)

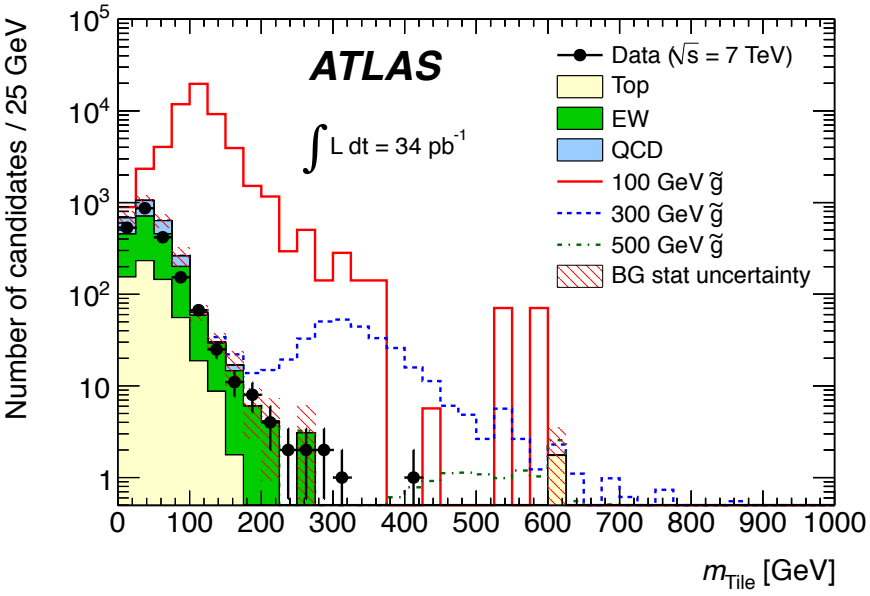


(b)

Figure 6.11: The distributions of reconstructed mass from Pixel (a) and Tile (b) for data and MC simulations of backgrounds and signal.

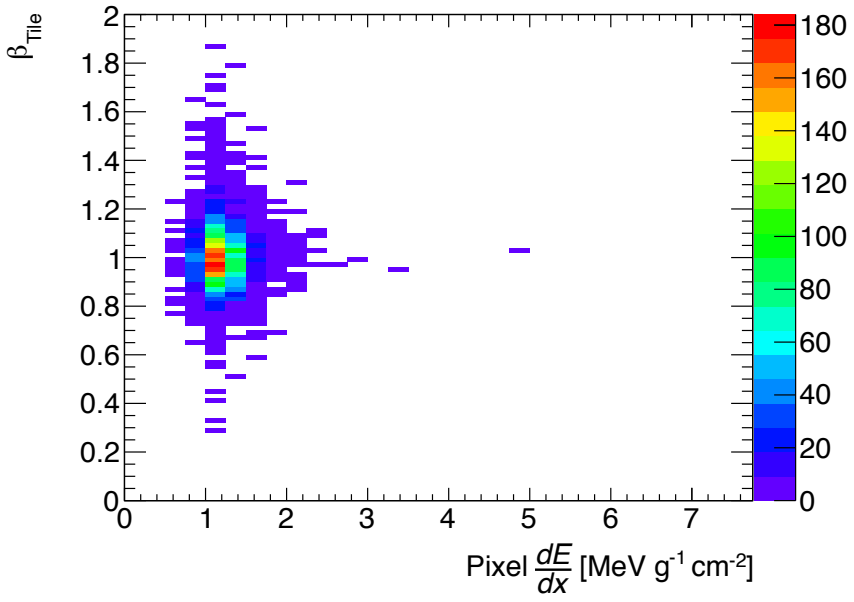


(a)

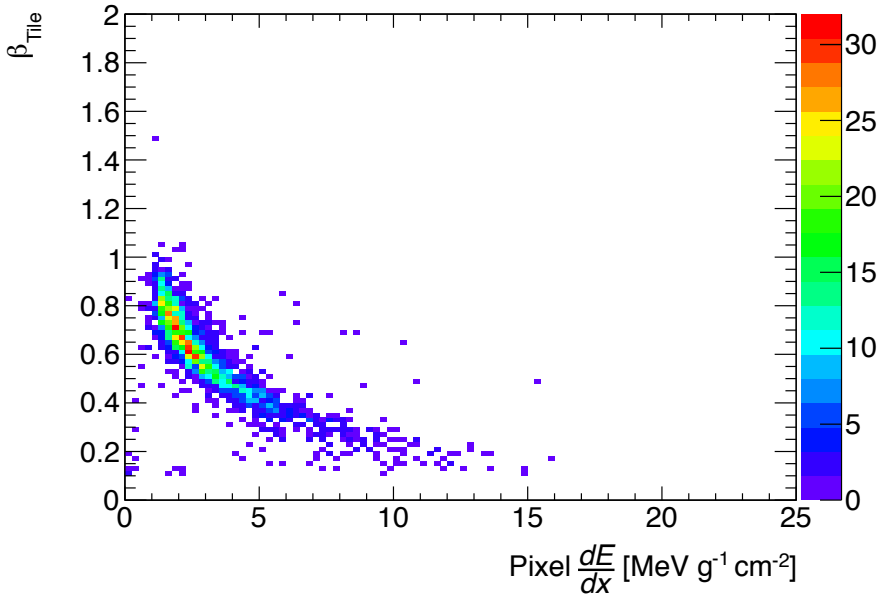


(b)

Figure 6.12: The two-dimensional distribution of $\beta_{\text{Tile}}$ and Pixel $dE/dx$ for (a) data and (b) a 500 GeV gluino $R$-hadron signal scenario.

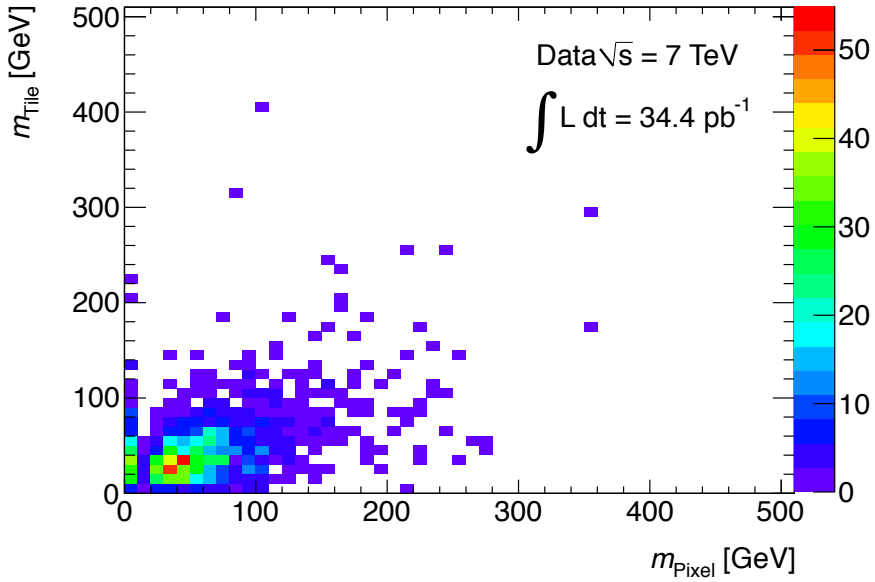


(a)

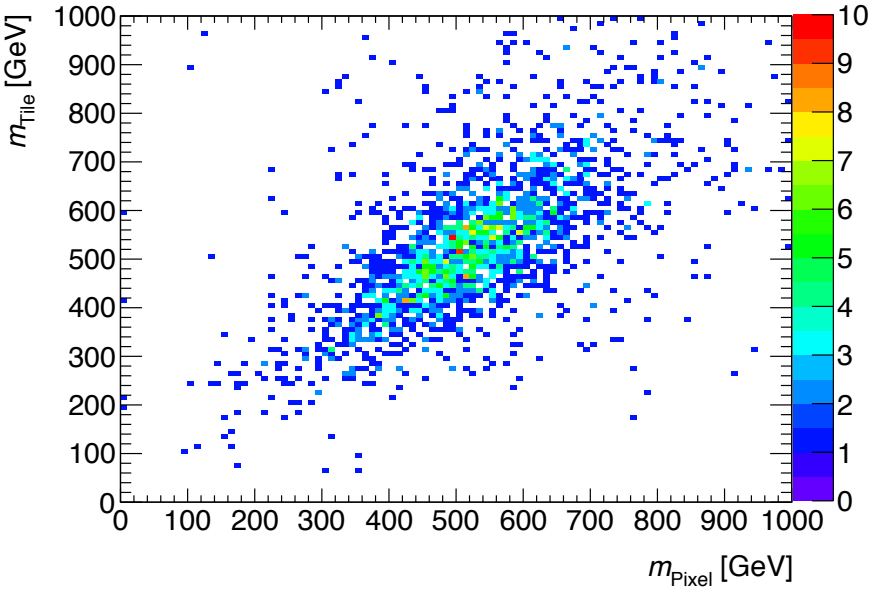


(b)

Figure 6.13: The 2D distribution for the candidate mass as determined with Pixel $dE/dx$ versus the mass estimated with $\beta_{\text{Tile}}$ for (a) data and (b) a 500 GeV gluino R-hadron signal scenario. For these plots, a relaxed Pixel $dE/dx$ requirement of 1.2 MeVg$^{-1}$cm$^2$ is used, to allow the 2D distribution to be visualized. With the nominal requirement of Pixel $dE/dx > 1.8$ MeVg$^{-1}$cm$^2$, only 36 events survive in the experimental data.

Table 6.4: Observed and expected event yields at different steps of the data selection procedure. The individual rows of the table correspond to the stages in the cut flow as defined in the text. The row denoted *Mass preselection* indicates the number of events having at least one candidate with a mass estimate from both subsystems. In addition to data, predictions from simulated SM background and signal processes are shown. Predicted yields are scaled to the integrated luminosity of the data sample using the cross section of each process.

| **Cut level** | **Data** | **Background** | **300 GeV $\tilde{g}$** | **500 GeV $\tilde{g}$** | **600 GeV $\tilde{g}$** | **200 GeV $\tilde{t}$** | **200 GeV $\tilde{b}$** |
|---|---|---|---|---|---|---|---|
| No cuts | - | - | $2.13 \times 10^3$ | 80.4 | 21.8 | 405 | 405 |
| Trigger | - | - | 616 | 25.6 | 6.96 | 109 | 108 |
| Candidate | 75466 | $68.0 \times 10^3$ | 416 | 17.6 | 4.80 | 87.4 | 67.9 |
| Vertex | 75461 | $68.0 \times 10^3$ | 416 | 17.6 | 4.80 | 87.4 | 67.9 |
| $\lvert\eta\rvert$ <1.7 | 64618 | $60.5 \times 10^3$ | 364 | 15.7 | 4.32 | 75.2 | 56.8 |
| Track quality | 59872 | $58.1 \times 10^3$ | 355 | 15.3 | 4.20 | 73.3 | 54.9 |
| $\Delta R > 0.5$ | 49205 | $49.4 \times 10^3$ | 349 | 15.1 | 4.13 | 72.7 | 54.5 |
| $p_{\mathrm{T}} > 50$ GeV | 5116 | $6.56 \times 10^3$ | 330 | 14.5 | 3.95 | 68.9 | 50.0 |
| Mass preselection | 36 | 56.0 | 184 | 9.70 | 2.75 | 32.6 | 18.9 |

## 6.3 Efficiencies

For this search both Tile and the Pixel Detector were required to provide a measurement of speed and continuous ionization energy loss, respectively. The algorithms used to calculate these quantities are described in detail in Sections 5.2-5.3. The criteria applied to ensure that the candidate provides a well measured Pixel $dE/dx$ and $\beta_{\mathrm{Tile}}$ are:

- The pseudorapidity was restricted to cover the central region in which Tile and the Pixel detector both return a measurement: $|\eta| < 1.7$.
- At least two pixel clusters are required.
- At least one Tile cell must have an energy exceeding 500 MeV.

### 6.3.1 Efficiency of the $m_{\mathrm{Tile}}$ measurement

Due to the criteria outlined above, the efficiency for reconstructing a value of $\beta_{\mathrm{Tile}}$ as a function of $\beta$, $p$, $\eta$ and $\phi$ are shown in Figure 6.14. In order to provide a mass measurement, the measured $\beta_{\mathrm{Tile}}$ has to fulfill $0 < \beta_{\mathrm{Tile}} < 1$. The resulting mass reconstruction efficiency is shown in Figure 6.15. The efficiency is highest for the $\beta$-interval used by this analysis, $0.4 \lesssim \beta \lesssim 0.8$. This is the region in which both Tile and the Pixel detector provide a speed measurement. The slightly lower efficiency at $\beta$ close to unity is due to the difference in expected ionization energy loss. The efficiency is approximately flat over $\eta$ and $\phi$ and rises as a function of momentum. The efficiency is severely degraded for $|\eta| \approx 1.6$, even though the track selection allows pseudo-rapidities up to 1.7. In Tile, high momentum tracks with $|\eta| > 1.6$ pass through at most one cell (see Figure 4.5),

which lowers the probability of having a crossed cell measuring an energy over threshold. The efficiency is higher for gluino *R*-hadrons than for squark *R*-hadrons due to the greater predicted energy loss from hadronic interactions for the gluino *R*-hadrons. The lower efficiency for *R*-hadrons formed from sbottoms compared to those containing stops is due to the fact that the sbottoms to a larger extent will be electrically neutral when reaching the Tile calorimeter, as discussed in Section 2.3.4.

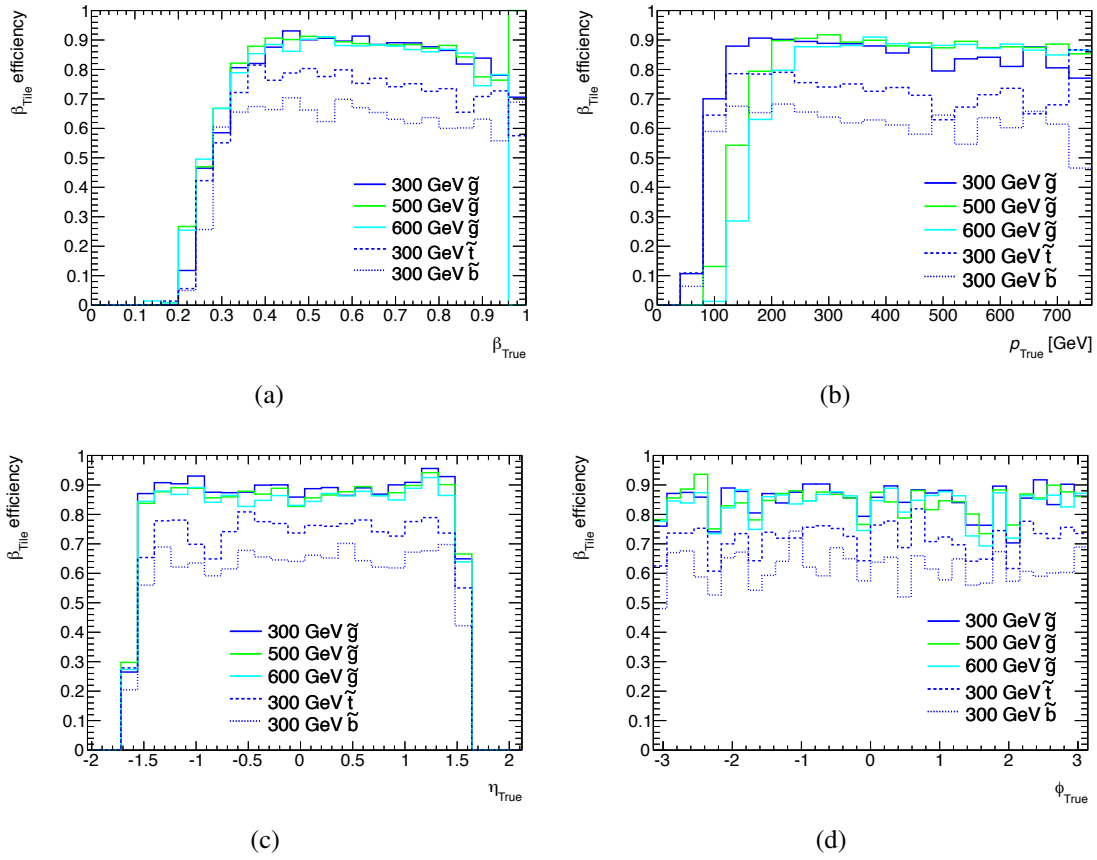


Figure 6.14: Predicted efficiency for Tile to provide a $\beta$ measurement for various types of *R*-hadrons as a function of the particle speed (a), momentum (b), pseudorapidity (c) and azimuthal angle (d), given that the *R*-hadron was reconstructed as a candidate.

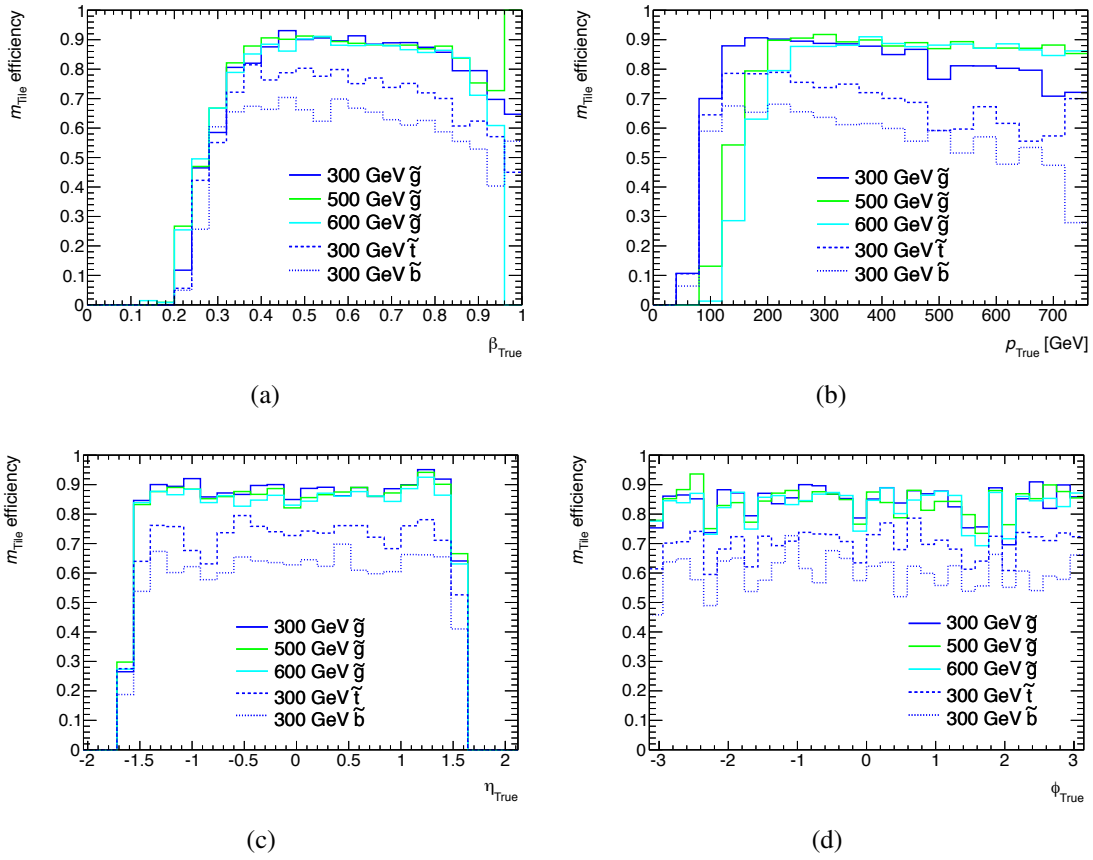


Figure 6.15: Predicted efficiency for Tile to provide a mass measurement for various types of $R$-hadrons as a function of the particle speed (a), momentum (b), pseudorapidity (c) and azimuthal angle (d), given that the $R$-hadron was reconstructed as a candidate.

### 6.3.2 Efficiency of the $m_{\text{Pixel}}$ measurement

The efficiencies for the Pixel detector to reconstruct a value of $dE/dx$ and a mass as a function of $\beta$, $p$, $\eta$ and $\phi$ are shown in Figures 6.16 and 6.17, respectively. Following the various kinematic selections and the Pixel $dE/dx$ requirements, the search is restricted to the region $0.3 \lesssim \beta \lesssim 0.8$. As for Tile, the efficiency is highest for the $\beta$-interval exploited by this analysis. Again, the fall at higher values of $\beta$ is due to kinematic effects: $R$-hadrons with higher values of $\beta$ have more MIP-like energy losses in the silicon, making it impossible to translate their measured $dE/dx$ to a $\beta\gamma$. The efficiency is approximately flat over $\eta$ and $\phi$ and rises as a function of momentum.

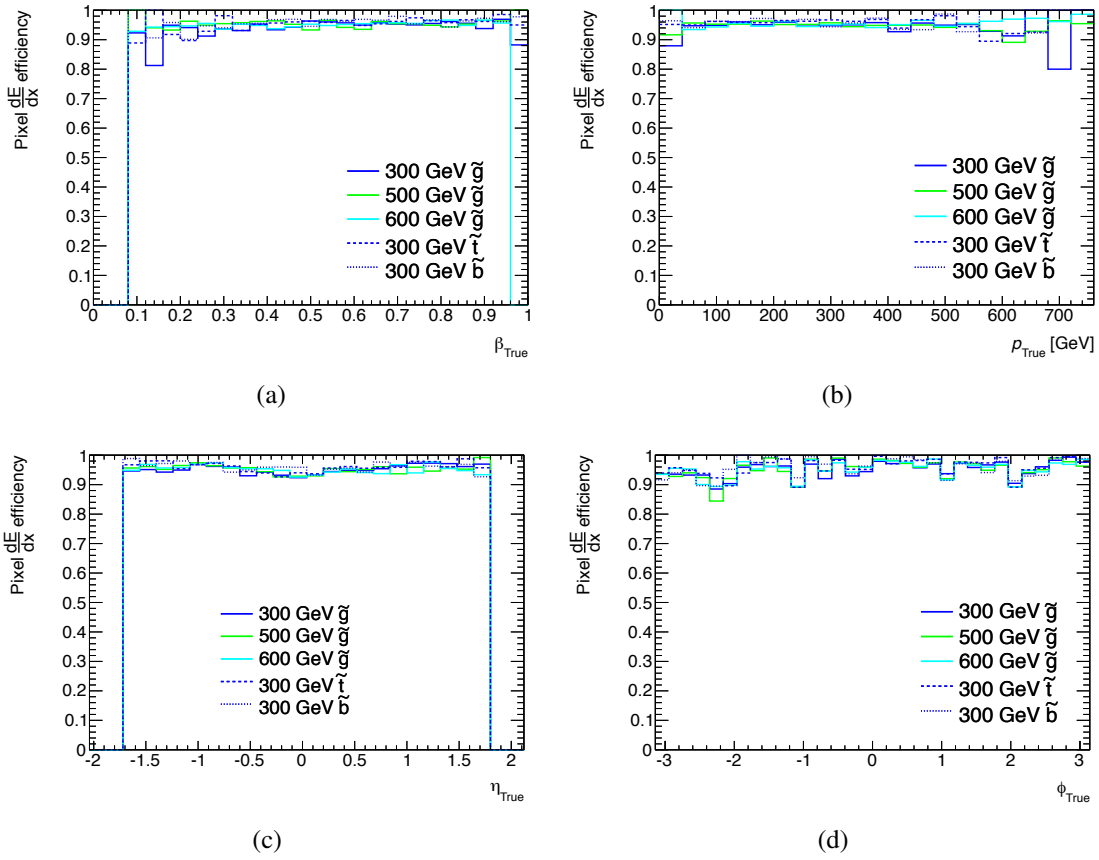


Figure 6.16: Predicted efficiency for the Pixel detector to provide a $dE/dx$ measurement for various types of $R$-hadrons as a function of the particle speed (a), momentum (b), pseudorapidity (c) and azimuthal angle (d), given that the gluino was reconstructed as a candidate.

### 6.3.3 Cut efficiencies for selected samples

Table 6.5 shows the selection efficiencies for each of the requirements imposed on the data events, both relative to the preceding requirement and cumulative, i.e. relative to all events passing the skimming criteria. Table 6.6 shows the same for the three classes of background processes, QCD, electroweak and top. Table 6.7 shows the equivalent results for the 100, 300 and 500 GeV gluino $R$-hadron samples. It is seen that the cumulative selection efficiencies for data and background are small at the later stages of the cut flow, while $R$-hadron efficiencies are generally around 10%. The low efficiency for the 100 GeV $R$-hadron sample is more than adequately compensated by the large cross section for this scenario.

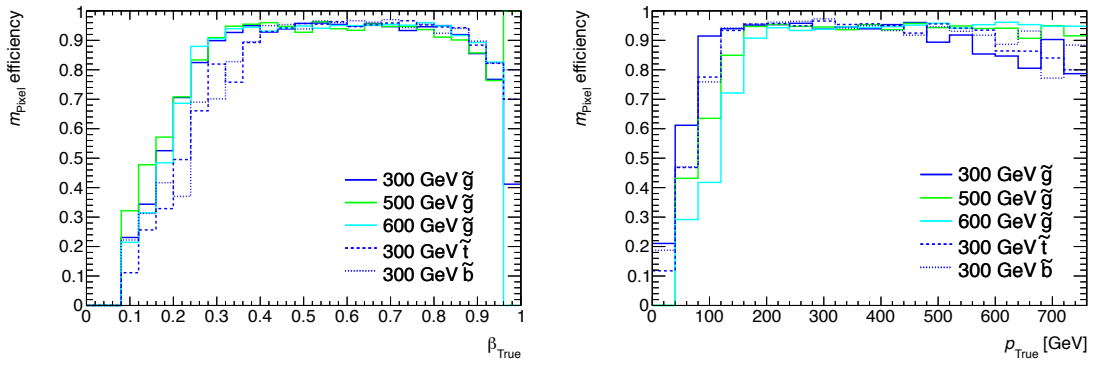


(a) (b)

(c) (d)

Figure 6.17: Predicted efficiency for the Pixel detector to provide a mass measurement for various types of *R*-hadrons as a function of the particle speed (a), momentum (b), pseudorapidity (c) and azimuthal angle (d), given that the gluino was reconstructed as a candidate.

| **Cut level** | **# events** | **Relative eff. (%)** | **Cumulative eff. (%)** |
|---|---|---|---|
| Skimming | 381647.00 | 100.00 | 100.00 |
| Trigger | 172358.00 | 45.16 | 45.16 |
| Vertex cleaning | 170187.00 | 98.74 | 44.59 |
| Track cleaning | 69644.00 | 40.92 | 18.25 |
| $\|\eta\| < 1.7$ | 59872.00 | 85.97 | 15.69 |
| $\Delta R > 0.5$ | 49205.00 | 82.18 | 12.89 |
| $p_{\mathrm{T}} > 50$ GeV | 5116.00 | 33.97 | 1.34 |
| Mass preselection | 36.00 | 0.70 | 0.01 |
| $m > 50$ GeV | 9.00 | 25.00 | 0.00 |
| $m > 100$ GeV | 0.00 | 0.00 | 0.00 |

Table 6.5: Selection efficiencies for each of the requirements imposed on the data events, both relative to the preceding requirement and cumulative, i.e. relative to all events passing the skimming criteria.

Efficiency table for QCD

| Cut level | # events | Relative eff. (%) | Cumulative eff. (%) |
|---|---|---|---|
| Skimming | 384361.59 | 100.00 | 100.00 |
| Trigger | 133499.19 | 34.73 | 34.73 |
| Vertex cleaning | 133498.39 | 100.00 | 34.73 |
| Track cleaning | 53135.55 | 39.80 | 13.82 |
| $\|\eta\| < 1.7$ | 48481.06 | 91.24 | 12.61 |
| $\Delta R > 0.5$ | 40003.18 | 82.51 | 10.41 |
| $p_{\mathrm{T}} > 50$ GeV | 2284.49 | 14.72 | 0.59 |
| Mass preselection | 4.31 | 0.19 | 0.00 |
| $m > 50$ GeV | 0.00 | 0.00 | 0.00 |
| $m > 100$ GeV | 0.00 | - | 0.00 |

Efficiency table for EW

| Cut level | # events | Relative eff. (%) | Cumulative eff. (%) |
|---|---|---|---|
| Skimming | 9196.60 | 100.00 | 100.00 |
| Trigger | 9168.06 | 99.69 | 99.69 |
| Vertex cleaning | 9168.06 | 100.00 | 99.69 |
| Track cleaning | 8430.52 | 91.96 | 91.67 |
| $\|\eta\| < 1.7$ | 6320.67 | 74.97 | 68.73 |
| $\Delta R > 0.5$ | 6270.63 | 99.21 | 68.18 |
| $p_{\mathrm{T}} > 50$ GeV | 2948.04 | 64.58 | 32.06 |
| Mass preselection | 33.07 | 1.12 | 0.36 |
| $m > 50$ GeV | 15.95 | 48.22 | 0.17 |
| $m > 100$ GeV | 0.00 | 0.00 | 0.00 |

Efficiency table for Top

| Cut level | # events | Relative eff. (%) | Cumulative eff. (%) |
|---|---|---|---|
| Skimming | 4823.52 | 100.00 | 100.00 |
| Trigger | 4530.06 | 93.92 | 93.92 |
| Vertex cleaning | 4527.89 | 99.95 | 93.87 |
| Track cleaning | 3694.10 | 81.59 | 76.59 |
| $\|\eta\| < 1.7$ | 3294.79 | 89.19 | 68.31 |
| $\Delta R > 0.5$ | 3169.58 | 96.20 | 65.71 |
| $p_{\mathrm{T}} > 50$ GeV | 1331.22 | 59.78 | 27.60 |
| Mass preselection | 18.60 | 1.40 | 0.39 |
| $m > 50$ GeV | 10.22 | 54.96 | 0.21 |
| $m > 100$ GeV | 0.00 | 0.00 | 0.00 |

Table 6.6: Selection efficiencies for each of the requirements imposed on the background simulations, both relative to the preceding requirement and cumulative, i.e. relative to all events passing the skimming criteria.

Efficiency table for 300 GeV $\tilde{g}$

| Cut level | # events | Relative eff. (%) | Cumulative eff. (%) |
|---|---|---|---|
| No cut | 2133.60 | 100.00 | 100.00 |
| Trigger | 615.89 | 28.87 | 28.87 |
| Vertex cleaning | 615.89 | 100.00 | 28.87 |
| Track cleaning | 405.99 | 65.92 | 19.03 |
| $\|\eta\| <1.7$ | 354.50 | 87.32 | 16.62 |
| $\Delta R > 0.5$ | 348.98 | 98.44 | 16.36 |
| $p_{\mathrm{T}} > 50$ GeV | 329.59 | 99.46 | 15.45 |
| Mass preselection | 184.12 | 55.86 | 8.63 |
| $m > 50$ GeV | 184.12 | 100.00 | 8.63 |
| $m > 100$ GeV | 183.93 | 99.90 | 8.62 |

Efficiency table for 500 GeV $\tilde{g}$

| Cut level | # events | Relative eff. (%) | Cumulative eff. (%) |
|---|---|---|---|
| No cut | 80.40 | 100.00 | 100.00 |
| Trigger | 25.55 | 31.78 | 31.78 |
| Vertex cleaning | 25.55 | 99.98 | 31.78 |
| Track cleaning | 17.09 | 66.91 | 21.26 |
| $\|\eta\| <1.7$ | 15.30 | 89.50 | 19.03 |
| $\Delta R > 0.5$ | 15.09 | 98.66 | 18.78 |
| $p_{\mathrm{T}} > 50$ GeV | 14.53 | 99.52 | 18.07 |
| Mass preselection | 9.65 | 66.44 | 12.01 |
| $m > 50$ GeV | 9.64 | 99.88 | 11.99 |
| $m > 100$ GeV | 9.64 | 100.00 | 11.99 |

Efficiency table for 600 GeV $\tilde{g}$

| Cut level | # events | Relative eff. (%) | Cumulative eff. (%) |
|---|---|---|---|
| No cut | 21.78 | 100.00 | 100.00 |
| Trigger | 6.96 | 31.96 | 31.96 |
| Vertex cleaning | 6.96 | 99.98 | 31.96 |
| Track cleaning | 4.67 | 67.11 | 21.44 |
| $\|\eta\| <1.7$ | 4.20 | 89.99 | 19.30 |
| $\Delta R > 0.5$ | 4.13 | 98.37 | 18.98 |
| $p_{\mathrm{T}} > 50$ GeV | 3.95 | 99.57 | 18.12 |
| Mass preselection | 2.75 | 69.81 | 12.65 |
| $m > 50$ GeV | 2.75 | 99.90 | 12.63 |
| $m > 100$ GeV | 2.75 | 100.00 | 12.63 |

Table 6.7: Selection efficiencies for each of the requirements imposed on the events in selected signal samples., both relative to the preceding requirement and cumulative, i.e. relative to all events passing the skimming criteria.

# 7 Background estimation

## 7.1 Sources of background

The Standard Model (SM) does not predict any physics processes featuring penetrating particles with masses of $\mathcal{O}(100\ \text{GeV})$. However, instrumental effects can make a low-mass SM particle look like a heavy long-lived object. Due to resolution effects, it is possible that the $\beta_{\text{Tile}}$ and Pixel $dE/dx$ measurements can fluctuate to values similar to what is expected for a slow heavy particle. In the same way, the momentum can be mismeasured. A high Pixel $dE/dx$ value combined with an overestimated momentum will conspire to look like a slow-moving charged particle. However, since the Pixel $dE/dx$ and $\beta_{\text{Tile}}$ measurements are independent, the background due to rare instrumental fluctuations in each observable can be reduced by requiring both subsystems to agree. For the signal, the quantities are expected to be correlated, and therefore such a cut does not reduce the signal efficiency to the same extent. Fluctuations in $p$ are greatly suppressed by the stringent ID hit requirements described in Section 6.2.1. Measures were also taken to limit the variations in the Pixel $dE/dx$ and $\beta_{\text{Tile}}$ with the cluster-cleaning procedure and cell-energy thresholds described in Sections 5.2 and 5.3, respectively.

While the simulation gives a good overall description of the background, it fails to perfectly account for the details of the Pixel $dE/dx$ and $\beta_{\text{Tile}}$ distributions (see Figures 5.3 and 5.8). In addition, the simulation cannot precisely predict the amount of background at high masses due to lack of statistics in the tails of the distributions. To circumvent these shortcomings, and to automatically include several instrumental effects, an approach based only on experimental data was used to estimate the background.

Figure 7.1 illustrates how different regions in $p$-$\beta$ space can give rise to large masses. Each curve corresponds to a specific reconstructed mass and indicates what combinations of $p$ and $\beta$ will give rise to the given mass. As an example, a particle with true momentum $p_{\text{true}} = 100$ GeV and speed $\beta_{\text{true}} \approx 1$ can appear to have a mass of approximately 200 GeV if the reconstructed momentum and $\beta$ are mismeasured as $p_{\text{rec}} = 260$ GeV and $\beta_{\text{rec}} = 0.8$. The background estimation method must therefore take into account mismeasurements of both momentum and speed.

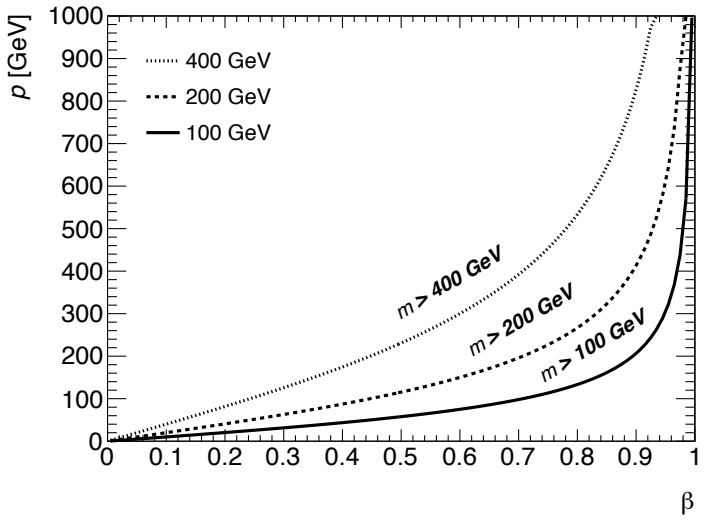


Figure 7.1: Diagram illustrating the different regions in reconstructed $p$-$\beta$ space which can combine to produce a mass greater than 100, 200 and 400 GeV.

## 7.2 Description of the method

The method used to estimate the expected background combines random momenta with random Pixel $dE/dx$ and $\beta_{\text{Tile}}$ measurements to produce mass spectra, relying only on experimental data. However, it assumes that there is no correlation between these measured quantities. Using a large sample of candidates with $p_{\text{T}} > 10$ GeV from the experimental data, the linear correlations between the reconstructed momentum and measurements of Pixel $dE/dx$ and $\beta_{\text{Tile}}$ illustrated in Figure 7.2, were determined. They are found to be $\rho_{p,dE/dx} = 0.006 \pm 0.017$ and $\rho_{p,\beta} = -0.012 \pm 0.017$, i.e. statistically consistent with zero.

The lack of correlations allows us to combine a randomly selected momentum value with randomly selected $dE/dx$ and $\beta_{\text{Tile}}$ values in order to generate random masses. By repeating this several times for each candidate passing the preselection criteria, a smooth background estimate is constructed. The $dE/dx$ distribution used to draw random numbers from is taken from candidates in a control region (10 GeV$<p_{\text{T}}<$20 GeV), which is expected to have very low signal contamination. The relativistic rise in $dE/dx$ with momentum is reduced due to the density effect [100] and is not expected to influence the background estimate significantly at higher masses. The $\beta_{\text{Tile}}$ distribution used is taken from the candidates passing the preselection. This is motivated by the observation that while the mean of the distribution does not depend on $\beta$, the width is affected slightly, as larger energy deposits gives better resolution in $\beta$ (see Section 5.3.4). When using a $\beta_{\text{Tile}}$ spectrum extracted from low-$p_{\text{T}}$ candidates, this affects the shape of the background estimate. For this reason, the candidates passing the preselection were used instead. Though some signal could contaminate this sample, the de-correlating effect of combining ran-

dom momenta with random $\beta_{\text{Tile}}$ values will deteriorate any mass peak, only resulting in a slightly distorted mass distribution. Figure 7.3 shows the momentum distribution for candidates passing the preselection described in Section 6.2. The drop in the lowest bin is caused by a combination of the binning and the kinematic requirements applied to the sample.

## 7.3 Estimation of uncertainty

To estimate the systematic uncertainties of the background estimates, different kinematic selections were used to extract the distributions of Pixel $dE/dx$ and $\beta_{\text{Tile}}$. In addition, alternative normalization schemes were tried, as well as manually introduced correlations between momentum and $dE/dx$ and/or $\beta_{\text{Tile}}$. Varying the kinematic region used to extract the reference distributions of $dE/dx$ and $\beta_{\text{Tile}}$ had the largest impact with differences of around 25%. Also, different methods of normalization and comparisons to data in the same regions show differences up to 15%. The effect of introducing a linear correlation of 5% amounted to about 5% change in background. Overall, this amounts to a systematic uncertainty on the background estimates of 30%. This number was cross-checked by comparing the number of background events predicted at low mass and comparing with the number observed in data, and the agreement was found to be within 30%. Though this relative uncertainty is large, the expected amount of background is generally very low and the final result is not particularly sensitive to the relative uncertainty of the background estimate.

## 7.4 Performance

After the preselection, 5208 candidates remain in 5116 events, which are subject to analysis of their ionization response in the Pixel detector and timing measurements from the Tile calorimeter.

First the estimate from the Pixel detector is considered by itself. The mass spectrum produced by the background estimation method described above can be seen in Figure 7.4, where it is compared to data. Good agreement between the background prediction and data is observed. The background estimates are 50.2 11.5, 3.05 events above the 100, 200, 300 GeV mass thresholds, respectively. The corresponding numbers of events observed in the experimental data are 49 (13, 1).

The corresponding Tile calorimeter mass spectra is shown in Figure 7.5. The estimated number of background events above the 100, 200, 300 GeV mass thresholds are 142, 17.3, 4.41 which agrees within the estimated uncertainty with the 123 12, 2 events observed in data.

When requiring both the Tile and the Pixel subsystems to give a mass above 100 and 200 GeV, the predicted background counts are 2.3 and 0.24 events, respectively, and no events are observed in the data.

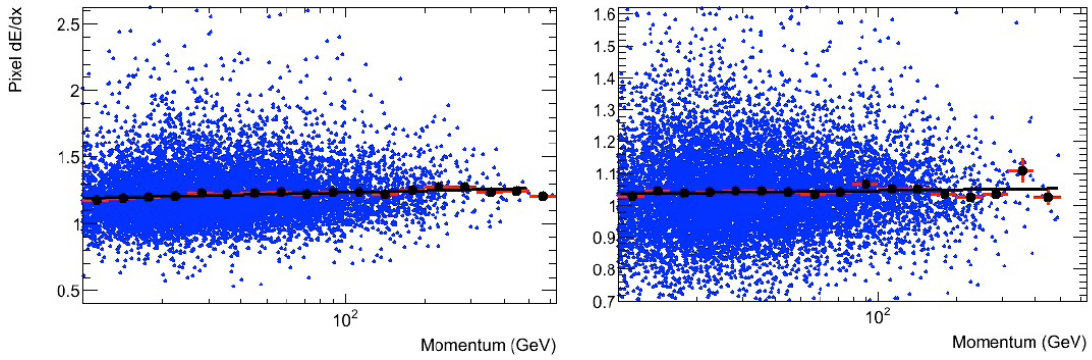


Figure 7.2: Pixel $dE/dx$ (left) and $\beta_{\text{Tile}}$ (right) vs. with reconstructed momentum. Linear fits to the averages of the $p$-binned distributions are shown as an indication of the correlations.

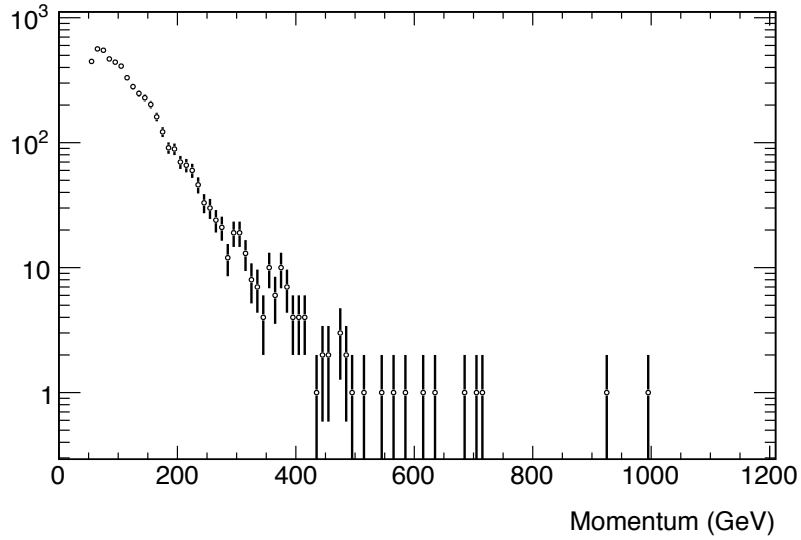


Figure 7.3: Distribution of momentum of selected candidates.

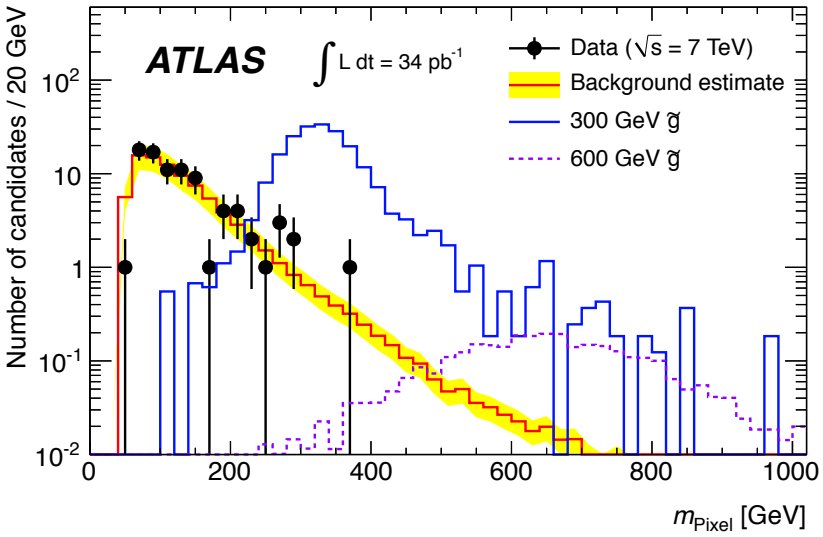


Figure 7.4: Mass spectrum as measured by the Pixel detector compared to the background prediction and expected signal for two $R$-hadron mass hypotheses.

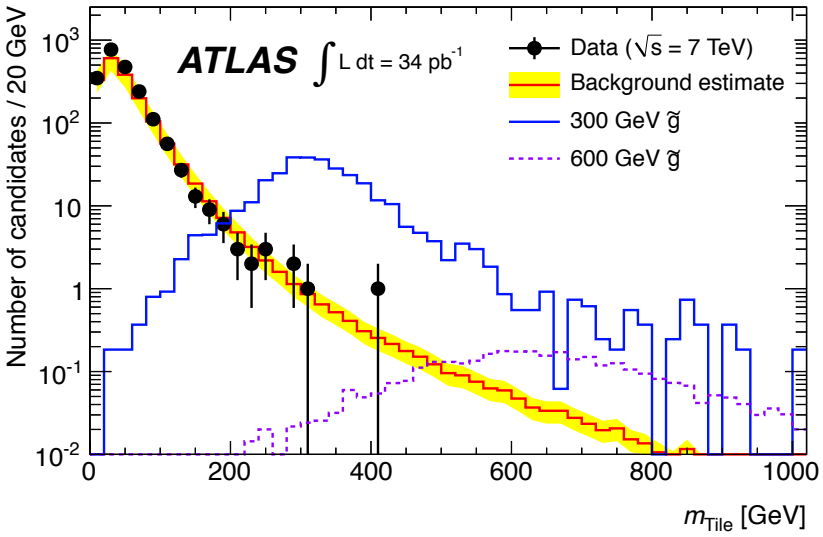


Figure 7.5: Mass spectrum as measured by the Tile calorimeter compared to the background prediction and expected signal for two $R$-hadron mass hypotheses.

# 8 Effects of systematic uncertainties

In order to extract a limit on the production cross sections and masses for long-lived gluinos and squarks, it is necessary to consider sources of systematic uncertainties. The estimate of the expected background is based on data alone and by design therefore includes several experimental uncertainties. Because of this, many sources of uncertainty only affect the predicted signal yield. A list of systematic uncertainties together with descriptions of the methods used to estimate their magnitudes are given below.

## 8.1 Experimental uncertainties

Most of the uncertainties investigated are of experimental nature, and these are summarized in this section, divided into those affecting the expected signal yield and those related to the background estimates.

### 8.1.1 Uncertainties affecting the expected signal yield

#### Trigger efficiency uncertainty

The uncertainty in the shape of the turn-on curve for the trigger, i.e. the determination of its efficiency as a function of `MET_Topo`, results in an uncertainty of a few percent in the trigger efficiency (see Section 6.1.4). The uncertainty of the efficiency of the $E_{\mathrm{T}}^{\mathrm{miss}}$-based trigger is dominated by the uncertainty of the scale of `MET_Topo`. This contribution varies with mass and ranges from -12.6%/+13.4% to -7.1%/+7.1% for the 100 GeV and 700 GeV *R*-hadron samples, respectively.

#### Simulation of dead regions

The simulation gives an imperfect description of the dead modules, cells and sensors in the SMP-sensitive subsystems used in this search. Assessing the maximum impact of this inaccuracy gives an uncertainty of 1-2% on the predicted signal efficiency and this is included as a systematic uncertainty. This is described in greater detail in Appendix B together with studies of how the number of selected events per nanobarn varied over time at several stages of the selection.

### Tile Energy scale

*R*-hadrons typically leave several GeV of energy as they propagate through the detector. A conservative estimate of the energy scale uncertainty for low-energy hadrons (down to approximately 2 GeV) is 5% [130]. To test the sensitivity of the search to this scale uncertainty, the energies were scaled by $\pm 10\%$. This affects the number of *R*-hadrons passing the selection by less than 1%.

### Simulation of Tile timing

As described in Section 5.3, the simulated cell times are smeared with random numbers from a gaussian distribution of width 1.42 ns in order to approximately reproduce the timing resolution observed in data. Smearing with random numbers from a gaussian with a width of 2 ns instead, the signal efficiency changed by less than 1%. Introducing a shift of all cell times in a representative signal MC sample with 2 ns results in less than 1% difference in the signal efficiency. To put the magnitude of this shift into context, the cell times are aligned using $Z \to \mu^+\mu^-$ to a precision of $\sim$100 ps.

### Simulation of Pixel $dE/dx$

In Section 5.2 it is shown that the simulation reproduces the Pixel $dE/dx$ spectra reasonably well. However, there are some small discrepancies. To investigate the influence of an imperfect simulation, each value of Pixel $dE/dx$ was smeared according to a gaussian distribution with a width of 5% of that value. This is sufficient to ensure that the width of the bulk of the Pixel $dE/dx$ distribution is covered, and affects the signal efficiencies by less than 1%. The sensitivity to the scale uncertainty of the Pixel $dE/dx$ measurement was also investigated. A shift in the Pixel $dE/dx$ scale of 3% was applied which gave a difference of less than 1% on the signal yield.

### ID momentum mismeasurement

The description of the *R*-hadron transverse momentum resolution in the simulation is imperfect. A smearing function defined by the ATLAS muon reconstruction community was therefore applied in the analysis to correctly reproduce the transverse momentum resolution observed in data. To test the sensitivity to this smearing, the magnitude of the prescribed smearing was doubled. This resulted in an difference of less than 1% on the number of signal events passing the selections.

### Pile-up

The signal samples used for the main results were prepared without any simulated pile-up (see Section 5.4.1). To estimate the effect of pile-up on the signal efficiency, signal samples with on average approximately two in-time pile-up events overlaid on each signal event were studied for a selected set of signal samples. The efficiency was evaluated for

a few stages in the cut-flow table and the relative difference in the number of selected events and candidates are summarized in Table 8.1. The effect is that the signal efficiency increases by $\sim$1%, which in this context is negligible.

| Cut level | No pile-up | With pile-up | Relative difference |
|---|---|---|---|
| **500 GeV $\tilde{g}$** | | | |
| `EF_xe40_noMu` (events) | 3822 | 3862 | +1.0% |
| $p_{\mathrm{T}} > 50$ GeV (candidates) | 2629 | 2664 | +1.3% |
| $m > 100$ GeV (candidates) | 1692 | 1708 | +0.9% |
| **600 GeV $\tilde{g}$** | | | |
| `EF_xe40_noMu` (events) | 4150 | 4173 | +0.55% |
| $p_{\mathrm{T}} > 50$ GeV (candidates) | 2892 | 2910 | +0.6% |
| $m > 100$ GeV (candidates) | 1871 | 1895 | +1.3% |
| **300 GeV $\tilde{t}$** | | | |
| `EF_xe40_noMu` (events) | 2970 | 3011 | +1.4% |
| $p_{\mathrm{T}} > 50$ GeV (candidates) | 2405 | 2426 | +0.9% |
| $m > 100$ GeV (candidates) | 1459 | 1473 | +1.0% |

Table 8.1: Acceptance for three representative signal samples with and without pile-up simulation. In these pile-up simulations, an average of two pile-up events were overlaid with the signal process in the digitization step, followed by reconstruction.

#### Integrated luminosity

Since the signal yields are scaled to the integrated luminosity of the data according to the cross sections of each considered scenario, they depend linearly on the uncertainty of the measured integrated luminosity. This uncertainty was estimated to be 11% [131].

### 8.1.2 Uncertainty of background estimates

As described in Section 7.3, the largest uncertainties come from the choice of kinematic region used for extracting $dE/dx$ and $\beta_{\mathrm{Tile}}$ reference distributions, and from the choice of normalization scheme. The total estimated relative uncertainty on the background estimate is 30%.

## 8.2 Theoretical uncertainties affecting the expected signal yield

### Limited accuracy of QCD calculations used to model the *R*-hadron production

Uncertainties arise due to the treatment of higher orders in perturbative QCD models and the assumed parton densities.

- In the sought signal processes, higher-order QCD radiation leads to jets and missing transverse energy which allows triggering on them. These effects are modeled by the parton shower algorithm in PYTHIA, which is based on a perturbative QCD leading logarithm expansion. Radiation from the heavy squark/gluino is suppressed by phase space effects and initial state radiation (ISR) is therefore dominantly responsible [132]. Following consultation with the PYTHIA author, a prescription for estimating the effects of uncertainties associated with the ISR prediction was designed. Variations of ISR parameters, `parp(67)` and `parp(64)` were studied. The sets `parp(67)=6.0, parp(64)=0.25` and `parp(67)=0.5, parp(64)=4.0` were used [40]. These settings control renormalization-style scales associated with the parton shower algorithm and modify the phase space in which emissions can occur. These variations affect the amount of *R*-hadron events passing the selection by up to 8.7%. It was verified that these variations also affected predictions of measurements of inclusive multijet production [133]. In this case, the predicted ratios of jet muliplicities change by around 20% (approximately the size of the experimental uncertainty) for the various ISR settings, while still providing a reasonable description of the measured data.

- The PROSPINO [123] next-to-leading order program is used to estimate the cross section for the pair production of gluinos and squarks. The renormalization scale was by default set to the mass of the produced sparticle, but varying this parameter up and down by a factor two leads to shifts in the cross section by approximately $\pm 15\%$. This can be seen in Figure 5.11.

- Variations due to the assumed PDFs were also studied. The difference in obtained cross section when using CTEQ6.6 [124] and MSTW 2008 [134] is less than 5%.

For the QCD errors, each source was added in quadrature, though the uncertainties on final state predictions from PYTHIA and the total cross section from PROSPINO can potentially be correlated. The total uncertainty from these two sources is $\sim 17\%$ which arises from individual contributions of $\sim 15\%$ and $\sim 9\%$.

### Uncertainties due to choice of *R*-hadron scattering model

As described in Section 5.4.3, a set of simulations based on different scattering models is available. Since the models are assumptions of the search, variations in predicted signal yield are not treated as a systematic uncertainty. Rather, as shown in Section 9.1, separate results are presented for different models.

# 9 Results

## 9.1 Final selection, yields and limits

For each *R*-hadron mass hypothesis, the position and the width of the expected mass peak were determined and the results are listed in Table 9.1. The signal region is defined as events containing candidates having masses above the peak position minus twice the width of this distribution. This means the size of the signal regions for the signal scenarios vary with the mass resolution. The table summarizes the number of expected gluino signal candidates passing the relevant mass requirement for the Pixel detector separately, the Tile calorimeter separately, and both detectors in combination. In addition, the corresponding background estimates from the data-driven method are shown, and finally the number of events in data, again requiring both the Pixel and Tile mass estimates to pass the mass requirement.

Corresponding tables for gluinos using Regge and intermediate models (see Section 5.4.3) are shown in tables 9.2 and 9.3. In order to enable comparison between gluino models, the signal regions have been chosen to be the same and thus the background estimates are identical as can be seen from comparing these tables. The corresponding results for sbottoms and stops are shown in Tables 9.4 and 9.5 respectively. For all considered signal hypotheses, the observed number of events in the data matches those expected from the background estimate. Since no significant excess is seen, cross section limits are extracted for each case.

| Nominal | $m_{Pixel}$ | $\sigma_{Pixel}$ | $m_{\text{Tile}}$ | $\sigma_{\text{Tile}}$ | Number of signal cand. | | | Number of background cand. | | | $N_{Data}$ |
|---|---|---|---|---|---|---|---|---|---|---|---|
| mass (GeV) | (GeV) | (GeV) | (GeV) | (GeV) | Pixel | Tile | Comb. | Pixel | Tile | Comb. | |
| 100 | 107 | 10 | 109 | 19 | 15898 | 49300 | 13912 | 61 | 330 | 5.4 | 5 |
| 200 | 214 | 24 | 211 | 36 | 1417 | 2471 | 1235 | 19 | 61 | 0.87 | 0 |
| 300 | 324 | 40 | 315 | 56 | 202 | 304 | 173 | 6.5 | 17 | 0.22 | 0 |
| 400 | 425 | 67 | 415 | 75 | 43 | 57 | 37 | 3.4 | 7.2 | 0.082 | 0 |
| 500 | 533 | 94 | 513 | 106 | 11 | 13 | 9.2 | 1.82 | 4.4 | 0.044 | 0 |
| 600 | 641 | 125 | 624 | 145 | 3.1 | 3.5 | 2.6 | 1.08 | 3.2 | 0.028 | 0 |
| 700 | 727 | 149 | 714 | 168 | 0.99 | 1.07 | 0.84 | 0.74 | 2.10 | 0.018 | 0 |

Table 9.1: Expected number of signal and background events for Pixel and Tile separately and combined. The mass peaks from Figures 7.4 and 7.5 are fitted with a gaussian, and the expected number of events are evaluated in a region from $2\sigma_m$ below the fitted central value and up. A few selected high-mass data events are visualized in event display images in Appendix C.

| Nominal | $m_{Pixel}$ | $\sigma_{Pixel}$ | $m_{\text{Tile}}$ | $\sigma_{\text{Tile}}$ | Number of signal cand. | | | Number of background cand. | | | $N_{Data}$ |
|---|---|---|---|---|---|---|---|---|---|---|---|
| mass (GeV) | (GeV) | (GeV) | (GeV) | (GeV) | Pixel | Tile | Comb. | Pixel | Tile | Comb. | |
| 100 | 107 | 10 | 109 | 19 | 19985 | 37401 | 13536 | 61 | 330 | 5.4 | 5 |
| 300 | 324 | 40 | 315 | 56 | 218 | 216 | 127 | 6.5 | 17 | 0.22 | 0 |
| 500 | 533 | 94 | 513 | 106 | 12 | 9.3 | 6.8 | 1.82 | 4.4 | 0.044 | 0 |
| 700 | 727 | 149 | 714 | 168 | 0.99 | 0.75 | 0.59 | 0.74 | 2.1 | 0.018 | 0 |

Table 9.2: Expected number of signal and background events for Pixel and Tile separately and combined for gluinos using the Regge model (see Chapter 5.4.3).

| Nominal | $m_{Pixel}$ | $\sigma_{Pixel}$ | $m_{\text{Tile}}$ | $\sigma_{\text{Tile}}$ | Number of signal cand. | | | Number of background cand. | | | $N_{Data}$ |
|---|---|---|---|---|---|---|---|---|---|---|---|
| mass (GeV) | (GeV) | (GeV) | (GeV) | (GeV) | Pixel | Tile | Comb. | Pixel | Tile | Comb. | |
| 100 | 107 | 10 | 109 | 19 | 16780 | 32559 | 8440 | 61 | 330 | 5.4 | 5 |
| 300 | 324 | 40 | 315 | 56 | 203 | 201 | 114 | 6.5 | 17 | 0.22 | 0 |
| 500 | 533 | 94 | 513 | 106 | 11 | 9.1 | 6.4 | 1.82 | 4.4 | 0.044 | 0 |
| 700 | 727 | 149 | 714 | 168 | 1.01 | 0.72 | 0.58 | 0.74 | 2.1 | 0.018 | 0 |

Table 9.3: Expected number of signal and background events for Pixel and Tile separately and combined for gluinos using the ntermediate model (see Section 5.4.3).

| Nominal | $m_{Pixel}$ | $\sigma_{Pixel}$ | $m_{\text{Tile}}$ | $\sigma_{\text{Tile}}$ | Number of signal cand. | | | Number of background cand. | | | $N_{Data}$ |
|---|---|---|---|---|---|---|---|---|---|---|---|
| mass (GeV) | (GeV) | (GeV) | (GeV) | (GeV) | Pixel | Tile | Comb. | Pixel | Tile | Comb. | |
| 100 | 110 | 12 | 101 | 21 | 347 | 634 | 196 | 61 | 445 | 7.1 | 6 |
| 200 | 219 | 28 | 205 | 36 | 31 | 35 | 19 | 21 | 68 | 0.99 | 0 |
| 300 | 324 | 45 | 302 | 55 | 4.4 | 4.3 | 2.8 | 7.5 | 21 | 0.26 | 0 |
| 400 | 436 | 72 | 409 | 84 | 0.89 | 0.78 | 0.54 | 3.4 | 9.4 | 0.11 | 0 |
| 500 | 545 | 102 | 508 | 105 | 0.22 | 0.19 | 0.14 | 1.92 | 4.7 | 0.046 | 0 |

Table 9.4: Expected number of signal and background events for Pixel and Tile separately and combined for sbottoms

| Nominal | $m_{Pixel}$ | $\sigma_{Pixel}$ | $m_{\text{Tile}}$ | $\sigma_{\text{Tile}}$ | Number of signal cand. | | | Number of background cand. | | | $N_{Data}$ |
|---|---|---|---|---|---|---|---|---|---|---|---|
| mass (GeV) | (GeV) | (GeV) | (GeV) | (GeV) | Pixel | Tile | Comb. | Pixel | Tile | Comb. | |
| 100 | 108 | 11 | 102 | 18 | 558 | 1190 | 413 | 61 | 383 | 6.2 | 6 |
| 200 | 218 | 25 | 202 | 35 | 46 | 60 | 34 | 19 | 68 | 0.97 | 0 |
| 300 | 328 | 45 | 306 | 57 | 5.8 | 7.0 | 4.3 | 7.0 | 21 | 0.26 | 0 |
| 400 | 435 | 70 | 408 | 81 | 1.15 | 1.28 | 0.85 | 3.2 | 8.7 | 0.097 | 0 |
| 500 | 535 | 92 | 513 | 109 | 0.30 | 0.32 | 0.22 | 1.82 | 5.0 | 0.049 | 0 |

Table 9.5: Expected number of signal and background events for Pixel and Tile separately and combined for stops

In order to calculate the limits, systematic uncertainties and statistical fluctuations in the expected background must be taken into account. To handle the possibility of fluctuations in the number of background events, the fact that it is expected to be distributed according to a poissonian can be used. If we expect $n_b$ background events, the probability $p$ of observing $n_0$ or more due to poisson fluctuations is given by

$$p = \sum_{i=n_0}^{\infty} \frac{n_b^i e^{-n_b}}{i!}. \tag{9.1}$$

If $p \to 0$ it implies a significant deviation from the background expectation.

The cross section $\sigma$ for a process is given can be calculated through

$$\sigma = \frac{N}{\varepsilon \mathscr{L}}, \tag{9.2}$$

where $N$ is the number of observed events, $\varepsilon = N/N_{\text{produced}}$ is the efficiency for observing them and $\mathscr{L}$ is the integrated luminosity of the data in which the $N$ events were observed.

The limit is calculated by inverting equation (9.1) to determine how many signal events could be contained within the combined expectations for signal ($s$) and background ($b$), given the observation of $N$ events and a significance less than some value. In practice, this calls for the maximization of $s$ in equation (9.3) with a fixed value of $\alpha$,

$$CL_{s+b} = 1 - \alpha = \sum_{i=0}^{n} e^{-(s+b)} \frac{(s+b)^i}{i!}. \tag{9.3}$$

The largest possible value of $s$ is then calculated under the constraint that the probability $p$ of it being due to fluctuations in $s+b$ is less than $\alpha$ [4]. The confidence level $CL$ is traditionally set to 95%, i.e. $\alpha = 5\%$.

Relying on equation (9.3) can lead to unintuitively strong limits in case of downward fluctutations. Instead the method used seek to neutralize the problem of background fluctuations by introducing a ratio of the $p$-values of the signal plus background hypothesis and a background-only hypothesis. This is called the $CL_s$ method [135] and is summarized by equation (9.4).

$$CL_s \equiv \frac{CL_{s+b}}{CL_b} = 1 - \alpha = \frac{\sum_{i=0}^{n} \frac{(s+b)^i}{i!} e^{-(s+b)}}{\sum_{i=0}^{n} \frac{b^i}{i!} e^{-b}} \tag{9.4}$$

As a cross-check, the limits were also computed using an implementation of the Feldman-Cousins method [136] which gave consistent results.

Effects due to systematic uncertainties are included by adding by adding random numbers to $b$ and $s$ from gaussian distributions with widths defined by the uncertainties. The nominal signal is then maximized with specific numbers, smeared as just described. This

is repeated a large number of times for different sampled values from the smearing distributions. The final upper limit is then taken as the mean of the result from each cycle. Combining equation (9.1) with this smearing method the final expression is formed,

$$CL_s \equiv 1-\alpha = \frac{\sum_{i=0}^{n} \frac{(\mathscr{L}\sigma\varepsilon_{smeared}+b_{smeared})^i}{i!} e^{-(\mathscr{L}\sigma\varepsilon_{smeared}+b_{smeared})}}{\sum_{i=0}^{n} \frac{b_{smeared}^i}{i!} e^{-b_{smeared}}}, \tag{9.5}$$

which is maximized for $\sigma$ with the requirement that $\alpha = 0.05$. The final result is plotted along with the predicted production cross sections for gluinos and squarks, calculated with PROSPINO in Figure 9.1.

The resulting limit on the gluino mass is approximately 586 GeV at 95% C.L. as can be inferred from Figure 9.1. Correspondingly the stop and sbottom limits at 95% C.L. are 309 GeV and 294 GeV, respectively. These limits include the discussed systematic uncertainties on the expected signal yields ($\sim 20\%$ depending on mass point as described in Chapter 8) as well as on the data-driven background estimate uncertainty (30%), as described above. Limits were also calculated for the intermediate and the regge models defined in Section 5.4.3. The resulting limits are shown in Figure 9.2. The limits on gluino *R*-hadrons are found to be 566 GeV for the Regge case and 562 GeV for the Intermediate case. The mass limits for the alternative scattering models are lower since the gluino *R*-hadrons quickly become neutral particles in ATLAS which degrades the selection efficiency.

## 9.2 Summary and conclusions

Experimental $pp$ collision data corresponding to an integrated luminosity of 34 pb$^{-1}$ were recorded with the ATLAS detector during 2010. A search for gluino and squark *R*-hadrons based on energy loss and time-of-flight information from the Pixel detector and Tile calorimeter, respectively, was performed in events triggered by a $E_{\mathrm{T}}^{\mathrm{miss}}$ signature. The final yields are in agreement with those predicted by the data-driven background estimation method, and no excess was observed. Upper limits were therefore calculated for the production cross sections of *R*-hadrons of various types and masses. Since the cross section for gluino and squark production can be calculated as a function of mass, direct pair-production of long-lived gluinos, stops and sbottoms could be excluded in specific mass regions. Hadronizing gluinos up to a mass of between 562 GeV and 586 GeV (depending on hadronic scattering model) were excluded at 95% C.L. Stable sbottom and stop squarks were excluded at 95% up to a mass of 294 GeV and 309 GeV, respectively. All of these mass limits are the world's most stringent collider limits published to date for long-lived supersymmetric particles with color charge.

A search based on the same dataset and a muon-like signature was published by ATLAS after the work presented in this thesis [58]. No signal was observed and the resulting limits are close to those presented here. Finally, results from a search published by the CMS collaboration using a smaller dataset are also consistent with this work [56].

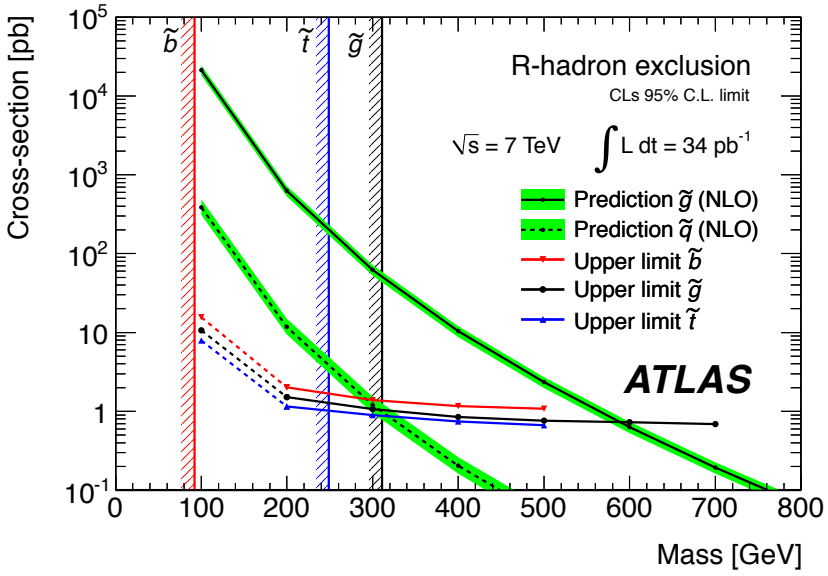


Figure 9.1: Cross section limits as a function of mass for *R*-hadrons. The intersections between the cross section limits and the corresponding theoretical prediction excludes $m_{\tilde{g}} < 586$ GeV, $m_{\tilde{t}} < 309$ GeV and $m_{\tilde{b}} < 294$ GeV.

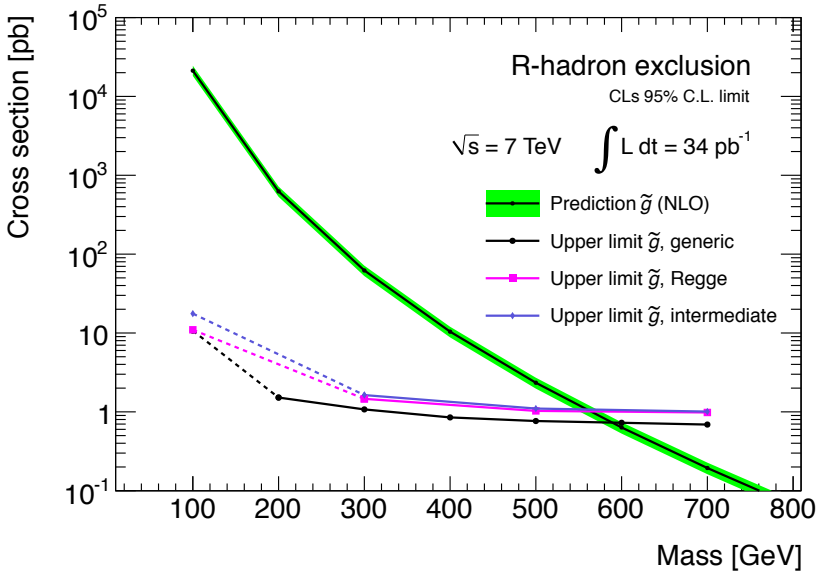


Figure 9.2: Cross section limits as a function of mass for gluino *R*-hadrons for the three different models of hadronic scattering considered. The intersections show that masses below 586 GeV (generic), 566 GeV (Regge) and 562 GeV (intermediate) are excluded.

# Part IV

# Details for Paper II:

# Search for massive long-lived highly ionising particles with the ATLAS detector at the LHC

*"Här kan vi inte stanna,*
*släng era kartor*
*vi följer ån.*
*Dit vattnet rinner, dit går jag*
*och har jag någon med mig*
*heter det vi."*

– Daniel Boyacioglu

# About Part IV

As outlined in Section 2.3, motivations exist for searching for highly ionizing particles (HIPs) at the LHC. Furthermore, putative HIPs would be produced at unknown rates, and therefore it may be possible to discover them with relatively modest amounts of integrated luminosity when reaching a new energy regime. This part of the thesis contains details pertaining to the early search for HIPs reported in Paper II. In the same manner as for Part III, it should be remarked that the presentation here does not presuppose that the reader has digested the journal article itself, however doing so could provide a useful overview for the details documented in the following chapters.

Searches for HIPs have been made in cosmic rays [137] and at colliders [7]. They have been a natural part of the early data exploitation program at colliders and were performed at LEP [138, 139, 140] and the Tevatron [141, 142, 143, 144]. As a consequence of the unavailability of full-fledged theoretical calculations for the production process of HIPs, empty-handed searches usually quote their results as cross section limits for a range in charge and mass for well-defined kinematic models rather than ruling out the existence of a specific particle within a certain mass range.

This part is organized similarly to Part III. Chapter 10 outlines the signature expected from a HIP produced in the ATLAS detector, followed by a definition of the scope of the search. This is followed by a discussion of electron-ion recombination and its consequences on the measured energy loss. This chapter also includes information regarding the simulated physics processes used to produce the results. The selection criteria applied to the data sample are described in Chapter 11 along with definitions of the acceptance and studies of the efficiencies for identifying HIPs of various electric charge and mass. The method used to estimate the background is described in Chapter 12. The final event yields are presented in Chapter 13 which also summarizes the results in the form of limits on the production cross section of HIPs possessing electric charges $6e \leq |q| \leq 17e$ and masses up to 1 TeV.

# 10 Expected detector response for highly ionizing particles

As was argued in the introduction of the corresponding chapter in Part III, it is of the utmost importance to understand the expected response of new physics in the detector when constructing a search, in particular when looking for particles which unusual signatures are expected. The expected response to HIPs in ATLAS is in this chapter first reviewed in an overview section. The scope of the search is then defined before details pertaining electron-ion recombination effects are discussed. This is followed by a section treating aspects specific to producing simulated HIP samples, and details regarding the samples used for this analysis.

## 10.1 Overview

Following the description of the expected interactions of HIPs passing through matter in Section 2.3.4, an overview of their possible detector signatures is presented here.

The ATLAS detector is well-suited to detect HIPs although the expected signature depends greatly on the charge of the HIP and its kinematics. In general, the magnitude of the electric (and/or magnetic) charge of the HIP determines its penetration depth in the detector. HIPs with very high charge are more likely to come to a stop early in the detector, e.g. already in the inner tracking volume, owing to catastrophic ionization energy loss. As discussed in relation to hadron-like and muon-like SMPs, particles with moderate charge are expected to penetrate further into the detector and could yield a muon-like signature, albeit with enhanced signals due to increased ionization.

This search was designed for HIPs leaving an electron-like signature in the detector. This includes a track measured in the ID tracking system followed by significant energy losses in the electromagnetic calorimeter, but no signal in the hadronic layers or the MS. At energies typical for LHC production processes this signature is typical of HIPs with $6e < |q| < 17e$ since their energy losses bring them to a stop in the EM calorimeter. The signature thus resembles that of an electron losing anomalously large amounts of energy through ionization. The presence of a HIP can in ATLAS be inferred from measurements of the fraction of hits along an associated track exceeding the high threshold in the TRT. In addition to this, the shape of the clustered energy depositions in the EM calorimeter serves as a discriminator for separating HIPs and particles from background processes [145].

## 10.2 Scope of the search

As stated above, the sought electron-like signature limits the sensitivity in electric charge to $6e \lesssim |q| \lesssim 17e$. Despite the precautions taken to limit the sensitivity to the bending effects expected for tracks from magnetically charged particles, these scenarios need to be studied with dedicated simulations to assess the efficiency for magnetic monopole scenarios. Also, for particles with $|q| > 17e$ or equivalent (Dirac monopoles are equivalent to $q = 68.5e$ in terms of ionization), $\delta$-electrons contaminate the trackers with hits significantly. Long range delta electrons can produce track segments which intersect the main track and potentially be reconstructed as independent tracks. If the cluster is matched to the wrong track, it can cause a selected signal candidate to fail the TRT related set of cuts. For these reasons a more detailed study is needed to assess and minimize the impact of this effect on the efficiency for HIPs with $|q| > 17e$. Furthermore, to correctly predict the response to high-$q$ HIPs, the implementation of Birks' law [146] in the ATLAS simulation framework needs to be modified, as described in the following section. Low-luminosity data enable searches for low charges thanks to low EM trigger energy thresholds. Particles with $|q| < 6e$ would, however, be difficult to trigger on with a trigger based on clusters in the EM calorimeter due to their reduced energy deposition. For targeting the lower end of the charge spectrum, a muon signature would be more appropriate since low-charge HIPs are likely to punch through the calorimeters and be reconstructed as muon objects. That signature falls outside the scope of the studies presented in this thesis. As a consequence of the arguments presented above, the interpretation of the results in this search is limited to scenarios with HIPs possessing electric charges in the range $6e < |q| < 17e$.

## 10.3 Birks' law in LAr

Electron-ion recombination reduces the recorded energy in a LAr detector. The ratio of visible to true energy $E/E_0$ increases with the applied electric field, and decreases with increasing $dE/dx$. The latter can intuitively be motivated by combinatorics. The more concentrated the energy deposition is, the higher the density of ionized atoms and free electrons will be, leading to a larger fraction of electrons that will recombine before being captured by the electric field. This effect is thus especially important for highly charged particles.

Simulation of recombination effects in ATLAS is implemented using the so-called Birks' law [146], which provides a phenomenological parametrization of $E/E_0$ as a function of the applied electric field $E_\mathrm{D}$, the density $\rho$, the energy loss $dE/dx$, a normalization parameter $A$ and Birks' parameter $k$, as described by equation (10.1).

$$\frac{E}{E_0} = \frac{A}{1 + \frac{dE}{dx}\frac{k}{E_\mathrm{D}\rho}} \tag{10.1}$$

Cosmic-ray muon and proton data from the ICARUS experiment for electric fields between 0.2 and 0.5 kV/cm yields $k = 0.0486$ kV/cm·g/(cm$^2$MeV) [147]. This value of

Birks' parameter was chosen for the ATLAS implementation of Birks' correction under the naive assumption that it can be extrapolated to an electric field $E_{\mathrm{D}} = 10$ kV/cm. This implementation improves the MC description of test-beam data for minimum ionizing particles, when the normalization parameter $A$ is chosen so that the response to electrons is not changed, i.e. $A = 1.008$ [102].

The main concern when applying Birks' correction with these default parameter values in the simulation of highly charged particles is that the parameter $k$ depends on the scale of $dE/dx$, meaning a single Birks parametrization is not expected to give a good fit to the data in a large range in $dE/dx$.

Another important consideration when applying Birks' correction is the treatment of $\delta$-electrons[1)]. The $\delta$-electrons are expected to reduce the quenching effect by transporting some of the energy deposition away from the particle trajectory.

Energy deposition measurements for relativistic heavy ions [147, 148, 149, 150] punching through a layer of a LAr detector can be used to test the validity of Birks' parametrization for describing the charge output in LAr for highly charged particles. For this purpose, a standalone GEANT4 [121] simulation of a LAr detector was used to model the heavy ion results of Refs. [148, 149, 150]. Highly charged particles were used in the simulation, neglecting the effect of hadronic interactions. The electric field was varied and the fraction of visible energy $E/E_0$ was obtained from the simulated $dE/dx$ and Birks' parametrization with default ATLAS parameter values. The simulation was performed both with and without simulating the production of $\delta$-electrons. The simulated results are compared to the data in Figure 10.1. These results show that the current implementation of the ATLAS simulation slightly underestimates the quenching effects due to electron-ion recombination for ions up to Ne ($q = 10e$), while the reverse is true for the heavier ions. Figure 10.2 shows that the relative difference in the $E/E_0$ ratio for data and simulation (for electric fields between 7–10 kV/cm) is within $\pm 15\%$ for all studied elements up to Fe ($q = 26e$). This corresponds to a region where $E/E_0$ is between 0.20 and 0.60 for $E_{\mathrm{D}} = 10$ kV/cm (see Figure 10.1). Thus, a systematic uncertainty of $\pm 15\%$ in the fraction of visible energy in the ATLAS LAr due to the modeling of recombination effects is assumed in this regime of $dE/dx$. As particles with $6e < |q| < 17e$ stopping in the LAr calorimeters in ATLAS are in the same regime of $dE/dx$, this uncertainty is used for estimating the systematic uncertainty for their energy loss.

[1)] A highly ionizing particle passing through matter can kick off energetic electrons from deep atomic layers, which can then travel macroscopic distances into the detector. These are called $\delta$-electrons, or $\delta$-rays.

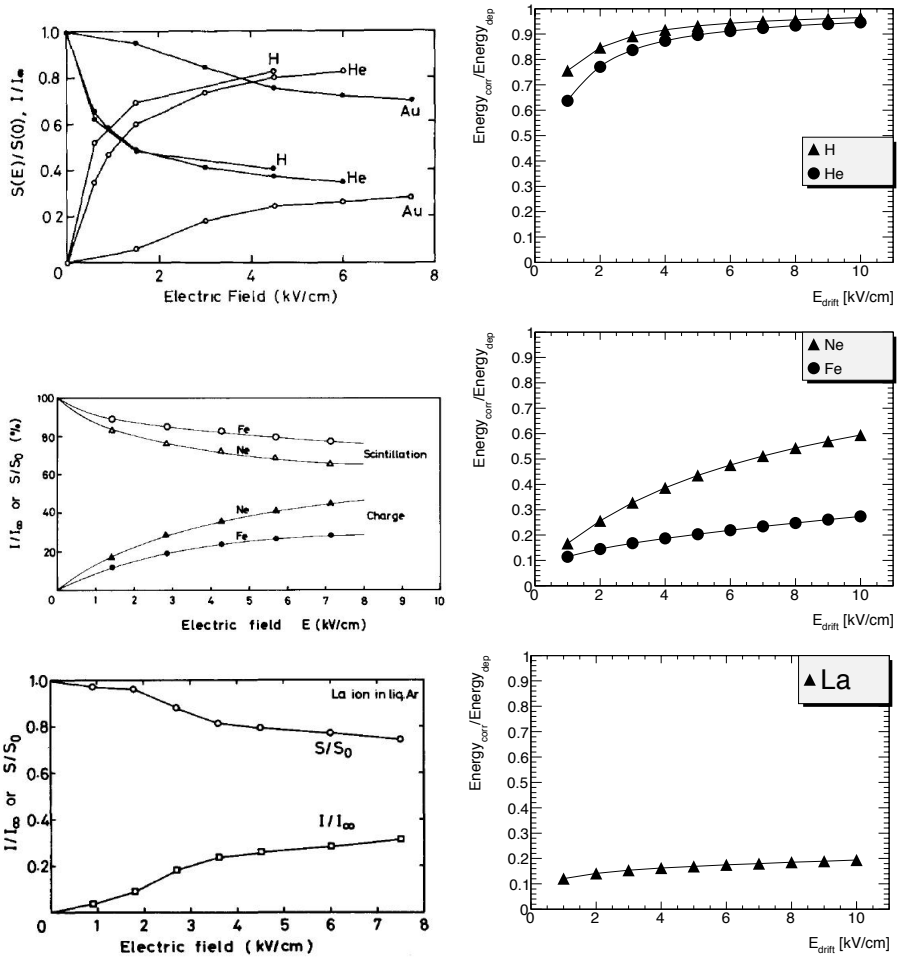


Figure 10.1: Fraction of visible energy to total energy for relativistic heavy ions as a function of the applied electric field in a LAr detector, as measured by experiments (top left [148], middle left [149] and bottom left [150], where the rising curves are from measurements of released electric charge and the decreasing ones show scintillation light measurements), and on the right the corresponding results from standalone GEANT4 simulations including the application of Birks' parametrization with default ATLAS values. The simulation was made including $\delta$-electrons, as in the samples used in this search.

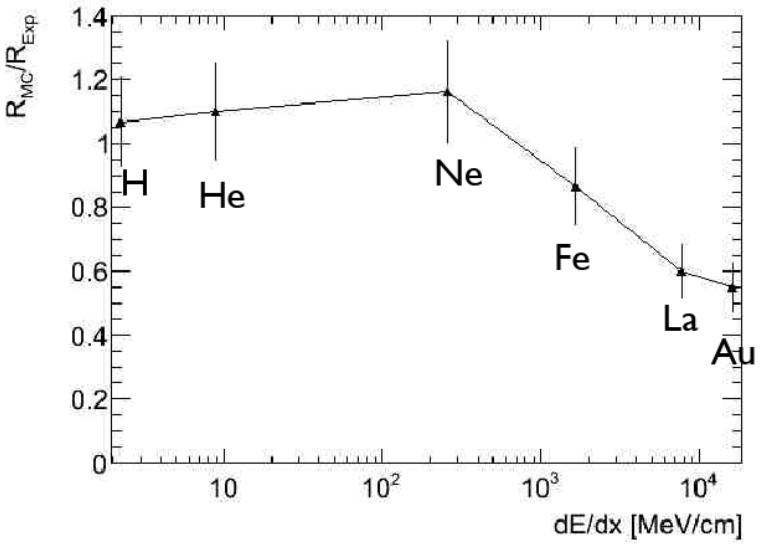


Figure 10.2: Ratio of the visible energy fraction from the simulation $R_{\mathrm{MC}}$ to the one from experimental heavy ion data $R_{\mathrm{exp}}$ (where $R = E/E_0$), for an electric field of 7 kV/cm. Error bars come from the experimental uncertainties quoted in the publications. For elements in the range Ne-Fe, corresponding to the $dE/dx$ regime relevant to this search, the relative difference between $R_{\mathrm{MC}}$ and $R_{\mathrm{exp}}$ is $\pm 15\%$.

## 10.4 Monte Carlo

General MC sample production details in ATLAS were reviewed in Section 5.4.1, and only details specific to the simulated samples used in Paper II are described here.

### 10.4.1 Signal processes

Though perhaps slightly confusing, the HIPs produced here are called "$Q$-balls". The name is appropriate in the sense that they are simple balls of electric charge but, though they share similar expected detector signatures, they have little to do with the theory-inspired $Q$-balls described in e.g. Ref. [42]. Information related to the event generation and detector simulation steps is given below while technical details related to the digitization and reconstruction are omitted.

#### Event generation

As discussed in Section 2.3.2, no reliable models exist for the production of highly charged particles. Therefore the choice of kinematics for simulated samples is arbitrary. Though the underlying process could differ significantly, a Drell-Yan process is used. This process provides well-defined kinematics for a typical 2-to-2 process, which can be used as benchmark and facilitate comparison between different experiments.

The event generation was performed using the PYTHIA MC generator [40]. Technically the program was configured to generate muons with the desired $Q$-ball mass using the $q\bar{q} \to \gamma^* \to f\bar{f}$ process, applying the requirement $m_{\gamma^*} > 2m_{Q\text{ball}}$ to produce pairs of massive particles. The event record of the final state was then manipulated to replace the particle codes of the two muons to those of $Q$-balls according to the PDG standard [6].

Masses of 200, 500 and 1000 GeV and charges of $6e$, $10e$, $17e$ were considered and samples were produced for all mass-charge combinations. As illustrated in the top left distributions in Figure 10.3, the Drell-Yan process yields particles more central in pseudorapidity with increasing mass. The top right distributions show the initial kinetic energy spectra in the $\eta$ range relevant to this search ($|\eta| < 1.35$ as motivated in Section 11.1). The bottom left and bottom right distributions show the initial speed $\beta$ before and after applying the selection criteria described in Section 11.2, for $|\eta| < 1.35$.

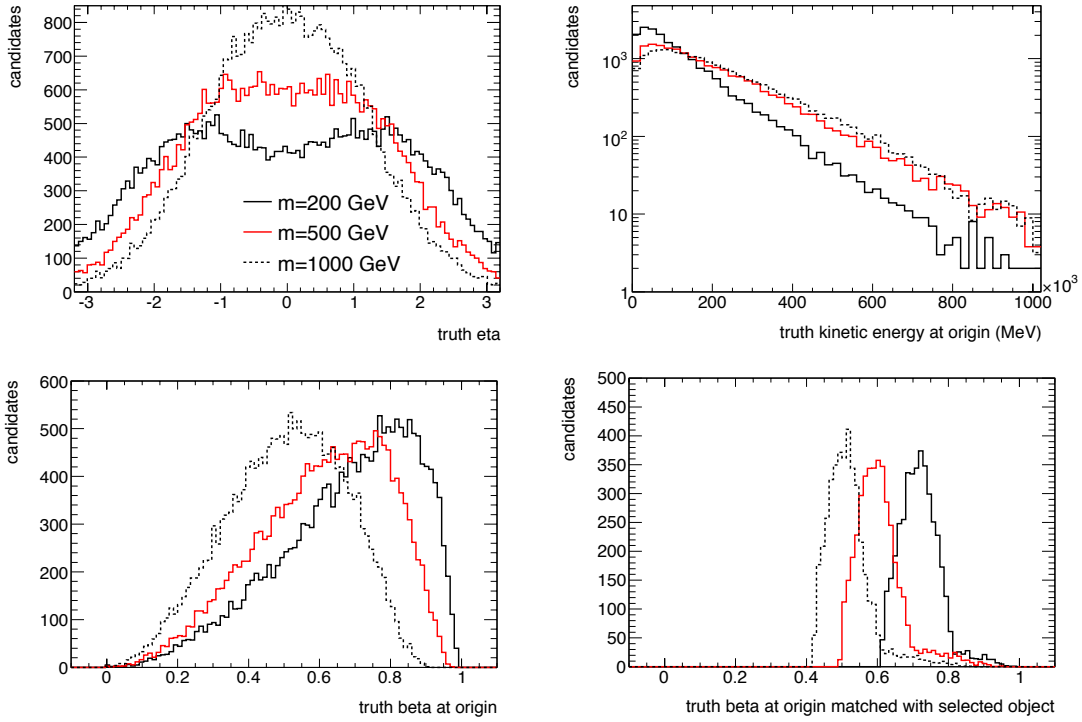


Figure 10.3: MC truth quantities for the Drell-Yan process with three different masses. Top left: $\eta$; top right: kinetic energy for $|\eta| < 1.35$; bottom left: $\beta$ for $|\eta| < 1.35$; bottom right: $\beta$ for selected events (with charge $10e$; selection cuts are defined in Section 11.2). The histograms are normalized to the same number of entries.

### GEANT4 simulation

A special extension to the GEANT4 simulation framework was implemented to extend the support to particles with high electric charge. This extension relies on the standard

GEANT4 ionization routines and includes e.g. behavior described by the Bethe-Bloch formula for the energy deposition and emissions of $\delta$-electrons.

### 10.4.2 Background processes

A data-driven method is used in this work to estimate the yields from SM background processes following the final selections described in Section 11.2. However, before putting any trust in the simulated signal samples, it must be demonstrated that the distributions of the relevant observables are well described by the MC. A sample of simulated background events is used for this purpose. This sample, labeled JF17 in the figures, consists of a mix of two-to-two SM processes, weighted by their cross sections. The generated events were filtered, requiring the transverse momentum $p_{\mathrm{T}} > 15$ GeV for the produced particles in the rest frame of the hard scatter. In addition, a true transverse energy larger than 17 GeV summed over the final state particles in a $\Delta\eta \times \Delta\phi \approx 0.12 \times 0.12$ window was required. The dominant process in this sample is QCD jet production. However, the sample also contains contributions from heavy quark and single prompt photon production. This sample contains $4 \times 10^7$ events and corresponds roughly to an integrated luminosity of 0.8 pb$^{-1}$. In the following figures in this part of the thesis, the JF17 sample is always normalized to the data.

# 11 Event and candidate selection

## 11.1 Trigger

This search relies on an electron-like signature, and consequently uses the lowest-threshold unprescaled electromagnetic trigger signature for the data taking period under consideration, `e10_medium`. This trigger looks for electrons with $p_{\mathrm{T}} > 10$ GeV that pass the "medium" electron identification criteria described below. As described in Section 4.6.1, so-called trigger towers with dimension $\Delta\eta \times \Delta\phi = 0.1 \times 0.1$ are used in the first-level calorimeter trigger . In each trigger tower the cells of the electromagnetic and hadronic calorimeters are summed. The identification of potential $e/\gamma$ candidates is done by looking for local maxima with a sliding window algorithm using $4 \times 4$ trigger towers. The most energetic of the four $1 \times 2$ or $2 \times 1$ combinations of the $2 \times 2$ core has to pass the electromagnetic cluster threshold of 5 GeV. If an event gives rise to this signature, it passes the `L1_EM5` trigger. In the Level-2 trigger it is possible to do more careful reconstruction of the energy depositions from the individual calorimeter cells. Tracks are reconstructed through fast tracking algorithms in the regions of interest pointed out by Level-1, and matched to the EM clusters. At the Event Filter (EF), algorithms similar to those run to reconstruct electrons in the offline software are used. The `L2_e10_medium` and `EF_e10_medium` triggers include requirements on the shower shape and a veto on hadronic leakage in order to reject jets [151]. The performance of this `em10_medium` signature is well understood in 7 TeV collision data [152], and the efficiency has been estimated to be approximately 94% for electrons with offline reconstructed $E_{\mathrm{T}} > 15$ GeV. Since a HIP stopping in the EMB would exhibit the characteristics of an excellent trigger object with high ID hit efficiency and an extremely narrow energetic EM cluster, there are no reasons to expect significant trigger efficiency losses not accounted for by the Monte Carlo (MC) simulation. Possible effects due to the increased time-of-flight of very massive particles have been investigated and are included in the summary of effects of systematic uncertainties in Section 13.2.

## 11.2 Data selection

Data from the trigger stream containing events that passed $e/\gamma$ trigger signatures as well as the `debug` stream were analyzed. The data was recorded between June and August, 2010, and correspond to an integrated luminosity of approximately 3.1 $\mathrm{pb}^{-1}$ after apply-

ing filtering requirements based on data quality.

### 11.2.1 Signal candidate definition

In ATLAS, electron reconstruction [153] is seeded by clusters with transverse energy $E_{\mathrm{T}} > 2.5$ GeV in the second layer of the electromagnetic calorimeter. Tracks reconstructed in the ID with $p_{\mathrm{T}} > 0.5$ GeV in an angular vicinity of the clusters are extrapolated to the second EM calorimeter layer. If close enough, the track with the best match to the barycenter of the cluster is kept as that belonging to the electron candidate. The standard offline electron identification is based on a set of cuts optimized in bins of $\eta$ and $E_{\mathrm{T}}$. Three sets of cuts are defined: loose, medium and tight. The medium definition which is imposed in this search implies requirements on the hadronic leakage, the shower shape variables involving the first and second layers of the EM calorimeter, and on tracking variables. An example of a shower shape variable based on the second layer in the EMB is the lateral shower width. Variables based on the first layer include the total shower width and the energy outside the shower core. The detector signature expected from HIPs fulfill these requirements as they produce clusters which are much narrower than EM showers. With respect to the track quality, at least one hit is required in the Pixel detector and at least seven hits in total in the silicon detectors (Pixel and SCT detectors). The transverse impact parameter is required to be less than 5 mm and the cluster-to-track matching must fulfill $\Delta\eta < 0.01$, $\Delta\phi < 0.02$.

Reconstructed electrons that in addition to the standard ATLAS "medium" requirements also has an offline cluster $E_{\mathrm{T}} > 15$ GeV and $\eta > 1.35$ are referred to as *candidates* in the following. The minimum $E_{\mathrm{T}}$ is required to guarantee that the candidates are in the plateau region of the trigger turn-on curve (see Section 11.1). The pseudorapidity requirement $|\eta| < 1.35$ is applied to avoid the transition region between the electromagnetic barrel and endcap. In addition, staying away from this region ensures the robustness of the cluster shape variables.

Distributions of electron $E_{\mathrm{T}}$, $p_{\mathrm{T}}$, $\eta$ and $\phi$ are shown in Figure 11.1 for candidates passing the selections described above. The shaded distribution corresponds to the simulated background processes, normalized to the data, and the dotted line illustrates the expected spectrum for $Q$-balls with $q = 10e$ and $m = 500$ GeV pair-produced through a Drell-Yan process. As for all following figures in this part of the thesis, the distributions representing simulated background and signal processes are normalized to the data.

### 11.2.2 Preselection

The preselection criteria are applied to ensure that the quality of the track and cluster associated with the electron object is good enough to enable a reliable computation of the final selection variables, and to provide a data sample with which to estimate the background to the search. Since one of the final selection variables is based on the response in the TRT, a preselection requirement is imposed on the number of TRT hits $N_{\mathrm{TRT}}$ on the

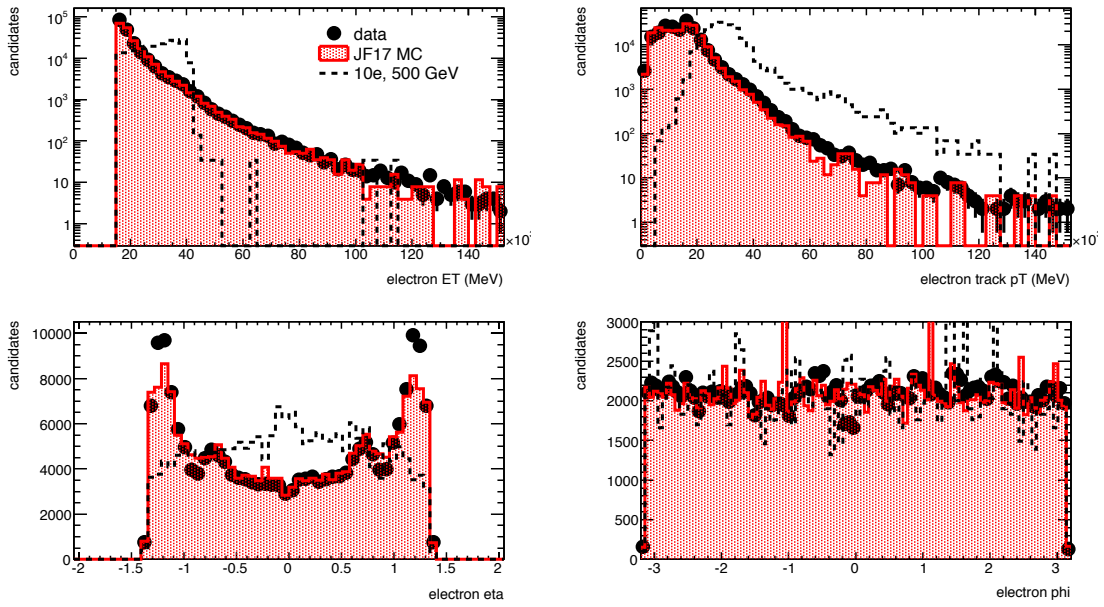


Figure 11.1: Cluster $E_{\mathrm{T}}$ (top left), track $p_{\mathrm{T}}$ (top right), $\eta$ (bottom left) and $\phi$ (bottom right) associated with all candidates, i.e. medium electron objects with $E_{\mathrm{T}} > 15$ GeV and $|\eta| < 1.35$.

track associated with the candidate, shown for experimental data and simulations in Figure 11.2. The other selection variables are related to the width of the associated cluster. Therefore, requirements are imposed on the energies in the three leading cluster cells in EM layer 1, denoted $E_{3,1}$, and EM layer 2, denoted $E_{3,2}$. Figure 11.3 shows the observed distributions for these variables, as well as the corresponding ones expected from signal and background simulations. In addition to the criteria described above, the preselection requires $N_{\mathrm{TRT}} > 10$, $E_{3,1} > 2$ GeV and $E_{3,2} > 4$ GeV.

Table 11.1 shows the event yields observed in experimental data and the simulated background and signal processes, at two stages of the selection. The "Filtering" column corresponds to events passing the trigger and having at least one reconstructed candidate. The preselection is defined in the above.

### 11.2.3 Final selection

The final selection criteria are applied to reject SM processes in order to enhance the signal-to-background ratio. The first criterion concerns the fraction of TRT high-threshold hits $f_{\mathrm{HT}}$ shown in Figure 11.4. An impressive separation between signal and background is seen, and a decent agreement between the simulated background and the experimental data. The remaining two variables used in the final selection reflect the width of the EM calorimeter cluster, and are denoted $w_1$ and $w_2$. They are defined as the fractions of the

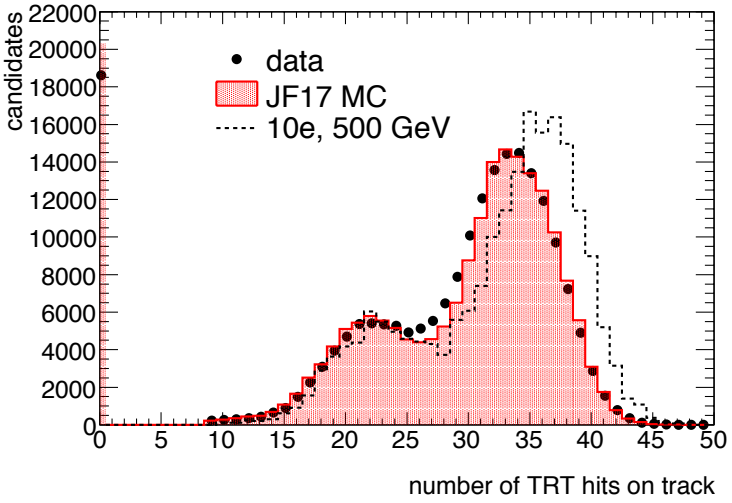


Figure 11.2: Number of TRT hits on tracks associated with candidates.

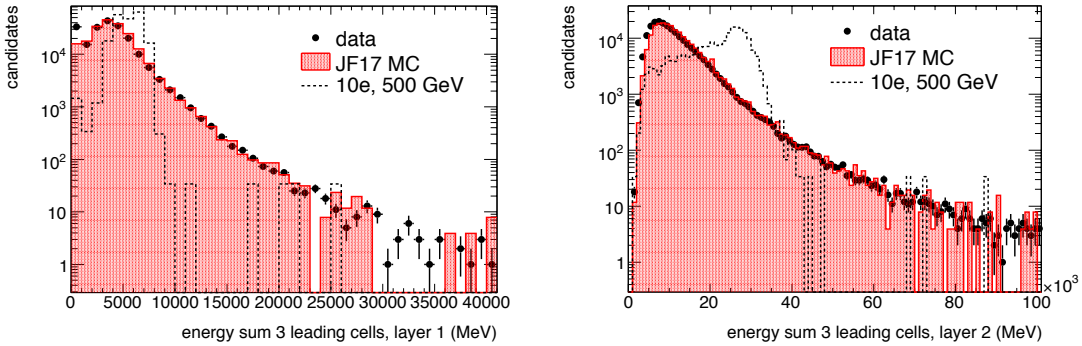


Figure 11.3: Energy in the three most energetic cells in EM layer 1 (left) and EM layer 2 (right) for the cluster associated with all candidates.

| Sample | Filtering | Preselection |
|---|---|---|
| Data | 205496 | 137117 |
| JF17 | 52518 | 38442 |
| Signal: $q$ / $m$ | | |
| 6$e$ / 200 GeV | 2283 | 2182 |
| 6$e$ / 500 GeV | 3250 | 3167 |
| 6$e$ / 1000 GeV | 3900 | 3797 |
| 10$e$ / 200 GeV | 3776 | 3667 |
| 10$e$ / 500 GeV | 5094 | 4952 |
| 10$e$ / 1000 GeV | 6408 | 6230 |
| 17$e$ / 200 GeV | 3202 | 2480 |
| 17$e$ / 500 GeV | 4846 | 4064 |
| 17$e$ / 1000 GeV | 5663 | 4951 |

Table 11.1: Number of events after filtering (including trigger and candidate requirements) and preselection. Each signal sample is based on 20000 pair-produced Drell-Yan events.

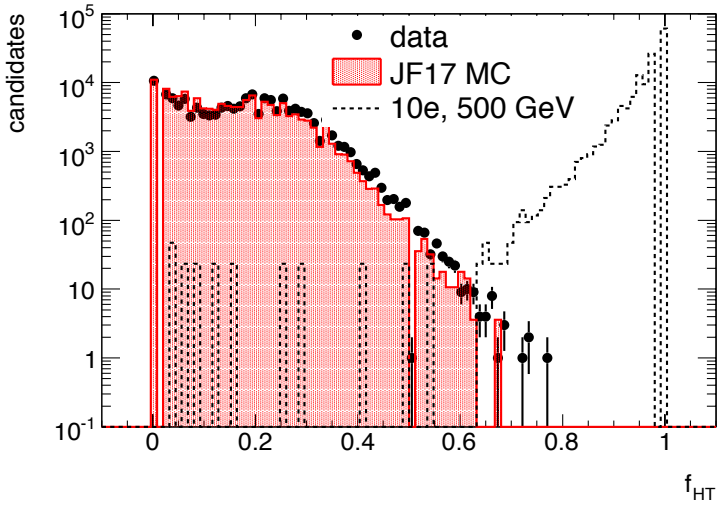


Figure 11.4: Fraction of TRT HT hits ($f_{\mathrm{HT}}$) associated with preselected candidates. The distributions predicted by simulations are normalized to the data.

cluster energy outside the three most energetic cells, in EM layer 1 and 2, respectively. Technically they are computed by looping over the cells in a given layer belonging to the cluster, and dividing the summed energy in all but the three leading cells by the total energy. Figure 11.5 shows the observed and expected distributions for these cluster width variables. It is clear that they also offer powerful discrimination between signal and back-

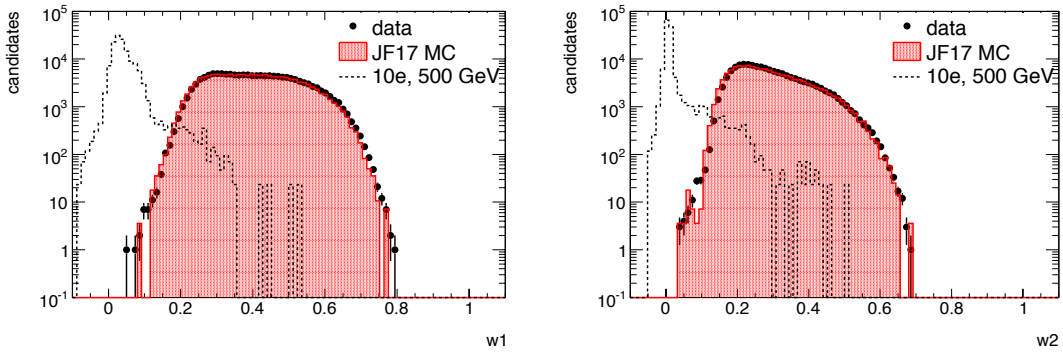


Figure 11.5: Fraction of energy not contained in the three most energetic cells in EM layer 1, $w_1$ (left), and EM layer 2, $w_2$ (right), for clusters associated with preselected candidates.

ground. Signal scenarios with different mass-charge combinations yield similar spectra as the ones shown for the $q = 10e$, $m = 500$ GeV sample in Figures 11.4 and 11.5.

Figure 11.6 shows the correlations between the TRT-based and cluster-based variables. The signal events are isolated in the lower right corner and it is clear that combining requirements on $f_{\mathrm{HT}}$ and $w_1/w_1$ results in a superior discrimination power in the analysis.

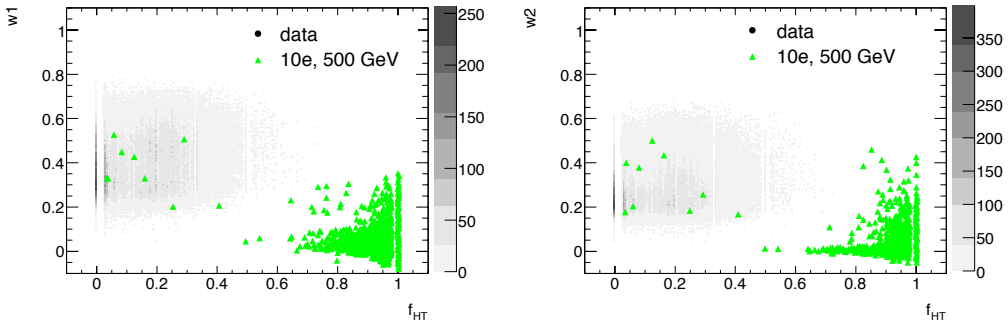


Figure 11.6: Fractions $w_1$ (left) and $w_2$ (right) versus $f_{\mathrm{HT}}$ associated with preselected candidates.

Motivated by the shapes of the predicted spectra for signal and backgrounds for $f_{\mathrm{HT}}$, $w_1$, and $w_2$ in Figures 11.4 and 11.5, the final selection requirements in this search were determined to be $f_{\mathrm{HT}} > 0.65$, $w_1 < 0.20$ and $w_2 < 0.15$. The thresholds were chosen to

yield a very small ($\ell^+\ell^-1$) predicted background while retaining high signal selection efficiencies.

## 11.3 Acceptance and stopping

This search is sensitive only to particles stopping near or inside the LAr detector due to the veto on hadronic leakage required by the "medium" electron identification criteria. This effectively rejects HIPs which traverse the EM calorimeter and also deposit energy in the Tile calorimeter. Furthermore, there are criteria concerning the cluster shape in EM layer 2. The search is therefore sensitive only to particles stopping in either EM layer 2 or EM layer 3.

Since the stopping position is crucial to the type of detector signature a HIP will give rise to, and it depends greatly on the kinematics for which there are no reliable theoretical predictions, an attempt is made to define the acceptance in terms of both geometry and kinematics.

To facilitate this, a careful study of where HIPs of various masses and charges stop within ATLAS was performed. The signal MC samples described in Section 10.4.1 were processed with GEANT4 which propagates the HIPs along their trajectories. When a HIP has lost all of its kinetic energy, the position is recorded. These positions were then used to form a map of where in ATLAS the particles stopped. Table 11.2 shows the probabilities for a HIP produced with Drell-Yan kinematics to stop within EM layer 2 or 3. The numbers in the parentheses indicate the probabilities that at least one of the two produced particles in the event stops in the sensitive volume. The relative uncertainty in these numbers due to statistical uncertainty is of the order of 2%.

| Mass [GeV] | $q = 6e$ | $q = 10e$ | $q = 17e$ |
|---|---|---|---|
| 200 | 0.12 (0.16) | 0.21 (0.27) | 0.20 (0.26) |
| 500 | 0.12 (0.15) | 0.21 (0.26) | 0.25 (0.31) |
| 1000 | 0.17 (0.22) | 0.24 (0.31) | 0.24 (0.30) |

Table 11.2: Fractions of particles stopping within EM layer 2 or 3 within $|\eta| < 1.35$ assuming Drell-Yan kinematics. The numbers in the parentheses indicate the probability that at least one of the two HIPs produced in the event stops in the sensitive volume.

As expected, particles with higher electric charges ionize more and are brought to a stop earlier in the detector. For the case of $q = 6e$, there is a large acceptance loss due to particles punching through the EM calorimeter. For $q = 10e$, the bulk of the stopping positions is around the EM calorimeter, which results in the maximum efficiency. For the $q = 17e$ scenario, a large loss in efficiency is caused by particles stopping before the second EM calorimeter layer.

The variations with mass can be explained by a combination of two effects. With Drell-Yan kinematics, the pseudorapidity spectrum becomes more central with increasing

mass, as shown in the top left distributions of Figure 10.3. This increases the probability for candidates to pass the $|\eta| < 1.35$ requirement which enhances the acceptance. In addition, the speed decreases with increasing mass (as shown in bottom left plot of Figure 10.3), and the ionization energy loss increases for decreasing $\beta$. This means that for a given charge the HIPs are stopped closer to the interaction point for higher masses. Depending on the charge, increasing mass can lead to an increase in acceptance ($6e$) or a decrease in acceptance ($17e$). Combining these effects a qualitative understanding of the numbers in Table 11.2 is obtained.

Highly charged particles within the energy range where they have a high probability to stop in the second layer of the EMB also have a high probability to trigger the event, be reconstructed as electron objects and pass the subsequent selection cuts. This corresponds to the darker areas in Figure 11.7, which shows the selection efficiencies as a function of the true pseudorapidity and kinetic energy at origin for various signal scenarios. The efficiency within these regions is almost flat and relatively high (0.5–0.9). These areas in the $\eta$-$E_{\text{kin}}$ plane can therefore be defined as the sought kinematic acceptances. For each signal scenario the corresponding acceptance region can be encompassed by a parallelo-

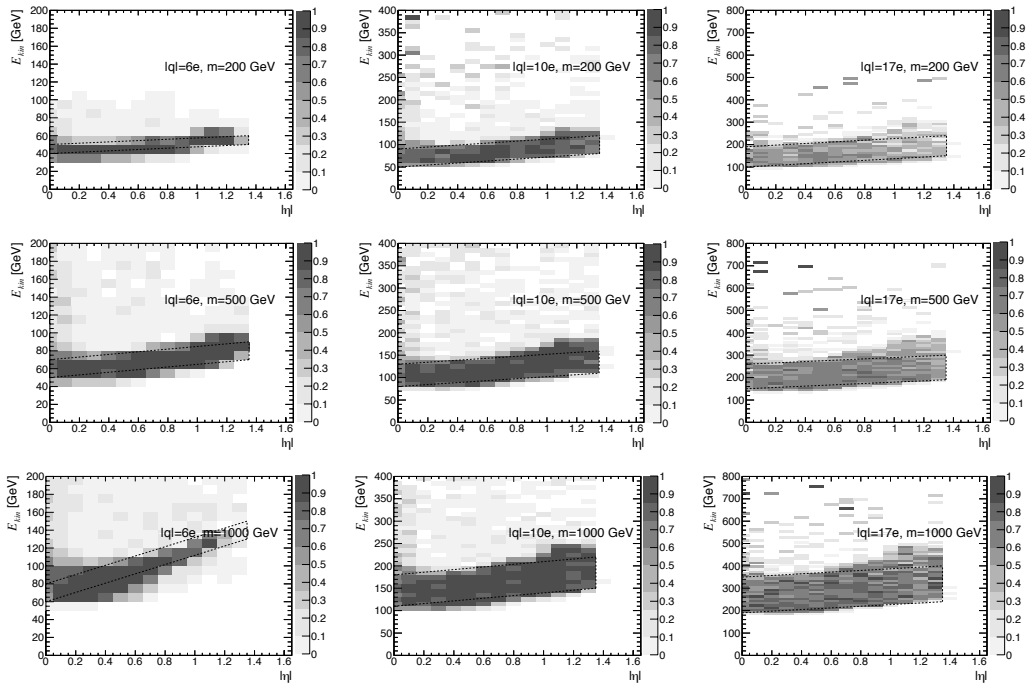


Figure 11.7: Two-dimensional distributions indicating the probabilities to pass all offline selection criteria as functions of pseudorapidity and kinetic energy for HIPs with charges $6e$, $10e$ and $17e$ (left, middle and right) and masses 200, 500 and 1000 GeV (top, middle, bottom). The darker area corresponds to the kinetic range where the particles stop in the second layer of the EM calorimeter barrel. The corners of each area are defined by the values in Table 11.3.

| Signal: $q$ / $m$ | $E_{\text{kin}}^{\text{min}}$ $\lvert\eta\rvert = 0$ | $\lvert\eta\rvert = 1.35$ | $E_{\text{kin}}^{\text{max}}$ $\lvert\eta\rvert = 0$ | $\lvert\eta\rvert = 1.35$ |
|---|---|---|---|---|
| 6$e$ / 200 GeV | 40 | 50 | 50 | 60 |
| 6$e$ / 500 GeV | 50 | 70 | 70 | 90 |
| 6$e$ / 1000 GeV | 60 | 130 | 80 | 150 |
| 10$e$ / 200 GeV | 50 | 80 | 90 | 120 |
| 10$e$ / 500 GeV | 80 | 110 | 130 | 160 |
| 10$e$ / 1000 GeV | 110 | 150 | 180 | 220 |
| 17$e$ / 200 GeV | 100 | 150 | 190 | 240 |
| 17$e$ / 500 GeV | 150 | 190 | 260 | 300 |
| 17$e$ / 1000 GeV | 190 | 240 | 350 | 400 |

Table 11.3: Kinetic energies (in GeV) defining the range of good acceptance for HIPs with the masses and electric charges considered in this search. The coordinates in the $|\eta|$-$E_{\text{kin}}$ plane corresponds to the corners of a parallelogram (see Figure 11.7 for more details).

gram, defined by its four corners as listed in Table 11.3. For the $q = 6e$, $m = 1000$ GeV case, the slightly different shape of the dark area (bottom left in Figure 11.7) is explained by the fact that particles with this charge and mass stopping in the EMB have relatively low speed and are more delayed if they are produced at low energy and relatively high $\eta$. A large delay causes the energy pulse to be poorly reconstructed at trigger level for low energy and relatively high $\eta$.

## 11.4 Selection efficiencies

The selection efficiencies $\varepsilon$, including requirements on offline objects as well as trigger, given that the HIPs are in the acceptance defined in Table 11.3 are shown in Table 11.4. The mass dependence is generally small. Overall selection efficiencies for Drell-Yan kinematics $\varepsilon_{DY}$ are summarized in Table 11.5. The Drell-Yan efficiencies are the total fractions of MC signal events passing the selections defined in Section 11.2, and include both acceptance and efficiency.

Systematic effects which are not included in the MC simulation can cause the central value of the efficiency to shift. The uncertainties due to Birks' correction are slightly asymmetric. To account for their asymmetry when computing the final results (the method assumes symmetric uncertainties, see Chapter 13), the efficiencies are slightly shifted and the mean value of both sides of the systematic uncertainty related to Birks' correction is used. The impact of this adjustment on the final result is minimal. Another effect not modeled to a satisfactory precision in the MC is the potential loss in Level-1 trigger efficiency due to the risk of slow HIPs triggering in the subsequent bunch crossing. This effect is only significant for the $q = 6e$, $m = 1000$ GeV case, for which a potential loss

is estimated to 25%. The central value of the efficiency for this charge and mass point is thus shifted by $-25\%$, and a conservative systematic uncertainty of $\pm 25\%$ is assumed. The shifted efficiency values are shown in the right side of Tables 11.4 and 11.5.

| Mass [GeV] | $q = 6e$ | $q = 10e$ | $q = 17e$ | $q = 6e$ | $q = 10e$ | $q = 17e$ |
|---|---|---|---|---|---|---|
| 200 | 0.84 | 0.83 | 0.49 | 0.82 | 0.82 | 0.48 |
| 500 | 0.88 | 0.87 | 0.63 | 0.87 | 0.86 | 0.62 |
| 1000 | 0.76 | 0.87 | 0.71 | 0.56 | 0.86 | 0.70 |

Table 11.4: Expected fractions of selected signal events assuming kinematics inside the acceptance regions defined by the values in Table 11.3 (this includes efficiency and trigger). The left table shows the raw output of the MC simulation, and the right table shows the efficiency values adjusted for effects which are not simulated in the MC.

| Mass [GeV] | $q = 6e$ | $q = 10e$ | $q = 17e$ | $q = 6e$ | $q = 10e$ | $q = 17e$ |
|---|---|---|---|---|---|---|
| 200 | 0.11 | 0.18 | 0.11 | 0.10 | 0.18 | 0.11 |
| 500 | 0.15 | 0.24 | 0.20 | 0.15 | 0.24 | 0.19 |
| 1000 | 0.18 | 0.30 | 0.24 | 0.13 | 0.30 | 0.24 |

Table 11.5: Efficiencies identically defined to those in Table 11.4 but for signal events assuming Drell-Yan kinematics.

## 11.5 Trigger efficiency

The trigger efficiency, defined as the probability that a signal event passing the offline selection passes the e10_medium chain, is predicted by the MC simulation to be higher than 0.94 in the signal MC samples (see Table 11.6).

| Mass [GeV] | $q = 6e$ | $q = 10e$ | $q = 17e$ |
|---|---|---|---|
| 200 | 0.99 | 0.96 | 0.94 |
| 500 | 0.99 | 0.97 | 0.94 |
| 1000 | 0.98 | 0.99 | 0.96 |

Table 11.6: Trigger efficiencies estimated by the MC simulation after offline selection cuts are applied, assuming kinematics inside the acceptance regions defined by the values in Table 11.3.

# 12 Background estimation method

In this chapter, a method for estimating the expected background in the signal region based on data alone is described. The method, commonly called the *ABCD* method, exploits the fact that requirements on two quantities can be used to split a set of events into four distinct subsets. If the quantities have large discriminating power and a small correlation, the yields in three of the subsets can be used to make a prediction about the yield in the fourth.

## 12.1 Correlations between selection variables

Three variables are used to go from preselection to final selection, which means several combinations exist for the choice of the two quantities. Since the method relies on the two quantities being independent, an important factor to consider before choosing is the correlations between the available variables. Linear correlation coefficients were determined for the three combinations of $w_1$, $w_2$ and $f_{\mathrm{HT}}$ using two-dimensional distributions obtained from the data:

$$\rho_{f_{\mathrm{HT}},w_1} = 0.18 \qquad \rho_{f_{\mathrm{HT}},w_2} = 0.15 \qquad \rho_{w_1,w_2} = 0.54 \tag{12.1}$$

The two variables related to the cluster width, $w_1$ and $w_2$, are strongly correlated and cannot be considered independent. To nevertheless take advantage of their combined discriminating power, they are joined in one single cut.

There is a slight positive correlation between $w_i$ and $f_{\mathrm{HT}}$. The sign of the correlation indicates that the variables tend to vary in the same direction for background, i.e. a low $w_i$ (which is expected for signal) is more likely to be associated with a low $f_{\mathrm{HT}}$ (which is expected for background). Because of this, the assumption that the two variables are independent leads to a conservative background estimate. A potential phenomenon that could explain (part of) this correlation is that tracks with many HT hits in the TRT can be caused by two particles following the same trajectory, which could lead to a wider EM cluster than the average.

## 12.2 Selection probabilities for independent variables

The following two selection cuts are applied to preselected candidates in order to reject background:

- Requirement 1: $f_{\mathrm{HT}} > 0.65$
- Requirement 2: $w_1 < 0.20$ && $w_2 < 0.15$

where Requirement 2 combines $w_1 < 0.20$ and $w_2 < 0.15$ with a logical AND, requiring both inequalities to be true. Using these selections, the preselected candidates are divided into four subsamples defined in Table 12.1. The candidates failing both requirements are

| | Fail Req. 1 $f_{\mathrm{HT}} \leq 0.65$ | Pass Req. 1 $f_{\mathrm{HT}} > 0.65$ |
|---|---|---|
| Pass Req. 2: $w_1 < 0.20$ AND $w_2 < 0.15$ | $A$ | $D$ |
| Fail Req. 2: $w_1 \geq 0.20$ OR $w_2 \geq 0.15$ | $B$ | $C$ |

Table 12.1: Table showing how the preselected candidates are divided into the four subsets used in the background estimation method.

found in subsample $B$. The candidates passing only Requirement 1 or 2 are in subsamples $C$ and $A$, respectively. The region defined by passing both requirements represent the signal region, $D$. Assuming the two requirements are independent, the probability of passing Requirement 1 does not depend on whether or not the candidate passes Requirement 2. Therefore,

$$\frac{N_A}{N_D} = \frac{N_B}{N_C} \Longleftrightarrow N_D = \frac{N_A N_C}{N_B}, \tag{12.2}$$

where $N_i$ corresponds to the candidate yield in subsample $i$. Denoting the probability of passing Requirement 1 and 2 $p_{f_{\mathrm{HT}}} = \frac{N_C}{N_B+N_C}$ and $p_w = \frac{N_A}{N_A+N_B}$, respectively, and the total number of preselected candidates $N_{\mathrm{pre}}$, the expected yield in the signal region due to background can be expressed as

$$N_D = N_{\mathrm{pre}} p_{f_{\mathrm{HT}}} p_w. \tag{12.3}$$

Figure 12.1 illustrates with the square markers the fraction of preselected events outside the signal region which are selected by Requirements 1 (a) and 2 (b). The calculation of the final background estimate in the signal region is deferred to the next chapter where the final yields are presented.

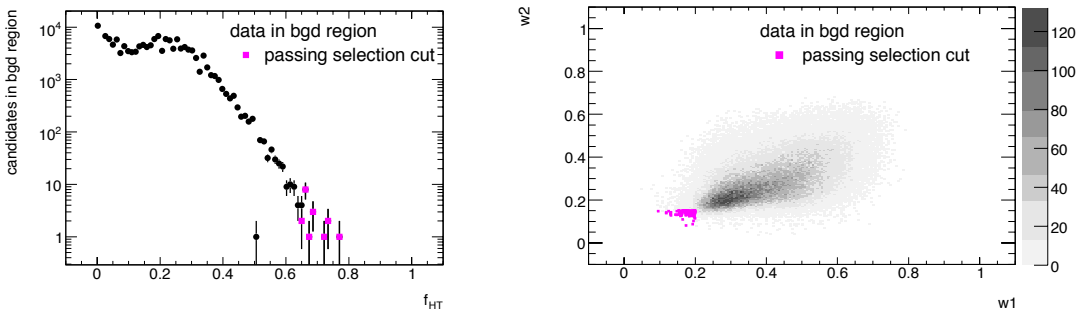


(a) (b)

Figure 12.1: (a) Distribution of $f_{\mathrm{HT}}$ for preselected candidates in the background region where either $w_1$ or $w_2$ fails the selection cut. (b) shows $w_1$ versus $w_2$ for preselected candidates in the background region where $f_{\mathrm{HT}}$ fails the selection cut. Candidates in the signal regions at high $f_{\mathrm{HT}}$ in (a) and low $w_1$ and $w_2$ in (b) are drawn with colored square markers.

### 12.2.1 Sensitivity to $f_{\mathrm{HT}}$, $w_1$ and $w_2$ threshold values

In order to test the robustness of the background estimation method, relaxed versions of the final selection requirements were tested to allow some background to pass the selection. Applying $f_{\mathrm{HT}} > 0.45$, $w_1 < 0.30$ and $w_2 < 0.25$, the estimated number of background events was 182, and the observed number of events passing the selection in the data was 46. This confirms that the method overestimates the background close to the signal region and is thus conservative. The overestimate of the background has been checked and found qualitatively consistent with the observed correlations between $w_i$ and $f_{\mathrm{HT}}$, which by design are assumed to be consistent with zero in the background estimation method. The relative increase in signal efficiency is small, 3.6% on average, when using the relaxed the requirements above. The effect of tightening the requirements was also investigated, resulting in a background estimate two orders of magnitude smaller than with the nominal thresholds, while reducing the signal efficiencies by a few percent. As explained in the following section, the predicted background is negligible already with the nominal requirements, so it is not desirable to further suppress it at the cost of losing signal efficiency.

# 13 Results

## 13.1 Final yields and predictions

Applying the final selections as described in Section 11.2.3 to the data and the simulated samples, the final yields in Table 13.1 are obtained. No event in the experimental data passes the final selection.

In the regions defined in Chapter 12 the following event yields were observed: $N_A$: 143, $N_B$: 137342, $N_C$: 18, $N_D$: 0. Inserting these values into the expressions for the probabilities of passing each individual requirement in the final selection gives $p_{f_{\mathrm{HT}}} = (1.3 \pm 0.3) \times 10^{-4}$ and $p_w = (1.0 \pm 0.1) \times 10^{-3}$. Inserting these probabilities together with $N_{\mathrm{pre}} = 137503$ into equation (12.3) yields a final predicted background of $0.019 \pm 0.005$ (stat.) events in the signal region, which is compatible with the observation.

| Sample | Filtering | Preselection | Final selection |
|---|---|---|---|
| Data | 205496 | 137117 | 0 |
| JF17 | 52518 | 38442 | 0 |
| Signal: $q$ / $m$ | | | |
| 6$e$ / 200 GeV | 2283 | 2182 | 2094 |
| 6$e$ / 500 GeV | 3250 | 3167 | 3041 |
| 6$e$ / 1000 GeV | 3900 | 3797 | 3637 |
| 10$e$ / 200 GeV | 3776 | 3667 | 3527 |
| 10$e$ / 500 GeV | 5094 | 4952 | 4782 |
| 10$e$ / 1000 GeV | 6408 | 6230 | 6040 |
| 17$e$ / 200 GeV | 3202 | 2480 | 2273 |
| 17$e$ / 500 GeV | 4846 | 4064 | 3910 |
| 17$e$ / 1000 GeV | 5663 | 4951 | 4805 |

Table 13.1: Number of events after filtering (including trigger and candidate requirements), preselection and final selection. Each signal sample is based on 20000 pair-produced Drell-Yan events.

## 13.2 Summary of systematic uncertainties

A summary of the systematic uncertainties affecting the selection efficiencies for signal scenarios is given in Table 13.2, along with their estimated resulting impact on the signal efficiencies. The table shows example numbers based on signal samples with $m_{Q\text{ball}} =$ 500 GeV. A cursory review of each of the uncertainties listed in the table can be found below.

| Source | $q = 6e$ | $q = 10e$ | $q = 17e$ |
|---|---|---|---|
| Birks' correction | 0.16 | 0.06 | 0.04 |
| $\delta$-electrons | 0.03 | 0.03 | 0.03 |
| Detector material density | 0.06 | 0.06 | 0.06 |
| Cross-talk | 0.02 | 0.02 | 0.02 |
| Inactive detector description | 0.02 | 0.02 | 0.02 |
| Timing effects | 0.01 | 0.01 | 0.01 |
| PDF uncertainty | 0.03 | 0.03 | 0.03 |
| MC statistics | 0.02 | 0.02 | 0.02 |
| Total | 0.18 | 0.10 | 0.09 |

Table 13.2: Relative systematic uncertainty estimates in the signal selection efficiencies for particles with mass 500 GeV. The mass dependence in these numbers is generally small (see Table 13.3), except in the particular case of $q = 6e$, $m = 1000$ GeV where timing effects contribute significantly.

The uncertainties related to Birks' correction are related to the modeling of electron-ion recombination in the simulations, as discussed in some detail in Section 10.3.

Within the GEANT4 simulation, there exists a parameter that controls the cut-off range related to the treatment of $\delta$-electrons, and there is an uncertainty on the value for this parameter. The $\delta$-electrons contaminate the tracker with extra hits which can give rise to additional reconstructed tracks near the candidates. If one of these tracks is accidentally matched to a candidate, it is likely to not pass the $f_{\text{HT}}$ requirement. To estimate the sensitivity to the chosen parameters value, special simulations were run where the default value was scaled up and down by a factor of 2, yielding shifts in the signal efficiencies of approximately $\pm 3\%$.

Since the stopping positions of the HIPs in ATLAS are determined by the amount of material in the detector, the selection efficiencies are sensitive to imperfections in the detector geometry model used in the simulations. To test the sensitivity of the selection efficiency to these effects, simulations with alternative geometry models were performed. A model with an additional 10% material in the inner detector was tested, as was one with 5-20% extra material between various EM calorimeter layers. The total relative effect on the signal efficiency was estimated in this way to be 6%.

In the EM calorimeter, energy deposited in a given cell can give rise to signals in

adjacent cells, known as a "cross-talk" effect. This effect is modeled in the simulation of the EM calorimeter. However, since this should affect the shower shape variables used in this analysis, the simulation was run with the effect doubled. This reduces the overall efficiency with less than 2%

During long periods of detector operation, modules and individual channels of the EM calorimeter can suffer from periods of malfunction. This is not modeled correctly by the simulations, and the impact of this on the signal efficiency was therefore investigated. This effect was estimated to degrade the reconstruction efficiency of electrons by 2%.

For very slow-moving HIPs, there is a risk that the energy depositions are so late that they trigger in the bunch crossing after they were produced. This effects starts to become significant for delays of 10 ns or more, corresponding to a constant speed $\beta < 0.37$. Since HIPs undergo dramatic energy losses, they are expected to slow down as they pass through the detector. The only signal sample for which this is a significant effect is the $q = 6e$ and $m = 1000$ GeV. The true $\beta$ spectrum for the HIPs passing the selection peaks between 0.32 to 0.47. Approximately 50% of the candidates in this sample at risk of causing a late trigger [154, 155]. Since this is not modeled with sufficient accuracy in the simulations, the efficiency is scaled down by 25% and an additional systematic uncertainty of 25% is assigned to this sample only.

The choice of parton density function used in the event generation affects the kinematics. To test the sensitivity of the efficiencies for signal with the Drell-Yan kinematics, seven different PDF sets were tested. The resulting relative uncertainty on the efficiency from these tests was determined to be approximately 3%.

Due to the limited statistics of the simulated signal samples, an uncertainty arises in the efficiencies due to poisson fluctuations. This uncertainty was determined to approximately 2%

After combining all effects, the total relative systematic uncertainties in the selection efficiency for signal in the charge and mass ranges considered here are reported in Table 13.3. They are generally dominated by the uncertainties in Birks' correction.

| Mass [GeV] | $q = 6e$ | $q = 10e$ | $q = 17e$ |
|---|---|---|---|
| 200 | 0.245 | 0.111 | 0.093 |
| 500 | 0.172 | 0.097 | 0.087 |
| 1000 | 0.282 | 0.095 | 0.088 |

Table 13.3: Total relative systematic uncertainties in signal efficiency, combining the effects of all investigated sources.

The uncertainty on the integrated luminosity has been estimated to 11% [131].

## 13.3 Limits

In the zero background hypothesis, assuming Poisson statistics, the following limit in the number of signal events $N$ is obtained: $N < 3.0$ (95% confidence level) [4].

The following expression describes the cross section $\sigma$:

$$\sigma = \frac{N}{\varepsilon \mathscr{L}}, \tag{13.1}$$

where $N$ is the number of observed events, $\mathscr{L}$ is the integrated luminosity and $\varepsilon$ is the total selection efficiency which varies between the considered signal scenarios.

$N = 0$ is observed, and zero background events are expected. In absence of both signal and background, a limit is put on $\sigma$ using a standard bayesian approach [156], where systematic uncertainties in $\mathscr{L}$ and $\varepsilon$ are taken into account assuming they are gaussian and independent, using a flat distribution as the prior. The resulting 95% confidence level (C.L.) cross section limits assuming Drell-Yan kinematics are shown in Table 13.4. Limits on the effective cross section for particles produced in the regions of kinematic acceptance defined in Table 11.3 were also computed and are shown in Table 13.5, assuming the same systematic uncertainties as above. These cross section limits were compared with results from independent calculations and found to agree within 0.2 pb.

| Mass [GeV] | $q = 6e$ | $q = 10e$ | $q = 17e$ |
|---|---|---|---|
| 200 | 11.5 | 5.9 | 9.1 |
| 500 | 7.2 | 4.3 | 5.3 |
| 1000 | 9.3 | 3.4 | 4.3 |

Table 13.4: Upper limits on the production cross section for long-lived massive particles with high electric charges produced in pairs with Drell-Yan kinematics, in picobarn, at 95% C.L.

| Mass [GeV] | $q = 6e$ | $q = 10e$ | $q = 17e$ |
|---|---|---|---|
| 200 | 1.4 | 1.2 | 2.1 |
| 500 | 1.2 | 1.2 | 1.6 |
| 1000 | 2.2 | 1.2 | 1.5 |

Table 13.5: Upper limits at 95% C.L. for long-lived massive particles with high electric charges produced in regions of pseudorapidity and kinetic energy as defined in Table 11.3, in picobarn, at 95% C.L.

Using these results, cross section limits can be obtained at generator level for any given model of kinematics. This can be done by dividing the limits calculated for the kinematic acceptance regions with the fraction of events where at least one HIP is in

the given $\eta$-$E_{\text{kin}}$ region. A limit obtained through this method is conservative since the efficiency for selecting HIPs outside of the acceptance is better than zero, as can be seen in Figure 11.7. As a cross-check, this exercise was done with the Drell-Yan pair-production model, and the result overestimates the more accurate values in Table 13.4 by an average factor of 1.7.

## 13.4 Summary and conclusions

Experimental data recorded with the ATLAS experiment corresponding to 3.1 pb$^{-1}$ of 7 TeV collisions were analyzed in search for highly ionizing particles (HIPs). The sought signature featured electron-like objects and was based on standard electron trigger and object identification algorithms. For the final selection, powerful HIP-sensitive variables based on the fraction of high-threshold hits in the Transition Radiation Tracker and shower shape variables based on the electromagnetic barrel calorimeter were employed.

No event in the experimental data passed the selection, where the background expectation from a data-driven method was $0.019 \pm 0.005$ events. Since no excess was observed, limits were calculated for the production cross section for highly charged objects in the charge range $6e \leq |q| \leq 17e$ and masses ranging from 200-1000 GeV. Assuming kinematics similar to those from Drell-Yan pair production, the upper limits obtained for the considered charge and mass range are less than 12 pb at 95% confidence level. The systematic uncertainties are dominated by uncertainties in the integrated luminosity and in the fraction of visible energy in the LAr detector from the deposits from HIPs.

Model-independent limits were also calculated by defining kinematic acceptance regions and quoting efficiencies and cross section limits for particles produced with kinematics in these intervals. This information enables interpretations of these limits for any production model. These limits are the first constraints set on long-lived highly ionizing particle production with $|q| \gg e$ at the LHC.

# A Background composition

Even though the Monte Carlo simulations of the background processes are not used in the calculations of the final result, they can be used to teach us something about our background composition since they in yield and most distributions match the data quite well. Figure A.1 shows the types of particles that give rise to the candidates passing the preselection in the background Monte Carlo samples. The vast majority of the candidates are real muons, and the dominating processes are electroweak, primarily $W$+jets where the $W$-boson decays through $W \to \mu\nu$.

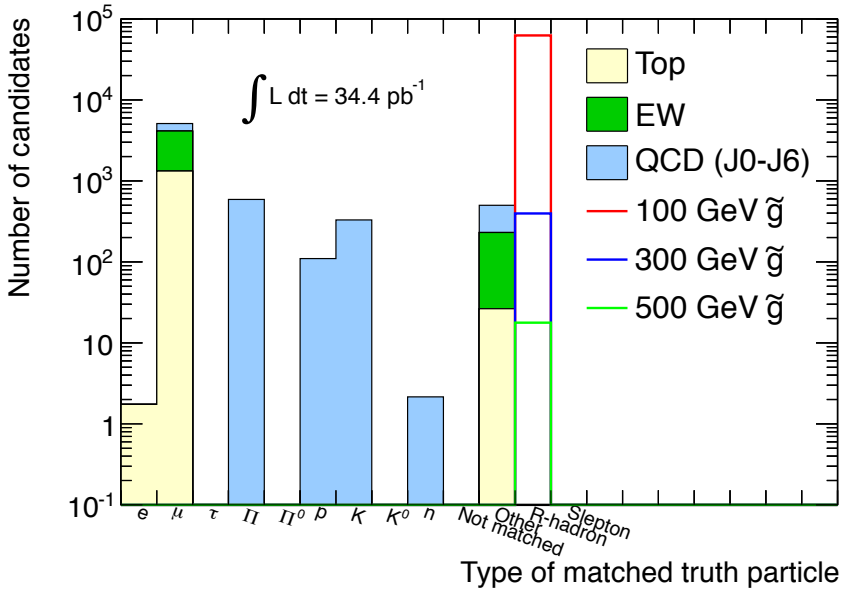


Figure A.1: The type of true particles that are matched to candidates surviving the $p_{\mathrm{T}} >$ 50 GeV cut in the background Monte Carlo samples.

# B Time dependence

During long periods of data taking the performance of the detectors can vary and there can be temporary problems that compromise the integrity of the recorded data. Though data exhibiting problems like this are expected to be discarded by employing the standard ATLAS data quality filtering, the time dependence of the selection efficiencies have been investigated to verify that they were stable throughout the period when the experimental data used in Paper I was recorded. Figure B.1 shows the number of selected events per $\text{nb}^{-1}$ as a function of run number. The top plot illustrates the number of selected events per $\text{nb}^{-1}$ after requiring trigger, and the second one shows the same after requiring at least one candidate passing the preselection criteria described in Section 6, but with $p_{\text{T}} > 25$ GeV rather than $p_{\text{T}} > 50$ GeV. The `JetTauEtmiss` and `debug` streams are shown separately. In subfigures (c) and (d) the same distributions are shown for the JetTauEtmiss stream on a linear scale, and the curve resulting from a fit with a 0th order polynomial is overlaid.

Figure B.2 shows that the proton mass as measured by the Pixel $dE/dx$ method is stable within 1% over a 9-month period with luminosities ranging from $10^{27}$ $\text{cm}^{-2}\text{s}^{-1}$ to $10^{32}$ $\text{cm}^{-2}\text{s}^{-1}$ [100].

The distributions of Pixel $dE/dx$ and Tile $\beta$ were also compared for different run periods to check for discrepancies indicative of detector problems, but no such significant deviations were observed.

During the running periods considered in this work, not all parts of the SMPs-sensitive detectors were operating. For TileCal, the Pixel and TRT subsystems 3.8%, 3% and 2% of the modules, respectively, were not operational. In the simulation dead regions corresponding to 3.3%, 2.6% and 1.6% of the aforementioned subsystems were considered. The effect of inadequate simulation of dead regions would therefore affect the predicted signal efficiency by 1-2%, which is a tiny effect compared to other systematic uncertainties described in Section 8.

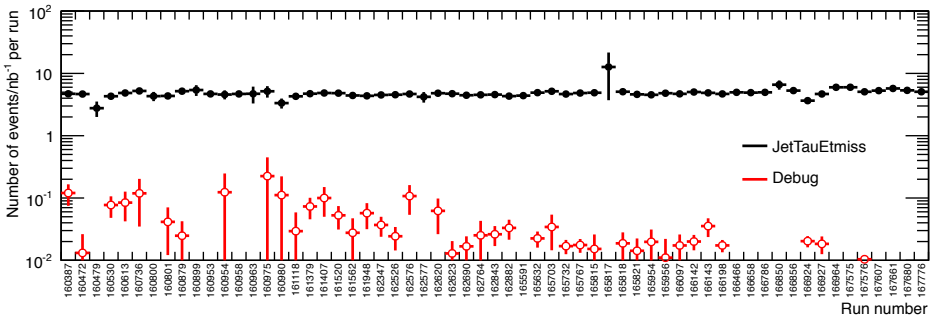


(a)

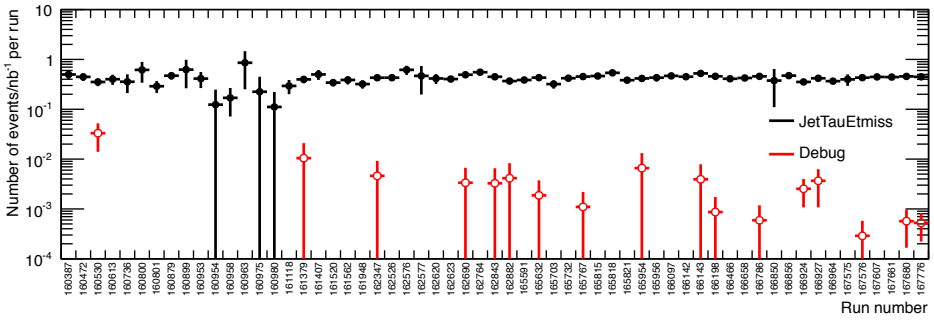


(b)

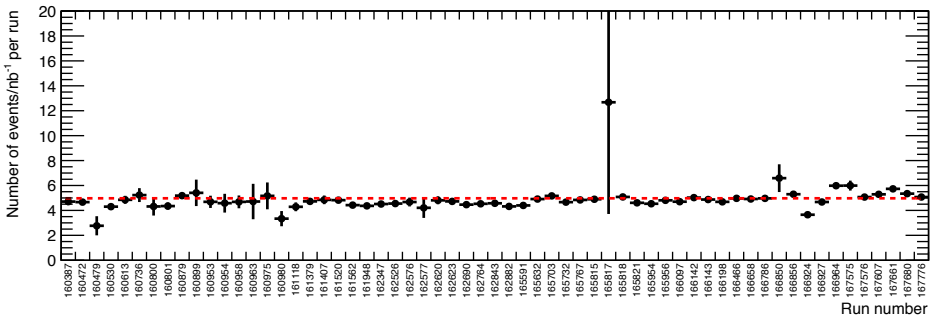


(c)

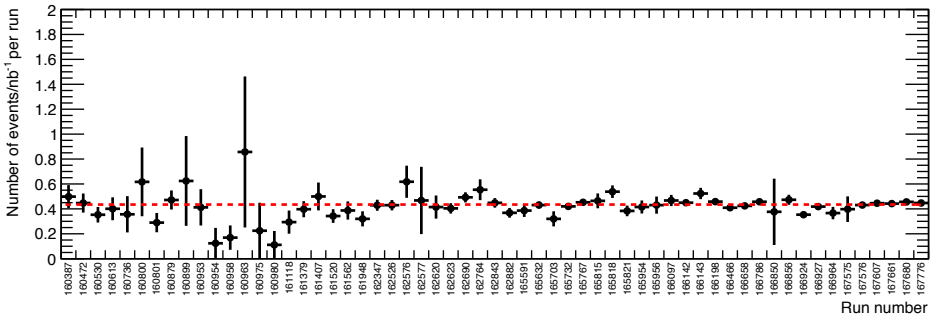


(d)

Figure B.1: Number of selected events per nb$^{-1}$ as a function of run number after requring (a) trigger, and (b) at least one candidate with $p_{\mathrm{T}} > 25$ GeV.

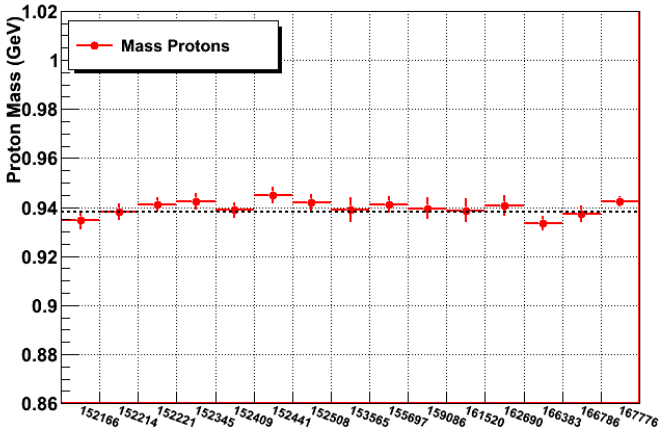


Figure B.2: Fitted proton peak mass values as a function of run number for a data recorded with a mimimum-bias trigger. The runs span over 9 months of ATLAS data taking and 5 orders of magnitude of luminosity.

# C Event display images

A few selected signal-like events in data are here visualized using the ATLAS event display package VP1 [157]. The colored cones represent reconstructed jets, and the arrows represent the direction and magnitude of the $E_{\mathrm{T}}^{\mathrm{miss}}$.

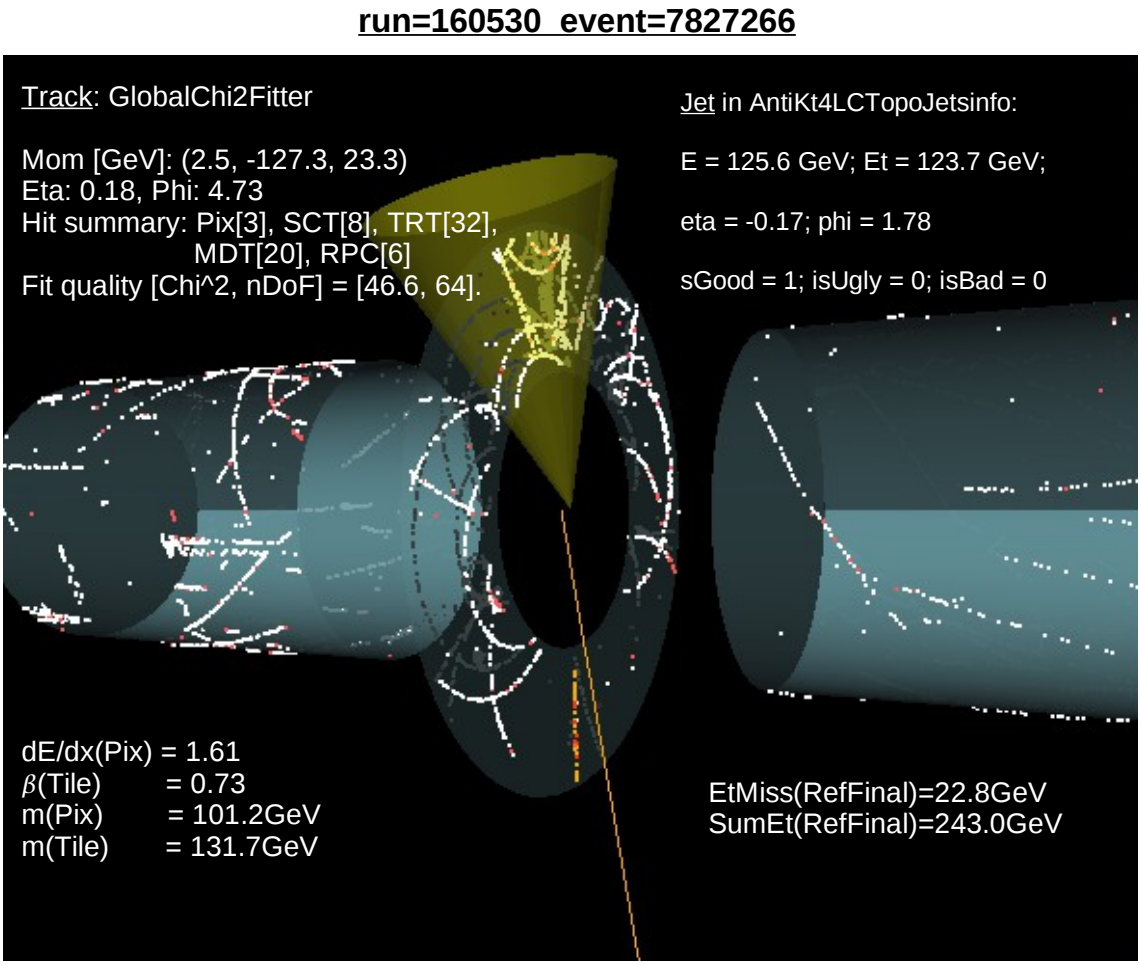


Figure C.1: Event display of signal-like collision event.

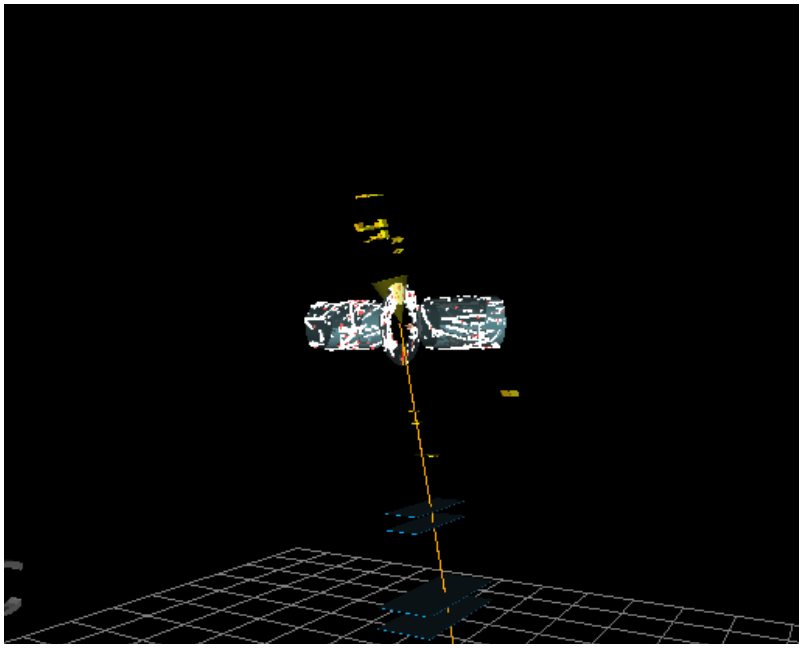

Figure C.2: Alternative view of the event displayed in Figure C.1.

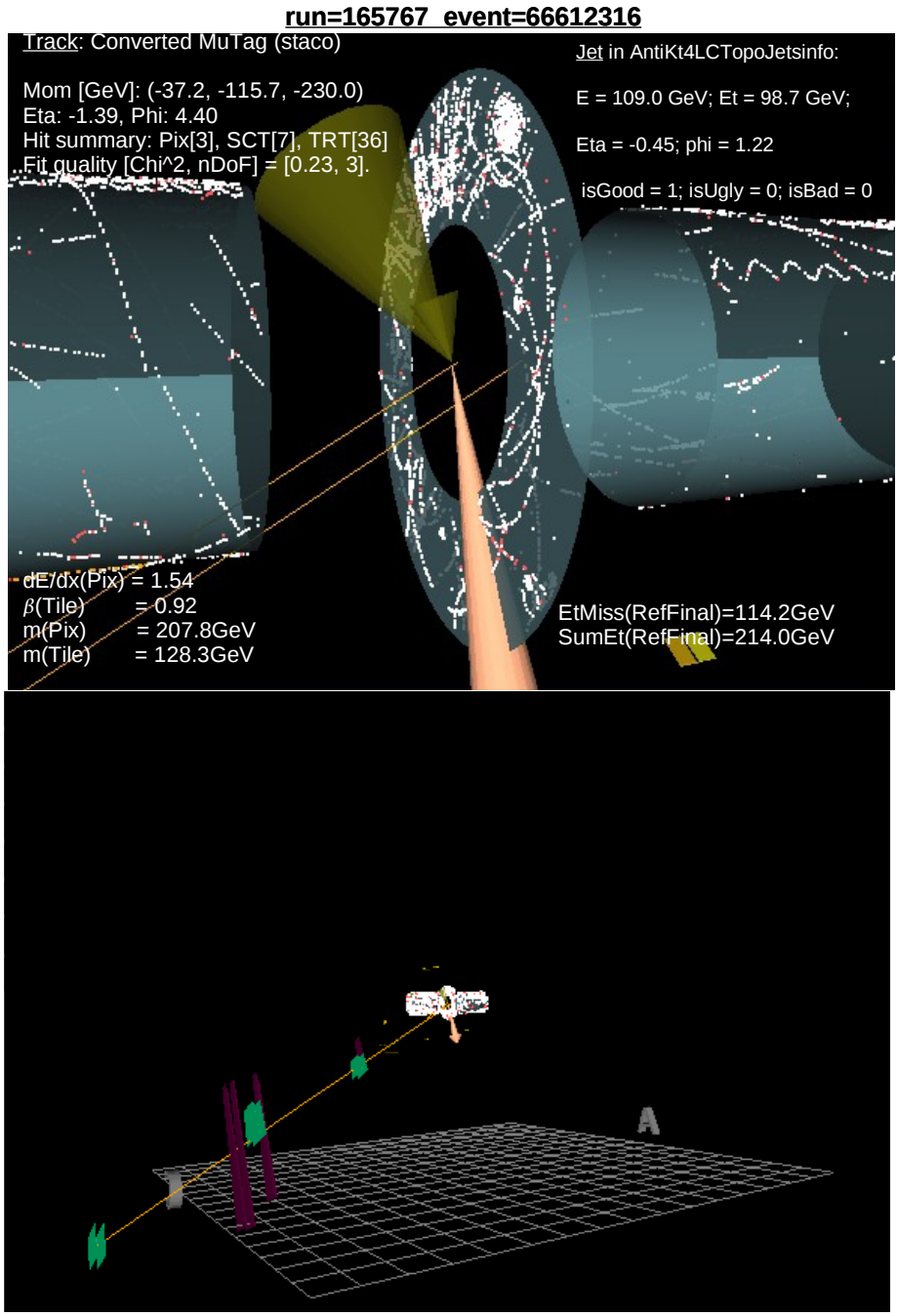


Figure C.3: Event display of signal-like collision event.

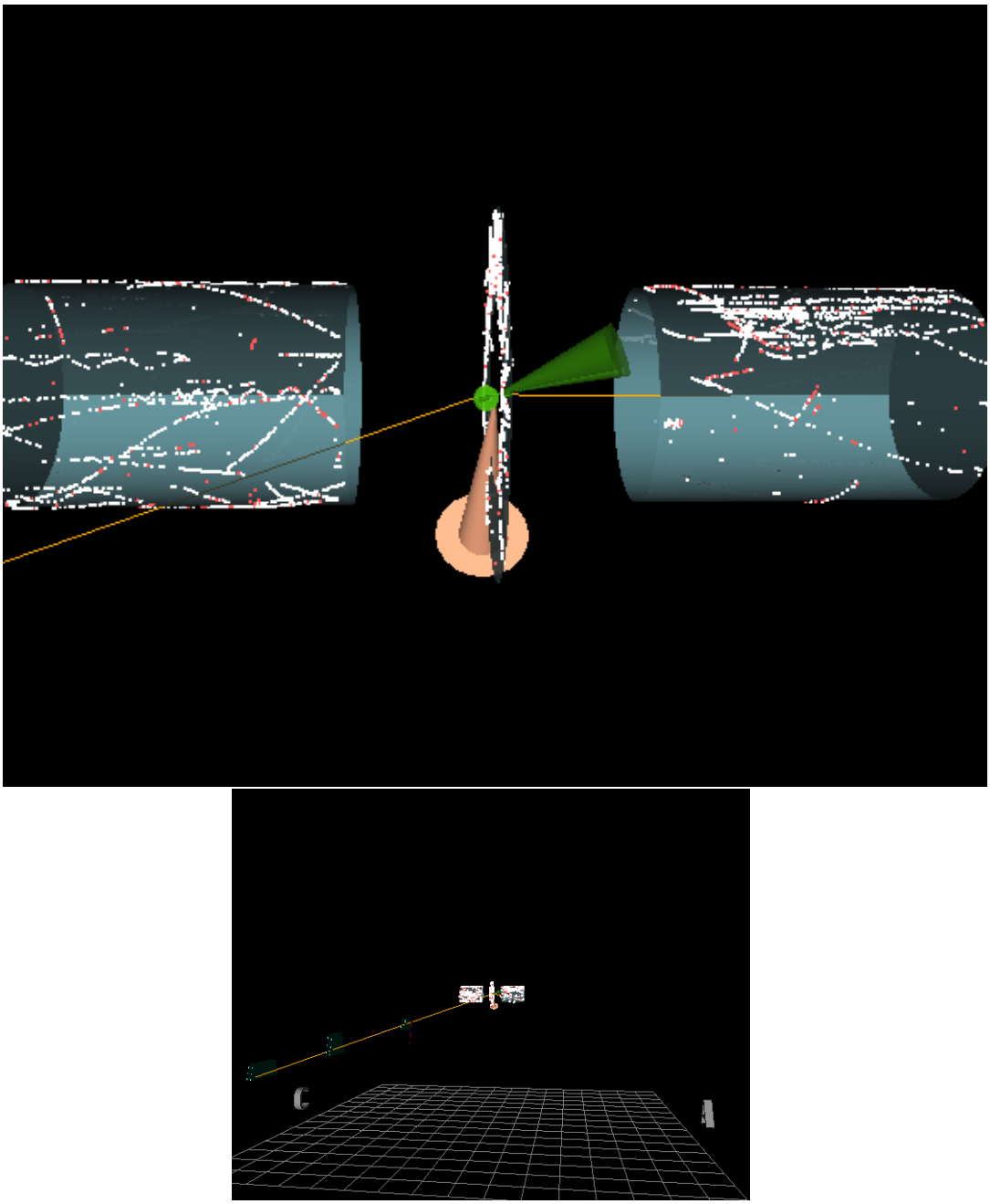

Figure C.4: Event display of a simulated 500 GeV gluino event (generic model).

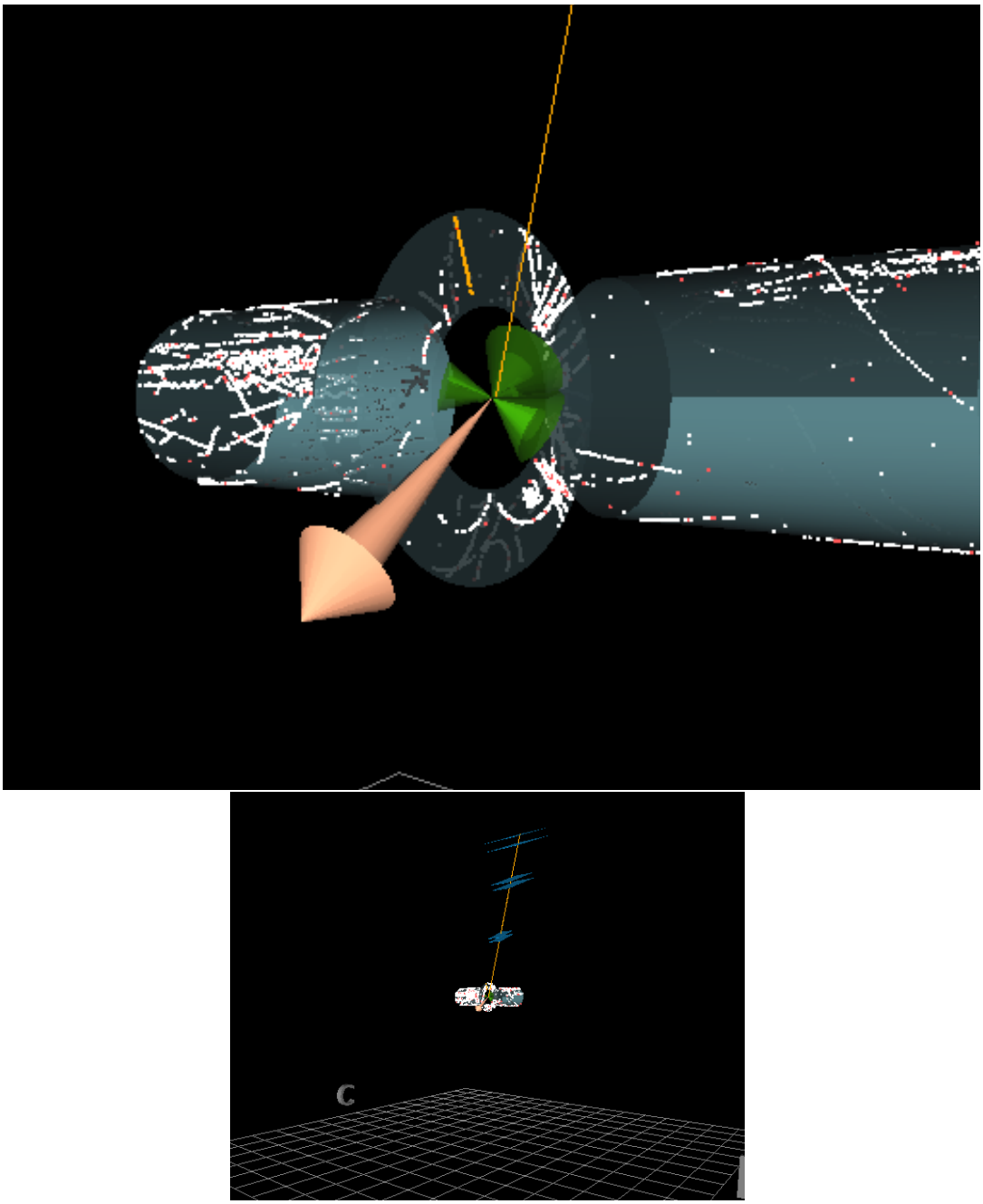

Figure C.5: Event display of a simulated 500 GeV stop event (regge model).

# List of Figures

# List of Tables

# Bibliography


[1] C. Ohm. Phase and intensity monitoring of the particle beams at the ATLAS experiment. *MSc Thesis, Linköping University, The Department of Physics, Chemistry and Biology*, 2007.

[2] S. Hellman, M. Johansen, R. Mackeprang, P. Mermod, D. Milstead, C. Ohm, and A. Solodkov. Measuring time-of-flight and identifying exotic stable massive particles with the ATLAS Tile calorimeter. Technical Report ATL-TILECAL-INT-2010-006, CERN, Geneva, Sep 2010.

[3] D. Griffiths. *Introduction to Elementary Particles*. WILEY-VCH, second edition edition, 2008.

[4] Particle Data Group. Review of particle physics. *Phys. Lett.*, B667:1, 2008.

[5] V.W. Hughes and T. Kinoshita. Anomalous g values of the electron and muon. *Rev.Mod.Phys.*, 71:S133–S139, 1999.

[6] Particle Data Group. Review of particle physics. *Journal of Physics G: Nuclear and Particle Physics*, 37(7A):075021, 2010.

[7] M. Fairbairn et al. Stable massive particles at colliders. *Phys. Rept.*, 438:1–63, 2007.

[8] G. Bertone, D. Hooper, and J. Silk. Particle dark matter: Evidence, candidates and constraints. *Phys. Rept.*, 405:279–390, 2005.

[9] L. Bergstrom. Nonbaryonic dark matter: Observational evidence and detection methods. *Rept.Prog.Phys.*, 63:793, 2000.

[10] WMAP Collaboration. Five-Year Wilkinson Microwave Anisotropy Probe Observations: Cosmological Interpretation. *Astrophys. J. Suppl.*, 180:330–376, 2009.

[11] R. *et al.* Barate. Search for the standard model Higgs boson at LEP. *Phys. Lett.*, B565:61–75, 2003.

[12] CDF and D0 collaborations. Combined CDF and D0 Upper limits on Standard Model Higgs-boson production with up to 6.7 $\text{fb}^{-1}$ of data. *Fermilab conference note*, FERMILAB-CONF-10-257-E, 2010.

[13] The ATLAS Collaboration. Combination of the searches for the Higgs boson in 1 $fb^{-1}$ of data taken with the ATLAS detector at 7 TeV center-of-mass Energy. Technical Report ATLAS-CONF-2011-112, CERN, Geneva, Aug 2011.

[14] The CMS Collaboration. SM Higgs combination. *CMS conference note*, CMS-PAS-HIG-11-011, 2011.

[15] J. Erler. The Mass of the Higgs Boson in the Standard Electroweak Model. *Phys.Rev.*, D81:051301, 2010.

[16] H. Flacher, M. Goebel, J. Haller, A. Hocker, K. Monig, et al. Revisiting the Global Electroweak Fit of the Standard Model and Beyond with Gfitter. *Eur.Phys.J.*, C60:543–583, 2009.

[17] ALEPH Collaboration, DELPHI Collaboration, L3 Collaboration, OPAL Collaboration, SLD Collaboration, LEP Electroweak Working Group, SLD Electroweak Group, and SLD Heavy Flavour Group. Precision electroweak measurements on the *Z* resonance. *Phys.Rept.*, 427:257–454, 2006.

[18] Super-Kamiokande Collaboration. Evidence for an oscillatory signature in atmospheric neutrino oscillation. *Phys. Rev. Lett.*, 93:101801, 2004.

[19] S. P. Martin. A Supersymmetry primer. 1997.

[20] G. F. Giudice and R. Rattazzi. Theories with gauge-mediated supersymmetry breaking. *Phys. Rept.*, 322:419–499, 1999.

[21] N. Arkani-Hamed and S. Dimopoulos. Supersymmetric unification without low energy supersymmetry and signatures for fine-tuning at the LHC. *JHEP*, 06:073, 2005.

[22] G. Servant and T. M. P. Tait. Is the lightest Kaluza-Klein particle a viable dark matter candidate? *Nucl. Phys.*, B650:391–419, 2003.

[23] N. Arkani-Hamed, S. Dimopoulos, and G. R. Dvali. The hierarchy problem and new dimensions at a millimeter. *Phys. Lett.*, B429:263–272, 1998.

[24] D. Hooper and S. Profumo. Dark matter and collider phenomenology of universal extra dimensions. *Phys.Rept.*, 453:29–115, 2007.

[25] C. F. Kolda. Gauge-mediated supersymmetry breaking: Introduction, review and update. *Nucl. Phys. Proc. Suppl.*, 62:266–275, 1998.

[26] H. Baer, K. Cheung, and J. F. Gunion. A heavy gluino as the lightest supersymmetric particle. *Phys. Rev.*, D59:075002, 1999.

[27] S. J. Gates, Jr. and O. Lebedev. Searching for supersymmetry in hadrons. *Phys. Lett.*, B477:216–222, 2000.

[28] A. Mafi and S. Raby. An analysis of a heavy gluino LSP at CDF : the heavy gluino window. *Phys. Rev.*, D62:035003, 2000.

[29] M.B. Chertok, G.D. Kribs, Y. Nomura, W. Orejudos, B. Schumm, et al. Phenomenology of a constrained standard model from an extra dimension. page P310, 2001.

[30] G. F. Giudice and A. Romanino. Split supersymmetry. *Nucl. Phys.*, B699:65–89, 2004.

[31] N. Arkani-Hamed, S. Dimopoulos, G. F. Giudice, and A. Romanino. Aspects of split supersymmetry. *Nucl. Phys.*, B709:3–46, 2005.

[32] H. K. Dreiner. An introduction to explicit R-parity violation. 1997.

[33] E. L. Berger and Z. Sullivan. Lower limits on R parity violating couplings in supersymmetry. *Phys. Rev. Lett.*, 92:201801, 2004.

[34] R. Barbier, C. Berat, M. Besancon, M. Chemtob, A. Deandrea, et al. R-parity violating supersymmetry. *Phys.Rept.*, 420:1–202, 2005.

[35] A.R. Raklev. Massive Metastable Charged (S)Particles at the LHC. 2009.

[36] R. Mackeprang. Stable Heavy Hadrons in ATLAS. *Ph.D. Thesis, University of Copenhagen*, 2007.

[37] A.C. Kraan. Interactions of heavy stable hadronizing particles. *Eur. Phys. J.*, C37:91–104, 2004.

[38] R. Mackeprang and A. Rizzi. Interactions of coloured heavy stable particles in matter. *Eur. Phys. J.*, C50:353–362, 2007.

[39] R. Mackeprang and D.A. Milstead. An updated description of heavy-hadron interactions. *Eur. Phys. J.*, C66:493–501, 2010.

[40] T. Sjostrand, S. Mrenna, and P. Skands. PYTHIA 6.4 Physics and Manual. *JHEP*, 05:026, 2006.

[41] G. Corcella et al. HERWIG 6.5: an event generator for Hadron Emission Reactions With Interfering Gluons (including supersymmetric processes). *JHEP*, 01:010, 2001.

[42] A. Kusenko and M.E. Shaposhnikov. Supersymmetric Q-balls as dark matter. *Phys. Lett.*, B418:46–54, 1998.

[43] B. Koch, M. Bleicher, and H. Stöcker. Black holes at lhc? *Journal of Physics G: Nuclear and Particle Physics*, 34(8):S535, 2007.

[44] J. S. Schwinger. Magnetic charge and quantum field theory. *Phys. Rev.*, 144:1087–1093, 1966.

[45] P. A. M. Dirac. Quantized Singularities in the Electromagnetic Field. *Proc.Roy.Soc.Lond.*, A133:60–72, 1931.

[46] P. A. M. Dirac. The Theory of magnetic poles. *Phys.Rev.*, 74:817–830, 1948.

[47] The ALEPH Collaboration. Search for stable hadronizing squarks and gluinos in e+ e- collisions up to s**(1/2) = 209-GeV. *Eur. Phys. J.*, C31:327–342, 2003.

[48] The DELPHI Collaboration. A search for heavy stable and longlived squarks and sleptons in e+ e- collisions at energies from 130-GeV to 183-GeV. *Phys. Lett.*, B444:491–502, 1998.

[49] The DELPHI Collaboration. Search for an LSP gluino at LEP with the DELPHI detector. *Eur. Phys. J.*, C26:505–525, 2003.

[50] The CDF Collaboration. Search for long-lived charged massive particles in $\bar{p}p$ collisions at $\sqrt{s} = 1.8$ TeV. *Phys. Rev. Lett.*, 90:131801, 2003.

[51] The D0 Collaboration. Search for Long-Lived Charged Massive Particles with the D0 Detector. *Phys. Rev. Lett.*, 102:161802, 2009.

[52] The CDF Collaboration. Search for Heavy Stable Particles at the Fermilab Collider. *Phys.Rev.Lett.*, 63:1447, 1989.

[53] The CDF Collaboration. Limits on the production of massive stable charged particles. *Phys.Rev.*, D46:1889–1894, 1992.

[54] The CDF Collaboration. Search for Long-Lived Massive Charged Particles in 1.96-TeV p anti-p Collisions. *Phys.Rev.Lett.*, 103:021802, 2009.

[55] G.F. Farrar, R. Mackeprang, D. Milstead, and J.P. Roberts. Limit on the mass of a long-lived or stable gluino. 2010. * Temporary entry *.

[56] CMS Collaboration. Search for Heavy Stable Charged Particles in pp collisions at $\sqrt{(s)} = 7$ TeV. 2011. * Temporary entry *.

[57] The CMS Collaboration. Search for Stopped Gluinos in pp collisions at $\sqrt{s} =$ 7 TeV. *Phys.Rev.Lett.*, 106:011801, 2011.

[58] ATLAS collaboration. Search for Heavy Long-Lived Charged Particles with the ATLAS detector in pp collisions at sqrt(s) = 7 TeV. *Phys. Lett.*, B703:428–446, 2011.

[59] The CMS Collaboration. Search for heavy stable charged particles. *CMS conference note*, CMS-PAS-EXO-11-022, 2011.

[60] The CDF Collaboration. Search for Long-Lived Massive Charged Particles in 1.96 TeV $\bar{p}p$ Collisions. *Phys. Rev. Lett.*, 103:021802, 2009.

[61] The OPAL Collaboration. Search for stable and long-lived massive charged particles in e+ e- collisions at s**(1/2) = 130-GeV to 209-GeV. *Phys. Lett.*, B572:8–20, 2003.

[62] The L3 Collaboration. Search for heavy neutral and charged leptons in $e^+e^-$ annihilation at LEP. *Phys. Lett.*, B517:75–85, 2001.

[63] The ALEPH Collaboration. Search for gauge mediated SUSY breaking topologies in $e^+e^-$ collisions at center-of-mass energies up to 209-GeV. *Eur. Phys. J.*, C25:339–351, 2002.

[64] The DELPHI Collaboration. Search for supersymmetric particles in light gravitino scenarios and sleptons NLSP. *Eur. Phys. J.*, C27:153–172, 2003.

[65] The OPAL Collaboration. Searches for gauge-mediated supersymmetry breaking topologies in e+ e- collisions at LEP2. *Eur. Phys. J.*, C46:307–341, 2006.

[66] The ALEPH Collaboration. Search for charginos nearly mass degenerate with the lightest neutralino in e+ e- collisions at centre-of-mass energies up to 209-GeV. *Phys. Lett.*, B533:223–236, 2002.

[67] The DELPHI Collaboration. Search for charginos nearly mass-degenerate with the lightest neutralino. *Eur. Phys. J.*, C11:1–17, 1999.

[68] The L3 Collaboration. Search for charginos with a small mass difference with the lightest supersymmetric particle at $\sqrt{s}$ = 189 GeV. *Phys. Lett.*, B482:31–42, 2000.

[69] K. Kinoshita et. al. Search for highly ionizing particles in $e^+e^-$ annihilations at $\sqrt{s} = 91.1\ GeV$. *Phys. Rev. D*, 46:881, 1992.

[70] J. Pinfold et. al. A search for highly ionizing particles produced at the OPAL intersection point at LEP. *Phys. Lett. B*, 316:407–411, 1993.

[71] D. Javorsek, D. Elmore, E. Fischbach, D. Granger, T. Miller, D. Oliver, and V. Teplitz. Search for anomalously heavy nuclei in gold and iron. *Phys. Rev. D*, 65:072003, Apr 2002.

[72] T. K. Hemmick, D. Elmore, T. Gentile, P. W. Kubik, S. L. Olsen, D. Ciampa, D. Nitz, H. Kagan, P. Haas, P. F. Smith, B. B. McInteer, and J. Bigeleisen. Search for low-$z$ nuclei containing massive stable particles. *Phys. Rev. D*, 41:2074–2080, Apr 1990.

[73] S. Dimopoulos, D. Eichler, R. Esmailzadeh, and G.D. Starkman. Getting a charge out of dark matter. *Phys. Rev. D*, 41:2388–2397, Apr 1990.

[74] A. Arvanitaki, C. Davis, P.W. Graham, A. Pierce, and J.G. Wacker. Limits on split supersymmetry from gluino cosmology. *Phys. Rev. D*, 72:075011, Oct 2005.

[75] A. Arvanitaki, S. Dimopoulos, A. Pierce, S. Rajendran, and Jay G. Wacker. Stopping gluinos. *Phys. Rev.*, D76:055007, 2007.

[76] The D0 Collaboration. Search for stopped gluinos from $p\bar{p}$ collisions at $\sqrt{s}$ = 1.96-TeV. *Phys. Rev. Lett.*, 99:131801, 2007.

[77] R. K. Bock and A. Vasilescu. *The particle detector briefbook*. Springer, 1998.

[78] The ATLAS Collaboration. Expected Performance of the ATLAS Experiment - Detector, Trigger and Physics. 2009.

[79] Y. R. de Boer, A. B. Kaidalov, D. A. Milstead, and O. I. Piskounova. Interactions of Heavy Hadrons using Regge Phenomenology and the Quark Gluon String Model. *J. Phys.*, G35:075009, 2008.

[80] W. Kilian, T. Plehn, P. Richardson, and E. Schmidt. Split supersymmetry at colliders. *Eur. Phys. J.*, C39:229–243, 2005.

[81] G. R. Farrar and P. Fayet. Phenomenology of the Production, Decay, and Detection of New Hadronic States Associated with Supersymmetry. *Phys. Lett.*, B76:575–579, 1978.

[82] M. S. Chanowitz and S. R. Sharpe. Spectrum of gluino bound states. *Phys. Lett.*, B126:225, 1983.

[83] G. R. Farrar. Light gluinos. *Phys. Rev. Lett.*, 53:1029, 1984.

[84] P. D. B. Collins. Regge theory and particle physics. *Phys. Rept.*, 1:103–234, 1971.

[85] P. D. B. Collins. *An Introduction to Regge theory and high-energy physics*. Cambridge Univesity Press, 1977.

[86] L. Evans and P. Bryant (editors). LHC machine. *JINST*, 3:S08001, 2008.

[87] The ALICE Collaboration. The ALICE experiment at the CERN LHC. *JINST*, 3:S08002, 2008.

[88] The ATLAS Collaboration. The ATLAS Experiment at the CERN Large Hadron Collider. *JINST*, 3:S08003, 2008.

[89] The CMS Collaboration. The CMS experiment at the CERN LHC. *JINST*, 3:S08004, 2008.

[90] The LHCb Collaboration. The LHCb detector at the LHC. *JINST*, 3:S08005, 2008.

[91] P. Jenni, M. Nessi, M. Nordberg, and K. Smith. *ATLAS high-level trigger, data-acquisition and controls: Technical Design Report*. Technical Design Report ATLAS. CERN, Geneva, 2003.

[92] E. V. Shuryak. The QCD vacuum, hadrons and the superdense matter. *"World Sci. Lect. Notes Phys."*, 71:1–618, 2004.

[93] P. Collier. Standard filling schemes for various lhc operation modes. Technical report, CERN, 2004. Engineering specification, LHC project document no. LHC-OP-ES-0003 rev 1.0.

[94] K. Schindl. The injector chain for the LHC. Technical Report CERN-OPEN-99-052, CERN, Jan 1999.

[95] The ATLAS Collaboration. ATLAS Inner Detector Technical Design Report, volume 1 & 2. Technical Report LHCC/97-16, LHCC/97-17, CERN, 30 April 1997.

[96] The LAr Calorimeter Collaboration. ATLAS Liquid Argon Calorimeter Technical Design Report. Technical Report LHCC 96-41, CERN, 15 December 1996.

[97] The Tile Calorimeter Collaboration. ATLAS Tile Calorimeter Technical Design Report. Technical Report LHCC 96-42, CERN, 15 December 1996.

[98] The ATLAS Collaboration. ATLAS Muon Spectrometer Technical Design Report. Technical Report LHCC/97-22, CERN, 5 June 1997.

[99] The ATLAS Collaboration. Expected performance of the atlas experiment: detector, trigger and physics. Technical Report arXiv:0901.0512. CERN-OPEN-2008-020, CERN, Geneva, 2009.

[100] The ATLAS Collaboration. dE/dx measurement in the ATLAS Pixel detector and its use for particle identification. Technical Report ATLAS-CONF-2011-016, CERN, Geneva, Mar 2011.

[101] E. Abat *et al.* The ATLAS TRT electronics. *JINST*, 3:P06007, 2008.

[102] The ATLAS Collaboration. Response and Shower Topology of 2 to 180 GeV Pions Measured with the ATLAS Barrel Calorimeter at the CERN Test-beam and Comparison to Monte Carlo Simulations. Technical Report ATL-CAL-PUB-2010-001, CERN, 2010.

[103] K.-J. Grahn. ATLAS Calorimetry: Hadronic Calibration Studies. *Licentiate thesis, http://urn.kb.se/resolve?urn=urn:nbn:se:kth:diva-9423*, 2008.

[104] The ATLAS electromagnetic barrel calorimeter collaboration. Energy linearity and resolution of the atlas electromagnetic barrel calorimeter in an electron test-beam. *Nuclear Instruments and Methods in Physics Research Section A: Accelerators, Spectrometers, Detectors and Associated Equipment*, 568(2):601 – 623, 2006.

[105] The ATLAS Collaboration. ATLAS First-Level Trigger: Technical design report. 1998.

[106] T. Pauly *et al.* ATLAS Level-1 trigger timing-in strategies. Technical Report ATL-DAQ-CONF-2005-035. ATL-COM-DAQ-2005-036. CERN-ATL-DAQ-CONF-2005-035, CERN, 2005.

[107] Z. Guzik and R. Jacobsson. Proposal for a beam phase and intensity monitor for the LHCb experiment. Technical Report LHCb-2006-055. CERN-LHCb-2006-055, CERN, 2006. Prepared for 12th Workshop on Electronics for LHC and Future Experiments (LECC 2006), Valencia, Spain, 25-29 Sep 2006.

[108] A. C. Kraan, J. B. Hansen, and P. Nevski. Discovery potential of R-hadrons with the ATLAS detector. *Eur. Phys. J.*, C49:623–640, 2007.

[109] S. Hellman et al. Mass measurements of R-hadrons at ATLAS. *ATL-PHYS-PUB-2006-005*, 2006.

[110] R. Leitner et al. Time resolution of the ATLAS Tile calorimeter and its performance for a measurement of heavy stable particles. *ATL-TILECAL-PUB-2007-002*, 2007.

[111] S. Hellman, D. Milstead, and M. Ramstedt. A strategy to detect and identify gluino *R*-hadrons with the ATLAS experiment at the LHC. *ATL-PHYS-PUB-2006-005*, 2006.

[112] S. Tarem, S. Bressler, H. Nomoto, and A. Di Mattia. Trigger and reconstruction for heavy long-lived charged particles with the ATLAS detector. *Eur. Phys. J.*, C62:281–292, 2009.

[113] G. Aad et al. ATLAS Pixel detector electronics and sensors. *JINST*, 3:P07007, 2008.

[114] S Meroli, D Passeri, and L Servoli. Energy loss measurement for charged particles in very thin silicon layers. *Journal of Instrumentation*, 6(06):P06013, 2011.

[115] J. Poveda. Energy reconstruction in the hadronic Tile calorimeter and early SUSY fully hadronic searches in ATLAS. *University of Valencia,CERN-THESIS-2008-094*, 2008.

[116] M. Volpi et al. Time inter-calibration of the TileCal/ATLAS hadronic calorimeter with the first LHC beam data. *ATL-TILECAL-PUB-2009-008*, 2009.

[117] T. Del Prete and I Vivarelli. The timing of the Tile Calorimeter using laser events. *ATL-TILECAL-2003-009*, 2003.

[118] B. Meirose and R.J. Teuscher. Time of flight analysis using cosmic ray muons in the ATLAS Tile Calorimeter. *ATL-TILECAL-PUB-2008-004*, 2008.

[119] C. Ohm and T. Pauly. The atlas beam pick-up based timing system. *Nuclear Instruments and Methods in Physics Research Section A: Accelerators, Spectrometers, Detectors and Associated Equipment*, 623(1):558 – 560, 2010. 1st International Conference on Technology and Instrumentation in Particle Physics.

[120] S. Frixione and B. R. Webber. The MC@NLO 3.3 event generator. 2006.

[121] GEANT4 Collaboration. GEANT4: A simulation toolkit. *Nucl. Instrum. Meth.*, A506:250–303, 2003.

[122] B. Andersson, G. Gustafson, G. Ingelman, and T. Sjostrand. Parton gragmentation and string dynamics. *Phys. Rept.*, 97:31–145, 1983.

[123] W. Beenakker, R. Hopker, and M. Spira. PROSPINO: A Program for the production of supersymmetric particles in next-to-leading order QCD. 1996.

[124] Pavel M. Nadolsky, Hung-Liang Lai, Qing-Hong Cao, Joey Huston, Jon Pumplin, et al. Implications of CTEQ global analysis for collider observables. *Phys.Rev.*, D78:013004, 2008.

[125] JoAnne L. Hewett, Ben Lillie, Manuel Masip, and Thomas G. Rizzo. Signatures of long-lived gluinos in split supersymmetry. *JHEP*, 09:070, 2004.

[126] W Lampl, S Laplace, D Lelas, P Loch, H Ma, S Menke, S Rajagopalan, D Rousseau, S Snyder, and G Unal. Calorimeter clustering algorithms: Description and performance. Technical Report ATL-LARG-PUB-2008-002. ATL-COM-LARG-2008-003, CERN, Geneva, Apr 2008.

[127] M. Cacciari, G. P. Salam, and G. Soyez. The anti-$k_t$ jet clustering algorithm. *JHEP*, 0804:063, 2008.

[128] M Simonyan. Hadron response and shower development in the atlas calorimeters. Technical Report ATL-CAL-PROC-2010-001, CERN, Geneva, Aug 2010.

[129] I Aracena et al. The ATLAS missing-$E_T$ trigger performance with initial LHC runs at $\sqrt(s) = 7$ TeV. Technical Report ATL-COM-DAQ-2010-191, CERN, Geneva, Oct 2010.

[130] The ATLAS Collaboration. Response and shower topology of 2 to 180 GeV pions measured with the ATLAS barrel calorimeter at the CERN test-beam and comparison to Monte Carlo simulations. *ATL-CAL-PUB-2010-001*, 2010.

[131] The ATLAS Collaboration. Luminosity determination using the atlas detector. Technical Report ATLAS-CONF-2010-060, CERN, Geneva, Jul 2010.

[132] T. Plehn, D. Rainwater, and Peter Z. Skands. Squark and gluino production with jets. *Phys.Lett.*, B645:217–221, 2007.

[133] The ATLAS Collaboration. Measurements of multijet production cross sections in proton-proton collisions at 7 TeV center-of-mass energy with the ATLAS Detector. *ATLAS-CONF-2010-084*, 2010.

[134] A.D. Martin, W.J. Stirling, R.S. Thorne, and G. Watt. Parton distributions for the LHC. *Eur.Phys.J.*, C63:189–285, 2009.

[135] A L Read. Modified frequentist analysis of search results (the $cl_s$ method). Technical Report CERN-OPEN-2000-205, CERN, 2000.

[136] Gary J. Feldman and Robert D. Cousins. Unified approach to the classical statistical analysis of small signals. *Phys. Rev. D*, 57:3873–3889, Apr 1998.

[137] S. Cecchini et al. Results of the Search for Strange Quark Matter and Q-balls with the SLIM Experiment. *Eur. Phys. J.*, C57:525–533, 2008.

[138] J.L. Pinfold, R. Du, K. Kinoshita, B. Lorazo, B. Price and M. Regimbald. A search for highly ionizing particles produced at the OPAL intersection point at LEP. *Phys. Lett. B*, 316:407, 1993.

[139] The OPAL Collaboration. Search for Dirac magnetic monopoles in $e^+e^-$ collisions with the OPAL detector at LEP2. *Phys. Lett. B*, 663:37, 2008.

[140] K. Kinoshita, R. Du, G. Giacomelli, L. Patrizii, F. Predieri, P. Serra, M. Spurio, and J.L. Pinfold. Search for highly ionizing particles in $e^+e^-$ annigilations at $\sqrt{s} = 91.1$ GeV. *Phys. Rev. D*, 46:R881, 1992.

[141] P.B. Price, R. Guoxiao and K. Kinoshita. Search for Highly Ionizing Particles at the Fermilab Proton-Antiproton Collider. *Phys. Rev. Lett.*, 59:2523, 1987.

[142] P.B. Price, J. Guiru and K. Kinoshita. High-luminosity search for highly ionizing particles at the Fermilab collider. *Phys. Rev. Lett.*, 65:149, 1990.

[143] M. Bertani *et al.* Search for Magnetic Monopoles at the Tevatron Collider. *Europh. Lett.*, 12:613, 1990.

[144] The CDF Collaboration. Direct Search for Dirac Magnetic Monopoles in $p\bar{p}$ Collisions at $\sqrt{s} = 1.96$ TeV. *Phys. Rev. Lett.*, 96:201801, 2006.

[145] P. Mermod, R. Mackeprang, D. Milstead, C. Ohm, and A. Penson. Identifying highly ionizing particles with the ATLAS electromagnetic calorimeter. *ATL-LARG-INT-2010-002*, 2010.

[146] J. B. Birks. Theory of the Response of Organic Scintillation Crystals to Short-Range Particles. *Phys. Rev.*, 86:569, 1952.

[147] S. Amoruso *et al.* Study of electron combination in liquid argon with the ICARUS TPC. *Nucl. Instrum. Meth. A*, 523:275, 2004.

[148] E. Shibamura *et al.* Ionization and Scintillation Produced by Relativistic Au, He and H Ions in Liquid Argon. *Nucl. Instrum. Meth. A*, 260:437, 1987.

[149] T. Doke *et al.* Scintillation Yields by Relativistic heavy Ions and the Relation Between Ionization and Scintillation in Liquid Argon. *Nucl. Instrum. Meth. A*, 235:136, 1985.

[150] H.J. Crawford *et al.* Ionization and Scintillation Signals Produced by Relativistic La Ions in Liquid Argon. *Nucl. Instrum. Meth. A*, 256:47, 1987.

[151] The ATLAS Collaboration. Performance of the electron and photon trigger in p-p collisions at a centre of mass energy of 900 gev. Technical Report ATLAS-CONF-2010-022, CERN, Geneva, Jul 2010.

[152] The ATLAS Collaboration. Commissioning of atlas electron and photon trigger selection. *Journal of Physics: Conference Series*, 293(1):012027, 2011.

[153] The ATLAS Collaboration. Electron and photon reconstruction and identification in ATLAS: expected performance at high energy and results at 900 GeV. Technical Report ATLAS-CONF-2010-005, CERN, Geneva, Jun 2010.

[154] R Achenbach *et al.* The ATLAS Level-1 Calorimeter Trigger . *JINST*, 3:P03001, 2008.

[155] D R Hadley. Digital filtering performance in the atlas level-1 calorimeter trigger: Rt2010 proceedings draft. Technical Report ATL-COM-DAQ-2010-070, CERN, Geneva, May 2010. Proceedings deadline is : 28th May 2010.

[156] J. Heinrich, C. Blocker, Conway, L. J., Demortier, L. Lyons, G. Punzi, and P. K. Sinervo. Interval estimation in the presence of nuisance parameters. 2004.

[157] T. Kittelmann, V. Tsulaia, J. Boudreau, and E. Moyse. The virtual point 1 event display for the atlas experiment. *Journal of Physics: Conference Series*, 219(3):032012, 2010.

Physics Letters B 701 (2011) 1–19

Contents lists available at ScienceDirect

Physics Letters B

www.elsevier.com/locate/physletb

# Search for stable hadronising squarks and gluinos with the ATLAS experiment at the LHC ☆

ATLAS Collaboration *

ARTICLE INFO

*Article history:*
Received 10 March 2011
Received in revised form 5 May 2011
Accepted 5 May 2011
Available online 13 May 2011
Editor: H. Weerts

*Keywords:*
Supersymmetry
Long-lived particle
*R*-hadron
Limit

ABSTRACT

Hitherto unobserved long-lived massive particles with electric and/or colour charge are predicted by a range of theories which extend the Standard Model. In this Letter a search is performed at the ATLAS experiment for slow-moving charged particles produced in proton–proton collisions at 7 TeV centre-of-mass energy at the LHC, using a data-set corresponding to an integrated luminosity of 34 $pb^{-1}$. No deviations from Standard Model expectations are found. This result is interpreted in a framework of supersymmetry models in which coloured sparticles can hadronise into long-lived bound hadronic states, termed *R*-hadrons, and 95% CL limits are set on the production cross-sections of squarks and gluinos. The influence of *R*-hadron interactions in matter was studied using a number of different models, and lower mass limits for stable sbottoms and stops are found to be 294 and 309 GeV respectively. The lower mass limit for a stable gluino lies in the range from 562 to 586 GeV depending on the model assumed. Each of these constraints is the most stringent to date.



## 1. Introduction

The discovery of exotic stable massive particles (SMPs)[1] at the LHC would be of fundamental significance. The motivation for SMP searches at ATLAS arises, for example, from proposed solutions to the gauge hierarchy problem, which involve previously unseen particles with TeV-scale masses [1,2]. The ATLAS experiment has recently searched for SMPs with large electric charge [3]. SMPs possessing colour charge represent another class of exotic particle which can be sought. Hadronising SMPs are anticipated in a wide range of exotic physics models [1] that extend the Standard Model (SM). For example, these particles appear in both *R*-parity conserving supersymmetry (SUSY) and universal extra dimensions. The possibility of direct pair production through the strong nuclear force implies large production cross-sections. Searches for these particles are thus an important component of the early data exploitation programs of the LHC experiments [4]. In this Letter, the first limits from the ATLAS experiment are presented on the production of coloured, hadronising SMPs in proton–proton collisions at 7 TeV centre-of-mass energy at the LHC. Results are presented in the context of SUSY models predicting the existence of *R*-hadrons [5], which are heavy objects formed from a coloured sparticle (squark or gluino) and light SM partons.

SMPs produced at LHC energies typically possess the following characteristics: they are penetrating[2] and propagate at a low enough speed that they can be observed as being subluminal using measurements of time-of-flight and specific ionisation energy loss [1]. Previous searches for *R*-hadrons have typically been based on either the signature of a highly ionising particle in an inner tracking system [7–9] or a slow-moving muon-like object [9–11]. The latter limits rely on the assumption that the *R*-hadron is electrically charged when it leaves the calorimeter and can thus be detected in an outer muon system. However, hadronic scattering of *R*-hadrons in the dense calorimeter material, and the properties of different mass hierarchies for the *R*-hadrons, may render most of the produced *R*-hadrons electrically neutral in the muon system [12]. Such an effect is expected for *R*-hadrons formed from sbottom-like squarks [13]; the situation for gluino-based *R*-hadrons is unclear, with different models giving rise to different phenomenologies. The previous mass limit for gluino *R*-hadrons with minimal sensitivity to scattering uncertainties is 311 GeV at 95% confidence level [9] from the CMS Collaboration.

☆ © CERN, for the benefit of the ATLAS Collaboration.

* *E-mail address:* atlas.publications@cern.ch.

[1] The term stable is taken in this Letter to mean that the particle has a decay length comparable to the size of the ATLAS detector or longer.

[2] A small fraction of SMPs can be brought to rest by interactions in the detector. Should they have finite lifetimes an alternative approach to the direct detection of SMPs would be to observe their decays [6].

0370-2693/
doi:10.1016/j.physletb.2011.05.010

The ATLAS detector contains a number of subsystems which provide information which can be used to distinguish SMPs from particles moving at velocities close to the speed of light. Two complementary subsystems used in this work are the pixel detector, which measures ionisation energy loss ($\mathrm{d}E/\mathrm{d}x$), and the tile calorimeter, which measures the time-of-flight from the interaction point for particles which traverse it. Furthermore, since there is no requirement that a candidate be reconstructed in the outer muon spectrometer, the search is robust to theoretical uncertainties on the fraction of $R$-hadrons that are charged when leaving the calorimeter system. The analysis extends the mass limits beyond already published limits and represents the first dedicated direct search for sbottom $R$-hadrons at a hadron collider.

## 2. Simulation of $R$-hadrons and background processes

Monte Carlo simulations are used primarily to determine the efficiency of the $R$-hadron selection together with the associated systematic uncertainties. Predicted backgrounds are estimated using data, as described in Section 4. However, simulated samples of background processes (QCD and $t\bar{t}$, $W$ and $Z$ production) are used to optimise the $R$-hadron selections, without biasing the selection in data.

Pair production of $\tilde{g}\tilde{g}$, $\tilde{t}\bar{\tilde{t}}$ and $\tilde{b}\bar{\tilde{b}}$ is simulated in Pythia [14] using the DW tune [15,16]. The string hadronisation model [17], incorporating specialised hadronisation routines [1] is used to produce final states containing $R$-hadrons. For gluino scenarios the probability for a gluino to form a gluon–gluino bound state, based on a colour octet model, is assumed to be 10% [1]. The simulation of $R$-hadron interactions in matter is handled by dedicated Geant4 routines [18,19] based on three different models with alternative assumptions. $R$-hadrons containing squarks are simulated using the model described in Ref. [13]. This model is motivated by extrapolations from SM heavy quark hadron spectra. It furthermore employs a triple-Regge formalism to describe hadronic scattering. For gluino $R$-hadrons there are less strict theoretical constraints since no SM analogue exists for a heavy colour octet. Consequently a physics model is chosen, as described in Refs. [20,21]. This model has been used in other publications [6,9,22] and it imposes few constraints on allowed stable states. Doubly charged $R$-hadrons and a wide variety of charge reversal signatures in the detector are possible. Hadronic scattering is described through a purely phase space driven approach. More recent models for the hadronic scattering of gluino $R$-hadrons predict that the majority of all produced $R$-hadrons will be electrically neutral after just a few hadronic interactions. One of these models is an extension of the triple-Regge model used to describe squark $R$-hadrons [12]. Another is the bag-model based calculation presented in Ref. [23]. Independent results for gluino $R$-hadrons are presented here for these models.

The simulated samples have gluino (squark) masses in the range 100–700 GeV (100–500 GeV), roughly matching the sensitivity that can be achieved given the statistical precision of the data sample on which the present analysis is based. The cross-sections of the individual samples are normalised to the predictions of the Prospino NLO program [24] using CTEQ 6.6 parton density functions (PDFs) [25]. All other sparticles are set to high mass and are decoupled from the calculations used in this work.

## 3. The ATLAS detector

The ATLAS detector is described in detail in Ref. [26]. Below, some features of the subsystems most important for the present analysis are outlined.

### 3.1. Specific energy loss from the pixel detector

As the innermost sub-detector in ATLAS, the silicon-based pixel detector contributes to precision tracking in the region[3] $|\eta| < 2.5$. The sensitive detectors of the pixel detector barrel are placed on three concentric cylinders around the beam-line, whereas each end-cap consists of three disks arranged perpendicular to the beam axis. The pixel detector therefore typically provides at least three measurements for each track. In the barrel (end-cap) the intrinsic accuracy is 10 μm in the $r$–$\phi$ plane and 115 μm in the $z$ ($r$)-direction. The integrated time during which a signal exceeds threshold has a sub-linear dependence on the charge deposited in each pixel. This has been measured in dedicated calibration scans, enabling an energy loss measurement for charged particles using the pixel detector.

The charge released by a track crossing the pixel detector is rarely contained within just one pixel. Neighbouring pixels are joined together to form clusters, and the charge of a cluster is calculated by summing up the charges of all pixels after applying a calibration correction. The specific energy loss, $\mathrm{d}E/\mathrm{d}x$, is estimated as an average of the individual cluster $\mathrm{d}E/\mathrm{d}x$ measurements (charge collected in the cluster, corrected for the track length in the sensor), for the clusters associated with the track. To reduce the effects of the Landau tail, the $\mathrm{d}E/\mathrm{d}x$ of the track is calculated as the truncated mean of the individual cluster measurements. In the study presented here at least two clusters are required for the pixel detector $\mathrm{d}E/\mathrm{d}x$ measurement ($\mathrm{d}E/\mathrm{d}x_{\mathrm{Pixel}}$). Further details and performance of the method are described in [27].

### 3.2. Time-of-flight from the tile calorimeter

The ATLAS tile calorimeter is a sampling calorimeter that constitutes the barrel part of the hadronic calorimetry in ATLAS. It is situated in the region $2.3 < r < 4.3$ m, covering $|\eta| \lesssim 1.7$, and uses iron as the passive material and plastic scintillators as active layers. Along the beam axis, the tile calorimeter is logically subdivided into four partitions, each segmented in equal intervals of azimuthal angle ($\phi$) into 64 modules. The modules are further divided into cells, which are grouped radially in three layers, covering 0.1 units in $\eta$ in the first two layers and 0.2 in the third. Two bundles of wavelength-shifting fibres, associated with each cell, guide the scintillation light from the exposed sides of the module to photomultiplier tubes. The signal from each photomultiplier tube is digitised using dual ADCs covering different dynamic ranges. Analysing seven consecutive samplings with an interval of 25 ns allows the amplitude, pedestal value and peak position in time to be extracted. The tile calorimeter provides a timing resolution of 1–2 ns per cell for energy deposits typical of minimum-ionising particles (MIPs). The measured times have been corrected for drifts in the LHC clock using high-precision timing measurements from a beam pick-up system [28] and calibrated such that energy depositions associated with muons from $Z$-boson decays are aligned at $t = 0$ in both data and simulations.

Although the readout electronics have been optimised to provide the best possible timing resolution for $\beta = 1$ particles, the performance for slower particles ($0.3 < \beta < 1$) is not seriously compromised. In addition, SMPs tend to traverse the entire tile calorimeter, leaving statistically independent signals in up to six cells.

[3] ATLAS uses a right-handed coordinate system with its origin at the nominal interaction point (IP) in the centre of the detector and the $z$-axis along the beam pipe. The $x$-axis points from the IP to the centre of the LHC ring, and the $y$-axis points upward. Cylindrical coordinates $(r, \phi)$ are used in the transverse plane, $\phi$ being the azimuthal angle around the beam pipe. The pseudorapidity is defined in terms of the polar angle $\theta$ as $\eta = -\ln\tan(\theta/2)$.

**Table 1**
Observed and expected event yields at different steps of the data selection procedure. The individual rows of the table correspond to the stages in the cut flow as defined in the text. The rows denoted *Mass preselection* and *Final selection* indicate the number of events having at least one candidate with a mass estimate from both subsystems and passing the final mass cuts, respectively. These selections are defined in Section 5. In addition to data and background, predictions from the signal simulations are shown. Predicted yields are scaled to the integrated luminosity of the data sample.

| Cut level | Data | Background | 300 GeV $\tilde{g}$ | 500 GeV $\tilde{g}$ | 600 GeV $\tilde{g}$ | 200 GeV $\tilde{t}$ | 200 GeV $\tilde{b}$ |
|---|---|---|---|---|---|---|---|
| No cuts | – | – | $2.13 \times 10^3$ | 80.4 | 21.8 | 405 | 405 |
| Trigger | – | – | 616 | 25.6 | 6.96 | 109 | 108 |
| Candidate particle | 75 466 | $68.0 \times 10^3$ | 416 | 17.6 | 4.80 | 87.4 | 67.9 |
| Vertex | 75 461 | $68.0 \times 10^3$ | 416 | 17.6 | 4.80 | 87.4 | 67.9 |
| $\lvert\eta\rvert < 1.7$ | 64 618 | $60.5 \times 10^3$ | 364 | 15.7 | 4.32 | 75.2 | 56.8 |
| Track quality | 59 872 | $58.1 \times 10^3$ | 355 | 15.3 | 4.20 | 73.3 | 54.9 |
| $\Delta R > 0.5$ | 49 205 | $49.4 \times 10^3$ | 349 | 15.1 | 4.13 | 72.7 | 54.5 |
| $p_T > 50$ GeV | 5116 | $6.56 \times 10^3$ | 330 | 14.5 | 3.95 | 68.9 | 50.0 |
| Mass preselection | 36 | 56.0 | 184 | 9.70 | 2.75 | 32.6 | 18.9 |
| Final selection | – | – | 173 | 9.17 | 2.62 | 30.6 | 17.5 |

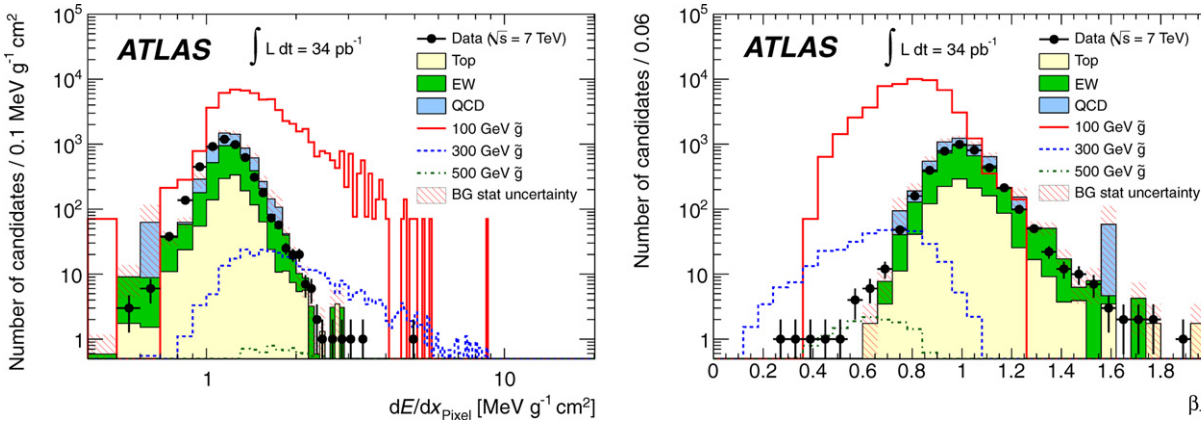


**Fig. 1.** Distributions of $dE/dx_{Pixel}$ (left) and $\beta_{Tile}$ (right) in data after the transverse momentum selection $p_T > 50$ GeV. Spectra for simulated background processes are plotted for comparison. The uncertainty shown on the background is the Monte Carlo statistical uncertainty.

The time-of-flight and hence the speed, $\beta$, of an $R$-hadron candidate can be deduced from time measurements in the tile calorimeter cells along the candidate trajectory. All cells along the particle trajectory with an energy deposition larger than 500 MeV are used to make an independent estimate of $\beta$. The time resolution has been shown to improve with the energy measured in the cell [29], so the cells are combined using an average weighted by cell energy to get a velocity measurement ($\beta_{Tile}$). Combining the measurements from all cells results in a time resolution of $\sim 1$ ns.

## 4. Event selection

The data sample used in this work corresponds to an integrated luminosity of 34 pb$^{-1}$. Final states with $R$-hadrons can also contain jets and missing transverse energy ($E_T^{miss}$) arising from QCD radiation which can be used to select candidate events. Due to the large cross-section for jet production at the LHC, triggering on jets with low transverse energy is not feasible. A superior trigger efficiency for the signal is obtained by using a trigger on missing transverse energy utilising only calorimeter information [30] (a full description of the ATLAS trigger system is given in [26]). Using an $E_T^{miss}$-based trigger is possible since $R$-hadrons would typically deposit only a small fraction of their energy as they propagate through the ATLAS calorimeters. The trigger threshold applied is $E_T^{miss} = 40$ GeV which gives an efficiency ranging from approximately 15% for a gluino-mass of 100 GeV to 32% for a 600 GeV mass. The missing transverse energy trigger is based on a level-1 trigger decision derived from coarsely segmented energy measurements, followed by a decision at the higher-level trigger based on the full granularity of the ATLAS calorimeter.

### 4.1. Selection of R-hadron candidates

Table 1 shows the cut flow of the analysis. After the trigger selection, each event is required to contain a track with a transverse momentum greater than 10 GeV. This track must be matched either to a muon reconstructed in the muon spectrometer or to a cluster in the tile calorimeter. The track is required to have MIP-compatible energy depositions in the calorimeter. Such an event is referred to in the table as a *candidate event*. Each event is required to contain at least one good primary vertex, to which at least three tracks are associated. Only tracks in the central region ($|\eta| < 1.7$) are considered. This matches the acceptance of the tile calorimeter. To ensure well measured kinematics, track quality requirements are made: the track must have at least two hits in the pixel detector, at least six hits in the silicon-strip Semiconductor Tracker, and at least six associated hits in the Transition Radiation Tracker (TRT). Jet objects are reconstructed using the anti-$k_t$ jet clustering algorithm [31,32] with a distance parameter of 0.4. In order to suppress backgrounds from jet production, the distance in $\eta$–$\phi$ space between the candidate and any jet with $E_T \geqslant 40$ GeV must be greater than $\Delta R = \sqrt{(\Delta\eta)^2 + (\Delta\phi)^2} = 0.5$. Finally, the measured transverse momentum of the candidate must be greater than 50 GeV.

After the selection, 5208 candidate particles in 5116 events are observed. Fig. 1 shows the $dE/dx_{Pixel}$ and $\beta_{Tile}$ distributions for these candidates together with background simulations. As can be seen, the $\beta_{Tile}$ measurements are centred around one. The width of the distribution, as determined by a Gaussian fit around the bulk of the data, is $\sim 0.1$. Reasonable agreement between data and the background simulations is observed, although the latter calcula-

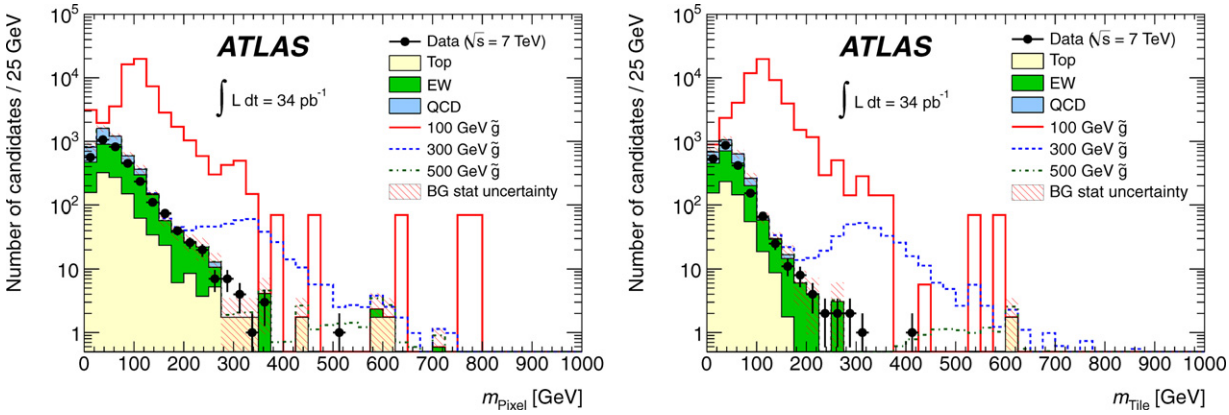


**Fig. 2.** Mass estimated by the pixel detector (left) and the tile calorimeter (right). To obtain a mass estimate, a cut of $\mathrm{d}E/\mathrm{d}x_{\mathrm{Pixel}} > 1.1$ MeV g$^{-1}$ cm$^2$ is imposed for the pixel detector distribution. This is a looser cut than used in the analysis itself. For the tile calorimeter, the requirement is that $\beta_{\mathrm{Tile}} < 1$.

tions are not used in any quantitative way in the analysis. The expected distributions for signal particles are overlaid and scaled to the luminosity of the data by their production cross-section, illustrating the sensitivity of these observables to $R$-hadrons.

## 5. Mass reconstruction

For each candidate, the mass is estimated by dividing its momentum by $\beta\gamma$, determined either from pixel detector ionisation or from the tile calorimeter time-of-flight. In the pixel detector, the following simplified Bethe–Bloch equation gives a good description of the relation between the most probable value ($\mathcal{M}_{\frac{\mathrm{d}E}{\mathrm{d}x}}$) of $\mathrm{d}E/\mathrm{d}x_{\mathrm{Pixel}}$ and $\beta\gamma$ in the range relevant to this analysis ($0.2 < \beta\gamma < 1.5$):

$$\mathcal{M}_{\frac{\mathrm{d}E}{\mathrm{d}x}}(\beta) = \frac{p_1}{\beta^{p_3}} \ln\left(1 + (p_2\beta\gamma)^{p_5}\right) - p_4 \qquad (1)$$

To find $\beta$, and hence a mass estimate, this equation must be solved for $\beta$, identifying the measured $\mathrm{d}E/\mathrm{d}x_{\mathrm{Pixel}}$ with $\mathcal{M}_{\frac{\mathrm{d}E}{\mathrm{d}x}}$. This requires the $\mathrm{d}E/\mathrm{d}x_{\mathrm{Pixel}}$ value to be above that of a MIP. The parameters $p_1$–$p_5$ in Eq. (1) are determined from fits to SM particles with well-known masses and ionisation properties, $p$, $K$ and $\pi$ [27], and provide a relative $\mathrm{d}E/\mathrm{d}x_{\mathrm{Pixel}}$ resolution of about 10% in the asymptotic region ($\beta\gamma > 1.5$). To reduce the backgrounds further, the final selection requires that $\mathrm{d}E/\mathrm{d}x_{\mathrm{Pixel}} > 1.8$ MeV g$^{-1}$ cm$^2$ compared to $\mathrm{d}E/\mathrm{d}x_{\mathrm{Pixel}} \sim 1.1$ MeV g$^{-1}$ cm$^2$ deposited by a MIP. In the tile calorimeter, the $\beta$-values are required to be less than 1.

The pixel detector and the tile calorimeter provide independent measurements from which the mass of the SMP candidate can be estimated. Making requirements on both mass estimates is a powerful means to suppress the tails in the individual distributions arising from instrumental effects. In Fig. 2 the estimated mass distributions based on $\mathrm{d}E/\mathrm{d}x_{\mathrm{Pixel}}$ and $\beta_{\mathrm{Tile}}$ are shown after the 50 GeV transverse momentum cut of the event selection. In contrast to the other figures in this Letter, the signal distributions are stacked on top of the background to illustrate the total expected spectra for the signal + background scenarios.

To establish signal regions for each mass hypothesis, the mean, $\mu$, and Gaussian width, $\sigma$, of the mass peak is determined for both the pixel detector and the tile calorimeter measurement. The signal region is then defined to be the region above the fitted mean minus twice the width (i.e. $m_{\mathrm{Pixel}} > \mu_{\mathrm{Pixel}} - 2\sigma_{\mathrm{Pixel}}$ for the mass as estimated by the pixel detector and $m_{\mathrm{Tile}} > \mu_{\mathrm{Tile}} - 2\sigma_{\mathrm{Tile}}$ for the mass as estimated by the tile calorimeter). The final signal region is defined by applying both of the individual mass requirements.

## 6. Background estimation

Rather than relying on simulations to predict the tails of the $\mathrm{d}E/\mathrm{d}x_{\mathrm{Pixel}}$ and $\beta_{\mathrm{Tile}}$ distributions, a data-driven method is used to estimate the background. No significant correlations between the measurements of momentum, $\mathrm{d}E/\mathrm{d}x_{\mathrm{Pixel}}$, and $\beta_{\mathrm{Tile}}$ are observed. This is exploited to estimate the amount of background arising from instrumental effects. Estimates for the background distributions of the mass estimates are obtained by combining random momentum values (after the kinematic cuts defined above) with random measurements of $\mathrm{d}E/\mathrm{d}x_{\mathrm{Pixel}}$ and $\beta_{\mathrm{Tile}}$. The sampling is performed from candidates passing the kinematic cuts defined in Section 4.1 for the case of $\beta_{\mathrm{Tile}}$, while $\mathrm{d}E/\mathrm{d}x_{\mathrm{Pixel}}$ is extracted from a sample fulfilling $10 < p_T < 20$ GeV.

The sampling process is repeated many times to reduce fluctuations and the resulting estimates are normalised to match the number of events in data. The resulting background estimates can be seen in Fig. 3 for the pixel detector (requiring $\mathrm{d}E/\mathrm{d}x_{\mathrm{Pixel}} > 1.8$ MeV g$^{-1}$ cm$^2$) and the tile calorimeter (requiring $\beta_{\mathrm{Tile}} < 1$) separately. As can be seen from the figures, there is a good overall agreement between the distribution of candidates in data and the background estimate. The expected background at high mass is generally small.

Combining the pixel detector and the tile calorimeter mass estimates as described in Section 5 further reduces the background while retaining most of the expected signal. In contrast to the individual background estimates shown in Fig. 3, the combined background is obtained by combining one random momentum value with random measurements of both $\mathrm{d}E/\mathrm{d}x_{\mathrm{Pixel}}$ and $\beta_{\mathrm{Tile}}$. The agreement between the distribution of candidates in data and the background estimate is good. This is seen in Table 2, which contains the event yields in the signal regions defined in Section 5 for the gluino signal, for the estimated background and for real data. The table also contains the means and the widths of the estimated mass distributions, which are used to determine the signal regions, as described in Section 5. Using combined data, there are no events containing a candidate with mass greater than 100 GeV. There are five candidates observed for the 100 GeV mass hypothesis, for which the mass window extends to values less than 100 GeV.

## 7. Systematic uncertainties and checks

A number of sources of systematic uncertainties are investigated. This section describes uncertainties arising due to the limited accuracy of theory calculations used in this work together with experimental uncertainties affecting the signal efficiency and background estimate.

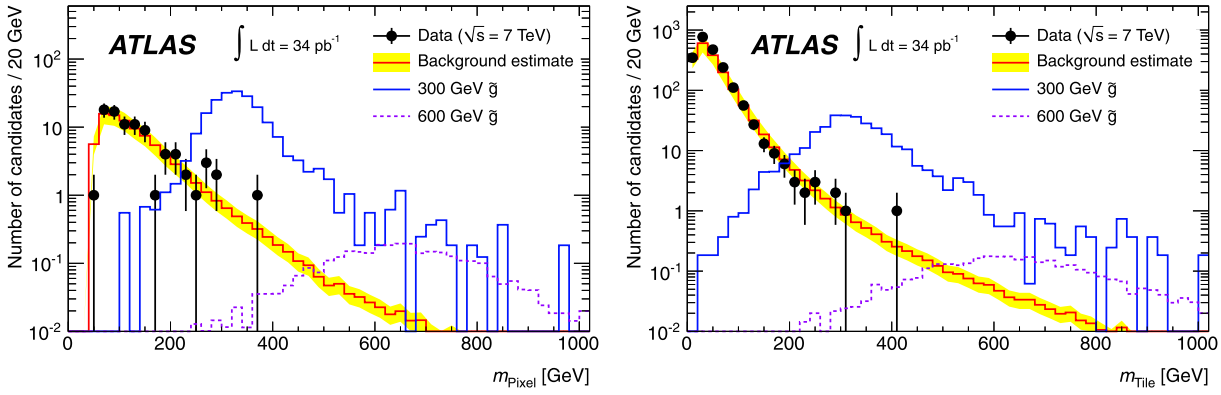


**Fig. 3.** Background estimates for the pixel detector (left) and the tile calorimeter (right). Signal samples are superimposed on the background estimate. The total systematic uncertainty of the background estimate is indicated by the error band.

**Table 2**
Expected number of signal and background events for the pixel detector and the tile calorimeter separately and combined for gluino mass hypotheses between 100 and 700 GeV. The fitted means and widths of the estimated mass distributions are shown on the left. To the right of the vertical line, the number of signal and estimated background events are shown in the relevant signal regions, along with the number of events observed in data. Systematic uncertainties are discussed in Section 7.

| Nominal mass (GeV) | $\mu_{\text{Pixel}}$ (GeV) | $\sigma_{\text{Pixel}}$ (GeV) | $\mu_{\text{Tile}}$ (GeV) | $\sigma_{\text{Tile}}$ (GeV) | No. of signal cand. ($\tilde{g}$) | | | Est. no. of bkg. cand. | | | $N_{\text{Data}}$ Comb. |
|---|---|---|---|---|---|---|---|---|---|---|---|
| | | | | | Pixel | Tile | Comb. | Pixel | Tile | Comb. | |
| 100 | 107 | 10 | 109 | 19 | 15 898 | 49 300 | 13 912 | 61 | 330 | 5.4 | 5 |
| 200 | 214 | 24 | 211 | 36 | 1417 | 2471 | 1235 | 19 | 61 | 0.87 | 0 |
| 300 | 324 | 40 | 315 | 56 | 202 | 304 | 173 | 6.5 | 17 | 0.22 | 0 |
| 400 | 425 | 67 | 415 | 75 | 43 | 57 | 37 | 3.4 | 7.2 | 0.082 | 0 |
| 500 | 533 | 94 | 513 | 106 | 11 | 13 | 9.2 | 1.82 | 4.4 | 0.044 | 0 |
| 600 | 641 | 125 | 624 | 145 | 3.1 | 3.5 | 2.6 | 1.08 | 3.2 | 0.028 | 0 |
| 700 | 727 | 149 | 714 | 168 | 0.99 | 1.07 | 0.84 | 0.74 | 2.1 | 0.018 | 0 |

Uncertainties due to the limited accuracy of perturbative QCD calculations are studied in the following way. The production cross-section from Prospino is calculated using the sparticle mass as the renormalisation scale with uncertainties estimated by varying the renormalisation and factorisation scales upward and downward by a factor of two in accordance with Ref. [24]. This leads to a broadly mass-independent uncertainty of $\sim 15\%$ in the event yield. When substituting the MSTW 2008 NLO PDF set [33] for CTEQ 6.6 a variation of less than 5% is observed. Variations of scale parameters used in Pythia to model higher-order radiation are also performed within the range allowed by data [4]. This leads to an uncertainty of $\sim 10\%$ in the signal efficiency.

A systematic shift in the scale of the missing transverse energy in the simulation of the signal would lead to a change in trigger efficiency and hence signal acceptance. This uncertainty is estimated by varying the missing transverse energy by the corresponding scale uncertainty [34]. The result is an effect of 7–13% on the relative signal efficiency. Based on the difference between the trigger efficiency for data and the simulation for events containing a $W$ boson decaying muonically, a further 3–5% systematic uncertainty is applied. Both of these effects depend on the mass of the signal sample, and the larger uncertainties apply to the low-mass scenarios.

Uncertainties arising from track reconstruction are also studied. To quantify the impact of data/simulation differences in track reconstruction efficiency, a 2% uncertainty on the signal yield is assumed [35]. No further degradation of this efficiency or of the data/simulation agreement is observed for slow particles within the $\beta$ range probed by this analysis [27]. To account for differences in detector alignment between the simulation and data, a smearing is applied to the track $p_{\text{T}}$ which describes the performance observed for high-$p_{\text{T}}$ muons as a function of $\eta$ and $p_{\text{T}}$. Doubling the smearing has a negligible effect on the predicted yields.

Only calorimeter cells measuring an energy above a threshold of 500 MeV are used in the calculation of $\beta_{\text{Tile}}$. To study the impact of this threshold on the efficiency of the measurement, the tile calorimeter cell energy scale is varied by $\pm 5\%$ [36] leading to a small ($\leqslant 1\%$) effect on the predicted yields of $R$-hadrons which fall into the individual signal regions. The predicted cell time distributions are smeared to match the data. To evaluate the sensitivity of the signal yield to this smearing, the smearing is applied twice, and the impact is seen to be less than 1%.

To estimate the effects of an imperfect description of the $\mathrm{d}E/\mathrm{d}x_{\text{Pixel}}$ resolution by the simulation, individual values of $\mathrm{d}E/\mathrm{d}x_{\text{Pixel}}$ are smeared according to a Gaussian function with width 5% [27]. Furthermore, to study possible effects due to a global $\mathrm{d}E/\mathrm{d}x_{\text{Pixel}}$ scale uncertainty, the scale is shifted by $\pm 3\%$. These variations are motivated by observed differences between data and Monte Carlo simulations and they change the predicted number of events passing the signal selections by less than 1%.

Adding the above errors in quadrature together with an 11% uncertainty from the luminosity measurement [37], a total systematic uncertainty of 17–20% on the signal event yield is estimated, where the larger uncertainty applies to the low-mass scenarios. The systematic uncertainty on the background estimate is found to be 30%. This arises from contributing uncertainties in the $\mathrm{d}E/\mathrm{d}x_{\text{Pixel}}$ and $\beta_{\text{Tile}}$ distributions (25%) and the use of different methods to determine the absolute normalisation of the background prediction (15%).

As a final cross-check of the consistency of the analysis, the TRT was used. The TRT is a straw-based gas detector, and the time in which any signal exceeds the threshold is read out. This time provides an estimate of continuous energy loss and is usable

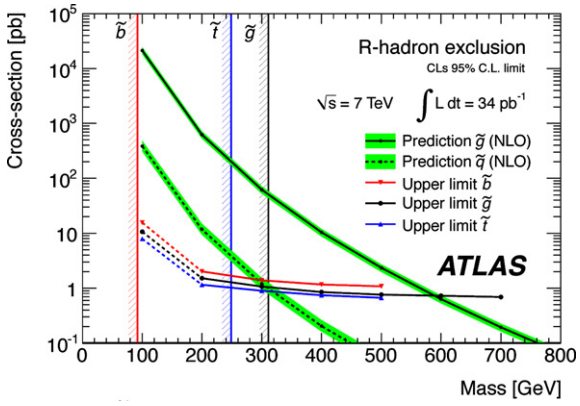


**Fig. 4.** Cross-section limits at 95% CL as a function of sparticle mass. Since five candidate events are observed for the mass windows used for the 100 GeV mass hypotheses, the mass points between 100 and 200 GeV are connected with a dotted line. This indicates that fluctuations in the excluded cross-section will occur. The mass limits quoted in the text are inferred by comparing the cross-section limits with the model predictions. Systematic uncertainties from the choice of PDF and the choice of renormalisation and factorisation scales are represented as a band in the cross-section curves. Previous mass limits are indicated by shaded vertical lines for sbottom (ALEPH), stop (CDF) and gluino (CMS).

for particle identification [38]. The measurement is similar to (but independent of) the pixel detector time-over-threshold measurement, on which $\mathrm{d}E/\mathrm{d}x_{\mathrm{Pixel}}$ is based. No deviations from backgrounds expectations are observed, and the TRT thus provides an additional confirmation that no signal was missed.

## 8. Exclusion limits

Given an expected cross-section as calculated by Prospino and our computed efficiency, the expected number of signal events as a function of mass is determined and a lower limit on the $R$-hadron mass using the $CL_s$ method [39] is calculated. The results for the signal models defined in Section 2 are summarised in Fig. 4.

The observed 95% CL limits are 294 GeV for sbottom $R$-hadrons and 309 GeV for stop $R$-hadrons, while the lower limit for the mass of a hadronising gluino is 586 GeV. These limits include the systematic uncertainties on the signal cross-section and efficiency, as well as on the data-driven background estimate, as described above. Evaluating the mass limits for gluino $R$-hadrons using the triple-Regge based model and bag-model calculation of Ref. [23], gives 566 and 562 GeV respectively. The lower mass limits from ATLAS are shown in Fig. 4 and compared with earlier results from ALEPH [8] (sbottom), CDF [11] (stop), and CMS [9] (gluino). The ATLAS limits have a higher mass reach than those obtained from the previous searches.

## 9. Summary

A search has been performed for slow-moving squark- (stop and sbottom) and gluino-based $R$-hadrons, pair-produced in proton–proton collisions at 7 TeV centre-of-mass energy at the ATLAS detector at the LHC. Candidate $R$-hadrons were sought which left a high transverse momentum track associated with energy depositions in the calorimeter. Observables sensitive to $R$-hadron speed (ionisation energy loss and time-of-flight) were used to suppress backgrounds and allow the reconstruction of the candidate mass. The influence of the scattering of $R$-hadrons in matter on the search sensitivity was studied using a range of phenomenological scattering models. At 95% confidence level the most conservative lower limits on the masses of stable sbottoms, stops and gluinos are 294, 309, and 562 GeV, respectively. Each of these limits are the most stringent to date.

## Acknowledgements

We wish to thank CERN for the efficient commissioning and operation of the LHC during this initial high-energy data-taking period as well as the support staff from our institutions without whom ATLAS could not be operated efficiently. We would also like to thank Torbjörn Sjöstrand and Tilman Plehn for their assistance in the preparation of the theory calculations used in this work.

We acknowledge the support of ANPCyT, Argentina; YerPhI, Armenia; ARC, Australia; BMWF, Austria; ANAS, Azerbaijan; SSTC, Belarus; CNPq and FAPESP, Brazil; NSERC, NRC and CFI, Canada; CERN; CONICYT, Chile; CAS, MOST and NSFC, China; COLCIENCIAS, Colombia; MSMT CR, MPO CR and VSC CR, Czech Republic; DNRF, DNSRC and Lundbeck Foundation, Denmark; ARTEMIS, European Union; IN2P3–CNRS, CEA-DSM/IRFU, France; GNAS, Georgia; BMBF, DFG, HGF, MPG and AvH Foundation, Germany; GSRT, Greece; ISF, MINERVA, GIF, DIP and Benoziyo Center, Israel; INFN, Italy; MEXT and JSPS, Japan; CNRST, Morocco; FOM and NWO, Netherlands; RCN, Norway; MNiSW, Poland; GRICES and FCT, Portugal; MERYS (MECTS), Romania; MES of Russia and ROSATOM, Russian Federation; JINR; MSTD, Serbia; MSSR, Slovakia; ARRS and MVZT, Slovenia; DST/NRF, South Africa; MICINN, Spain; SRC and Wallenberg Foundation, Sweden; SER, SNSF and Cantons of Bern and Geneva, Switzerland; NSC, Taiwan; TAEK, Turkey; STFC, the Royal Society and Leverhulme Trust, United Kingdom; DOE and NSF, United States of America.

The crucial computing support from all WLCG partners is acknowledged gratefully, in particular from CERN and the ATLAS Tier-1 facilities at TRIUMF (Canada), NDGF (Denmark, Norway, Sweden), CC-IN2P3 (France), KIT/GridKA (Germany), INFN–CNAF (Italy), NL-T1 (Netherlands), PIC (Spain), ASGC (Taiwan), RAL (UK) and BNL (USA) and in the Tier-2 facilities worldwide.

## Open access



## References

[1] M. Fairbairn, et al., Phys. Rep. 438 (2007) 1, doi:10.1016/j.physrep.2006.10.002, arXiv:hep-ph/0611040.
[2] A.R. Raklev, Mod. Phys. Lett. A 24 (2009) 1955, arXiv:0908.0315.
[3] ATLAS Collaboration, Phys. Lett. B 698 (2011) 353, arXiv:1102.0459.
[4] ATLAS Collaboration, Expected performance of the ATLAS experiment – detector, trigger and physics, arXiv:0901.0512.
[5] G.R. Farrar, P. Fayet, Phys. Lett. B 76 (1978) 575, doi:10.1016/0370-2693(78)90858-4.
[6] CMS Collaboration, Phys. Rev. Lett. 106 (2011) 011801, doi:10.1103/PhysRevLett.106.011801, arXiv:1011.5861.
[7] P. Abreu, et al., Phys. Lett. B 444 (1998) 491, doi:10.1016/S0370-2693(98)01443-9, arXiv:hep-ex/9811007.
[8] A. Heister, et al., Eur. Phys. J. C 31 (2003) 327, doi:10.1140/epjc/s2003-01376-0, arXiv:hep-ex/0305071.
[9] CMS Collaboration, JHEP 2011 (2011) 1, doi:10.1007/JHEP03(2011)024.
[10] D0 Collaboration, Phys. Rev. Lett. 102 (2009) 161802, doi:10.1103/PhysRevLett.102.161802, arXiv:0809.4472.
[11] CDF Collaboration, Phys. Rev. Lett. 103 (2009) 021802, doi:10.1103/PhysRevLett.103.021802, arXiv:0902.1266.
[12] R. Mackeprang, D. Milstead, Eur. Phys. J. C 66 (2010) 493, doi:10.1140/epjc/s10052-010-1262-1, arXiv:0908.1868.
[13] Y.R. de Boer, A.B. Kaidalov, D.A. Milstead, O.I. Piskounova, J. Phys. G 35 (2008) 075009, doi:10.1088/0954-3899/35/7/075009, arXiv:0710.3930.
[14] T. Sjostrand, S. Mrenna, P. Skands, JHEP 0605 (2006) 026, arXiv:hep-ph/0603175, Pythia 6.423 was used in this work.
[15] TeV4LHC QCD Working Group, arXiv:hep-ph/0610012.

[16] T. Sjostrand, M. van Zijl, Phys. Rev. D 36 (1987) 2019, doi:10.1103/PhysRevD.36.2019.
[17] B. Andersson, G. Gustafson, G. Ingelman, T. Sjostrand, Phys. Rep. 97 (1983) 31, doi:10.1016/0370-1573(83)90080-7.
[18] GEANT4 Collaboration, Nucl. Instrum. Methods A 506 (2003) 250, doi:10.1016/S0168-9002(03)01368-8.
[19] ATLAS Collaboration, Eur. Phys. J. C 70 (2010) 823, doi:10.1140/epjc/s10052-010-1429-9, arXiv:1005.4568, GEANT4.9.2.PATCH02.ATLAS05 was used in this work.
[20] A.C. Kraan, Eur. Phys. J. C 37 (2004) 91, doi:10.1140/epjc/s2004-01997-7, arXiv:hep-ex/0404001.
[21] R. Mackeprang, A. Rizzi, Eur. Phys. J. C 50 (2007) 353, doi:10.1140/epjc/s10052-007-0252-4, arXiv:hep-ph/0612161.
[22] A.C. Kraan, J.B. Hansen, P. Nevski, Eur. Phys. J. C 49 (2007) 623, doi:10.1140/epjc/s10052-006-0162-x, arXiv:hep-ex/0511014.
[23] G. Farrar, R. Mackeprang, D. Milstead, J. Roberts, JHEP 1102 (2011) 018, doi:10.1007/JHEP02(2011)018, arXiv:1011.2964.
[24] W. Beenakker, R. Hopker, M. Spira, P.M. Zerwas, Nucl. Phys. B 492 (1997) 51, doi:10.1016/S0550-3213(97)00084-9, arXiv:hep-ph/9610490, PROSPINO2.1 was used in this work.
[25] P.M. Nadolsky, H.-L. Lai, Q.-H. Cao, J. Huston, J. Pumplin, et al., Phys. Rev. D 78 (2008) 013004, doi:10.1103/PhysRevD.78.013004, arXiv:0802.0007.
[26] ATLAS Collaboration, JINST 3 (2008) S08003, doi:10.1088/1748-0221/3/08/S08003.
[27] ATLAS Collaboration, $dE/dx$ measurement in the ATLAS Pixel Detector and its use for particle identification, ATLAS-CONF-2011-016.
[28] C. Ohm, T. Pauly, Nucl. Instrum. Methods A 623 (2010) 558, doi:10.1016/j.nima.2010.03.069, arXiv:0905.3648.
[29] R. Leitner, et al., Time resolution of the ATLAS Tile calorimeter and its performance for a measurement of heavy stable particles, ATL-TILECAL-PUB-2007-002.
[30] ATLAS Collaboration, The implementation of the ATLAS missing $E_T$ triggers for the initial LHC operation, ATL-DAQ-PUB-2011-001.
[31] M. Cacciari, G.P. Salam, G. Soyez, JHEP 0804 (2008) 063, doi:10.1088/1126-6708/2008/04/063, arXiv:0802.1189.
[32] M. Cacciari, G.P. Salam, Phys. Lett. B 641 (2006) 57, doi:10.1016/j.physletb.2006.08.037, arXiv:hep-ph/0512210.
[33] A. Martin, W. Stirling, R. Thorne, G. Watt, Eur. Phys. J. C 63 (2009) 189, doi:10.1140/epjc/s10052-009-1072-5, arXiv:0901.0002.
[34] ATLAS Collaboration, Eur. Phys. J. C 71 (2011) 1512, doi:10.1140/epjc/s10052-010-1512-2, arXiv:1009.5908.
[35] ATLAS Collaboration, Phys. Lett. B 688 (2010) 21, doi:10.1016/j.physletb.2010.03.064, arXiv:1003.3124.
[36] ATLAS Collaboration, Response and shower topology of 2 to 180 GeV pions measured with the ATLAS barrel calorimeter at the CERN test-beam and comparison to Monte Carlo simulations, ATL-CAL-PUB-2010-001.
[37] ATLAS Collaboration, Luminosity determination in pp collisions at $\sqrt{s} = 7$ TeV using the ATLAS detector at the LHC, arXiv:1101.2185.
[38] E. Abat, J. Abdallah, T. Addy, P. Adragna, M. Aharrouche, et al., JINST 5 (2010) P11006, doi:10.1088/1748-0221/5/11/P11006.
[39] A.L. Read, Modified frequentist analysis of search results (the $CL_s$ method), CERN-OPEN-2000-205.

## ATLAS Collaboration

G. Aad [48], B. Abbott [111], J. Abdallah [11], A.A. Abdelalim [49], A. Abdesselam [118], O. Abdinov [10], B. Abi [112], M. Abolins [88], H. Abramowicz [153], H. Abreu [115], E. Acerbi [89a,89b], B.S. Acharya [164a,164b], D.L. Adams [24], T.N. Addy [56], J. Adelman [175], M. Aderholz [99], S. Adomeit [98], P. Adragna [75], T. Adye [129], S. Aefsky [22], J.A. Aguilar-Saavedra [124b,a], M. Aharrouche [81], S.P. Ahlen [21], F. Ahles [48], A. Ahmad [148], M. Ahsan [40], G. Aielli [133a,133b], T. Akdogan [18a], T.P. Åkesson [79], G. Akimoto [155], A.V. Akimov [94], M.S. Alam [1], M.A. Alam [76], S. Albrand [55], M. Aleksa [29], I.N. Aleksandrov [65], M. Aleppo [89a,89b], F. Alessandria [89a], C. Alexa [25a], G. Alexander [153], G. Alexandre [49], T. Alexopoulos [9], M. Alhroob [20], M. Aliev [15], G. Alimonti [89a], J. Alison [120], M. Aliyev [10], P.P. Allport [73], S.E. Allwood-Spiers [53], J. Almond [82], A. Aloisio [102a,102b], R. Alon [171], A. Alonso [79], M.G. Alviggi [102a,102b], K. Amako [66], P. Amaral [29], C. Amelung [22], V.V. Ammosov [128], A. Amorim [124a,b], G. Amorós [167], N. Amram [153], C. Anastopoulos [139], T. Andeen [34], C.F. Anders [20], K.J. Anderson [30], A. Andreazza [89a,89b], V. Andrei [58a], M.-L. Andrieux [55], X.S. Anduaga [70], A. Angerami [34], F. Anghinolfi [29], N. Anjos [124a], A. Annovi [47], A. Antonaki [8], M. Antonelli [47], S. Antonelli [19a,19b], J. Antos [144b], F. Anulli [132a], S. Aoun [83], L. Aperio Bella [4], R. Apolle [118], G. Arabidze [88], I. Aracena [143], Y. Arai [66], A.T.H. Arce [44], J.P. Archambault [28], S. Arfaoui [29,c], J.-F. Arguin [14], E. Arik [18a,*], M. Arik [18a], A.J. Armbruster [87], O. Arnaez [81], C. Arnault [115], A. Artamonov [95], G. Artoni [132a,132b], D. Arutinov [20], S. Asai [155], R. Asfandiyarov [172], S. Ask [27], B. Åsman [146a,146b], L. Asquith [5], K. Assamagan [24], A. Astbury [169], A. Astvatsatourov [52], G. Atoian [175], B. Aubert [4], B. Auerbach [175], E. Auge [115], K. Augsten [127], M. Aurousseau [145a], N. Austin [73], R. Avramidou [9], D. Axen [168], C. Ay [54], G. Azuelos [93,d], Y. Azuma [155], M.A. Baak [29], G. Baccaglioni [89a], C. Bacci [134a,134b], A.M. Bach [14], H. Bachacou [136], K. Bachas [29], G. Bachy [29], M. Backes [49], M. Backhaus [20], E. Badescu [25a], P. Bagnaia [132a,132b], S. Bahinipati [2], Y. Bai [32a], D.C. Bailey [158], T. Bain [158], J.T. Baines [129], O.K. Baker [175], M.D. Baker [24], S. Baker [77], F. Baltasar Dos Santos Pedrosa [29], E. Banas [38], P. Banerjee [93], Sw. Banerjee [169], D. Banfi [29], A. Bangert [137], V. Bansal [169], H.S. Bansil [17], L. Barak [171], S.P. Baranov [94], A. Barashkou [65], A. Barbaro Galtieri [14], T. Barber [27], E.L. Barberio [86], D. Barberis [50a,50b], M. Barbero [20], D.Y. Bardin [65], T. Barillari [99], M. Barisonzi [174], T. Barklow [143], N. Barlow [27], B.M. Barnett [129], R.M. Barnett [14], A. Baroncelli [134a], A.J. Barr [118], F. Barreiro [80], J. Barreiro Guimarães da Costa [57], P. Barrillon [115], R. Bartoldus [143], A.E. Barton [71], D. Bartsch [20], R.L. Bates [53], L. Batkova [144a], J.R. Batley [27], A. Battaglia [16], M. Battistin [29], G. Battistoni [89a], F. Bauer [136], H.S. Bawa [143], B. Beare [158], T. Beau [78], P.H. Beauchemin [118], R. Beccherle [50a], P. Bechtle [41], H.P. Beck [16], M. Beckingham [48], K.H. Becks [174], A.J. Beddall [18c], A. Beddall [18c], V.A. Bednyakov [65], C. Bee [83], M. Begel [24], S. Behar Harpaz [152], P.K. Behera [63], M. Beimforde [99], C. Belanger-Champagne [166], P.J. Bell [49], W.H. Bell [49], G. Bella [153], L. Bellagamba [19a], F. Bellina [29], G. Bellomo [89a,89b], M. Bellomo [119a], A. Belloni [57],

K. Belotskiy [96], O. Beltramello [29], S. Ben Ami [152], O. Benary [153], D. Benchekroun [135a], C. Benchouk [83], M. Bendel [81], B.H. Benedict [163], N. Benekos [165], Y. Benhammou [153], D.P. Benjamin [44], M. Benoit [115], J.R. Bensinger [22], K. Benslama [130], S. Bentvelsen [105], D. Berge [29], E. Bergeaas Kuutmann [41], N. Berger [4], F. Berghaus [169], E. Berglund [49], J. Beringer [14], K. Bernardet [83], P. Bernat [77], R. Bernhard [48], C. Bernius [24], T. Berry [76], A. Bertin [19a,19b], F. Bertinelli [29], F. Bertolucci [122a,122b], M.I. Besana [89a,89b], N. Besson [136], S. Bethke [99], W. Bhimji [45], R.M. Bianchi [29], M. Bianco [72a,72b], O. Biebel [98], S.P. Bieniek [77], J. Biesiada [14], M. Biglietti [132a,132b], H. Bilokon [47], M. Bindi [19a,19b], S. Binet [115], A. Bingul [18c], C. Bini [132a,132b], C. Biscarat [177], U. Bitenc [48], K.M. Black [21], R.E. Blair [5], J.-B. Blanchard [115], G. Blanchot [29], C. Blocker [22], J. Blocki [38], A. Blondel [49], W. Blum [81], U. Blumenschein [54], G.J. Bobbink [105], V.B. Bobrovnikov [107], A. Bocci [44], C.R. Boddy [118], M. Boehler [41], J. Boek [174], N. Boelaert [35], S. Böser [77], J.A. Bogaerts [29], A. Bogdanchikov [107], A. Bogouch [90,*], C. Bohm [146a], V. Boisvert [76], T. Bold [163,e], V. Boldea [25a], M. Bona [75], V.G. Bondarenko [96], M. Boonekamp [136], G. Boorman [76], C.N. Booth [139], P. Booth [139], S. Bordoni [78], C. Borer [16], A. Borisov [128], G. Borissov [71], I. Borjanovic [12a], S. Borroni [132a,132b], K. Bos [105], D. Boscherini [19a], M. Bosman [11], H. Boterenbrood [105], D. Botterill [129], J. Bouchami [93], J. Boudreau [123], E.V. Bouhova-Thacker [71], C. Boulahouache [123], C. Bourdarios [115], N. Bousson [83], A. Boveia [30], J. Boyd [29], I.R. Boyko [65], N.I. Bozhko [128], I. Bozovic-Jelisavcic [12b], J. Bracinik [17], A. Braem [29], E. Brambilla [72a,72b], P. Branchini [134a], G.W. Brandenburg [57], A. Brandt [7], G. Brandt [15], O. Brandt [54], U. Bratzler [156], B. Brau [84], J.E. Brau [114], H.M. Braun [174], B. Brelier [158], J. Bremer [29], R. Brenner [166], S. Bressler [152], D. Breton [115], N.D. Brett [118], P.G. Bright-Thomas [17], D. Britton [53], F.M. Brochu [27], I. Brock [20], R. Brock [88], T.J. Brodbeck [71], E. Brodet [153], F. Broggi [89a], C. Bromberg [88], G. Brooijmans [34], W.K. Brooks [31b], G. Brown [82], E. Brubaker [30], P.A. Bruckman de Renstrom [38], D. Bruncko [144b], R. Bruneliere [48], S. Brunet [61], A. Bruni [19a], G. Bruni [19a], M. Bruschi [19a], T. Buanes [13], F. Bucci [49], J. Buchanan [118], N.J. Buchanan [2], P. Buchholz [141], R.M. Buckingham [118], A.G. Buckley [45], S.I. Buda [25a], I.A. Budagov [65], B. Budick [108], V. Büscher [81], L. Bugge [117], D. Buira-Clark [118], E.J. Buis [105], O. Bulekov [96], M. Bunse [42], T. Buran [117], H. Burckhart [29], S. Burdin [73], T. Burgess [13], S. Burke [129], E. Busato [33], P. Bussey [53], C.P. Buszello [166], F. Butin [29], B. Butler [143], J.M. Butler [21], C.M. Buttar [53], J.M. Butterworth [77], W. Buttinger [27], T. Byatt [77], S. Cabrera Urbán [167], M. Caccia [89a,89b], D. Caforio [19a,19b], O. Cakir [3a], P. Calafiura [14], G. Calderini [78], P. Calfayan [98], R. Calkins [106], L.P. Caloba [23a], R. Caloi [132a,132b], D. Calvet [33], S. Calvet [33], R. Camacho Toro [33], A. Camard [78], P. Camarri [133a,133b], M. Cambiaghi [119a,119b], D. Cameron [117], J. Cammin [20], S. Campana [29], M. Campanelli [77], V. Canale [102a,102b], F. Canelli [30], A. Canepa [159a], J. Cantero [80], L. Capasso [102a,102b], M.D.M. Capeans Garrido [29], I. Caprini [25a], M. Caprini [25a], D. Capriotti [99], M. Capua [36a,36b], R. Caputo [148], C. Caramarcu [25a], R. Cardarelli [133a], T. Carli [29], G. Carlino [102a], L. Carminati [89a,89b], B. Caron [159a], S. Caron [48], C. Carpentieri [48], G.D. Carrillo Montoya [172], A.A. Carter [75], J.R. Carter [27], J. Carvalho [124a,f], D. Casadei [108], M.P. Casado [11], M. Cascella [122a,122b], C. Caso [50a,50b,*], A.M. Castaneda Hernandez [172], E. Castaneda-Miranda [172], V. Castillo Gimenez [167], N.F. Castro [124a], G. Cataldi [72a], F. Cataneo [29], A. Catinaccio [29], J.R. Catmore [71], A. Cattai [29], G. Cattani [133a,133b], S. Caughron [88], D. Cauz [164a,164c], A. Cavallari [132a,132b], P. Cavalleri [78], D. Cavalli [89a], M. Cavalli-Sforza [11], V. Cavasinni [122a,122b], A. Cazzato [72a,72b], F. Ceradini [134a,134b], A.S. Cerqueira [23a], A. Cerri [29], L. Cerrito [75], F. Cerutti [47], S.A. Cetin [18b], F. Cevenini [102a,102b], A. Chafaq [135a], D. Chakraborty [106], K. Chan [2], B. Chapleau [85], J.D. Chapman [27], J.W. Chapman [87], E. Chareyre [78], D.G. Charlton [17], V. Chavda [82], S. Cheatham [71], S. Chekanov [5], S.V. Chekulaev [159a], G.A. Chelkov [65], H. Chen [24], L. Chen [2], S. Chen [32c], T. Chen [32c], X. Chen [172], S. Cheng [32a], A. Cheplakov [65], V.F. Chepurnov [65], R. Cherkaoui El Moursli [135d], V. Chernyatin [24], E. Cheu [6], S.L. Cheung [158], L. Chevalier [136], F. Chevallier [136], G. Chiefari [102a,102b], L. Chikovani [51], J.T. Childers [58a], A. Chilingarov [71], G. Chiodini [72a], M.V. Chizhov [65], G. Choudalakis [30], S. Chouridou [137], I.A. Christidi [77], A. Christov [48], D. Chromek-Burckhart [29], M.L. Chu [151], J. Chudoba [125], G. Ciapetti [132a,132b], K. Ciba [37], A.K. Ciftci [3a], R. Ciftci [3a], D. Cinca [33], V. Cindro [74], M.D. Ciobotaru [163], C. Ciocca [19a,19b], A. Ciocio [14], M. Cirilli [87], M. Ciubancan [25a], A. Clark [49], P.J. Clark [45], W. Cleland [123], J.C. Clemens [83], B. Clement [55], C. Clement [146a,146b], R.W. Clifft [129], Y. Coadou [83], M. Cobal [164a,164c], A. Coccaro [50a,50b], J. Cochran [64], P. Coe [118], J.G. Cogan [143], J. Coggeshall [165], E. Cogneras [177], C.D. Cojocaru [28], J. Colas [4], A.P. Colijn [105], C. Collard [115], N.J. Collins [17], C. Collins-Tooth [53], J. Collot [55], G. Colon [84], R. Coluccia [72a,72b], G. Comune [88], P. Conde Muiño [124a], E. Coniavitis [118], M.C. Conidi [11], M. Consonni [104], S. Constantinescu [25a], C. Conta [119a,119b], F. Conventi [102a,g], J. Cook [29], M. Cooke [14],

B.D. Cooper [77], A.M. Cooper-Sarkar [118], N.J. Cooper-Smith [76], K. Copic [34], T. Cornelissen [50a,50b], M. Corradi [19a], F. Corriveau [85,h], A. Cortes-Gonzalez [165], G. Cortiana [99], G. Costa [89a], M.J. Costa [167], D. Costanzo [139], T. Costin [30], D. Côté [29], R. Coura Torres [23a], L. Courneyea [169], G. Cowan [76], C. Cowden [27], B.E. Cox [82], K. Cranmer [108], M. Cristinziani [20], G. Crosetti [36a,36b], R. Crupi [72a,72b], S. Crépé-Renaudin [55], C. Cuenca Almenar [175], T. Cuhadar Donszelmann [139], S. Cuneo [50a,50b], M. Curatolo [47], C.J. Curtis [17], P. Cwetanski [61], H. Czirr [141], Z. Czyczula [117], S. D'Auria [53], M. D'Onofrio [73], A. D'Orazio [132a,132b], A. Da Rocha Gesualdi Mello [23a], P.V.M. Da Silva [23a], C. Da Via [82], W. Dabrowski [37], A. Dahlhoff [48], T. Dai [87], C. Dallapiccola [84], S.J. Dallison [129,*], M. Dam [35], M. Dameri [50a,50b], D.S. Damiani [137], H.O. Danielsson [29], R. Dankers [105], D. Dannheim [99], V. Dao [49], G. Darbo [50a], G.L. Darlea [25b], C. Daum [105], J.P. Dauvergne [29], W. Davey [86], T. Davidek [126], N. Davidson [86], R. Davidson [71], M. Davies [93], A.R. Davison [77], E. Dawe [142], I. Dawson [139], J.W. Dawson [5,*], R.K. Daya [39], K. De [7], R. de Asmundis [102a], S. De Castro [19a,19b], P.E. De Castro Faria Salgado [24], S. De Cecco [78], J. de Graat [98], N. De Groot [104], P. de Jong [105], C. De La Taille [115], B. De Lotto [164a,164c], L. De Mora [71], L. De Nooij [105], M. De Oliveira Branco [29], D. De Pedis [132a], P. de Saintignon [55], A. De Salvo [132a], U. De Sanctis [164a,164c], A. De Santo [149], J.B. De Vivie De Regie [115], S. Dean [77], D.V. Dedovich [65], J. Degenhardt [120], M. Dehchar [118], M. Deile [98], C. Del Papa [164a,164c], J. Del Peso [80], T. Del Prete [122a,122b], A. Dell'Acqua [29], L. Dell'Asta [89a,89b], M. Della Pietra [102a,g], D. della Volpe [102a,102b], M. Delmastro [29], P. Delpierre [83], N. Delruelle [29], P.A. Delsart [55], C. Deluca [148], S. Demers [175], M. Demichev [65], B. Demirkoz [11], J. Deng [163], S.P. Denisov [128], D. Derendarz [38], J.E. Derkaoui [135c], F. Derue [78], P. Dervan [73], K. Desch [20], E. Devetak [148], P.O. Deviveiros [158], A. Dewhurst [129], B. DeWilde [148], S. Dhaliwal [158], R. Dhullipudi [24,i], A. Di Ciaccio [133a,133b], L. Di Ciaccio [4], A. Di Girolamo [29], B. Di Girolamo [29], S. Di Luise [134a,134b], A. Di Mattia [88], B. Di Micco [29], R. Di Nardo [133a,133b], A. Di Simone [133a,133b], R. Di Sipio [19a,19b], M.A. Diaz [31a], F. Diblen [18c], E.B. Diehl [87], H. Dietl [99], J. Dietrich [48], T.A. Dietzsch [58a], S. Diglio [115], K. Dindar Yagci [39], J. Dingfelder [20], C. Dionisi [132a,132b], P. Dita [25a], S. Dita [25a], F. Dittus [29], F. Djama [83], R. Djilkibaev [108], T. Djobava [51], M.A.B. do Vale [23a], A. Do Valle Wemans [124a], T.K.O. Doan [4], M. Dobbs [85], R. Dobinson [29,*], D. Dobos [42], E. Dobson [29], M. Dobson [163], J. Dodd [34], O.B. Dogan [18a,*], C. Doglioni [118], T. Doherty [53], Y. Doi [66,*], J. Dolejsi [126], I. Dolenc [74], Z. Dolezal [126], B.A. Dolgoshein [96,*], T. Dohmae [155], M. Donadelli [23b], M. Donega [120], J. Donini [55], J. Dopke [174], A. Doria [102a], A. Dos Anjos [172], M. Dosil [11], A. Dotti [122a,122b], M.T. Dova [70], J.D. Dowell [17], A.D. Doxiadis [105], A.T. Doyle [53], Z. Drasal [126], J. Drees [174], N. Dressnandt [120], H. Drevermann [29], C. Driouichi [35], M. Dris [9], J.G. Drohan [77], J. Dubbert [99], T. Dubbs [137], S. Dube [14], E. Duchovni [171], G. Duckeck [98], A. Dudarev [29], F. Dudziak [64], M. Dührssen [29], I.P. Duerdoth [82], L. Duflot [115], M.-A. Dufour [85], M. Dunford [29], H. Duran Yildiz [3b], R. Duxfield [139], M. Dwuznik [37], F. Dydak [29], D. Dzahini [55], M. Düren [52], W.L. Ebenstein [44], J. Ebke [98], S. Eckert [48], S. Eckweiler [81], K. Edmonds [81], C.A. Edwards [76], I. Efthymiopoulos [49], W. Ehrenfeld [41], T. Ehrich [99], T. Eifert [29], G. Eigen [13], K. Einsweiler [14], E. Eisenhandler [75], T. Ekelof [166], M. El Kacimi [4], M. Ellert [166], S. Elles [4], F. Ellinghaus [81], K. Ellis [75], N. Ellis [29], J. Elmsheuser [98], M. Elsing [29], R. Ely [14], D. Emeliyanov [129], R. Engelmann [148], A. Engl [98], B. Epp [62], A. Eppig [87], J. Erdmann [54], A. Ereditato [16], D. Eriksson [146a], J. Ernst [1], M. Ernst [24], J. Ernwein [136], D. Errede [165], S. Errede [165], E. Ertel [81], M. Escalier [115], C. Escobar [167], X. Espinal Curull [11], B. Esposito [47], F. Etienne [83], A.I. Etienvre [136], E. Etzion [153], D. Evangelakou [54], H. Evans [61], L. Fabbri [19a,19b], C. Fabre [29], K. Facius [35], R.M. Fakhrutdinov [128], S. Falciano [132a], A.C. Falou [115], Y. Fang [172], M. Fanti [89a,89b], A. Farbin [7], A. Farilla [134a], J. Farley [148], T. Farooque [158], S.M. Farrington [118], P. Farthouat [29], D. Fasching [172], P. Fassnacht [29], D. Fassouliotis [8], B. Fatholahzadeh [158], A. Favareto [89a,89b], L. Fayard [115], S. Fazio [36a,36b], R. Febbraro [33], P. Federic [144a], O.L. Fedin [121], I. Fedorko [29], W. Fedorko [88], M. Fehling-Kaschek [48], L. Feligioni [83], D. Fellmann [5], C.U. Felzmann [86], C. Feng [32d], E.J. Feng [30], A.B. Fenyuk [128], J. Ferencei [144b], J. Ferland [93], B. Fernandes [124a,b], W. Fernando [109], S. Ferrag [53], J. Ferrando [118], V. Ferrara [41], A. Ferrari [166], P. Ferrari [105], R. Ferrari [119a], A. Ferrer [167], M.L. Ferrer [47], D. Ferrere [49], C. Ferretti [87], A. Ferretto Parodi [50a,50b], M. Fiascaris [30], F. Fiedler [81], A. Filipčič [74], A. Filippas [9], F. Filthaut [104], M. Fincke-Keeler [169], M.C.N. Fiolhais [124a,f], L. Fiorini [11], A. Firan [39], G. Fischer [41], P. Fischer [20], M.J. Fisher [109], S.M. Fisher [129], J. Flammer [29], M. Flechl [48], I. Fleck [141], J. Fleckner [81], P. Fleischmann [173], S. Fleischmann [174], T. Flick [174], L.R. Flores Castillo [172], M.J. Flowerdew [99], F. Föhlisch [58a], M. Fokitis [9], T. Fonseca Martin [16], D.A. Forbush [138], A. Formica [136], A. Forti [82], D. Fortin [159a], J.M. Foster [82], D. Fournier [115], A. Foussat [29], A.J. Fowler [44], K. Fowler [137], H. Fox [71], P. Francavilla [122a,122b],

S. Franchino [119a,119b], D. Francis [29], T. Frank [171], M. Franklin [57], S. Franz [29], M. Fraternali [119a,119b], S. Fratina [120], S.T. French [27], R. Froeschl [29], D. Froidevaux [29], J.A. Frost [27], C. Fukunaga [156], E. Fullana Torregrosa [29], J. Fuster [167], C. Gabaldon [29], O. Gabizon [171], T. Gadfort [24], S. Gadomski [49], G. Gagliardi [50a,50b], P. Gagnon [61], C. Galea [98], E.J. Gallas [118], M.V. Gallas [29], V. Gallo [16], B.J. Gallop [129], P. Gallus [125], E. Galyaev [40], K.K. Gan [109], Y.S. Gao [143,j], V.A. Gapienko [128], A. Gaponenko [14], F. Garberson [175], M. Garcia-Sciveres [14], C. García [167], J.E. García Navarro [49], R.W. Gardner [30], N. Garelli [29], H. Garitaonandia [105], V. Garonne [29], J. Garvey [17], C. Gatti [47], G. Gaudio [119a], O. Gaumer [49], B. Gaur [141], L. Gauthier [136], I.L. Gavrilenko [94], C. Gay [168], G. Gaycken [20], J.-C. Gayde [29], E.N. Gazis [9], P. Ge [32d], C.N.P. Gee [129], D.A.A. Geerts [105], Ch. Geich-Gimbel [20], K. Gellerstedt [146a,146b], C. Gemme [50a], A. Gemmell [53], M.H. Genest [98], S. Gentile [132a,132b], M. George [54], S. George [76], P. Gerlach [174], A. Gershon [153], C. Geweniger [58a], H. Ghazlane [135b], P. Ghez [4], N. Ghodbane [33], B. Giacobbe [19a], S. Giagu [132a,132b], V. Giakoumopoulou [8], V. Giangiobbe [122a,122b], F. Gianotti [29], B. Gibbard [24], A. Gibson [158], S.M. Gibson [29], G.F. Gieraltowski [5], L.M. Gilbert [118], M. Gilchriese [14], V. Gilewsky [91], D. Gillberg [28], A.R. Gillman [129], D.M. Gingrich [2,d], J. Ginzburg [153], N. Giokaris [8], R. Giordano [102a,102b], F.M. Giorgi [15], P. Giovannini [99], P.F. Giraud [136], P. Girtler [62], D. Giugni [89a], P. Giusti [19a], B.K. Gjelsten [117], L.K. Gladilin [97], C. Glasman [80], J. Glatzer [48], A. Glazov [41], K.W. Glitza [174], G.L. Glonti [65], J. Godfrey [142], J. Godlewski [29], M. Goebel [41], T. Göpfert [43], C. Goeringer [81], C. Gössling [42], T. Göttfert [99], S. Goldfarb [87], D. Goldin [39], T. Golling [175], S.N. Golovnia [128], A. Gomes [124a,b], L.S. Gomez Fajardo [41], R. Gonçalo [76], J. Goncalves Pinto Firmino Da Costa [41], L. Gonella [20], A. Gonidec [29], S. Gonzalez [172], S. González de la Hoz [167], M.L. Gonzalez Silva [26], S. Gonzalez-Sevilla [49], J.J. Goodson [148], L. Goossens [29], P.A. Gorbounov [95], H.A. Gordon [24], I. Gorelov [103], G. Gorfine [174], B. Gorini [29], E. Gorini [72a,72b], A. Gorišek [74], E. Gornicki [38], S.A. Gorokhov [128], V.N. Goryachev [128], B. Gosdzik [41], M. Gosselink [105], M.I. Gostkin [65], M. Gouanère [4], I. Gough Eschrich [163], M. Gouighri [135a], D. Goujdami [135a], M.P. Goulette [49], A.G. Goussiou [138], C. Goy [4], I. Grabowska-Bold [163,e], V. Grabski [176], P. Grafström [29], C. Grah [174], K.-J. Grahn [147], F. Grancagnolo [72a], S. Grancagnolo [15], V. Grassi [148], V. Gratchev [121], N. Grau [34], H.M. Gray [34,k], J.A. Gray [148], E. Graziani [134a], O.G. Grebenyuk [121], D. Greenfield [129], T. Greenshaw [73], Z.D. Greenwood [24,l], I.M. Gregor [41], P. Grenier [143], E. Griesmayer [46], J. Griffiths [138], N. Grigalashvili [65], A.A. Grillo [137], S. Grinstein [11], P.L.Y. Gris [33], Y.V. Grishkevich [97], J.-F. Grivaz [115], J. Grognuz [29], M. Groh [99], E. Gross [171], J. Grosse-Knetter [54], J. Groth-Jensen [79], M. Gruwe [29], K. Grybel [141], V.J. Guarino [5], D. Guest [175], C. Guicheney [33], A. Guida [72a,72b], T. Guillemin [4], S. Guindon [54], H. Guler [85,m], J. Gunther [125], B. Guo [158], J. Guo [34], A. Gupta [30], Y. Gusakov [65], V.N. Gushchin [128], A. Gutierrez [93], P. Gutierrez [111], N. Guttman [153], O. Gutzwiller [172], C. Guyot [136], C. Gwenlan [118], C.B. Gwilliam [73], A. Haas [143], S. Haas [29], C. Haber [14], R. Hackenburg [24], H.K. Hadavand [39], D.R. Hadley [17], P. Haefner [99], F. Hahn [29], S. Haider [29], Z. Hajduk [38], H. Hakobyan [176], J. Haller [54], K. Hamacher [174], P. Hamal [113], A. Hamilton [49], S. Hamilton [161], H. Han [32a], L. Han [32b], K. Hanagaki [116], M. Hance [120], C. Handel [81], P. Hanke [58a], C.J. Hansen [166], J.R. Hansen [35], J.B. Hansen [35], J.D. Hansen [35], P.H. Hansen [35], P. Hansson [143], K. Hara [160], G.A. Hare [137], T. Harenberg [174], D. Harper [87], R.D. Harrington [21], O.M. Harris [138], K. Harrison [17], J. Hartert [48], F. Hartjes [105], T. Haruyama [66], A. Harvey [56], S. Hasegawa [101], Y. Hasegawa [140], S. Hassani [136], M. Hatch [29], D. Hauff [99], S. Haug [16], M. Hauschild [29], R. Hauser [88], M. Havranek [20], B.M. Hawes [118], C.M. Hawkes [17], R.J. Hawkings [29], D. Hawkins [163], T. Hayakawa [67], D. Hayden [76], H.S. Hayward [73], S.J. Haywood [129], E. Hazen [21], M. He [32d], S.J. Head [17], V. Hedberg [79], L. Heelan [28], S. Heim [88], B. Heinemann [14], S. Heisterkamp [35], L. Helary [4], M. Heldmann [48], M. Heller [115], S. Hellman [146a,146b], C. Helsens [11], R.C.W. Henderson [71], M. Henke [58a], A. Henrichs [54], A.M. Henriques Correia [29], S. Henrot-Versille [115], F. Henry-Couannier [83], C. Hensel [54], T. Henß [174], Y. Hernández Jiménez [167], R. Herrberg [15], A.D. Hershenhorn [152], G. Herten [48], R. Hertenberger [98], L. Hervas [29], N.P. Hessey [105], A. Hidvegi [146a], E. Higón-Rodriguez [167], D. Hill [5,*], J.C. Hill [27], N. Hill [5], K.H. Hiller [41], S. Hillert [20], S.J. Hillier [17], I. Hinchliffe [14], E. Hines [120], M. Hirose [116], F. Hirsch [42], D. Hirschbuehl [174], J. Hobbs [148], N. Hod [153], M.C. Hodgkinson [139], P. Hodgson [139], A. Hoecker [29], M.R. Hoeferkamp [103], J. Hoffman [39], D. Hoffmann [83], M. Hohlfeld [81], M. Holder [141], A. Holmes [118], S.O. Holmgren [146a], T. Holy [127], J.L. Holzbauer [88], Y. Homma [67], L. Hooft van Huysduynen [108], T. Horazdovsky [127], C. Horn [143], S. Horner [48], K. Horton [118], J.-Y. Hostachy [55], T. Hott [99], S. Hou [151], M.A. Houlden [73], A. Hoummada [135a], J. Howarth [82], D.F. Howell [118], I. Hristova [41], J. Hrivnac [115], I. Hruska [125], T. Hryn'ova [4], P.J. Hsu [175], S.-C. Hsu [14], G.S. Huang [111],

Z. Hubacek [127], F. Hubaut [83], F. Huegging [20], T.B. Huffman [118], E.W. Hughes [34], G. Hughes [71], R.E. Hughes-Jones [82], M. Huhtinen [29], P. Hurst [57], M. Hurwitz [14], U. Husemann [41], N. Huseynov [65,n], J. Huston [88], J. Huth [57], G. Iacobucci [102a], G. Iakovidis [9], M. Ibbotson [82], I. Ibragimov [141], R. Ichimiya [67], L. Iconomidou-Fayard [115], J. Idarraga [115], M. Idzik [37], P. Iengo [4], O. Igonkina [105], Y. Ikegami [66], M. Ikeno [66], Y. Ilchenko [39], D. Iliadis [154], D. Imbault [78], M. Imhaeuser [174], M. Imori [155], T. Ince [20], J. Inigo-Golfin [29], P. Ioannou [8], M. Iodice [134a], G. Ionescu [4], A. Irles Quiles [167], K. Ishii [66], A. Ishikawa [67], M. Ishino [66], R. Ishmukhametov [39], C. Issever [118], S. Istin [18a], Y. Itoh [101], A.V. Ivashin [128], W. Iwanski [38], H. Iwasaki [66], J.M. Izen [40], V. Izzo [102a], B. Jackson [120], J.N. Jackson [73], P. Jackson [143], M.R. Jaekel [29], V. Jain [61], K. Jakobs [48], S. Jakobsen [35], J. Jakubek [127], D.K. Jana [111], E. Jankowski [158], E. Jansen [77], A. Jantsch [99], M. Janus [20], G. Jarlskog [79], L. Jeanty [57], K. Jelen [37], I. Jen-La Plante [30], P. Jenni [29], A. Jeremie [4], P. Jež [35], S. Jézéquel [4], H. Ji [172], W. Ji [81], J. Jia [148], Y. Jiang [32b], M. Jimenez Belenguer [41], G. Jin [32b], S. Jin [32a], O. Jinnouchi [157], M.D. Joergensen [35], D. Joffe [39], L.G. Johansen [13], M. Johansen [146a,146b], K.E. Johansson [146a], P. Johansson [139], S. Johnert [41], K.A. Johns [6], K. Jon-And [146a,146b], G. Jones [82], R.W.L. Jones [71], T.W. Jones [77], T.J. Jones [73], O. Jonsson [29], C. Joram [29], P.M. Jorge [124a,b], J. Joseph [14], X. Ju [130], V. Juranek [125], P. Jussel [62], V.V. Kabachenko [128], S. Kabana [16], M. Kaci [167], A. Kaczmarska [38], P. Kadlecik [35], M. Kado [115], H. Kagan [109], M. Kagan [57], S. Kaiser [99], E. Kajomovitz [152], S. Kalinin [174], L.V. Kalinovskaya [65], S. Kama [39], N. Kanaya [155], M. Kaneda [155], T. Kanno [157], V.A. Kantserov [96], J. Kanzaki [66], B. Kaplan [175], A. Kapliy [30], J. Kaplon [29], D. Kar [43], M. Karagoz [118], M. Karnevskiy [41], K. Karr [5], V. Kartvelishvili [71], A.N. Karyukhin [128], L. Kashif [172], A. Kasmi [39], R.D. Kass [109], A. Kastanas [13], M. Kataoka [4], Y. Kataoka [155], E. Katsoufis [9], J. Katzy [41], V. Kaushik [6], K. Kawagoe [67], T. Kawamoto [155], G. Kawamura [81], M.S. Kayl [105], V.A. Kazanin [107], M.Y. Kazarinov [65], S.I. Kazi [86], J.R. Keates [82], R. Keeler [169], R. Kehoe [39], M. Keil [54], G.D. Kekelidze [65], M. Kelly [82], J. Kennedy [98], C.J. Kenney [143], M. Kenyon [53], O. Kepka [125], N. Kerschen [29], B.P. Kerševan [74], S. Kersten [174], K. Kessoku [155], C. Ketterer [48], M. Khakzad [28], F. Khalil-zada [10], H. Khandanyan [165], A. Khanov [112], D. Kharchenko [65], A. Khodinov [148], A.G. Kholodenko [128], A. Khomich [58a], T.J. Khoo [27], G. Khoriauli [20], N. Khovanskiy [65], V. Khovanskiy [95], E. Khramov [65], J. Khubua [51], G. Kilvington [76], H. Kim [7], M.S. Kim [2], P.C. Kim [143], S.H. Kim [160], N. Kimura [170], O. Kind [15], B.T. King [73], M. King [67], R.S.B. King [118], J. Kirk [129], G.P. Kirsch [118], L.E. Kirsch [22], A.E. Kiryunin [99], D. Kisielewska [37], T. Kittelmann [123], A.M. Kiver [128], H. Kiyamura [67], E. Kladiva [144b], J. Klaiber-Lodewigs [42], M. Klein [73], U. Klein [73], K. Kleinknecht [81], M. Klemetti [85], A. Klier [171], A. Klimentov [24], R. Klingenberg [42], E.B. Klinkby [35], T. Klioutchnikova [29], P.F. Klok [104], S. Klous [105], E.-E. Kluge [58a], T. Kluge [73], P. Kluit [105], S. Kluth [99], E. Kneringer [62], J. Knobloch [29], E.B.F.G. Knoops [83], A. Knue [54], B.R. Ko [44], T. Kobayashi [155], M. Kobel [43], B. Koblitz [29], M. Kocian [143], A. Kocnar [113], P. Kodys [126], K. Köneke [29], A.C. König [104], S. Koenig [81], S. König [48], L. Köpke [81], F. Koetsveld [104], P. Koevesarki [20], T. Koffas [29], E. Koffeman [105], F. Kohn [54], Z. Kohout [127], T. Kohriki [66], T. Koi [143], T. Kokott [20], G.M. Kolachev [107], H. Kolanoski [15], V. Kolesnikov [65], I. Koletsou [89a], J. Koll [88], D. Kollar [29], M. Kollefrath [48], S.D. Kolya [82], A.A. Komar [94], J.R. Komaragiri [142], T. Kondo [66], T. Kono [41,o], A.I. Kononov [48], R. Konoplich [108,p], N. Konstantinidis [77], A. Kootz [174], S. Koperny [37], S.V. Kopikov [128], K. Korcyl [38], K. Kordas [154], V. Koreshev [128], A. Korn [14], A. Korol [107], I. Korolkov [11], E.V. Korolkova [139], V.A. Korotkov [128], O. Kortner [99], S. Kortner [99], V.V. Kostyukhin [20], M.J. Kotamäki [29], S. Kotov [99], V.M. Kotov [65], C. Kourkoumelis [8], V. Kouskoura [154], A. Koutsman [105], R. Kowalewski [169], T.Z. Kowalski [37], W. Kozanecki [136], A.S. Kozhin [128], V. Kral [127], V.A. Kramarenko [97], G. Kramberger [74], O. Krasel [42], M.W. Krasny [78], A. Krasznahorkay [108], J. Kraus [88], A. Kreisel [153], F. Krejci [127], J. Kretzschmar [73], N. Krieger [54], P. Krieger [158], K. Kroeninger [54], H. Kroha [99], J. Kroll [120], J. Kroseberg [20], J. Krstic [12a], U. Kruchonak [65], H. Krüger [20], Z.V. Krumshteyn [65], A. Kruth [20], T. Kubota [155], S. Kuehn [48], A. Kugel [58c], T. Kuhl [174], D. Kuhn [62], V. Kukhtin [65], Y. Kulchitsky [90], S. Kuleshov [31b], C. Kummer [98], M. Kuna [83], N. Kundu [118], J. Kunkle [120], A. Kupco [125], H. Kurashige [67], M. Kurata [160], Y.A. Kurochkin [90], V. Kus [125], W. Kuykendall [138], M. Kuze [157], P. Kuzhir [91], O. Kvasnicka [125], R. Kwee [15], A. La Rosa [29], L. La Rotonda [36a,36b], L. Labarga [80], J. Labbe [4], C. Lacasta [167], F. Lacava [132a,132b], H. Lacker [15], D. Lacour [78], V.R. Lacuesta [167], E. Ladygin [65], R. Lafaye [4], B. Laforge [78], T. Lagouri [80], S. Lai [48], E. Laisne [55], M. Lamanna [29], C.L. Lampen [6], W. Lampl [6], E. Lancon [136], U. Landgraf [48], M.P.J. Landon [75], H. Landsman [152], J.L. Lane [82], C. Lange [41], A.J. Lankford [163], F. Lanni [24], K. Lantzsch [29], V.V. Lapin [128,*], S. Laplace [78], C. Lapoire [20], J.F. Laporte [136], T. Lari [89a], A.V. Larionov [128], A. Larner [118], C. Lasseur [29], M. Lassnig [29], W. Lau [118], P. Laurelli [47], A. Lavorato [118], W. Lavrijsen [14], P. Laycock [73], A.B. Lazarev [65], A. Lazzaro [89a,89b],

O. Le Dortz [78], E. Le Guirriec [83], C. Le Maner [158], E. Le Menedeu [136], M. Leahu [29], A. Lebedev [64], C. Lebel [93], T. LeCompte [5], F. Ledroit-Guillon [55], H. Lee [105], J.S.H. Lee [150], S.C. Lee [151], L. Lee [175], M. Lefebvre [169], M. Legendre [136], A. Leger [49], B.C. LeGeyt [120], F. Legger [98], C. Leggett [14], M. Lehmacher [20], G. Lehmann Miotto [29], X. Lei [6], M.A.L. Leite [23b], R. Leitner [126], D. Lellouch [171], J. Lellouch [78], M. Leltchouk [34], V. Lendermann [58a], K.J.C. Leney [145b], T. Lenz [174], G. Lenzen [174], B. Lenzi [136], K. Leonhardt [43], S. Leontsinis [9], C. Leroy [93], J.-R. Lessard [169], J. Lesser [146a], C.G. Lester [27], A. Leung Fook Cheong [172], J. Levêque [4], D. Levin [87], L.J. Levinson [171], M.S. Levitski [128], M. Lewandowska [21], G.H. Lewis [108], M. Leyton [15], B. Li [83], H. Li [172], S. Li [32b], X. Li [87], Z. Liang [39], Z. Liang [118,q], B. Liberti [133a], P. Lichard [29], M. Lichtnecker [98], K. Lie [165], W. Liebig [13], R. Lifshitz [152], J.N. Lilley [17], A. Limosani [86], M. Limper [63], S.C. Lin [151,r], F. Linde [105], J.T. Linnemann [88], E. Lipeles [120], L. Lipinsky [125], A. Lipniacka [13], T.M. Liss [165], D. Lissauer [24], A. Lister [49], A.M. Litke [137], C. Liu [28], D. Liu [151,s], H. Liu [87], J.B. Liu [87], M. Liu [32b], S. Liu [2], Y. Liu [32b], M. Livan [119a,119b], S.S.A. Livermore [118], A. Lleres [55], S.L. Lloyd [75], E. Lobodzinska [41], P. Loch [6], W.S. Lockman [137], S. Lockwitz [175], T. Loddenkoetter [20], F.K. Loebinger [82], A. Loginov [175], C.W. Loh [168], T. Lohse [15], K. Lohwasser [48], M. Lokajicek [125], J. Loken [118], V.P. Lombardo [89a], R.E. Long [71], L. Lopes [124a,b], D. Lopez Mateos [34,k], M. Losada [162], P. Loscutoff [14], F. Lo Sterzo [132a,132b], M.J. Losty [159a], X. Lou [40], A. Lounis [115], K.F. Loureiro [162], J. Love [21], P.A. Love [71], A.J. Lowe [143], F. Lu [32a], J. Lu [2], L. Lu [39], H.J. Lubatti [138], C. Luci [132a,132b], A. Lucotte [55], A. Ludwig [43], D. Ludwig [41], I. Ludwig [48], J. Ludwig [48], F. Luehring [61], G. Luijckx [105], D. Lumb [48], L. Luminari [132a], E. Lund [117], B. Lund-Jensen [147], B. Lundberg [79], J. Lundberg [146a,146b], J. Lundquist [35], M. Lungwitz [81], A. Lupi [122a,122b], G. Lutz [99], D. Lynn [24], J. Lys [14], E. Lytken [79], H. Ma [24], L.L. Ma [172], J.A. Macana Goia [93], G. Maccarrone [47], A. Macchiolo [99], B. Maček [74], J. Machado Miguens [124a], D. Macina [49], R. Mackeprang [35], R.J. Madaras [14], W.F. Mader [43], R. Maenner [58c], T. Maeno [24], P. Mättig [174], S. Mättig [41], P.J. Magalhaes Martins [124a,f], L. Magnoni [29], E. Magradze [51], C.A. Magrath [104], Y. Mahalalel [153], K. Mahboubi [48], G. Mahout [17], C. Maiani [132a,132b], C. Maidantchik [23a], A. Maio [124a,b], S. Majewski [24], Y. Makida [66], N. Makovec [115], P. Mal [6], Pa. Malecki [38], P. Malecki [38], V.P. Maleev [121], F. Malek [55], U. Mallik [63], D. Malon [5], S. Maltezos [9], V. Malyshev [107], S. Malyukov [65], R. Mameghani [98], J. Mamuzic [12b], A. Manabe [66], L. Mandelli [89a], I. Mandić [74], R. Mandrysch [15], J. Maneira [124a], P.S. Mangeard [88], I.D. Manjavidze [65], A. Mann [54], P.M. Manning [137], A. Manousakis-Katsikakis [8], B. Mansoulie [136], A. Manz [99], A. Mapelli [29], L. Mapelli [29], L. March [80], J.F. Marchand [29], F. Marchese [133a,133b], M. Marchesotti [29], G. Marchiori [78], M. Marcisovsky [125], A. Marin [21,*], C.P. Marino [61], F. Marroquim [23a], R. Marshall [82], Z. Marshall [34,k], F.K. Martens [158], S. Marti-Garcia [167], A.J. Martin [175], B. Martin [29], B. Martin [88], F.F. Martin [120], J.P. Martin [93], Ph. Martin [55], T.A. Martin [17], B. Martin dit Latour [49], M. Martinez [11], V. Martinez Outschoorn [57], A.C. Martyniuk [82], M. Marx [82], F. Marzano [132a], A. Marzin [111], L. Masetti [81], T. Mashimo [155], R. Mashinistov [94], J. Masik [82], A.L. Maslennikov [107], M. Maß [42], I. Massa [19a,19b], G. Massaro [105], N. Massol [4], A. Mastroberardino [36a,36b], T. Masubuchi [155], M. Mathes [20], P. Matricon [115], H. Matsumoto [155], H. Matsunaga [155], T. Matsushita [67], C. Mattravers [118,t], J.M. Maugain [29], S.J. Maxfield [73], E.N. May [5], A. Mayne [139], R. Mazini [151], M. Mazur [20], M. Mazzanti [89a], E. Mazzoni [122a,122b], S.P. Mc Kee [87], A. McCarn [165], R.L. McCarthy [148], T.G. McCarthy [28], N.A. McCubbin [129], K.W. McFarlane [56], J.A. Mcfayden [139], H. McGlone [53], G. Mchedlidze [51], R.A. McLaren [29], T. Mclaughlan [17], S.J. McMahon [129], R.A. McPherson [169,h], A. Meade [84], J. Mechnich [105], M. Mechtel [174], M. Medinnis [41], R. Meera-Lebbai [111], T. Meguro [116], R. Mehdiyev [93], S. Mehlhase [41], A. Mehta [73], K. Meier [58a], J. Meinhardt [48], B. Meirose [79], C. Melachrinos [30], B.R. Mellado Garcia [172], L. Mendoza Navas [162], Z. Meng [151,s], A. Mengarelli [19a,19b], S. Menke [99], C. Menot [29], E. Meoni [11], P. Mermod [118], L. Merola [102a,102b], C. Meroni [89a], F.S. Merritt [30], A. Messina [29], J. Metcalfe [103], A.S. Mete [64], S. Meuser [20], C. Meyer [81], J.-P. Meyer [136], J. Meyer [173], J. Meyer [54], T.C. Meyer [29], W.T. Meyer [64], J. Miao [32d], S. Michal [29], L. Micu [25a], R.P. Middleton [129], P. Miele [29], S. Migas [73], L. Mijović [41], G. Mikenberg [171], M. Mikestikova [125], B. Mikulec [49], M. Mikuž [74], D.W. Miller [143], R.J. Miller [88], W.J. Mills [168], C. Mills [57], A. Milov [171], D.A. Milstead [146a,146b], D. Milstein [171], A.A. Minaenko [128], M. Miñano [167], I.A. Minashvili [65], A.I. Mincer [108], B. Mindur [37], M. Mineev [65], Y. Ming [130], L.M. Mir [11], G. Mirabelli [132a], L. Miralles Verge [11], A. Misiejuk [76], J. Mitrevski [137], G.Y. Mitrofanov [128], V.A. Mitsou [167], S. Mitsui [66], P.S. Miyagawa [82], K. Miyazaki [67], J.U. Mjörnmark [79], T. Moa [146a,146b], P. Mockett [138], S. Moed [57], V. Moeller [27], K. Mönig [41], N. Möser [20], S. Mohapatra [148], B. Mohn [13], W. Mohr [48], S. Mohrdieck-Möck [99], A.M. Moisseev [128,*], R. Moles-Valls [167], J. Molina-Perez [29], L. Moneta [49], J. Monk [77], E. Monnier [83], S. Montesano [89a,89b],

F. Monticelli [70], S. Monzani [19a,19b], R.W. Moore [2], G.F. Moorhead [86], C. Mora Herrera [49], A. Moraes [53], A. Morais [124a,b], N. Morange [136], J. Morel [54], G. Morello [36a,36b], D. Moreno [81], M. Moreno Llácer [167], P. Morettini [50a], M. Morii [57], J. Morin [75], Y. Morita [66], A.K. Morley [29], G. Mornacchi [29], M.-C. Morone [49], S.V. Morozov [96], J.D. Morris [75], H.G. Moser [99], M. Mosidze [51], J. Moss [109], R. Mount [143], E. Mountricha [9], S.V. Mouraviev [94], E.J.W. Moyse [84], M. Mudrinic [12b], F. Mueller [58a], J. Mueller [123], K. Mueller [20], T.A. Müller [98], D. Muenstermann [42], A. Muijs [105], A. Muir [168], Y. Munwes [153], K. Murakami [66], W.J. Murray [129], I. Mussche [105], E. Musto [102a,102b], A.G. Myagkov [128], M. Myska [125], J. Nadal [11], K. Nagai [160], K. Nagano [66], Y. Nagasaka [60], A.M. Nairz [29], Y. Nakahama [115], K. Nakamura [155], I. Nakano [110], G. Nanava [20], A. Napier [161], M. Nash [77,t], N.R. Nation [21], T. Nattermann [20], T. Naumann [41], G. Navarro [162], H.A. Neal [87], E. Nebot [80], P.Yu. Nechaeva [94], A. Negri [119a,119b], G. Negri [29], S. Nektarijevic [49], A. Nelson [64], S. Nelson [143], T.K. Nelson [143], S. Nemecek [125], P. Nemethy [108], A.A. Nepomuceno [23a], M. Nessi [29], S.Y. Nesterov [121], M.S. Neubauer [165], A. Neusiedl [81], R.M. Neves [108], P. Nevski [24], P.R. Newman [17], R.B. Nickerson [118], R. Nicolaidou [136], L. Nicolas [139], B. Nicquevert [29], F. Niedercorn [115], J. Nielsen [137], T. Niinikoski [29], A. Nikiforov [15], V. Nikolaenko [128], K. Nikolaev [65], I. Nikolic-Audit [78], K. Nikolopoulos [24], H. Nilsen [48], P. Nilsson [7], Y. Ninomiya [155], A. Nisati [132a], T. Nishiyama [67], R. Nisius [99], L. Nodulman [5], M. Nomachi [116], I. Nomidis [154], H. Nomoto [155], M. Nordberg [29], B. Nordkvist [146a,146b], P.R. Norton [129], J. Novakova [126], M. Nozaki [66], M. Nožička [41], I.M. Nugent [159a], A.-E. Nuncio-Quiroz [20], G. Nunes Hanninger [20], T. Nunnemann [98], E. Nurse [77], T. Nyman [29], B.J. O'Brien [45], S.W. O'Neale [17,*], D.C. O'Neil [142], V. O'Shea [53], F.G. Oakham [28,d], H. Oberlack [99], J. Ocariz [78], A. Ochi [67], S. Oda [155], S. Odaka [66], J. Odier [83], H. Ogren [61], A. Oh [82], S.H. Oh [44], C.C. Ohm [146a,146b], T. Ohshima [101], H. Ohshita [140], T.K. Ohska [66], T. Ohsugi [59], S. Okada [67], H. Okawa [163], Y. Okumura [101], T. Okuyama [155], M. Olcese [50a], A.G. Olchevski [65], M. Oliveira [124a,f], D. Oliveira Damazio [24], E. Oliver Garcia [167], D. Olivito [120], A. Olszewski [38], J. Olszowska [38], C. Omachi [67], A. Onofre [124a,u], P.U.E. Onyisi [30], C.J. Oram [159a], G. Ordonez [104], M.J. Oreglia [30], F. Orellana [49], Y. Oren [153], D. Orestano [134a,134b], I. Orlov [107], C. Oropeza Barrera [53], R.S. Orr [158], E.O. Ortega [130], B. Osculati [50a,50b], R. Ospanov [120], C. Osuna [11], G. Otero y Garzon [26], J.P. Ottersbach [105], M. Ouchrif [135c], F. Ould-Saada [117], A. Ouraou [136], Q. Ouyang [32a], M. Owen [82], S. Owen [139], A. Oyarzun [31b], O.K. Øye [13], V.E. Ozcan [18a], N. Ozturk [7], A. Pacheco Pages [11], C. Padilla Aranda [11], E. Paganis [139], F. Paige [24], K. Pajchel [117], S. Palestini [29], D. Pallin [33], A. Palma [124a,b], J.D. Palmer [17], Y.B. Pan [172], E. Panagiotopoulou [9], B. Panes [31a], N. Panikashvili [87], S. Panitkin [24], D. Pantea [25a], M. Panuskova [125], V. Paolone [123], A. Paoloni [133a,133b], A. Papadelis [146a], Th.D. Papadopoulou [9], A. Paramonov [5], W. Park [24,v], M.A. Parker [27], F. Parodi [50a,50b], J.A. Parsons [34], U. Parzefall [48], E. Pasqualucci [132a], A. Passeri [134a], F. Pastore [134a,134b], Fr. Pastore [29], G. Pásztor [49,w], S. Pataraia [172], N. Patel [150], J.R. Pater [82], S. Patricelli [102a,102b], T. Pauly [29], M. Pecsy [144a], M.I. Pedraza Morales [172], S.V. Peleganchuk [107], H. Peng [172], R. Pengo [29], A. Penson [34], J. Penwell [61], M. Perantoni [23a], K. Perez [34,k], T. Perez Cavalcanti [41], E. Perez Codina [11], M.T. Pérez García-Estañ [167], V. Perez Reale [34], I. Peric [20], L. Perini [89a,89b], H. Pernegger [29], R. Perrino [72a], P. Perrodo [4], S. Persembe [3a], V.D. Peshekhonov [65], O. Peters [105], B.A. Petersen [29], J. Petersen [29], T.C. Petersen [35], E. Petit [83], A. Petridis [154], C. Petridou [154], E. Petrolo [132a], F. Petrucci [134a,134b], D. Petschull [41], M. Petteni [142], R. Pezoa [31b], A. Phan [86], A.W. Phillips [27], P.W. Phillips [129], G. Piacquadio [29], E. Piccaro [75], M. Piccinini [19a,19b], A. Pickford [53], S.M. Piec [41], R. Piegaia [26], J.E. Pilcher [30], A.D. Pilkington [82], J. Pina [124a,b], M. Pinamonti [164a,164c], A. Pinder [118], J.L. Pinfold [2], J. Ping [32c], B. Pinto [124a,b], O. Pirotte [29], C. Pizio [89a,89b], R. Placakyte [41], M. Plamondon [169], W.G. Plano [82], M.-A. Pleier [24], A.V. Pleskach [128], A. Poblaguev [24], S. Poddar [58a], F. Podlyski [33], L. Poggioli [115], T. Poghosyan [20], M. Pohl [49], F. Polci [55], G. Polesello [119a], A. Policicchio [138], A. Polini [19a], J. Poll [75], V. Polychronakos [24], D.M. Pomarede [136], D. Pomeroy [22], K. Pommès [29], L. Pontecorvo [132a], B.G. Pope [88], G.A. Popeneciu [25a], D.S. Popovic [12a], A. Poppleton [29], X. Portell Bueso [48], R. Porter [163], C. Posch [21], G.E. Pospelov [99], S. Pospisil [127], I.N. Potrap [99], C.J. Potter [149], C.T. Potter [85], G. Poulard [29], J. Poveda [172], R. Prabhu [77], P. Pralavorio [83], S. Prasad [57], R. Pravahan [7], S. Prell [64], K. Pretzl [16], L. Pribyl [29], D. Price [61], L.E. Price [5], M.J. Price [29], P.M. Prichard [73], D. Prieur [123], M. Primavera [72a], K. Prokofiev [108], F. Prokoshin [31b], S. Protopopescu [24], J. Proudfoot [5], X. Prudent [43], H. Przysiezniak [4], S. Psoroulas [20], E. Ptacek [114], J. Purdham [87], M. Purohit [24,v], P. Puzo [115], Y. Pylypchenko [117], J. Qian [87], Z. Qian [83], Z. Qin [41], A. Quadt [54], D.R. Quarrie [14], W.B. Quayle [172], F. Quinonez [31a], M. Raas [104], V. Radescu [58b], B. Radics [20], T. Rador [18a], F. Ragusa [89a,89b], G. Rahal [177],

A.M. Rahimi [109], C. Rahm [24], S. Rajagopalan [24], S. Rajek [42], M. Rammensee [48], M. Rammes [141], M. Ramstedt [146a,146b], K. Randrianarivony [28], P.N. Ratoff [71], F. Rauscher [98], E. Rauter [99], M. Raymond [29], A.L. Read [117], D.M. Rebuzzi [119a,119b], A. Redelbach [173], G. Redlinger [24], R. Reece [120], K. Reeves [40], A. Reichold [105], E. Reinherz-Aronis [153], A. Reinsch [114], I. Reisinger [42], D. Reljic [12a], C. Rembser [29], Z.L. Ren [151], A. Renaud [115], P. Renkel [39], B. Rensch [35], M. Rescigno [132a], S. Resconi [89a], B. Resende [136], P. Reznicek [98], R. Rezvani [158], A. Richards [77], R. Richter [99], E. Richter-Was [38,x], M. Ridel [78], S. Rieke [81], M. Rijpstra [105], M. Rijssenbeek [148], A. Rimoldi [119a,119b], L. Rinaldi [19a], R.R. Rios [39], I. Riu [11], G. Rivoltella [89a,89b], F. Rizatdinova [112], E. Rizvi [75], S.H. Robertson [85,h], A. Robichaud-Veronneau [49], D. Robinson [27], J.E.M. Robinson [77], M. Robinson [114], A. Robson [53], J.G. Rocha de Lima [106], C. Roda [122a,122b], D. Roda Dos Santos [29], S. Rodier [80], D. Rodriguez [162], Y. Rodriguez Garcia [15], A. Roe [54], S. Roe [29], O. Røhne [117], V. Rojo [1], S. Rolli [161], A. Romaniouk [96], V.M. Romanov [65], G. Romeo [26], D. Romero Maltrana [31a], L. Roos [78], E. Ros [167], S. Rosati [138], M. Rose [76], G.A. Rosenbaum [158], E.I. Rosenberg [64], P.L. Rosendahl [13], L. Rosselet [49], V. Rossetti [11], E. Rossi [102a,102b], L.P. Rossi [50a], L. Rossi [89a,89b], M. Rotaru [25a], I. Roth [171], J. Rothberg [138], I. Rottländer [20], D. Rousseau [115], C.R. Royon [136], A. Rozanov [83], Y. Rozen [152], X. Ruan [115], I. Rubinskiy [41], B. Ruckert [98], N. Ruckstuhl [105], V.I. Rud [97], G. Rudolph [62], F. Rühr [6], A. Ruiz-Martinez [64], E. Rulikowska-Zarebska [37], V. Rumiantsev [91,*], L. Rumyantsev [65], K. Runge [48], O. Runolfsson [20], Z. Rurikova [48], N.A. Rusakovich [65], D.R. Rust [61], J.P. Rutherfoord [6], C. Ruwiedel [14], P. Ruzicka [125], Y.F. Ryabov [121], V. Ryadovikov [128], P. Ryan [88], M. Rybar [126], G. Rybkin [115], N.C. Ryder [118], S. Rzaeva [10], A.F. Saavedra [150], I. Sadeh [153], H.F.-W. Sadrozinski [137], R. Sadykov [65], F. Safai Tehrani [132a,132b], H. Sakamoto [155], G. Salamanna [105], A. Salamon [133a], M. Saleem [111], D. Salihagic [99], A. Salnikov [143], J. Salt [167], B.M. Salvachua Ferrando [5], D. Salvatore [36a,36b], F. Salvatore [149], A. Salzburger [29], D. Sampsonidis [154], B.H. Samset [117], H. Sandaker [13], H.G. Sander [81], M.P. Sanders [98], M. Sandhoff [174], P. Sandhu [158], T. Sandoval [27], R. Sandstroem [105], S. Sandvoss [174], D.P.C. Sankey [129], A. Sansoni [47], C. Santamarina Rios [85], C. Santoni [33], R. Santonico [133a,133b], H. Santos [124a], J.G. Saraiva [124a,b], T. Sarangi [172], E. Sarkisyan-Grinbaum [7], F. Sarri [122a,122b], G. Sartisohn [174], O. Sasaki [66], T. Sasaki [66], N. Sasao [68], I. Satsounkevitch [90], G. Sauvage [4], J.B. Sauvan [115], P. Savard [158,d], V. Savinov [123], D.O. Savu [29], P. Savva [9], L. Sawyer [24,i], D.H. Saxon [53], L.P. Says [33], C. Sbarra [19a,19b], A. Sbrizzi [19a,19b], O. Scallon [93], D.A. Scannicchio [163], J. Schaarschmidt [115], P. Schacht [99], U. Schäfer [81], S. Schaetzel [58b], A.C. Schaffer [115], D. Schaile [98], R.D. Schamberger [148], A.G. Schamov [107], V. Scharf [58a], V.A. Schegelsky [121], D. Scheirich [87], M.I. Scherzer [14], C. Schiavi [50a,50b], J. Schieck [98], M. Schioppa [36a,36b], S. Schlenker [29], J.L. Schlereth [5], E. Schmidt [48], M.P. Schmidt [175,*], K. Schmieden [20], C. Schmitt [81], M. Schmitz [20], A. Schöning [58b], M. Schott [29], D. Schouten [142], J. Schovancova [125], M. Schram [85], C. Schroeder [81], N. Schroer [58c], S. Schuh [29], G. Schuler [29], J. Schultes [174], H.-C. Schultz-Coulon [58a], H. Schulz [15], J.W. Schumacher [20], M. Schumacher [48], B.A. Schumm [137], Ph. Schune [136], C. Schwanenberger [82], A. Schwartzman [143], Ph. Schwemling [78], R. Schwienhorst [88], R. Schwierz [43], J. Schwindling [136], W.G. Scott [129], J. Searcy [114], E. Sedykh [121], E. Segura [11], S.C. Seidel [103], A. Seiden [137], F. Seifert [43], J.M. Seixas [23a], G. Sekhniaidze [102a], D.M. Seliverstov [121], B. Sellden [146a], G. Sellers [73], M. Seman [144b], N. Semprini-Cesari [19a,19b], C. Serfon [98], L. Serin [115], R. Seuster [99], H. Severini [111], M.E. Sevior [86], A. Sfyrla [29], E. Shabalina [54], M. Shamim [114], L.Y. Shan [32a], J.T. Shank [21], Q.T. Shao [86], M. Shapiro [14], P.B. Shatalov [95], L. Shaver [6], C. Shaw [53], K. Shaw [164a,164c], D. Sherman [175], P. Sherwood [77], A. Shibata [108], S. Shimizu [29], M. Shimojima [100], T. Shin [56], A. Shmeleva [94], M.J. Shochet [30], D. Short [118], M.A. Shupe [6], P. Sicho [125], A. Sidoti [15], A. Siebel [174], F. Siegert [48], J. Siegrist [14], Dj. Sijacki [12a], O. Silbert [171], J. Silva [124a,b], Y. Silver [153], D. Silverstein [143], S.B. Silverstein [146a], V. Simak [127], O. Simard [136], Lj. Simic [12a], S. Simion [115], B. Simmons [77], M. Simonyan [35], P. Sinervo [158], N.B. Sinev [114], V. Sipica [141], G. Siragusa [81], A.N. Sisakyan [65], S.Yu. Sivoklokov [97], J. Sjölin [146a,146b], T.B. Sjursen [13], L.A. Skinnari [14], K. Skovpen [107], P. Skubic [111], N. Skvorodnev [22], M. Slater [17], T. Slavicek [127], K. Sliwa [161], T.J. Sloan [71], J. Sloper [29], V. Smakhtin [171], S.Yu. Smirnov [96], L.N. Smirnova [97], O. Smirnova [79], B.C. Smith [57], D. Smith [143], K.M. Smith [53], M. Smizanska [71], K. Smolek [127], A.A. Snesarev [94], S.W. Snow [82], J. Snow [111], J. Snuverink [105], S. Snyder [24], M. Soares [124a], R. Sobie [169,h], J. Sodomka [127], A. Soffer [153], C.A. Solans [167], M. Solar [127], J. Solc [127], U. Soldevila [167], E. Solfaroli Camillocci [132a,132b], A.A. Solodkov [128], O.V. Solovyanov [128], J. Sondericker [24], N. Soni [2], V. Sopko [127], B. Sopko [127], M. Sorbi [89a,89b], M. Sosebee [7], A. Soukharev [107], S. Spagnolo [72a,72b], F. Spanò [34], R. Spighi [19a], G. Spigo [29], F. Spila [132a,132b], E. Spiriti [134a], R. Spiwoks [29],

M. Spousta [126], T. Spreitzer [158], B. Spurlock [7], R.D. St. Denis [53], T. Stahl [141], J. Stahlman [120], R. Stamen [58a], E. Stanecka [29], R.W. Stanek [5], C. Stanescu [134a], S. Stapnes [117], E.A. Starchenko [128], J. Stark [55], P. Staroba [125], P. Starovoitov [91], A. Staude [98], P. Stavina [144a], G. Stavropoulos [14], G. Steele [53], P. Steinbach [43], P. Steinberg [24], I. Stekl [127], B. Stelzer [142], H.J. Stelzer [41], O. Stelzer-Chilton [159a], H. Stenzel [52], K. Stevenson [75], G.A. Stewart [53], J.A. Stillings [20], T. Stockmanns [20], M.C. Stockton [29], K. Stoerig [48], G. Stoicea [25a], S. Stonjek [99], P. Strachota [126], A.R. Stradling [7], A. Straessner [43], J. Strandberg [87], S. Strandberg [146a,146b], A. Strandlie [117], M. Strang [109], E. Strauss [143], M. Strauss [111], P. Strizenec [144b], R. Ströhmer [173], D.M. Strom [114], J.A. Strong [76,*], R. Stroynowski [39], J. Strube [129], B. Stugu [13], I. Stumer [24,*], J. Stupak [148], P. Sturm [174], D.A. Soh [151,q], D. Su [143], S. Subramania [2], Y. Sugaya [116], T. Sugimoto [101], C. Suhr [106], K. Suita [67], M. Suk [126], V.V. Sulin [94], S. Sultansoy [3d], T. Sumida [29], X. Sun [55], J.E. Sundermann [48], K. Suruliz [164a,164b], S. Sushkov [11], G. Susinno [36a,36b], M.R. Sutton [139], Y. Suzuki [66], Yu.M. Sviridov [128], S. Swedish [168], I. Sykora [144a], T. Sykora [126], B. Szeless [29], J. Sánchez [167], D. Ta [105], K. Tackmann [29], A. Taffard [163], R. Tafirout [159a], A. Taga [117], N. Taiblum [153], Y. Takahashi [101], H. Takai [24], R. Takashima [69], H. Takeda [67], T. Takeshita [140], M. Talby [83], A. Talyshev [107], M.C. Tamsett [24], J. Tanaka [155], R. Tanaka [115], S. Tanaka [131], S. Tanaka [66], Y. Tanaka [100], K. Tani [67], N. Tannoury [83], G.P. Tappern [29], S. Tapprogge [81], D. Tardif [158], S. Tarem [152], F. Tarrade [24], G.F. Tartarelli [89a], P. Tas [126], M. Tasevsky [125], E. Tassi [36a,36b], M. Tatarkhanov [14], C. Taylor [77], F.E. Taylor [92], G.N. Taylor [86], W. Taylor [159b], M. Teixeira Dias Castanheira [75], P. Teixeira-Dias [76], K.K. Temming [48], H. Ten Kate [29], P.K. Teng [151], S. Terada [66], K. Terashi [155], J. Terron [80], M. Terwort [41,o], M. Testa [47], R.J. Teuscher [158,h], C.M. Tevlin [82], J. Thadome [174], J. Therhaag [20], T. Theveneaux-Pelzer [78], M. Thioye [175], S. Thoma [48], J.P. Thomas [17], E.N. Thompson [84], P.D. Thompson [17], P.D. Thompson [158], A.S. Thompson [53], E. Thomson [120], M. Thomson [27], R.P. Thun [87], T. Tic [125], V.O. Tikhomirov [94], Y.A. Tikhonov [107], C.J.W.P. Timmermans [104], P. Tipton [175], F.J. Tique Aires Viegas [29], S. Tisserant [83], J. Tobias [48], B. Toczek [37], T. Todorov [4], S. Todorova-Nova [161], B. Toggerson [163], J. Tojo [66], S. Tokár [144a], K. Tokunaga [67], K. Tokushuku [66], K. Tollefson [88], M. Tomoto [101], L. Tompkins [14], K. Toms [103], A. Tonazzo [134a,134b], G. Tong [32a], A. Tonoyan [13], C. Topfel [16], N.D. Topilin [65], I. Torchiani [29], E. Torrence [114], E. Torró Pastor [167], J. Toth [83,w], F. Touchard [83], D.R. Tovey [139], D. Traynor [75], T. Trefzger [173], J. Treis [20], L. Tremblet [29], A. Tricoli [29], I.M. Trigger [159a], S. Trincaz-Duvoid [78], T.N. Trinh [78], M.F. Tripiana [70], N. Triplett [64], W. Trischuk [158], A. Trivedi [24,v], B. Trocmé [55], C. Troncon [89a], M. Trottier-McDonald [142], A. Trzupek [38], C. Tsarouchas [29], J.C.-L. Tseng [118], M. Tsiakiris [105], P.V. Tsiareshka [90], D. Tsionou [4], G. Tsipolitis [9], V. Tsiskaridze [48], E.G. Tskhadadze [51], I.I. Tsukerman [95], V. Tsulaia [123], J.-W. Tsung [20], S. Tsuno [66], D. Tsybychev [148], A. Tua [139], J.M. Tuggle [30], M. Turala [38], D. Turecek [127], I. Turk Cakir [3e], E. Turlay [105], R. Turra [89a,89b], P.M. Tuts [34], A. Tykhonov [74], M. Tylmad [146a,146b], M. Tyndel [129], D. Typaldos [17], H. Tyrvainen [29], G. Tzanakos [8], K. Uchida [20], I. Ueda [155], R. Ueno [28], M. Ugland [13], M. Uhlenbrock [20], M. Uhrmacher [54], F. Ukegawa [160], G. Unal [29], D.G. Underwood [5], A. Undrus [24], G. Unel [163], Y. Unno [66], D. Urbaniec [34], E. Urkovsky [153], P. Urquijo [49], P. Urrejola [31a], G. Usai [7], M. Uslenghi [119a,119b], L. Vacavant [83], V. Vacek [127], B. Vachon [85], S. Vahsen [14], C. Valderanis [99], J. Valenta [125], P. Valente [132a], S. Valentinetti [19a,19b], S. Valkar [126], E. Valladolid Gallego [167], S. Vallecorsa [152], J.A. Valls Ferrer [167], H. van der Graaf [105], E. van der Kraaij [105], R. Van Der Leeuw [105], E. van der Poel [105], D. van der Ster [29], B. Van Eijk [105], N. van Eldik [84], P. van Gemmeren [5], Z. van Kesteren [105], I. van Vulpen [105], W. Vandelli [29], G. Vandoni [29], A. Vaniachine [5], P. Vankov [41], F. Vannucci [78], F. Varela Rodriguez [29], R. Vari [132a], E.W. Varnes [6], D. Varouchas [14], A. Vartapetian [7], K.E. Varvell [150], V.I. Vassilakopoulos [56], F. Vazeille [33], G. Vegni [89a,89b], J.J. Veillet [115], C. Vellidis [8], F. Veloso [124a], R. Veness [29], S. Veneziano [132a], A. Ventura [72a,72b], D. Ventura [138], M. Venturi [48], N. Venturi [16], V. Vercesi [119a], M. Verducci [138], W. Verkerke [105], J.C. Vermeulen [105], A. Vest [43], M.C. Vetterli [142,d], I. Vichou [165], T. Vickey [145b,y], G.H.A. Viehhauser [118], S. Viel [168], M. Villa [19a,19b], M. Villaplana Perez [167], E. Vilucchi [47], M.G. Vincter [28], E. Vinek [29], V.B. Vinogradov [65], M. Virchaux [136,*], S. Viret [33], J. Virzi [14], A. Vitale [19a,19b], O. Vitells [171], M. Viti [41], I. Vivarelli [48], F. Vives Vaque [11], S. Vlachos [9], M. Vlasak [127], N. Vlasov [20], A. Vogel [20], P. Vokac [127], M. Volpi [11], G. Volpini [89a], H. von der Schmitt [99], J. von Loeben [99], H. von Radziewski [48], E. von Toerne [20], V. Vorobel [126], A.P. Vorobiev [128], V. Vorwerk [11], M. Vos [167], R. Voss [29], T.T. Voss [174], J.H. Vossebeld [73], A.S. Vovenko [128], N. Vranjes [12a], M. Vranjes Milosavljevic [12a], V. Vrba [125], M. Vreeswijk [105], T. Vu Anh [81], R. Vuillermet [29], I. Vukotic [115], W. Wagner [174], P. Wagner [120], H. Wahlen [174], J. Wakabayashi [101], J. Walbersloh [42], S. Walch [87], J. Walder [71],

R. Walker [98], W. Walkowiak [141], R. Wall [175], P. Waller [73], C. Wang [44], H. Wang [172], J. Wang [151], J. Wang [32d], J.C. Wang [138], R. Wang [103], S.M. Wang [151], A. Warburton [85], C.P. Ward [27], M. Warsinsky [48], P.M. Watkins [17], A.T. Watson [17], M.F. Watson [17], G. Watts [138], S. Watts [82], A.T. Waugh [150], B.M. Waugh [77], J. Weber [42], M. Weber [129], M.S. Weber [16], P. Weber [54], A.R. Weidberg [118], P. Weigell [99], J. Weingarten [54], C. Weiser [48], H. Wellenstein [22], P.S. Wells [29], M. Wen [47], T. Wenaus [24], S. Wendler [123], Z. Weng [151,q], T. Wengler [29], S. Wenig [29], N. Wermes [20], M. Werner [48], P. Werner [29], M. Werth [163], M. Wessels [58a], K. Whalen [28], S.J. Wheeler-Ellis [163], S.P. Whitaker [21], A. White [7], M.J. White [86], S. White [24], S.R. Whitehead [118], D. Whiteson [163], D. Whittington [61], F. Wicek [115], D. Wicke [174], F.J. Wickens [129], W. Wiedenmann [172], M. Wielers [129], P. Wienemann [20], C. Wiglesworth [73], L.A.M. Wiik [48], P.A. Wijeratne [77], A. Wildauer [167], M.A. Wildt [41,o], I. Wilhelm [126], H.G. Wilkens [29], J.Z. Will [98], E. Williams [34], H.H. Williams [120], W. Willis [34], S. Willocq [84], J.A. Wilson [17], M.G. Wilson [143], A. Wilson [87], I. Wingerter-Seez [4], S. Winkelmann [48], F. Winklmeier [29], M. Wittgen [143], M.W. Wolter [38], H. Wolters [124a,f], G. Wooden [118], B.K. Wosiek [38], J. Wotschack [29], M.J. Woudstra [84], K. Wraight [53], C. Wright [53], B. Wrona [73], S.L. Wu [172], X. Wu [49], Y. Wu [32b], E. Wulf [34], R. Wunstorf [42], B.M. Wynne [45], L. Xaplanteris [9], S. Xella [35], S. Xie [48], Y. Xie [32a], C. Xu [32b], D. Xu [139], G. Xu [32a], B. Yabsley [150], M. Yamada [66], A. Yamamoto [66], K. Yamamoto [64], S. Yamamoto [155], T. Yamamura [155], J. Yamaoka [44], T. Yamazaki [155], Y. Yamazaki [67], Z. Yan [21], H. Yang [87], U.K. Yang [82], Y. Yang [61], Y. Yang [32a], Z. Yang [146a,146b], S. Yanush [91], W.-M. Yao [14], Y. Yao [14], Y. Yasu [66], J. Ye [39], S. Ye [24], M. Yilmaz [3c], R. Yoosoofmiya [123], K. Yorita [170], R. Yoshida [5], C. Young [143], S. Youssef [21], D. Yu [24], J. Yu [7], J. Yu [32c,z], L. Yuan [32a,aa], A. Yurkewicz [148], V.G. Zaets [128], R. Zaidan [63], A.M. Zaitsev [128], Z. Zajacova [29], Yo.K. Zalite [121], L. Zanello [132a,132b], P. Zarzhitsky [39], A. Zaytsev [107], C. Zeitnitz [174], M. Zeller [175], P.F. Zema [29], A. Zemla [38], C. Zendler [20], A.V. Zenin [128], O. Zenin [128], T. Ženiš [144a], Z. Zenonos [122a,122b], S. Zenz [14], D. Zerwas [115], G. Zevi della Porta [57], Z. Zhan [32d], D. Zhang [32b], H. Zhang [88], J. Zhang [5], X. Zhang [32d], Z. Zhang [115], L. Zhao [108], T. Zhao [138], Z. Zhao [32b], A. Zhemchugov [65], S. Zheng [32a], J. Zhong [151,ab], B. Zhou [87], N. Zhou [163], Y. Zhou [151], C.G. Zhu [32d], H. Zhu [41], Y. Zhu [172], X. Zhuang [98], V. Zhuravlov [99], D. Zieminska [61], B. Zilka [144a], R. Zimmermann [20], S. Zimmermann [20], S. Zimmermann [48], M. Ziolkowski [141], R. Zitoun [4], L. Živković [34], V.V. Zmouchko [128,*], G. Zobernig [172], A. Zoccoli [19a,19b], Y. Zolnierowski [4], A. Zsenei [29], M. Zur Nedden [15], V. Zutshi [106], L. Zwalinski [29]

[1] *University at Albany, Albany, NY, United States*
[2] *Department of Physics, University of Alberta, Edmonton AB, Canada*
[3] [(a)] *Department of Physics, Ankara University, Ankara;* [(b)] *Department of Physics, Dumlupinar University, Kutahya;* [(c)] *Department of Physics, Gazi University, Ankara;* [(d)] *Division of Physics, TOBB University of Economics and Technology, Ankara;* [(e)] *Turkish Atomic Energy Authority, Ankara, Turkey*
[4] *LAPP, CNRS/IN2P3 and Université de Savoie, Annecy-le-Vieux, France*
[5] *High Energy Physics Division, Argonne National Laboratory, Argonne, IL, United States*
[6] *Department of Physics, University of Arizona, Tucson, AZ, United States*
[7] *Department of Physics, The University of Texas at Arlington, Arlington, TX, United States*
[8] *Physics Department, University of Athens, Athens, Greece*
[9] *Physics Department, National Technical University of Athens, Zografou, Greece*
[10] *Institute of Physics, Azerbaijan Academy of Sciences, Baku, Azerbaijan*
[11] *Institut de Física d'Altes Energies and Universitat Autònoma de Barcelona and ICREA, Barcelona, Spain*
[12] [(a)] *Institute of Physics, University of Belgrade, Belgrade;* [(b)] *Vinca Institute of Nuclear Sciences, Belgrade, Serbia*
[13] *Department for Physics and Technology, University of Bergen, Bergen, Norway*
[14] *Physics Division, Lawrence Berkeley National Laboratory and University of California, Berkeley, CA, United States*
[15] *Department of Physics, Humboldt University, Berlin, Germany*
[16] *Albert Einstein Center for Fundamental Physics and Laboratory for High Energy Physics, University of Bern, Bern, Switzerland*
[17] *School of Physics and Astronomy, University of Birmingham, Birmingham, United Kingdom*
[18] [(a)] *Department of Physics, Bogazici University, Istanbul;* [(b)] *Division of Physics, Dogus University, Istanbul;* [(c)] *Department of Physics Engineering, Gaziantep University, Gaziantep;* [(d)] *Department of Physics, Istanbul Technical University, Istanbul, Turkey*
[19] [(a)] *INFN Sezione di Bologna;* [(b)] *Dipartimento di Fisica, Università di Bologna, Bologna, Italy*
[20] *Physikalisches Institut, University of Bonn, Bonn, Germany*
[21] *Department of Physics, Boston University, Boston, MA, United States*
[22] *Department of Physics, Brandeis University, Waltham, MA, United States*
[23] [(a)] *Universidade Federal do Rio De Janeiro COPPE/EE/IF, Rio de Janeiro;* [(b)] *Instituto de Fisica, Universidade de Sao Paulo, Sao Paulo, Brazil*
[24] *Physics Department, Brookhaven National Laboratory, Upton, NY, United States*
[25] [(a)] *National Institute of Physics and Nuclear Engineering, Bucharest;* [(b)] *University Politehnica Bucharest, Bucharest;* [(c)] *West University in Timisoara, Timisoara, Romania*
[26] *Departamento de Física, Universidad de Buenos Aires, Buenos Aires, Argentina*
[27] *Cavendish Laboratory, University of Cambridge, Cambridge, United Kingdom*
[28] *Department of Physics, Carleton University, Ottawa, ON, Canada*
[29] *CERN, Geneva, Switzerland*
[30] *Enrico Fermi Institute, University of Chicago, Chicago, IL, United States*
[31] [(a)] *Departamento de Fisica, Pontificia Universidad Católica de Chile, Santiago;* [(b)] *Departamento de Física, Universidad Técnica Federico Santa María, Valparaíso, Chile*
[32] [(a)] *Institute of High Energy Physics, Chinese Academy of Sciences, Beijing;* [(b)] *Department of Modern Physics, University of Science and Technology of China, Anhui;* [(c)] *Department of Physics, Nanjing University, Jiangsu;* [(d)] *High Energy Physics Group, Shandong University, Shandong, China*
[33] *Laboratoire de Physique Corpusculaire, Clermont Université and Université Blaise Pascal and CNRS/IN2P3, Aubiere Cedex, France*
[34] *Nevis Laboratory, Columbia University, Irvington, NY, United States*

[35] Niels Bohr Institute, University of Copenhagen, Kobenhavn, Denmark
[36] [(a)] INFN Gruppo Collegato di Cosenza; [(b)] Dipartimento di Fisica, Università della Calabria, Arcavata di Rende, Italy
[37] Faculty of Physics and Applied Computer Science, AGH – University of Science and Technology, Krakow, Poland
[38] The Henryk Niewodniczanski Institute of Nuclear Physics, Polish Academy of Sciences, Krakow, Poland
[39] Physics Department, Southern Methodist University, Dallas, TX, United States
[40] University of Texas at Dallas, Richardson, TX, United States
[41] DESY, Hamburg and Zeuthen, Germany
[42] Institut für Experimentelle Physik IV, Technische Universität Dortmund, Dortmund, Germany
[43] Institut für Kern- und Teilchenphysik, Technical University Dresden, Dresden, Germany
[44] Department of Physics, Duke University, Durham, NC, United States
[45] SUPA – School of Physics and Astronomy, University of Edinburgh, Edinburgh, United Kingdom
[46] Fachhochschule Wiener Neustadt, Wiener Neustadt, Austria
[47] INFN Laboratori Nazionali di Frascati, Frascati, Italy
[48] Fakultät für Mathematik und Physik, Albert-Ludwigs-Universität, Freiburg i.Br., Germany
[49] Section de Physique, Université de Genève, Geneva, Switzerland
[50] [(a)] INFN Sezione di Genova; [(b)] Dipartimento di Fisica, Università di Genova, Genova, Italy
[51] Institute of Physics and HEP Institute, Georgian Academy of Sciences and Tbilisi State University, Tbilisi, Georgia
[52] II Physikalisches Institut, Justus-Liebig-Universität Giessen, Giessen, Germany
[53] SUPA – School of Physics and Astronomy, University of Glasgow, Glasgow, United Kingdom
[54] II Physikalisches Institut, Georg-August-Universität, Göttingen, Germany
[55] Laboratoire de Physique Subatomique et de Cosmologie, Université Joseph Fourier and CNRS/IN2P3 and Institut National Polytechnique de Grenoble, Grenoble, France
[56] Department of Physics, Hampton University, Hampton, VA, United States
[57] Laboratory for Particle Physics and Cosmology, Harvard University, Cambridge, MA, United States
[58] [(a)] Kirchhoff-Institut für Physik, Ruprecht-Karls-Universität Heidelberg, Heidelberg; [(b)] Physikalisches Institut, Ruprecht-Karls-Universität Heidelberg, Heidelberg;
[(c)] ZITI Institut für Technische Informatik, Ruprecht-Karls-Universität Heidelberg, Mannheim, Germany
[59] Faculty of Science, Hiroshima University, Hiroshima, Japan
[60] Faculty of Applied Information Science, Hiroshima Institute of Technology, Hiroshima, Japan
[61] Department of Physics, Indiana University, Bloomington, IN, United States
[62] Institut für Astro- und Teilchenphysik, Leopold-Franzens-Universität, Innsbruck, Austria
[63] University of Iowa, Iowa City, IA, United States
[64] Department of Physics and Astronomy, Iowa State University, Ames, IA, United States
[65] Joint Institute for Nuclear Research, JINR Dubna, Dubna, Russia
[66] KEK, High Energy Accelerator Research Organization, Tsukuba, Japan
[67] Graduate School of Science, Kobe University, Kobe, Japan
[68] Faculty of Science, Kyoto University, Kyoto, Japan
[69] Kyoto University of Education, Kyoto, Japan
[70] Instituto de Física La Plata, Universidad Nacional de La Plata and CONICET, La Plata, Argentina
[71] Physics Department, Lancaster University, Lancaster, United Kingdom
[72] [(a)] INFN Sezione di Lecce; [(b)] Dipartimento di Fisica, Università del Salento, Lecce, Italy
[73] Oliver Lodge Laboratory, University of Liverpool, Liverpool, United Kingdom
[74] Department of Physics, Jožef Stefan Institute and University of Ljubljana, Ljubljana, Slovenia
[75] Department of Physics, Queen Mary University of London, London, United Kingdom
[76] Department of Physics, Royal Holloway University of London, Surrey, United Kingdom
[77] Department of Physics and Astronomy, University College London, London, United Kingdom
[78] Laboratoire de Physique Nucléaire et de Hautes Energies, UPMC and Université Paris-Diderot and CNRS/IN2P3, Paris, France
[79] Fysiska institutionen, Lunds universitet, Lund, Sweden
[80] Departamento de Fisica Teorica C-15, Universidad Autonoma de Madrid, Madrid, Spain
[81] Institut für Physik, Universität Mainz, Mainz, Germany
[82] School of Physics and Astronomy, University of Manchester, Manchester, United Kingdom
[83] CPPM, Aix-Marseille Université and CNRS/IN2P3, Marseille, France
[84] Department of Physics, University of Massachusetts, Amherst, MA, United States
[85] Department of Physics, McGill University, Montreal, QC, Canada
[86] School of Physics, University of Melbourne, Victoria, Australia
[87] Department of Physics, The University of Michigan, Ann Arbor, MI, United States
[88] Department of Physics and Astronomy, Michigan State University, East Lansing, MI, United States
[89] [(a)] INFN Sezione di Milano; [(b)] Dipartimento di Fisica, Università di Milano, Milano, Italy
[90] B.I. Stepanov Institute of Physics, National Academy of Sciences of Belarus, Minsk, Belarus
[91] National Scientific and Educational Centre for Particle and High Energy Physics, Minsk, Belarus
[92] Department of Physics, Massachusetts Institute of Technology, Cambridge, MA, United States
[93] Group of Particle Physics, University of Montreal, Montreal, QC, Canada
[94] P.N. Lebedev Institute of Physics, Academy of Sciences, Moscow, Russia
[95] Institute for Theoretical and Experimental Physics (ITEP), Moscow, Russia
[96] Moscow Engineering and Physics Institute (MEPhI), Moscow, Russia
[97] Skobeltsyn Institute of Nuclear Physics, Lomonosov Moscow State University, Moscow, Russia
[98] Fakultät für Physik, Ludwig-Maximilians-Universität München, München, Germany
[99] Max-Planck-Institut für Physik (Werner-Heisenberg-Institut), München, Germany
[100] Nagasaki Institute of Applied Science, Nagasaki, Japan
[101] Graduate School of Science, Nagoya University, Nagoya, Japan
[102] [(a)] INFN Sezione di Napoli; [(b)] Dipartimento di Scienze Fisiche, Università di Napoli, Napoli, Italy
[103] Department of Physics and Astronomy, University of New Mexico, Albuquerque, NM, United States
[104] Institute for Mathematics, Astrophysics and Particle Physics, Radboud University Nijmegen/Nikhef, Nijmegen, Netherlands
[105] Nikhef National Institute for Subatomic Physics and University of Amsterdam, Amsterdam, Netherlands
[106] Department of Physics, Northern Illinois University, DeKalb, IL, United States
[107] Budker Institute of Nuclear Physics (BINP), Novosibirsk, Russia
[108] Department of Physics, New York University, New York, NY, United States
[109] Ohio State University, Columbus, OH, United States
[110] Faculty of Science, Okayama University, Okayama, Japan
[111] Homer L. Dodge Department of Physics and Astronomy, University of Oklahoma, Norman, OK, United States
[112] Department of Physics, Oklahoma State University, Stillwater, OK, United States

[113] Palacký University, RCPTM, Olomouc, Czech Republic
[114] Center for High Energy Physics, University of Oregon, Eugene, OR, United States
[115] LAL, Univ. Paris-Sud and CNRS/IN2P3, Orsay, France
[116] Graduate School of Science, Osaka University, Osaka, Japan
[117] Department of Physics, University of Oslo, Oslo, Norway
[118] Department of Physics, Oxford University, Oxford, United Kingdom
[119] [(a)] INFN Sezione di Pavia; [(b)] Dipartimento di Fisica Nucleare e Teorica, Università di Pavia, Pavia, Italy
[120] Department of Physics, University of Pennsylvania, Philadelphia, PA, United States
[121] Petersburg Nuclear Physics Institute, Gatchina, Russia
[122] [(a)] INFN Sezione di Pisa; [(b)] Dipartimento di Fisica E. Fermi, Università di Pisa, Pisa, Italy
[123] Department of Physics and Astronomy, University of Pittsburgh, Pittsburgh, PA, United States
[124] [(a)] Laboratorio de Instrumentacao e Fisica Experimental de Particulas – LIP, Lisboa, Portugal; [(b)] Departamento de Fisica Teorica y del Cosmos and CAFPE, Universidad de Granada, Granada, Spain
[125] Institute of Physics, Academy of Sciences of the Czech Republic, Praha, Czech Republic
[126] Faculty of Mathematics and Physics, Charles University in Prague, Praha, Czech Republic
[127] Czech Technical University in Prague, Praha, Czech Republic
[128] State Research Center Institute for High Energy Physics, Protvino, Russia
[129] Particle Physics Department, Rutherford Appleton Laboratory, Didcot, United Kingdom
[130] Physics Department, University of Regina, Regina SK, Canada
[131] Ritsumeikan University, Kusatsu, Shiga, Japan
[132] [(a)] INFN Sezione di Roma I; [(b)] Dipartimento di Fisica, Università La Sapienza, Roma, Italy
[133] [(a)] INFN Sezione di Roma Tor Vergata; [(b)] Dipartimento di Fisica, Università di Roma Tor Vergata, Roma, Italy
[134] [(a)] INFN Sezione di Roma Tre; [(b)] Dipartimento di Fisica, Università Roma Tre, Roma, Italy
[135] [(a)] Faculté des Sciences Ain Chock, Réseau Universitaire de Physique des Hautes Energies – Université Hassan II, Casablanca; [(b)] Centre National de l'Energie des Sciences Techniques Nucleaires, Rabat; [(c)] Faculté des Sciences, Université Mohamed Premier and LPTPM, Oujda; [(d)] Faculté des Sciences, Université Mohammed V, Rabat, Morocco
[136] DSM/IRFU (Institut de Recherches sur les Lois Fondamentales de l'Univers), CEA Saclay (Commissariat a l'Energie Atomique), Gif-sur-Yvette, France
[137] Santa Cruz Institute for Particle Physics, University of California Santa Cruz, Santa Cruz, CA, United States
[138] Department of Physics, University of Washington, Seattle, WA, United States
[139] Department of Physics and Astronomy, University of Sheffield, Sheffield, United Kingdom
[140] Department of Physics, Shinshu University, Nagano, Japan
[141] Fachbereich Physik, Universität Siegen, Siegen, Germany
[142] Department of Physics, Simon Fraser University, Burnaby, BC, Canada
[143] SLAC National Accelerator Laboratory, Stanford, CA, United States
[144] [(a)] Faculty of Mathematics, Physics & Informatics, Comenius University, Bratislava; [(b)] Department of Subnuclear Physics, Institute of Experimental Physics of the Slovak Academy of Sciences, Kosice, Slovak Republic
[145] [(a)] Department of Physics, University of Johannesburg, Johannesburg; [(b)] School of Physics, University of the Witwatersrand, Johannesburg, South Africa
[146] [(a)] Department of Physics, Stockholm University; [(b)] The Oskar Klein Centre, Stockholm, Sweden
[147] Physics Department, Royal Institute of Technology, Stockholm, Sweden
[148] Department of Physics and Astronomy, Stony Brook University, Stony Brook, NY, United States
[149] Department of Physics and Astronomy, University of Sussex, Brighton, United Kingdom
[150] School of Physics, University of Sydney, Sydney, Australia
[151] Institute of Physics, Academia Sinica, Taipei, Taiwan
[152] Department of Physics, Technion: Israel Inst. of Technology, Haifa, Israel
[153] Raymond and Beverly Sackler School of Physics and Astronomy, Tel Aviv University, Tel Aviv, Israel
[154] Department of Physics, Aristotle University of Thessaloniki, Thessaloniki, Greece
[155] International Center for Elementary Particle Physics and Department of Physics, The University of Tokyo, Tokyo, Japan
[156] Graduate School of Science and Technology, Tokyo Metropolitan University, Tokyo, Japan
[157] Department of Physics, Tokyo Institute of Technology, Tokyo, Japan
[158] Department of Physics, University of Toronto, Toronto, ON, Canada
[159] [(a)] TRIUMF, Vancouver, BC; [(b)] Department of Physics and Astronomy, York University, Toronto, ON, Canada
[160] Institute of Pure and Applied Sciences, University of Tsukuba, Ibaraki, Japan
[161] Science and Technology Center, Tufts University, Medford, MA, United States
[162] Centro de Investigaciones, Universidad Antonio Narino, Bogota, Colombia
[163] Department of Physics and Astronomy, University of California Irvine, Irvine, CA, United States
[164] [(a)] INFN Gruppo Collegato di Udine; [(b)] ICTP, Trieste; [(c)] Dipartimento di Fisica, Università di Udine, Udine, Italy
[165] Department of Physics, University of Illinois, Urbana, IL, United States
[166] Department of Physics and Astronomy, University of Uppsala, Uppsala, Sweden
[167] Instituto de Física Corpuscular (IFIC) and Departamento de Física Atómica, Molecular y Nuclear and Departamento de Ingenierá Electrónica and Instituto de Microelectrónica de Barcelona (IMB-CNM), University of Valencia and CSIC, Valencia, Spain
[168] Department of Physics, University of British Columbia, Vancouver, BC, Canada
[169] Department of Physics and Astronomy, University of Victoria, Victoria, BC, Canada
[170] Waseda University, Tokyo, Japan
[171] Department of Particle Physics, The Weizmann Institute of Science, Rehovot, Israel
[172] Department of Physics, University of Wisconsin, Madison, WI, United States
[173] Fakultät für Physik und Astronomie, Julius-Maximilians-Universität, Würzburg, Germany
[174] Fachbereich C Physik, Bergische Universität Wuppertal, Wuppertal, Germany
[175] Department of Physics, Yale University, New Haven, CT, United States
[176] Yerevan Physics Institute, Yerevan, Armenia
[177] Domaine scientifique de la Doua, Centre de Calcul CNRS/IN2P3, Villeurbanne Cedex, France

[a] Also at Laboratorio de Instrumentacao e Fisica Experimental de Particulas – LIP, Lisboa, Portugal.
[b] Also at Faculdade de Ciencias and CFNUL, Universidade de Lisboa, Lisboa, Portugal.
[c] Also at CPPM, Aix-Marseille Universite and CNRS/IN2P3, Marseille, France.
[d] Also at TRIUMF, Vancouver, BC, Canada.
[e] Also at Faculty of Physics and Applied Computer Science, AGH – University of Science and Technology, Krakow, Poland.
[f] Also at Department of Physics, University of Coimbra, Coimbra, Portugal.
[g] Also at Università di Napoli Parthenope, Napoli, Italy.

[h] Also at Institute of Particle Physics (IPP), Canada.
[i] Also at Louisiana Tech University, Ruston, LA, United States.
[j] Also at Department of Physics, California State University, Fresno, CA, United States.
[k] Also at California Institute of Technology, Pasadena, CA, United States.
[l] Also at Louisiana Tech University, Ruston, LA, Unites States.
[m] Also at Group of Particle Physics, University of Montreal, Montreal, QC, Canada.
[n] Also at Institute of Physics, Azerbaijan Academy of Sciences, Baku, Azerbaijan.
[o] Also at Institut für Experimentalphysik, Universität Hamburg, Hamburg, Germany.
[p] Also at Manhattan College, New York, NY, United States.
[q] Also at School of Physics and Engineering, Sun Yat-sen University, Guangzhou, China.
[r] Also at Academia Sinica Grid Computing, Institute of Physics, Academia Sinica, Taipei, Taiwan.
[s] Also at High Energy Physics Group, Shandong University, Shandong, China.
[t] Also at Particle Physics Department, Rutherford Appleton Laboratory, Didcot, United Kingdom.
[u] Also at Departamento de Fisica, Universidade de Minho, Braga, Portugal.
[v] Also at Department of Physics and Astronomy, University of South Carolina, Columbia, SC, United States.
[w] Also at KFKI Research Institute for Particle and Nuclear Physics, Budapest, Hungary.
[x] Also at Institute of Physics, Jagiellonian University, Kracow, Poland.
[y] Also at Department of Physics, Oxford University, Oxford, United Kingdom.
[z] Also at DSM/IRFU, CEA Saclay, Gif-sur-Yvette, France.
[aa] Also at Laboratoire de Physique Nucléaire et de Hautes Energies, UPMC and Université Paris-Diderot and CNRS/IN2P3, Paris, France.
[ab] Also at Department of Physics, Nanjing University, Jiangsu, China.
[*] Deceased.

Physics Letters B 698 (2011) 353–370

Contents lists available at ScienceDirect

Physics Letters B

www.elsevier.com/locate/physletb

# Search for massive long-lived highly ionising particles with the ATLAS detector at the LHC ☆

ATLAS Collaboration *

ARTICLE INFO

*Article history:*
Received 2 February 2011
Received in revised form 16 March 2011
Accepted 16 March 2011
Available online 23 March 2011
Editor: M. Cvetič

*Keywords:*
High-energy collider experiment
Long-lived particle
Highly ionising
New physics

ABSTRACT

A search is made for massive highly ionising particles with lifetimes in excess of 100 ns, with the ATLAS experiment at the Large Hadron Collider, using 3.1 pb$^{-1}$ of $pp$ collision data taken at $\sqrt{s} = 7$ TeV. The signature of energy loss in the ATLAS inner detector and electromagnetic calorimeter is used. No such particles are found and limits on the production cross section for electric charges $6e \leqslant |q| \leqslant 17e$ and masses 200 GeV $\leqslant m \leqslant$ 1000 GeV are set in the range 1–12 pb for different hypotheses on the production mechanism.



## 1. Introduction

The observation of a massive long-lived highly ionising particle (HIP) possessing a large electric charge $|q| \gg e$, where $e$ is the elementary charge, would represent striking evidence for physics beyond the Standard Model. Examples of putative particles which can give rise to HIP signatures include $Q$-balls [1], stable micro black-hole remnants [2], magnetic monopoles [3] and dyons [4]. Searches for HIPs are made in cosmic rays [5] and at colliders [3]; recent collider searches were performed at LEP [6–8] and the Tevatron [9–12]. Cross sections and event topologies associated with HIP production cannot be reliably predicted due to the fact that the coupling between a HIP and the photon is so strong that perturbative calculations are not possible. Therefore, search results at colliders are usually quoted as cross section limits in a range of charge and mass for given kinematics [3]. Also, for the same reason, limits obtained at different collision energies or for different types of collisions cannot be directly compared; rather, they are complementary.

HIP searches are part of a program of searches at the CERN Large Hadron Collider (LHC) which explore the multi-TeV energy regime. Further motivation is provided by the gauge hierarchy problem, to which proposed solutions typically postulate the existence of hitherto unobserved particles with TeV-scale masses. HIPs at the LHC can be sought at the dedicated MoEDAL plastic-track experiment [13] or, as in this work, via their active detection at a multipurpose detector.

Due to their assumed large mass (hundreds of GeV), HIPs are characterised by their non-relativistic speed. The expected large amounts of energy loss per unit length ($\mathrm{d}E/\mathrm{d}x$) through ionisation (no bremsstrahlung) are mainly due to the high particle charge, but also due to the low speed. The ATLAS detector is well suited to detect HIPs. A HIP with sufficient kinetic energy would leave a track in the inner detector tracking system of ATLAS and lose its energy on its way to and through the electromagnetic calorimeter, giving rise to an electron-like signature. The presence of a HIP can be inferred from measurements of the proportion of high-ionisation hits in the inner detector. In addition, assuming isolation, the lateral extent of the energy deposition in the calorimeter is a sensitive discriminant between HIPs and Standard Model particles.

The ranges of HIP charge, mass and lifetime for which unambiguous conclusions can be drawn are determined by the chosen trigger and event selections. The choice of an electromagnetic trigger limits the phase space to HIPs which stop in the electromagnetic calorimeter of ATLAS. The search is optimised for data collected at relatively low instantaneous luminosities (up to $10^{31}$ cm$^{-2}$ s$^{-1}$), for which a low (10 GeV) trigger transverse energy threshold is available. In the barrel region of the calorimeter, this gives access to energy depositions corresponding to HIPs with electric charges down to $6e$. Standard electron reconstruction algorithms are used, which implies that tracks which bend like electrically charged particles are sought. Particles with magnetic charge, or electric charge above $17e$, are not addressed here due to the bending along the beam axis in the case of a monopole, and due to effects from delta electrons and electron recombination in the active detector at the corresponding values of energy loss ($\mathrm{d}E/\mathrm{d}x > 2 \cdot 10^3$ MeV/cm). For such types of HIPs, more detailed studies are needed to assess and minimise the impact of these

☆ © CERN, for the benefit of the ATLAS Collaboration.

* *E-mail address:* atlas.publications@cern.ch.

0370-2693/
doi:10.1016/j.physletb.2011.03.033

effects on the selection efficiency. The 1000 GeV upper bound in mass sensitivity is determined by trigger timing constraints, as a significantly heavier HIP (with charge 17$e$ or lower) would be delayed by more than 12 ns with respect to $\beta = 1$ when it stops in the electromagnetic calorimeter (this corresponds to $\beta < 0.3$), and would thus risk being triggered in the next proton bunch crossing. The search is sensitive to HIP lifetimes larger than 100 ns since a particle which decays much earlier in the calorimeter (even after stopping) would spoil the signature of a narrow energy deposition.

## 2. The ATLAS detector

The ATLAS detector [14] is a multipurpose particle physics apparatus with a forward–backward symmetric cylindrical geometry and near $4\pi$ coverage in solid angle.[1] A thin superconducting solenoid magnet surrounding the inner part of the ATLAS detector produces a field of approximately 2 T along the beam axis.

Inner detector (ID) tracking is performed by silicon-based detectors and an outer tracker using straw tubes with particle identification capabilities based on transition radiation (Transition Radiation Tracker, TRT). The TRT is divided into barrel (covering the pseudorapidity range $|\eta| < 1.0$) and endcap ($0.8 < |\eta| < 2.0$) components. A track gives a typical number of straw hits of 36. At the front-end electronics of the TRT, discriminators are used to compare the signal against low and high thresholds. While the TRT has two hit threshold levels, there is no upper limit to the amount of ionisation in a straw which will lead to a signal [15], guaranteeing that highly ionising particles would not escape detection in the TRT. Rather, they would produce a large number of high-threshold (HT) hits along their trajectories. The amount of ionisation in a straw tube needed for a TRT HT hit is roughly equivalent to three times that expected from a minimum ionising particle.

Liquid-argon sampling electromagnetic (EM) calorimeters, which comprise accordion-shaped electrodes and lead absorbers, surround the ID. The EM calorimeter barrel ($|\eta| < 1.475$) is used in this search. It is segmented transversely and divided in three layers in depth, denoted first, second, and third layer, respectively. In front of the accordion calorimeter a thin presampler layer is used to correct for fluctuations of energy loss. The typical cell granularity ($\Delta\eta \times \Delta\phi$) of the EM barrel is $0.003 \times 0.1$ in the first layer and $0.025 \times 0.025$ in the second layer. The signal expected for a HIP in the considered charge range lies in a region in time and energy where the electronic response in EM calorimeter cells is well understood and does not saturate. The robustness of the EM calorimeter energy reconstruction has been studied in detail and pulse shape predictions are consistent with the measured signals [16].

The stopping power of a HIP in the ATLAS detector depends on its charge, mass and energy, as well as the material budget along its path. Details of the latter are given in Ref. [17] in terms of number of radiation lengths $X_0$, as a function of depth and pseudorapidity. The integrated radiation length between the interaction point and the exit of the TRT is 0.5 $X_0$ at $\eta = 0$ and 1.5 $X_0$ at $|\eta| = 1.3$. The additional amount of material before the first layer of the EM calorimeter is 2.0 $X_0$ at $\eta = 0$ and 3.5 $X_0$ at $|\eta| = 1.3$. The thicknesses of the first, second and third EM layers are 4.5 $X_0$, 16.5 $X_0$ and 1.5 $X_0$ at $\eta = 0$ and 3 $X_0$, 20 $X_0$ and 5 $X_0$ at $|\eta| = 1.3$, respectively.

[1] ATLAS uses a right-handed coordinate system with its origin at the nominal interaction point (IP) in the centre of the detector and the $z$-axis coinciding with the axis of the beam pipe. The $x$-axis points from the IP to the centre of the LHC ring, and the $y$ axis points upward. Cylindrical coordinates $(r, \phi)$ are used in the transverse plane, $\phi$ being the azimuthal angle around the beam pipe. The pseudorapidity is defined in terms of the polar angle $\theta$ as $\eta = -\ln\tan(\theta/2)$.

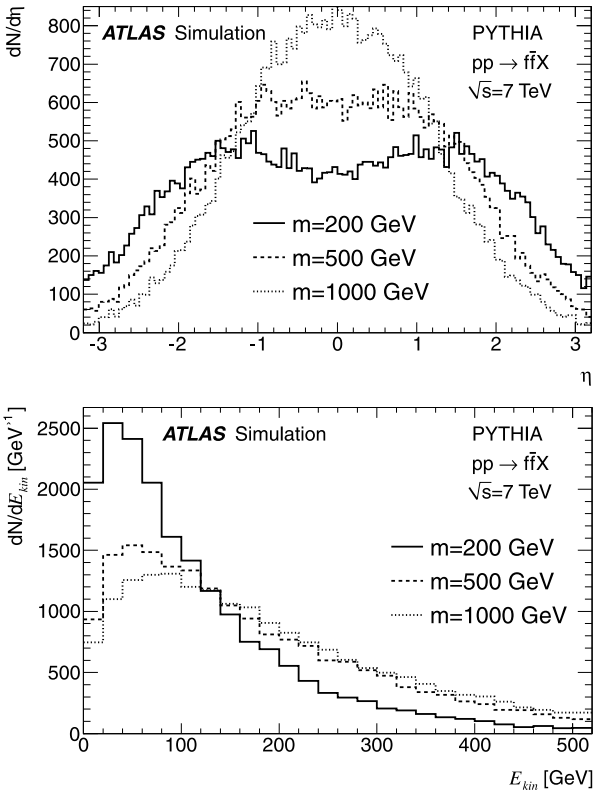


**Fig. 1.** Distributions of pseudorapidity $\eta$ (top) and kinetic energy $E_{kin}$ (bottom) at origin for heavy fermions produced with the Drell–Yan process. The latter is given with a requirement of $|\eta| < 1.35$. The distributions for the three different masses are normalised to the same number of entries.

## 3. Simulated event samples

Signal events are generated with the Pythia Monte Carlo (MC) event generator [18] according to the fermion pair production process: $p + p \to f + \bar{f} + X$. Ref. [19] is used for the parton distributions of the proton. Direct pair production implies that the HIPs are not part of a jet and thus isolated. A Drell–Yan-like production mechanism, modified to take into account the mass of the HIP [20], is used to model the kinematic properties of the HIPs. Generated $\eta$ distributions, as well as kinetic energy ($E_{kin}$) spectra in the central region ($|\eta| < 1.35$), are shown in Fig. 1 for the three mass points considered in this search.

An ATLAS detector simulation [21] based on Geant-4 [22] is used, where the particle interactions include secondary ionisation by delta electrons in addition to the standard ionisation process based on the Bethe–Bloch formula. A correction for electron–ion recombination effects in the EM calorimeter (Birks' correction) is applied, with typical visible energy fractions between 0.2 and 0.5 for the signal particles considered. Effects of delays are simulated, except for the ability to trigger slow-moving particles within the proton bunch crossing time, which is considered separately as a systematic uncertainty (see Section 6). Samples of approximately 20 000 events are produced for HIPs with masses of 200, 500 and 1000 GeV. For each mass point, HIPs with charges 6$e$, 10$e$ and 17$e$ are simulated.

A data-driven method is used in this work to estimate backgrounds surviving the final selections (see Section 4.2). However, in order to demonstrate that the distributions of the relevant observables are understood, a sample of simulated background events is used. The background sample, generated with Pythia [18] and labeled "Standard Model", consists mostly of QCD events in which

the hard subprocess is a strong 2-to-2 process with a matrix element transverse momentum cut-off of 15 GeV, but also includes contributions from heavy quark and vector boson production. A true transverse energy larger than 17 GeV in a typical first level trigger tower is also required. This sample contains $4 \cdot 10^7$ events and corresponds roughly to an integrated luminosity of 0.8 pb$^{-1}$.

## 4. Trigger and event selection

The collected data sample corresponds to an integrated luminosity of $3.1 \pm 0.3$ pb$^{-1}$, using a first level trigger based on energy deposits in the calorimeters. At the first level of the trigger, so-called trigger towers with dimension $\Delta\eta \times \Delta\phi = 0.1 \times 0.1$ are defined. In each trigger tower the cells of the electromagnetic or hadronic calorimeter are summed. EM clusters with fixed size $\Delta\eta \times \Delta\phi = 0.2 \times 0.2$ are sought and are retained if the total transverse energy ($E_T$) in an adjacent pair of their four trigger towers is above 5 GeV. Further electron-like higher level trigger requirements are imposed on the candidate, including $E_T > 10$ GeV, a matching to a track in the ID and a veto on hadronic leakage [23]. The efficiency of this trigger for the data under consideration is measured to be $(94.0 \pm 1.5)\%$ for electrons with $E_T > 15$ GeV and is well described by the simulation. The simulation predicts that a highly charged particle which stops in the EM barrel would be triggered with a similar efficiency or higher.

Offline electron candidates have cluster sizes of $\Delta\eta \times \Delta\phi = 0.075 \times 0.175$ in the EM barrel, with a matched track in a window of $\Delta\eta \times \Delta\phi = 0.05 \times 0.1$ amongst reconstructed tracks with transverse momentum larger than 0.5 GeV. Identification requirements corresponding to "medium" electrons [24], implying track and shower shape quality cuts, are applied to the candidates. These cuts filter out backgrounds but have a negligible impact on the signal, for which the cluster width is much narrower than for typical electrons. The cluster energy is estimated correcting for the energy deposited outside the active calorimeter regions, assuming an EM shower.

Further offline selections on the cluster transverse energy ($E_T > 15$ GeV) and pseudorapidity ($|\eta| < 1.35$) are imposed. The $E_T$ selection guarantees that the trigger efficiency is higher than 94% for the objects under study. The restriction of $|\eta| < 1.35$ excludes the transition region between the EM calorimeter barrel and endcap, reducing the probability for backgrounds to fake a narrow energy deposition.

### 4.1. Selection cuts

A loose selection based on TRT and EM calorimeter information is also imposed on the candidates to ensure that the quality of the track and cluster associated to the electron-like object is good enough to ensure the robustness of the HIP selection variables, and to provide a data sample with which to estimate the background rate. Only candidates with more than 10 TRT hits are retained. In addition to the $E_T > 15$ GeV cut for the EM cluster associated with the candidate, a significant fraction of the total cluster energy is required to be contained in six calorimeter cells among the first and second EM layers. This is done by requiring the summed energy in the three most energetic cells in each of the first and second layers to be greater than 2 and 4 GeV, respectively. Following these selections, 137 503 candidates remain in the data.

Two sets of observables are used in the final selection. The ID-based observable is the fraction, $f_{HT}$, of TRT hits on the track which pass the high threshold. The calorimeter-based discriminants are the fractions of energies outside of the three most energetic cells associated to a selected EM cluster, in the first and second EM calorimeter layers: $w_1$ and $w_2$.

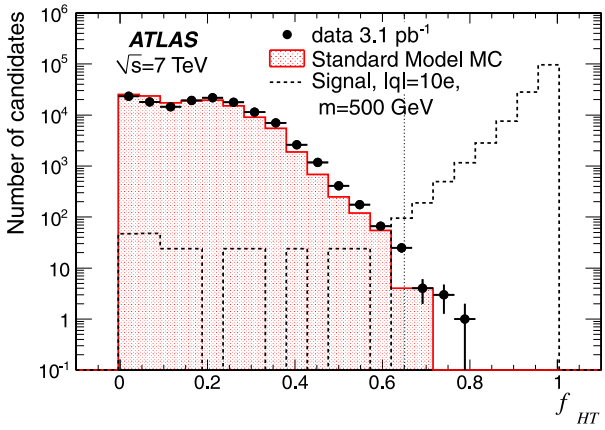


**Fig. 2.** Distribution of the fraction of TRT high-threshold hits for candidates satisfying the loose selection. Data (dots) are compared with area-normalised signal ($|q| = 10e$ and $m = 500$ GeV, dashed line) and Standard Model background (shaded area) simulations. The dotted line shows the selection cut value.

The $f_{HT}$ distribution for loosely selected candidates is shown in Fig. 2. The data extend up to $f_{HT} = 0.8$. The prediction of the signal simulation for a HIP of mass 500 GeV and charge $10e$ is also shown. It peaks at $f_{HT} \sim 1$ and has a small tail extending into the Standard Model region.

The distributions of $w_1$ and $w_2$ also provide good discrimination between signal and background, as shown in Fig. 3. For a signal, energy is deposited only in the few cells along the particle trajectory (as opposed to backgrounds which induce showers in the EM calorimeter) and the distributions peak around zero for both variables. The shapes of the measured distributions are well described by the background simulation. A faint double-peak structure is visible in data and in background simulations for the $f_{HT}$, $w_1$ and $w_2$ distributions in Figs. 2 and 3, where the main peak (closest to the signal) corresponds to electrons and the secondary peak corresponds to hadrons which fake the electron identification signature.

Finally, the following HIP selection is made: $f_{HT} > 0.65$, $w_1 < 0.20$ and $w_2 < 0.15$. For signal particles, these cuts reject only candidates in the tails of the distributions, and varying them has a minor impact on the efficiency; this feature is common to all considered charge and mass points. The cut values were chosen to yield a very small ($\ll 1$ event) expected background (see Section 4.2) while retaining a high ($\sim 96\%$) efficiency for the signal. No candidates in data or in simulated Standard Model events pass this selection.

### 4.2. Data-driven background estimation

A data-driven method is used to quantify the expected background yield after the HIP selection. Potential backgrounds consist mainly of electrons. For Standard Model candidates, the ID and calorimeter observables are correlated in a way that further suppresses the backgrounds (see Fig. 4). The background estimation assumes that $f_{HT}$ is uncorrelated with $w_1$ and $w_2$ and is thus conservative.

The yield of particle candidates passing the loose selection $N_{loose} = 137\,503$ can be divided into the following: $N_0$, $N_1$, $N_{f_{HT}}$, and $N_w$, which represent the number of candidates which satisfy both of the selections, neither of the selections, only the $f_{HT}$ selection, and only the $w_1$ and $w_2$ selections taken together, respectively. Even in the presence of a signal, $N_1$, $N_{f_{HT}}$ and $N_w$ would be dominantly composed of background events. The probability of a background candidate passing the TRT requirement is

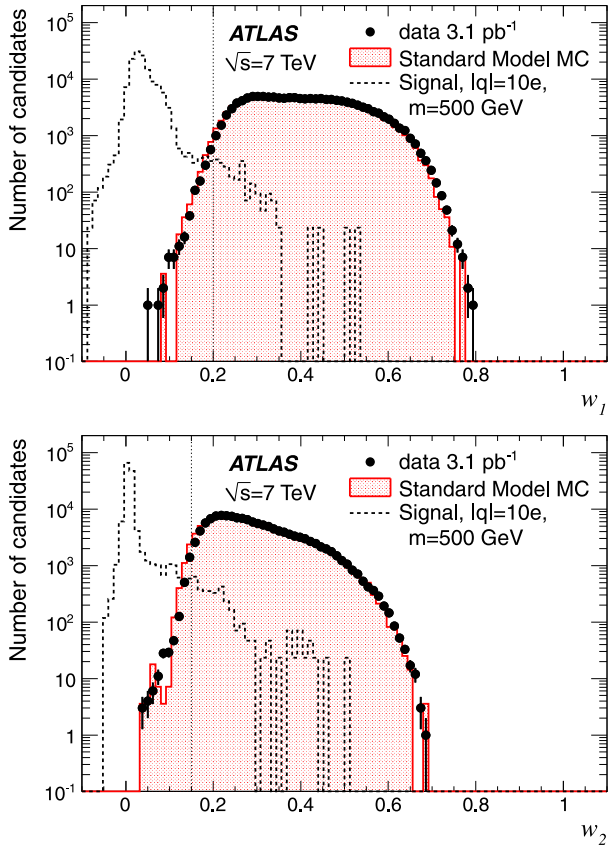


**Fig. 3.** Distributions of $w_1$ and $w_2$ following the loose selection. Data (dots) are compared with area-normalised signal ($|q| = 10e$ and $m = 500$ GeV, dashed lines) and Standard Model background (shaded area) simulations. Negative values are caused by pedestal fluctuations. Dotted lines show the selection cut values.

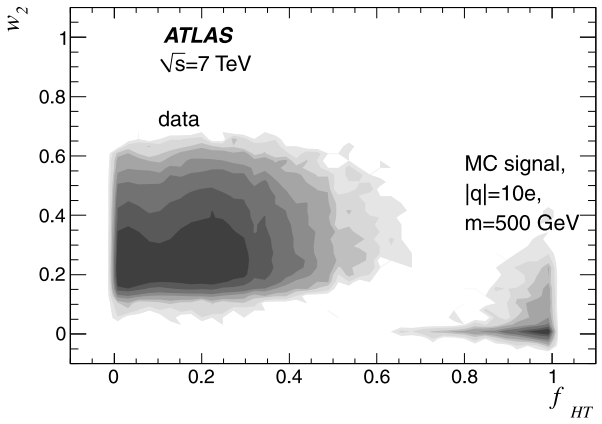


**Fig. 4.** Contours of $w_2$ versus $f_{HT}$ distributions following loose selection, showing the density of entries on a log scale. Data and signal Monte Carlo ($|q| = 10e$ and $m = 500$ GeV) are shown, and no candidates in the data appear near the signal region. The correlation factor between $w_2$ and $f_{HT}$ in the data is positive (coefficient 0.15); the same trend is also true for the correlation between $w_1$ and $f_{HT}$ (coefficient 0.18).

then $P_{f_{HT}} = \frac{N_{f_{HT}}}{(N_1+N_{f_{HT}})}$ and the probability to pass the calorimeter requirements is $P_w = \frac{N_w}{(N_1+N_w)}$, leading to an expectation of the number of background candidates entering the signal region: $N_{bg} = N_{loose} P_{f_{HT}} P_w$. The data sample yields $N_0 = 0$, $N_1 = 137\,342$, $N_{f_{HT}} = 18$ and $N_w = 143$, leading to $P_{f_{HT}} = (1.3 \pm 0.3) \cdot 10^{-4}$ and $P_w = (1.0 \pm 0.1) \cdot 10^{-3}$. The expected number of background candidates surviving the selection, and thereby the expected number of background events, is thus $N_{bg} = 0.019 \pm 0.005$. The quoted uncertainty is statistical.

## 5. Signal selection efficiency

### 5.1. Efficiencies in acceptance kinematic regions

The probability to retain a signal event can be factorised in two parts: acceptance (probability for a HIP in a region where the detector is sensitive) and efficiency (probability for this HIP to pass the selection cuts). The acceptance is defined here as the probability that at least one signal particle will be in the range $|\eta| < 1.35$ and stop in the second or third layer of the EM calorimeter. If this condition is satisfied, the simulation predicts a high probability to trigger on, reconstruct and select the event. This corresponds to the dark region in Fig. 5, which shows the predicted selection efficiency mapped as a function of the initial HIP pseudorapidity and kinetic energy, in the case of $|q| = 10e$ and $m = 500$ GeV. Such acceptance kinematic regions can be parametrised with three values defining three corners of a parallelogram. These parameters are summarised in Table 1. For HIPs produced inside such regions, the

**Table 1**
Kinetic energies (in GeV) defining the acceptance kinematic ranges for HIPs with the masses and electric charges considered in this search. The three columns correspond to the lower left, lower right, and upper left corners of parallelograms in the $(|\eta|, E_{kin})$ plane.

| $\|q\|$ | $m$ [GeV] | $E_{kin}^{min}$ ($\eta = 0$) | $E_{kin}^{min}$ ($\|\eta\| = 1.35$) | $E_{kin}^{max}$ ($\eta = 0$) |
|---|---|---|---|---|
| 6$e$ | 200 | 40 | 50 | 50 |
| 6$e$ | 500 | 50 | 70 | 70 |
| 6$e$ | 1000 | 60 | 130 | 80 |
| 10$e$ | 200 | 50 | 80 | 90 |
| 10$e$ | 500 | 80 | 110 | 130 |
| 10$e$ | 1000 | 110 | 150 | 180 |
| 17$e$ | 200 | 100 | 150 | 190 |
| 17$e$ | 500 | 150 | 190 | 260 |
| 17$e$ | 1000 | 190 | 240 | 350 |

**Table 2**
Expected fractions of HIP candidates passing the final selection, assuming they are isolated and produced inside the acceptance regions defined by the values in Table 1. Uncertainties due to MC statistics are quoted; other systematic uncertainties are discussed in Section 6.

| $m$ [GeV] | $\|q\| = 6e$ | $\|q\| = 10e$ | $\|q\| = 17e$ |
|---|---|---|---|
| 200 | $0.822 \pm 0.026$ | $0.820 \pm 0.015$ | $0.484 \pm 0.012$ |
| 500 | $0.868 \pm 0.021$ | $0.856 \pm 0.014$ | $0.617 \pm 0.011$ |
| 1000 | $0.558 \pm 0.019$ | $0.858 \pm 0.012$ | $0.700 \pm 0.012$ |

candidate selection efficiency is flat within 10% and takes values between 0.5 and 0.9 depending on the charge and mass (see Table 2). For $|q| = 17e$, the main source of inefficiency is the requirement on the number of TRT HT hits, which contributes up to 20% signal loss. This is largely due to the presence of track segments from delta electrons, which have a non-negligible probability to be chosen by the standard electron track matching algorithm. For low charges, inefficiencies are dominated by the cluster $E_T$ cut, typically accounting for $\sim 6\%$ loss. Other contributions, like trigger, electron reconstruction, and electron identification, can each cause 1–6% additional inefficiency.

### 5.2. Efficiencies for Drell–Yan kinematics

The estimated fractions of signal events where at least one candidate passes the final selection, assuming they are produced

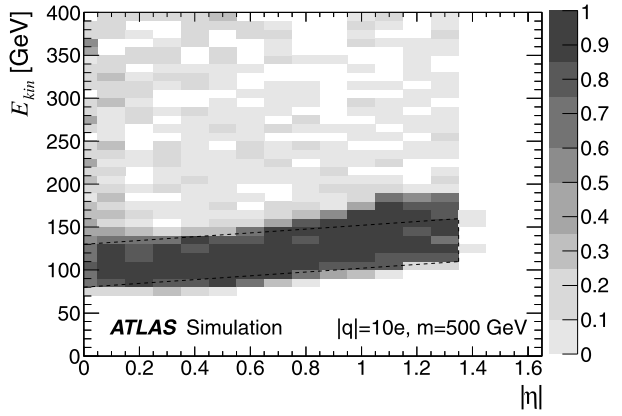


**Fig. 5.** Probability to pass all selection criteria as a function of pseudorapidity and kinetic energy at origin, for a HIP with charge 10$e$ and mass 500 GeV. The dark region corresponds to the kinetic range where the particle stops in or near the second layer of the EM calorimeter barrel and is parametrised with three energy values (dashed parallelogram, see Table 1).

**Table 3**
Expected fractions of signal events passing the final selection, assuming Drell–Yan kinematics. Uncertainties due to MC statistics are quoted; other systematic uncertainties are discussed in Section 6.

| $m$ [GeV] | $\|q\| = 6e$ | $\|q\| = 10e$ | $\|q\| = 17e$ |
|---|---|---|---|
| 200 | $0.102 \pm 0.002$ | $0.175 \pm 0.003$ | $0.112 \pm 0.002$ |
| 500 | $0.150 \pm 0.003$ | $0.236 \pm 0.003$ | $0.193 \pm 0.003$ |
| 1000 | $0.133 \pm 0.002$ | $0.299 \pm 0.004$ | $0.237 \pm 0.004$ |

with Drell–Yan kinematics, are shown in Table 3 for the values of charge and mass considered in this search. The dominant source of loss (70–85% loss) is from the kinematic acceptance, i.e., the production of HIPs with $|\eta| > 1.35$, as well as their stopping before they reach the second layer of the EM calorimeter, or after they reach the first layer of the hadronic calorimeter. The relative contributions from these various types of acceptance loss depend on mass and charge, as well as the kinematics of the assumed production model. The Drell–Yan production model implies that the fraction of HIPs produced in the acceptance region of pseudorapidity $|\eta| < 1.35$ is larger with increasing mass (see Fig. 1). Also, with the assumed energy spectra (bottom plot in Fig. 1), the acceptance is highest for intermediate charges ($|q| = 10e$), since HIPs with low charges tend to punch through the EM calorimeter and HIPs with high charges tend to stop before reaching it.

## 6. Systematic uncertainties

The major sources of systematic uncertainties affecting the efficiency estimation are summarised below. These mainly concern possible imperfections in the description of HIPs in the detector by the simulation.

- The recombination of electrons and ions in the sampling region of the EM calorimeter affects the measured current and thus the total visible energy. Recombination effects become larger with increasing $dE/dx$. In the ATLAS simulation, this is parametrised by Birks' law [25]. To estimate the uncertainty associated with the approximate modeling of recombination effects, predictions from the ATLAS implementation of Birks' correction [26] are compared to existing data of heavy ions punching through a layer of liquid argon [27–29]. In the range $2 \cdot 10^2$ MeV/cm $< dE/dx < 2 \cdot 10^3$ MeV/cm, which corresponds to typical HIP energy losses in the EM calorimeter for the charges and masses under consideration, the uncertainty in the simulated visible energy fraction is ±15%. This introduces between 4% and 23% uncertainty in the signal selection efficiency. The impact is largest for charge 6$e$, for which a lower visible energy would be more likely to push the candidate below the 15 GeV cluster $E_T$ threshold.
- The fraction of HIPs which stop in the detector prior to reaching the EM calorimeter is affected by the assumed amount of material in the GEANT-4 simulation. Varying the material density within the assumed uncertainty range ($\pm \sim 10\%$ [30]), independently in the ID and EM calorimeter volumes, leads to a 6% uncertainty in signal acceptance.
- The modeling of inactive or inefficient EM calorimeter regions in the simulation results in a 2% uncertainty in the signal efficiency.
- Cross-talk effects between EM calorimeter cells affect the $w_1$ and $w_2$ variables and this may not be accurately described by the simulation for large energy depositions per cell. The resulting uncertainty in signal efficiency is 2%.
- Secondary ionisation by delta electrons affects the track reconstruction and the calorimeter energy output. The amount of delta electrons in ATLAS detectors as described in GEANT-4 depends on the cutoff parameter (the radius beyond which delta electrons are considered separate from the mother particle). Varying this parameter results in a 3% uncertainty in the signal efficiency.
- For clusters delayed by more than 10 ns with respect to the expected arrival time of a highly relativistic particle, which corresponds to $\beta < 0.37$, there is a significant chance that the event is triggered in the next bunch crossing by the first level EM trigger. In most of the mass and charge range considered in this search, more than 99% of the particles which are energetic enough to reach the EM calorimeter and pass the event selection are in the high-efficiency range $\beta > 0.4$. The only exception is $|q| = 6e$ and $m = 1000$ GeV, for which the $\beta$ distribution after selection peaks between 0.32 and 0.47. The trigger efficiency loss is corrected for, resulting in an additional 25% uncertainty for this particular case.
- Uncertainties in the choice of parametrisation for the parton density functions (pdfs) of the proton have an impact on the event kinematics. To test this effect, events were generated (see Section 3) with 7 different pdfs from various sources [19, 31–34]. Assuming that acceptance variations due to the choice of pdf are Gaussian, the resulting relative uncertainty in the acceptance is 3%.
- The relative uncertainty in efficiency due to MC statistics is of the order of 2%.

**Table 4**
Relative systematic uncertainties in efficiency, combining in quadrature all the effects described in the text.

| $m$ [GeV] | $\|q\| = 6e$ | $\|q\| = 10e$ | $\|q\| = 17e$ |
|---|---|---|---|
| 200 | 25% | 11% | 9% |
| 500 | 17% | 10% | 9% |
| 1000 | 28% | 10% | 9% |

Other effects, like event pile-up and electron pick-up by positively charged particles, have been investigated and found to be negligible. Efficiency systematics are dominated by Birks' correction. The relative uncertainties in the signal selection efficiencies (Tables 2 and 3), obtained by adding all effects in quadrature, are shown in Table 4.

The systematic uncertainty in the absolute integrated luminosity is 11% [35].

**Table 5**
Inclusive HIP cross section upper limits (in pb) at 95% confidence level for isolated long-lived massive particles with high electric charges produced in regions of pseudorapidity and kinetic energy as defined in Table 1. Efficiencies in Table 2 and uncertainties in Table 4 were used in the cross section limit calculation.

| $m$ [GeV] | $\|q\| = 6e$ | $\|q\| = 10e$ | $\|q\| = 17e$ |
|---|---|---|---|
| 200 | 1.4 | 1.2 | 2.1 |
| 500 | 1.2 | 1.2 | 1.6 |
| 1000 | 2.2 | 1.2 | 1.5 |

**Table 6**
Pair production cross section upper limits (in pb) at 95% confidence level for long-lived massive particles with high electric charges, assuming a Drell–Yan mechanism. Efficiencies in Table 3 and uncertainties in Table 4 were used in the cross section limit calculation.

| $m$ [GeV] | $\|q\| = 6e$ | $\|q\| = 10e$ | $\|q\| = 17e$ |
|---|---|---|---|
| 200 | 11.5 | 5.9 | 9.1 |
| 500 | 7.2 | 4.3 | 5.3 |
| 1000 | 9.3 | 3.4 | 4.3 |

## 7. Upper limit on the cross section

A very low ($\ll 1$ event) background yield is expected and no events are observed to pass the selection. Knowing the integrated luminosity (3.1 pb$^{-1}$) and the selection efficiency for various model assumptions (Tables 2 and 3), cross section limits are obtained. This is done using a Bayesian statistical approach with a uniform prior for the signal and the standard assumption that the uncertainties in integrated luminosity (11%) and efficiency (Table 4) are Gaussian and independent. The limits are presented in Table 5 (for a particle produced in the acceptance kinematic region defined by Table 1) and in Table 6 (assuming Drell–Yan kinematics).

These limits can be approximately interpolated to intermediate values of mass and charge. Also, the limits quoted in Table 5 can be used to extract cross section limits for any given model of kinematics by correcting for the acceptance (fraction of events with at least one generated HIP in the ranges defined by Table 1): such a procedure yields conservative limits thanks to the fact that candidates beyond the sharp edges of the acceptance regions defined in Table 1 can also be accepted.

## 8. Summary

A search has been made for HIPs with lifetimes in excess of 100 ns produced in the ATLAS detector at the LHC using 3.1 pb$^{-1}$ of $pp$ collisions at $\sqrt{s} = 7$ TeV. The signature of high ionisation in an inner detector track matched to a narrow calorimeter cluster has been used. Upper cross section limits between 1.2 pb and 11.5 pb have been extracted for HIPs with electric charges between $6e$ and $17e$ and masses between 200 GeV and 1000 GeV, under two kinematics assumptions: a generic isolated HIP in a fiducial range of pseudorapidity and kinetic energy, or a Drell–Yan fermion pair production mechanism. HIP mass ranges above 800 GeV [11] are probed for the first time at a particle collider. These limits are the first constraints obtained on long-lived highly charged particle production at LHC collision energies.

## Open access



## References

[1] A. Kusenko, M.E. Shaposhnikov, Phys. Lett. B 418 (1998) 46, arXiv:hep-ph/9709492.
[2] B. Koch, M. Bleicher, H. Stoecker, J. Phys. G 34 (2007) 535, arXiv:hep-ph/0702187v2.
[3] M. Fairbairn, et al., Phys. Rep. 438 (2007) 1, arXiv:hep-ph/0611040.
[4] J.S. Schwinger, Phys. Rev. 144 (1966) 1087.
[5] SLIM Collaboration, Eur. Phys. J. C 57 (2008) 525, arXiv:0805.1797 [hep-ex].
[6] K. Kinoshita, et al., Phys. Rev. D 46 (1992) 881.
[7] J.L. Pinfold, et al., Phys. Lett. B 316 (1993) 407.
[8] OPAL Collaboration, Phys. Lett. B 663 (2008) 37, arXiv:0707.0404v1 [hep-ex].
[9] P.B. Price, G.-X. Ren, K. Kinoshita, Phys. Rev. Lett. 59 (1987) 2523.
[10] P.B. Price, G.-R. Jing, K. Kinoshita, Phys. Rev. Lett. 65 (1990) 149.
[11] M. Bertani, et al., Europhys. Lett. 12 (1990) 613.
[12] C.D.F. Collaboration, Phys. Rev. Lett. 96 (2006) 201801, arXiv:hep-ex/0509015v1.
[13] Moedal Collaboration, J. Pinfold, et al., Technical Design Report of the Moedal Experiment, CERN-LHCC-2009-006; MOEDAL-TDR-001, http://cdsweb.cern.ch/record/1181486, 2009.
[14] ATLAS Collaboration, G. Aad, et al., JINST 3 (2008) S08003.
[15] G. Abat, et al., JINST 3 (2008) P06007.
[16] ATLAS Collaboration, Eur. Phys. J. C 70 (2010) 723, arXiv:0912.2642v4 [physics.ins-det].
[17] ATLAS Collaboration, JINST 3 (2008) S08003.
[18] T. Sjostrand, S. Mrenna, P. Skands, JHEP 0605 (2006) 026, arXiv:hep-ph/0603175.
[19] A. Sherstnev, R.S. Thorne, Eur. Phys. J. C 55 (2008) 553, arXiv:0711.2473 [hep-ph].
[20] G.R. Kalbfleisch, W. Luo, K.A. Milton, E.H. Smith, M.G. Strauss, Phys. Rev. D 69 (2004) 052002, arXiv:hep-ex/0306045.
[21] ATLAS Collaboration, Eur. Phys. J. C 70 (2010) 823, arXiv:1005.4568v1 [physics.ins-det].
[22] GEANT4 Collaboration, S. Agostinelli, et al., Nucl. Instrum. Methods A 506 (2003) 250.
[23] ATLAS Collaboration, Performance of the electron and photon trigger in p–p collisions at $\sqrt{s} = 900$ GeV, ATLAS-CONF-2010-022, http://cdsweb.cern.ch/record/1277654, 2010.
[24] ATLAS Collaboration, JHEP 1012 (2010) 1, arXiv:1010.2130v1 [hep-ex].
[25] J. Birks, Phys. Rev. 86 (1952) 569.
[26] ATLAS Collaboration, Response and shower topology of 2 to 180 GeV pions measured with the ATLAS barrel calorimeter at the CERN test-beam and comparison to Monte Carlo simulations, ATL-CAL-PUB-2010-001, http://cdsweb.cern.ch/record/1263861, 2010.
[27] T. Doke, et al., Nucl. Instrum. Methods A 235 (1985) 136.
[28] E. Shibamura, et al., Nucl. Instrum. Methods A 260 (1987) 437.
[29] H.J. Crawford, et al., Nucl. Instrum. Methods A 256 (1987) 47.
[30] ATLAS Collaboration, Phys. Lett. B 688 (2010) 21, arXiv:1003.3124v2 [hep-ex].
[31] M. Gluck, E. Reya, A. Vogt, Z. Phys. C 67 (1995) 433.
[32] CTEQ Collaboration, H.L. Lai, et al., Eur. Phys. J. C 12 (2000) 375, arXiv:hep-ph/9903282.
[33] J. Pumplin, et al., JHEP 0207 (2002) 012, arXiv:hep-ph/0201195.
[34] A.D. Martin, W.J. Stirling, R.S. Thorne, G. Watt, Eur. Phys. J. C 63 (2009) 189, arXiv:0901.0002 [hep-ph].
[35] ATLAS Collaboration, Luminosity determination in pp collisions at $\sqrt{s} = 7$ TeV using the ATLAS detector at the LHC, arXiv:1101.2185v1 [hep-ex], Eur. Phys. J. C (2011), in press.

## ATLAS Collaboration

G. Aad [48], B. Abbott [111], J. Abdallah [11], A.A. Abdelalim [49], A. Abdesselam [118], O. Abdinov [10], B. Abi [112], M. Abolins [88], H. Abramowicz [153], H. Abreu [115], E. Acerbi [89a,89b], B.S. Acharya [164a,164b], D.L. Adams [24], T.N. Addy [56], J. Adelman [175], M. Aderholz [99], S. Adomeit [98], P. Adragna [75], T. Adye [129], S. Aefsky [22], J.A. Aguilar-Saavedra [124b,a], M. Aharrouche [81], S.P. Ahlen [21], F. Ahles [48], A. Ahmad [148], M. Ahsan [40],

G. Aielli [133a,133b], T. Akdogan [18a], T.P.A. Åkesson [79], G. Akimoto [155], A.V. Akimov [94], M.S. Alam [1], M.A. Alam [76], S. Albrand [55], M. Aleksa [29], I.N. Aleksandrov [65], M. Aleppo [89a,89b], F. Alessandria [89a], C. Alexa [25a], G. Alexander [153], G. Alexandre [49], T. Alexopoulos [9], M. Alhroob [20], M. Aliev [15], G. Alimonti [89a], J. Alison [120], M. Aliyev [10], P.P. Allport [73], S.E. Allwood-Spiers [53], J. Almond [82], A. Aloisio [102a,102b], R. Alon [171], A. Alonso [79], M.G. Alviggi [102a,102b], K. Amako [66], P. Amaral [29], C. Amelung [22], V.V. Ammosov [128], A. Amorim [124a,b], G. Amorós [167], N. Amram [153], C. Anastopoulos [139], T. Andeen [34], C.F. Anders [20], K.J. Anderson [30], A. Andreazza [89a,89b], V. Andrei [58a], M.-L. Andrieux [55], X.S. Anduaga [70], A. Angerami [34], F. Anghinolfi [29], N. Anjos [124a], A. Annovi [47], A. Antonaki [8], M. Antonelli [47], S. Antonelli [19a,19b], J. Antos [144b], F. Anulli [132a], S. Aoun [83], L. Aperio Bella [4], R. Apolle [118], G. Arabidze [88], I. Aracena [143], Y. Arai [66], A.T.H. Arce [44], J.P. Archambault [28], S. Arfaoui [29,c], J.-F. Arguin [14], E. Arik [18a,*], M. Arik [18a], A.J. Armbruster [87], S.R. Armstrong [24], O. Arnaez [81], C. Arnault [115], A. Artamonov [95], G. Artoni [132a,132b], D. Arutinov [20], S. Asai [155], R. Asfandiyarov [172], S. Ask [27], B. Åsman [146a,146b], L. Asquith [5], K. Assamagan [24], A. Astbury [169], A. Astvatsatourov [52], G. Atoian [175], B. Aubert [4], B. Auerbach [175], E. Auge [115], K. Augsten [127], M. Aurousseau [4], N. Austin [73], R. Avramidou [9], D. Axen [168], C. Ay [54], G. Azuelos [93,d], Y. Azuma [155], M.A. Baak [29], G. Baccaglioni [89a], C. Bacci [134a,134b], A.M. Bach [14], H. Bachacou [136], K. Bachas [29], G. Bachy [29], M. Backes [49], M. Backhaus [20], E. Badescu [25a], P. Bagnaia [132a,132b], S. Bahinipati [2], Y. Bai [32a], D.C. Bailey [158], T. Bain [158], J.T. Baines [129], O.K. Baker [175], M.D. Baker [24], S. Baker [77], F. Baltasar Dos Santos Pedrosa [29], E. Banas [38], P. Banerjee [93], Sw. Banerjee [169], D. Banfi [29], A. Bangert [137], V. Bansal [169], H.S. Bansil [17], L. Barak [171], S.P. Baranov [94], A. Barashkou [65], A. Barbaro Galtieri [14], T. Barber [27], E.L. Barberio [86], D. Barberis [50a,50b], M. Barbero [20], D.Y. Bardin [65], T. Barillari [99], M. Barisonzi [174], T. Barklow [143], N. Barlow [27], B.M. Barnett [129], R.M. Barnett [14], A. Baroncelli [134a], A.J. Barr [118], F. Barreiro [80], J. Barreiro Guimarães da Costa [57], P. Barrillon [115], R. Bartoldus [143], A.E. Barton [71], D. Bartsch [20], R.L. Bates [53], L. Batkova [144a], J.R. Batley [27], A. Battaglia [16], M. Battistin [29], G. Battistoni [89a], F. Bauer [136], H.S. Bawa [143], B. Beare [158], T. Beau [78], P.H. Beauchemin [118], R. Beccherle [50a], P. Bechtle [41], H.P. Beck [16], M. Beckingham [48], K.H. Becks [174], A.J. Beddall [18c], A. Beddall [18c], V.A. Bednyakov [65], C. Bee [83], M. Begel [24], S. Behar Harpaz [152], P.K. Behera [63], M. Beimforde [99], C. Belanger-Champagne [166], P.J. Bell [49], W.H. Bell [49], G. Bella [153], L. Bellagamba [19a], F. Bellina [29], G. Bellomo [89a,89b], M. Bellomo [119a], A. Belloni [57], K. Belotskiy [96], O. Beltramello [29], S. Ben Ami [152], O. Benary [153], D. Benchekroun [135a], C. Benchouk [83], M. Bendel [81], B.H. Benedict [163], N. Benekos [165], Y. Benhammou [153], D.P. Benjamin [44], M. Benoit [115], J.R. Bensinger [22], K. Benslama [130], S. Bentvelsen [105], D. Berge [29], E. Bergeaas Kuutmann [41], N. Berger [4], F. Berghaus [169], E. Berglund [49], J. Beringer [14], K. Bernardet [83], P. Bernat [115], R. Bernhard [48], C. Bernius [24], T. Berry [76], A. Bertin [19a,19b], F. Bertinelli [29], F. Bertolucci [122a,122b], M.I. Besana [89a,89b], N. Besson [136], S. Bethke [99], W. Bhimji [45], R.M. Bianchi [29], M. Bianco [72a,72b], O. Biebel [98], J. Biesiada [14], M. Biglietti [132a,132b], H. Bilokon [47], M. Bindi [19a,19b], A. Bingul [18c], C. Bini [132a,132b], C. Biscarat [177], U. Bitenc [48], K.M. Black [21], R.E. Blair [5], J.-B. Blanchard [115], G. Blanchot [29], C. Blocker [22], J. Blocki [38], A. Blondel [49], W. Blum [81], U. Blumenschein [54], G.J. Bobbink [105], V.B. Bobrovnikov [107], A. Bocci [44], R. Bock [29], C.R. Boddy [118], M. Boehler [41], J. Boek [174], N. Boelaert [35], S. Böser [77], J.A. Bogaerts [29], A. Bogdanchikov [107], A. Bogouch [90,*], C. Bohm [146a], V. Boisvert [76], T. Bold [163,e], V. Boldea [25a], M. Bona [75], M. Boonekamp [136], G. Boorman [76], C.N. Booth [139], P. Booth [139], S. Bordoni [78], C. Borer [16], A. Borisov [128], G. Borissov [71], I. Borjanovic [12a], S. Borroni [132a,132b], K. Bos [105], D. Boscherini [19a], M. Bosman [11], H. Boterenbrood [105], D. Botterill [129], J. Bouchami [93], J. Boudreau [123], E.V. Bouhova-Thacker [71], C. Boulahouache [123], C. Bourdarios [115], N. Bousson [83], A. Boveia [30], J. Boyd [29], I.R. Boyko [65], N.I. Bozhko [128], I. Bozovic-Jelisavcic [12b], J. Bracinik [17], A. Braem [29], E. Brambilla [72a,72b], P. Branchini [134a], G.W. Brandenburg [57], A. Brandt [7], G. Brandt [41], O. Brandt [54], U. Bratzler [156], B. Brau [84], J.E. Brau [114], H.M. Braun [174], B. Brelier [158], J. Bremer [29], R. Brenner [166], S. Bressler [152], D. Breton [115], N.D. Brett [118], P.G. Bright-Thomas [17], D. Britton [53], F.M. Brochu [27], I. Brock [20], R. Brock [88], T.J. Brodbeck [71], E. Brodet [153], F. Broggi [89a], C. Bromberg [88], G. Brooijmans [34], W.K. Brooks [31b], G. Brown [82], E. Brubaker [30], P.A. Bruckman de Renstrom [38], D. Bruncko [144b], R. Bruneliere [48], S. Brunet [61], A. Bruni [19a], G. Bruni [19a], M. Bruschi [19a], T. Buanes [13], F. Bucci [49], J. Buchanan [118], N.J. Buchanan [2], P. Buchholz [141], R.M. Buckingham [118], A.G. Buckley [45], S.I. Buda [25a], I.A. Budagov [65], B. Budick [108], V. Büscher [81], L. Bugge [117], D. Buira-Clark [118], E.J. Buis [105], O. Bulekov [96], M. Bunse [42], T. Buran [117], H. Burckhart [29], S. Burdin [73], T. Burgess [13], S. Burke [129], E. Busato [33], P. Bussey [53], C.P. Buszello [166],

F. Butin [29], B. Butler [143], J.M. Butler [21], C.M. Buttar [53], J.M. Butterworth [77], W. Buttinger [27], T. Byatt [77], S. Cabrera Urbán [167], M. Caccia [89a,89b], D. Caforio [19a,19b], O. Cakir [3a], P. Calafiura [14], G. Calderini [78], P. Calfayan [98], R. Calkins [106], L.P. Caloba [23a], R. Caloi [132a,132b], D. Calvet [33], S. Calvet [33], R. Camacho Toro [33], A. Camard [78], P. Camarri [133a,133b], M. Cambiaghi [119a,119b], D. Cameron [117], J. Cammin [20], S. Campana [29], M. Campanelli [77], V. Canale [102a,102b], F. Canelli [30], A. Canepa [159a], J. Cantero [80], L. Capasso [102a,102b], M.D.M. Capeans Garrido [29], I. Caprini [25a], M. Caprini [25a], D. Capriotti [99], M. Capua [36a,36b], R. Caputo [148], C. Caramarcu [25a], R. Cardarelli [133a], T. Carli [29], G. Carlino [102a], L. Carminati [89a,89b], B. Caron [159a], S. Caron [48], C. Carpentieri [48], G.D. Carrillo Montoya [172], S. Carron Montero [158], A.A. Carter [75], J.R. Carter [27], J. Carvalho [124a,f], D. Casadei [108], M.P. Casado [11], M. Cascella [122a,122b], C. Caso [50a,50b,*], A.M. Castaneda Hernandez [172], E. Castaneda-Miranda [172], V. Castillo Gimenez [167], N.F. Castro [124b,a], G. Cataldi [72a], F. Cataneo [29], A. Catinaccio [29], J.R. Catmore [71], A. Cattai [29], G. Cattani [133a,133b], S. Caughron [88], D. Cauz [164a,164c], A. Cavallari [132a,132b], P. Cavalleri [78], D. Cavalli [89a], M. Cavalli-Sforza [11], V. Cavasinni [122a,122b], A. Cazzato [72a,72b], F. Ceradini [134a,134b], A.S. Cerqueira [23a], A. Cerri [29], L. Cerrito [75], F. Cerutti [47], S.A. Cetin [18b], F. Cevenini [102a,102b], A. Chafaq [135a], D. Chakraborty [106], K. Chan [2], B. Chapleau [85], J.D. Chapman [27], J.W. Chapman [87], E. Chareyre [78], D.G. Charlton [17], V. Chavda [82], S. Cheatham [71], S. Chekanov [5], S.V. Chekulaev [159a], G.A. Chelkov [65], H. Chen [24], L. Chen [2], S. Chen [32c], T. Chen [32c], X. Chen [172], S. Cheng [32a], A. Cheplakov [65], V.F. Chepurnov [65], R. Cherkaoui El Moursli [135d], V. Chernyatin [24], E. Cheu [6], S.L. Cheung [158], L. Chevalier [136], F. Chevallier [136], G. Chiefari [102a,102b], L. Chikovani [51], J.T. Childers [58a], A. Chilingarov [71], G. Chiodini [72a], M.V. Chizhov [65], G. Choudalakis [30], S. Chouridou [137], I.A. Christidi [77], A. Christov [48], D. Chromek-Burckhart [29], M.L. Chu [151], J. Chudoba [125], G. Ciapetti [132a,132b], A.K. Ciftci [3a], R. Ciftci [3a], D. Cinca [33], V. Cindro [74], M.D. Ciobotaru [163], C. Ciocca [19a,19b], A. Ciocio [14], M. Cirilli [87], M. Ciubancan [25a], A. Clark [49], P.J. Clark [45], W. Cleland [123], J.C. Clemens [83], B. Clement [55], C. Clement [146a,146b], R.W. Clifft [129], Y. Coadou [83], M. Cobal [164a,164c], A. Coccaro [50a,50b], J. Cochran [64], P. Coe [118], J.G. Cogan [143], J. Coggeshall [165], E. Cogneras [177], C.D. Cojocaru [28], J. Colas [4], A.P. Colijn [105], C. Collard [115], N.J. Collins [17], C. Collins-Tooth [53], J. Collot [55], G. Colon [84], R. Coluccia [72a,72b], G. Comune [88], P. Conde Muiño [124a], E. Coniavitis [118], M.C. Conidi [11], M. Consonni [104], S. Constantinescu [25a], C. Conta [119a,119b], F. Conventi [102a,g], J. Cook [29], M. Cooke [14], B.D. Cooper [75], A.M. Cooper-Sarkar [118], N.J. Cooper-Smith [76], K. Copic [34], T. Cornelissen [50a,50b], M. Corradi [19a], F. Corriveau [85,h], A. Cortes-Gonzalez [165], G. Cortiana [99], G. Costa [89a], M.J. Costa [167], D. Costanzo [139], T. Costin [30], D. Côté [29], R. Coura Torres [23a], L. Courneyea [169], G. Cowan [76], C. Cowden [27], B.E. Cox [82], K. Cranmer [108], M. Cristinziani [20], G. Crosetti [36a,36b], R. Crupi [72a,72b], S. Crépé-Renaudin [55], C. Cuenca Almenar [175], T. Cuhadar Donszelmann [139], S. Cuneo [50a,50b], M. Curatolo [47], C.J. Curtis [17], P. Cwetanski [61], H. Czirr [141], Z. Czyczula [117], S. D'Auria [53], M. D'Onofrio [73], A. D'Orazio [132a,132b], A. Da Rocha Gesualdi Mello [23a], P.V.M. Da Silva [23a], C. Da Via [82], W. Dabrowski [37], A. Dahlhoff [48], T. Dai [87], C. Dallapiccola [84], S.J. Dallison [129,*], M. Dam [35], M. Dameri [50a,50b], D.S. Damiani [137], H.O. Danielsson [29], R. Dankers [105], D. Dannheim [99], V. Dao [49], G. Darbo [50a], G.L. Darlea [25b], C. Daum [105], J.P. Dauvergne [29], W. Davey [86], T. Davidek [126], N. Davidson [86], R. Davidson [71], M. Davies [93], A.R. Davison [77], E. Dawe [142], I. Dawson [139], J.W. Dawson [5,*], R.K. Daya [39], K. De [7], R. de Asmundis [102a], S. De Castro [19a,19b], P.E. De Castro Faria Salgado [24], S. De Cecco [78], J. de Graat [98], N. De Groot [104], P. de Jong [105], C. De La Taille [115], B. De Lotto [164a,164c], L. De Mora [71], L. De Nooij [105], M. De Oliveira Branco [29], D. De Pedis [132a], P. de Saintignon [55], A. De Salvo [132a], U. De Sanctis [164a,164c], A. De Santo [149], J.B. De Vivie De Regie [115], S. Dean [77], G. Dedes [99], D.V. Dedovich [65], J. Degenhardt [120], M. Dehchar [118], M. Deile [98], C. Del Papa [164a,164c], J. Del Peso [80], T. Del Prete [122a,122b], A. Dell'Acqua [29], L. Dell'Asta [89a,89b], M. Della Pietra [102a,g], D. della Volpe [102a,102b], M. Delmastro [29], P. Delpierre [83], N. Delruelle [29], P.A. Delsart [55], C. Deluca [148], S. Demers [175], M. Demichev [65], B. Demirkoz [11], J. Deng [163], S.P. Denisov [128], C. Dennis [118], D. Derendarz [38], J.E. Derkaoui [135c], F. Derue [78], P. Dervan [73], K. Desch [20], E. Devetak [148], P.O. Deviveiros [158], A. Dewhurst [129], B. DeWilde [148], S. Dhaliwal [158], R. Dhullipudi [24,i], A. Di Ciaccio [133a,133b], L. Di Ciaccio [4], A. Di Girolamo [29], B. Di Girolamo [29], S. Di Luise [134a,134b], A. Di Mattia [88], B. Di Micco [134a,134b], R. Di Nardo [133a,133b], A. Di Simone [133a,133b], R. Di Sipio [19a,19b], M.A. Diaz [31a], F. Diblen [18c], E.B. Diehl [87], H. Dietl [99], J. Dietrich [48], T.A. Dietzsch [58a], S. Diglio [115], K. Dindar Yagci [39], J. Dingfelder [20], C. Dionisi [132a,132b], P. Dita [25a], S. Dita [25a], F. Dittus [29], F. Djama [83], R. Djilkibaev [108], T. Djobava [51], M.A.B. do Vale [23a], A. Do Valle Wemans [124a], T.K.O. Doan [4], M. Dobbs [85],

R. Dobinson [29,*], D. Dobos [42], E. Dobson [29], M. Dobson [163], J. Dodd [34], O.B. Dogan [18a,*], C. Doglioni [118], T. Doherty [53], Y. Doi [66,*], J. Dolejsi [126], I. Dolenc [74], Z. Dolezal [126], B.A. Dolgoshein [96,*], T. Dohmae [155], M. Donadelli [23b], M. Donega [120], J. Donini [55], J. Dopke [174], A. Doria [102a], A. Dos Anjos [172], M. Dosil [11], A. Dotti [122a,122b], M.T. Dova [70], J.D. Dowell [17], A.D. Doxiadis [105], A.T. Doyle [53], Z. Drasal [126], J. Drees [174], N. Dressnandt [120], H. Drevermann [29], C. Driouichi [35], M. Dris [9], J.G. Drohan [77], J. Dubbert [99], T. Dubbs [137], S. Dube [14], E. Duchovni [171], G. Duckeck [98], A. Dudarev [29], F. Dudziak [115], M. Dührssen [29], I.P. Duerdoth [82], L. Duflot [115], M.-A. Dufour [85], M. Dunford [29], H. Duran Yildiz [3b], R. Duxfield [139], M. Dwuznik [37], F. Dydak [29], D. Dzahini [55], M. Düren [52], J. Ebke [98], S. Eckert [48], S. Eckweiler [81], K. Edmonds [81], C.A. Edwards [76], I. Efthymiopoulos [49], W. Ehrenfeld [41], T. Ehrich [99], T. Eifert [29], G. Eigen [13], K. Einsweiler [14], E. Eisenhandler [75], T. Ekelof [166], M. El Kacimi [4], M. Ellert [166], S. Elles [4], F. Ellinghaus [81], K. Ellis [75], N. Ellis [29], J. Elmsheuser [98], M. Elsing [29], R. Ely [14], D. Emeliyanov [129], R. Engelmann [148], A. Engl [98], B. Epp [62], A. Eppig [87], J. Erdmann [54], A. Ereditato [16], D. Eriksson [146a], J. Ernst [1], M. Ernst [24], J. Ernwein [136], D. Errede [165], S. Errede [165], E. Ertel [81], M. Escalier [115], C. Escobar [167], X. Espinal Curull [11], B. Esposito [47], F. Etienne [83], A.I. Etienvre [136], E. Etzion [153], D. Evangelakou [54], H. Evans [61], L. Fabbri [19a,19b], C. Fabre [29], K. Facius [35], R.M. Fakhrutdinov [128], S. Falciano [132a], A.C. Falou [115], Y. Fang [172], M. Fanti [89a,89b], A. Farbin [7], A. Farilla [134a], J. Farley [148], T. Farooque [158], S.M. Farrington [118], P. Farthouat [29], D. Fasching [172], P. Fassnacht [29], D. Fassouliotis [8], B. Fatholahzadeh [158], A. Favareto [89a,89b], L. Fayard [115], S. Fazio [36a,36b], R. Febbraro [33], P. Federic [144a], O.L. Fedin [121], I. Fedorko [29], W. Fedorko [88], M. Fehling-Kaschek [48], L. Feligioni [83], D. Fellmann [5], C.U. Felzmann [86], C. Feng [32d], E.J. Feng [30], A.B. Fenyuk [128], J. Ferencei [144b], J. Ferland [93], B. Fernandes [124a,j], W. Fernando [109], S. Ferrag [53], J. Ferrando [118], V. Ferrara [41], A. Ferrari [166], P. Ferrari [105], R. Ferrari [119a], A. Ferrer [167], M.L. Ferrer [47], D. Ferrere [49], C. Ferretti [87], A. Ferretto Parodi [50a,50b], M. Fiascaris [30], F. Fiedler [81], A. Filipčič [74], A. Filippas [9], F. Filthaut [104], M. Fincke-Keeler [169], M.C.N. Fiolhais [124a,f], L. Fiorini [11], A. Firan [39], G. Fischer [41], P. Fischer [20], M.J. Fisher [109], S.M. Fisher [129], J. Flammer [29], M. Flechl [48], I. Fleck [141], J. Fleckner [81], P. Fleischmann [173], S. Fleischmann [174], T. Flick [174], L.R. Flores Castillo [172], M.J. Flowerdew [99], F. Föhlisch [58a], M. Fokitis [9], T. Fonseca Martin [16], D.A. Forbush [138], A. Formica [136], A. Forti [82], D. Fortin [159a], J.M. Foster [82], D. Fournier [115], A. Foussat [29], A.J. Fowler [44], K. Fowler [137], H. Fox [71], P. Francavilla [122a,122b], S. Franchino [119a,119b], D. Francis [29], T. Frank [171], M. Franklin [57], S. Franz [29], M. Fraternali [119a,119b], S. Fratina [120], S.T. French [27], R. Froeschl [29], D. Froidevaux [29], J.A. Frost [27], C. Fukunaga [156], E. Fullana Torregrosa [29], J. Fuster [167], C. Gabaldon [29], O. Gabizon [171], T. Gadfort [24], S. Gadomski [49], G. Gagliardi [50a,50b], P. Gagnon [61], C. Galea [98], E.J. Gallas [118], M.V. Gallas [29], V. Gallo [16], B.J. Gallop [129], P. Gallus [125], E. Galyaev [40], K.K. Gan [109], Y.S. Gao [143,k], V.A. Gapienko [128], A. Gaponenko [14], F. Garberson [175], M. Garcia-Sciveres [14], C. García [167], J.E. García Navarro [49], R.W. Gardner [30], N. Garelli [29], H. Garitaonandia [105], V. Garonne [29], J. Garvey [17], C. Gatti [47], G. Gaudio [119a], O. Gaumer [49], B. Gaur [141], L. Gauthier [136], I.L. Gavrilenko [94], C. Gay [168], G. Gaycken [20], J.-C. Gayde [29], E.N. Gazis [9], P. Ge [32d], C.N.P. Gee [129], Ch. Geich-Gimbel [20], K. Gellerstedt [146a,146b], C. Gemme [50a], A. Gemmell [53], M.H. Genest [98], S. Gentile [132a,132b], F. Georgatos [9], S. George [76], P. Gerlach [174], A. Gershon [153], C. Geweniger [58a], H. Ghazlane [135d], P. Ghez [4], N. Ghodbane [33], B. Giacobbe [19a], S. Giagu [132a,132b], V. Giakoumopoulou [8], V. Giangiobbe [122a,122b], F. Gianotti [29], B. Gibbard [24], A. Gibson [158], S.M. Gibson [29], G.F. Gieraltowski [5], L.M. Gilbert [118], M. Gilchriese [14], V. Gilewsky [91], D. Gillberg [28], A.R. Gillman [129], D.M. Gingrich [2,d], J. Ginzburg [153], N. Giokaris [8], R. Giordano [102a,102b], F.M. Giorgi [15], P. Giovannini [99], P.F. Giraud [136], D. Giugni [89a], P. Giusti [19a], B.K. Gjelsten [117], L.K. Gladilin [97], C. Glasman [80], J. Glatzer [48], A. Glazov [41], K.W. Glitza [174], G.L. Glonti [65], J. Godfrey [142], J. Godlewski [29], M. Goebel [41], T. Göpfert [43], C. Goeringer [81], C. Gössling [42], T. Göttfert [99], S. Goldfarb [87], D. Goldin [39], T. Golling [175], N.P. Gollub [29], S.N. Golovnia [128], A. Gomes [124a,l], L.S. Gomez Fajardo [41], R. Gonçalo [76], L. Gonella [20], A. Gonidec [29], S. Gonzalez [172], S. González de la Hoz [167], M.L. Gonzalez Silva [26], S. Gonzalez-Sevilla [49], J.J. Goodson [148], L. Goossens [29], P.A. Gorbounov [95], H.A. Gordon [24], I. Gorelov [103], G. Gorfine [174], B. Gorini [29], E. Gorini [72a,72b], A. Gorišek [74], E. Gornicki [38], S.A. Gorokhov [128], V.N. Goryachev [128], B. Gosdzik [41], M. Gosselink [105], M.I. Gostkin [65], M. Gouanère [4], I. Gough Eschrich [163], M. Gouighri [135a], D. Goujdami [135a], M.P. Goulette [49], A.G. Goussiou [138], C. Goy [4], I. Grabowska-Bold [163,e], V. Grabski [176], P. Grafström [29], C. Grah [174], K.-J. Grahn [147], F. Grancagnolo [72a], S. Grancagnolo [15], V. Grassi [148], V. Gratchev [121], N. Grau [34], H.M. Gray [34,m], J.A. Gray [148], E. Graziani [134a], O.G. Grebenyuk [121], D. Greenfield [129], T. Greenshaw [73],

Z.D. Greenwood [24,i], I.M. Gregor [41], P. Grenier [143], E. Griesmayer [46], J. Griffiths [138], N. Grigalashvili [65], A.A. Grillo [137], K. Grimm [148], S. Grinstein [11], P.L.Y. Gris [33], Y.V. Grishkevich [97], J.-F. Grivaz [115], J. Grognuz [29], M. Groh [99], E. Gross [171], J. Grosse-Knetter [54], J. Groth-Jensen [79], M. Gruwe [29], K. Grybel [141], V.J. Guarino [5], C. Guicheney [33], A. Guida [72a,72b], T. Guillemin [4], S. Guindon [54], H. Guler [85,n], J. Gunther [125], B. Guo [158], J. Guo [34], A. Gupta [30], Y. Gusakov [65], V.N. Gushchin [128], A. Gutierrez [93], P. Gutierrez [111], N. Guttman [153], O. Gutzwiller [172], C. Guyot [136], C. Gwenlan [118], C.B. Gwilliam [73], A. Haas [143], S. Haas [29], C. Haber [14], R. Hackenburg [24], H.K. Hadavand [39], D.R. Hadley [17], P. Haefner [99], F. Hahn [29], S. Haider [29], Z. Hajduk [38], H. Hakobyan [176], J. Haller [54], K. Hamacher [174], A. Hamilton [49], S. Hamilton [161], H. Han [32a], L. Han [32b], K. Hanagaki [116], M. Hance [120], C. Handel [81], P. Hanke [58a], C.J. Hansen [166], J.R. Hansen [35], J.B. Hansen [35], J.D. Hansen [35], P.H. Hansen [35], P. Hansson [143], K. Hara [160], G.A. Hare [137], T. Harenberg [174], D. Harper [87], R.D. Harrington [21], O.M. Harris [138], K. Harrison [17], J. Hartert [48], F. Hartjes [105], T. Haruyama [66], A. Harvey [56], S. Hasegawa [101], Y. Hasegawa [140], S. Hassani [136], M. Hatch [29], D. Hauff [99], S. Haug [16], M. Hauschild [29], R. Hauser [88], M. Havranek [125], B.M. Hawes [118], C.M. Hawkes [17], R.J. Hawkings [29], D. Hawkins [163], T. Hayakawa [67], D. Hayden [76], H.S. Hayward [73], S.J. Haywood [129], E. Hazen [21], M. He [32d], S.J. Head [17], V. Hedberg [79], L. Heelan [28], S. Heim [88], B. Heinemann [14], S. Heisterkamp [35], L. Helary [4], M. Heldmann [48], M. Heller [115], S. Hellman [146a,146b], C. Helsens [11], R.C.W. Henderson [71], M. Henke [58a], A. Henrichs [54], A.M. Henriques Correia [29], S. Henrot-Versille [115], F. Henry-Couannier [83], C. Hensel [54], T. Henß [174], Y. Hernández Jiménez [167], R. Herrberg [15], A.D. Hershenhorn [152], G. Herten [48], R. Hertenberger [98], L. Hervas [29], N.P. Hessey [105], A. Hidvegi [146a], E. Higón-Rodriguez [167], D. Hill [5,*], J.C. Hill [27], N. Hill [5], K.H. Hiller [41], S. Hillert [20], S.J. Hillier [17], I. Hinchliffe [14], E. Hines [120], M. Hirose [116], F. Hirsch [42], D. Hirschbuehl [174], J. Hobbs [148], N. Hod [153], M.C. Hodgkinson [139], P. Hodgson [139], A. Hoecker [29], M.R. Hoeferkamp [103], J. Hoffman [39], D. Hoffmann [83], M. Hohlfeld [81], M. Holder [141], A. Holmes [118], S.O. Holmgren [146a], T. Holy [127], J.L. Holzbauer [88], R.J. Homer [17], Y. Homma [67], L. Hooft van Huysduynen [108], T. Horazdovsky [127], C. Horn [143], S. Horner [48], K. Horton [118], J.-Y. Hostachy [55], T. Hott [99], S. Hou [151], M.A. Houlden [73], A. Hoummada [135a], J. Howarth [82], D.F. Howell [118], I. Hristova [41], J. Hrivnac [115], I. Hruska [125], T. Hryn'ova [4], P.J. Hsu [175], S.-C. Hsu [14], G.S. Huang [111], Z. Hubacek [127], F. Hubaut [83], F. Huegging [20], T.B. Huffman [118], E.W. Hughes [34], G. Hughes [71], R.E. Hughes-Jones [82], M. Huhtinen [29], P. Hurst [57], M. Hurwitz [14], U. Husemann [41], N. Huseynov [65,o], J. Huston [88], J. Huth [57], G. Iacobucci [102a], G. Iakovidis [9], M. Ibbotson [82], I. Ibragimov [141], R. Ichimiya [67], L. Iconomidou-Fayard [115], J. Idarraga [115], M. Idzik [37], P. Iengo [4], O. Igonkina [105], Y. Ikegami [66], M. Ikeno [66], Y. Ilchenko [39], D. Iliadis [154], D. Imbault [78], M. Imhaeuser [174], M. Imori [155], T. Ince [20], J. Inigo-Golfin [29], P. Ioannou [8], M. Iodice [134a], G. Ionescu [4], A. Irles Quiles [167], K. Ishii [66], A. Ishikawa [67], M. Ishino [66], R. Ishmukhametov [39], T. Isobe [155], C. Issever [118], S. Istin [18a], Y. Itoh [101], A.V. Ivashin [128], W. Iwanski [38], H. Iwasaki [66], J.M. Izen [40], V. Izzo [102a], B. Jackson [120], J.N. Jackson [73], P. Jackson [143], M.R. Jaekel [29], V. Jain [61], K. Jakobs [48], S. Jakobsen [35], J. Jakubek [127], D.K. Jana [111], E. Jankowski [158], E. Jansen [77], A. Jantsch [99], M. Janus [20], G. Jarlskog [79], L. Jeanty [57], K. Jelen [37], I. Jen-La Plante [30], P. Jenni [29], A. Jeremie [4], P. Ježˇ [35], S. Jézéquel [4], H. Ji [172], W. Ji [81], J. Jia [148], Y. Jiang [32b], M. Jimenez Belenguer [29], G. Jin [32b], S. Jin [32a], O. Jinnouchi [157], M.D. Joergensen [35], D. Joffe [39], L.G. Johansen [13], M. Johansen [146a,146b], K.E. Johansson [146a], P. Johansson [139], S. Johnert [41], K.A. Johns [6], K. Jon-And [146a,146b], G. Jones [82], R.W.L. Jones [71], T.W. Jones [77], T.J. Jones [73], O. Jonsson [29], C. Joram [29], P.M. Jorge [124a,b], J. Joseph [14], X. Ju [130], V. Juranek [125], P. Jussel [62], V.V. Kabachenko [128], S. Kabana [16], M. Kaci [167], A. Kaczmarska [38], P. Kadlecik [35], M. Kado [115], H. Kagan [109], M. Kagan [57], S. Kaiser [99], E. Kajomovitz [152], S. Kalinin [174], L.V. Kalinovskaya [65], S. Kama [39], N. Kanaya [155], M. Kaneda [155], T. Kanno [157], V.A. Kantserov [96], J. Kanzaki [66], B. Kaplan [175], A. Kapliy [30], J. Kaplon [29], D. Kar [43], M. Karagoz [118], M. Karnevskiy [41], K. Karr [5], V. Kartvelishvili [71], A.N. Karyukhin [128], L. Kashif [57], A. Kasmi [39], R.D. Kass [109], A. Kastanas [13], M. Kataoka [4], Y. Kataoka [155], E. Katsoufis [9], J. Katzy [41], V. Kaushik [6], K. Kawagoe [67], T. Kawamoto [155], G. Kawamura [81], M.S. Kayl [105], V.A. Kazanin [107], M.Y. Kazarinov [65], S.I. Kazi [86], J.R. Keates [82], R. Keeler [169], R. Kehoe [39], M. Keil [54], G.D. Kekelidze [65], M. Kelly [82], J. Kennedy [98], C.J. Kenney [143], M. Kenyon [53], O. Kepka [125], N. Kerschen [29], B.P. Kerševan [74], S. Kersten [174], K. Kessoku [155], C. Ketterer [48], M. Khakzad [28], F. Khalil-zada [10], H. Khandanyan [165], A. Khanov [112], D. Kharchenko [65], A. Khodinov [148], A.G. Kholodenko [128], A. Khomich [58a], T.J. Khoo [27], G. Khoriauli [20], N. Khovanskiy [65], V. Khovanskiy [95], E. Khramov [65], J. Khubua [51], G. Kilvington [76],

H. Kim [7], M.S. Kim [2], P.C. Kim [143], S.H. Kim [160], N. Kimura [170], O. Kind [15], B.T. King [73], M. King [67], R.S.B. King [118], J. Kirk [129], G.P. Kirsch [118], L.E. Kirsch [22], A.E. Kiryunin [99], D. Kisielewska [37], T. Kittelmann [123], A.M. Kiver [128], H. Kiyamura [67], E. Kladiva [144b], J. Klaiber-Lodewigs [42], M. Klein [73], U. Klein [73], K. Kleinknecht [81], M. Klemetti [85], A. Klier [171], A. Klimentov [24], R. Klingenberg [42], E.B. Klinkby [35], T. Klioutchnikova [29], P.F. Klok [104], S. Klous [105], E.-E. Kluge [58a], T. Kluge [73], P. Kluit [105], S. Kluth [99], E. Kneringer [62], J. Knobloch [29], A. Knue [54], B.R. Ko [44], T. Kobayashi [155], M. Kobel [43], B. Koblitz [29], M. Kocian [143], A. Kocnar [113], P. Kodys [126], K. Köneke [29], A.C. König [104], S. Koenig [81], S. König [48], L. Köpke [81], F. Koetsveld [104], P. Koevesarki [20], T. Koffas [29], E. Koffeman [105], F. Kohn [54], Z. Kohout [127], T. Kohriki [66], T. Koi [143], T. Kokott [20], G.M. Kolachev [107], H. Kolanoski [15], V. Kolesnikov [65], I. Koletsou [89a], J. Koll [88], D. Kollar [29], M. Kollefrath [48], S.D. Kolya [82], A.A. Komar [94], J.R. Komaragiri [142], T. Kondo [66], T. Kono [41,p], A.I. Kononov [48], R. Konoplich [108,q], N. Konstantinidis [77], A. Kootz [174], S. Koperny [37], S.V. Kopikov [128], K. Korcyl [38], K. Kordas [154], V. Koreshev [128], A. Korn [14], A. Korol [107], I. Korolkov [11], E.V. Korolkova [139], V.A. Korotkov [128], O. Kortner [99], S. Kortner [99], V.V. Kostyukhin [20], M.J. Kotamäki [29], S. Kotov [99], V.M. Kotov [65], C. Kourkoumelis [8], V. Kouskoura [154], A. Koutsman [105], R. Kowalewski [169], T.Z. Kowalski [37], W. Kozanecki [136], A.S. Kozhin [128], V. Kral [127], V.A. Kramarenko [97], G. Kramberger [74], O. Krasel [42], M.W. Krasny [78], A. Krasznahorkay [108], J. Kraus [88], A. Kreisel [153], F. Krejci [127], J. Kretzschmar [73], N. Krieger [54], P. Krieger [158], K. Kroeninger [54], H. Kroha [99], J. Kroll [120], J. Kroseberg [20], J. Krstic [12a], U. Kruchonak [65], H. Krüger [20], Z.V. Krumshteyn [65], A. Kruth [20], T. Kubota [155], S. Kuehn [48], A. Kugel [58c], T. Kuhl [174], D. Kuhn [62], V. Kukhtin [65], Y. Kulchitsky [90], S. Kuleshov [31b], C. Kummer [98], M. Kuna [83], N. Kundu [118], J. Kunkle [120], A. Kupco [125], H. Kurashige [67], M. Kurata [160], Y.A. Kurochkin [90], V. Kus [125], W. Kuykendall [138], M. Kuze [157], P. Kuzhir [91], O. Kvasnicka [125], R. Kwee [15], A. La Rosa [29], L. La Rotonda [36a,36b], L. Labarga [80], J. Labbe [4], C. Lacasta [167], F. Lacava [132a,132b], H. Lacker [15], D. Lacour [78], V.R. Lacuesta [167], E. Ladygin [65], R. Lafaye [4], B. Laforge [78], T. Lagouri [80], S. Lai [48], E. Laisne [55], M. Lamanna [29], C.L. Lampen [6], W. Lampl [6], E. Lancon [136], U. Landgraf [48], M.P.J. Landon [75], H. Landsman [152], J.L. Lane [82], C. Lange [41], A.J. Lankford [163], F. Lanni [24], K. Lantzsch [29], V.V. Lapin [128,*], S. Laplace [78], C. Lapoire [20], J.F. Laporte [136], T. Lari [89a], A.V. Larionov [128], A. Larner [118], C. Lasseur [29], M. Lassnig [29], W. Lau [118], P. Laurelli [47], A. Lavorato [118], W. Lavrijsen [14], P. Laycock [73], A.B. Lazarev [65], A. Lazzaro [89a,89b], O. Le Dortz [78], E. Le Guirriec [83], C. Le Maner [158], E. Le Menedeu [136], M. Leahu [29], A. Lebedev [64], C. Lebel [93], T. LeCompte [5], F. Ledroit-Guillon [55], H. Lee [105], J.S.H. Lee [150], S.C. Lee [151], L. Lee [175], M. Lefebvre [169], M. Legendre [136], A. Leger [49], B.C. LeGeyt [120], F. Legger [98], C. Leggett [14], M. Lehmacher [20], G. Lehmann Miotto [29], M. Lehto [139], X. Lei [6], M.A.L. Leite [23b], R. Leitner [126], D. Lellouch [171], J. Lellouch [78], M. Leltchouk [34], V. Lendermann [58a], K.J.C. Leney [145b], T. Lenz [174], G. Lenzen [174], B. Lenzi [136], K. Leonhardt [43], S. Leontsinis [9], C. Leroy [93], J.-R. Lessard [169], J. Lesser [146a], C.G. Lester [27], A. Leung Fook Cheong [172], J. Levêque [83], D. Levin [87], L.J. Levinson [171], M.S. Levitski [128], M. Lewandowska [21], G.H. Lewis [108], M. Leyton [15], B. Li [83], H. Li [172], S. Li [32b], X. Li [87], Z. Liang [39], Z. Liang [118,r], B. Liberti [133a], P. Lichard [29], M. Lichtnecker [98], K. Lie [165], W. Liebig [13], R. Lifshitz [152], J.N. Lilley [17], A. Limosani [86], M. Limper [63], S.C. Lin [151,s], F. Linde [105], J.T. Linnemann [88], E. Lipeles [120], L. Lipinsky [125], A. Lipniacka [13], T.M. Liss [165], A. Lister [49], A.M. Litke [137], C. Liu [28], D. Liu [151,t], H. Liu [87], J.B. Liu [87], M. Liu [32b], S. Liu [2], Y. Liu [32b], M. Livan [119a,119b], S.S.A. Livermore [118], A. Lleres [55], S.L. Lloyd [75], E. Lobodzinska [41], P. Loch [6], W.S. Lockman [137], S. Lockwitz [175], T. Loddenkoetter [20], F.K. Loebinger [82], A. Loginov [175], C.W. Loh [168], T. Lohse [15], K. Lohwasser [48], M. Lokajicek [125], J. Loken [118], V.P. Lombardo [89a], R.E. Long [71], L. Lopes [124a,b], D. Lopez Mateos [34,m], M. Losada [162], P. Loscutoff [14], F. Lo Sterzo [132a,132b], M.J. Losty [159a], X. Lou [40], A. Lounis [115], K.F. Loureiro [162], J. Love [21], P.A. Love [71], A.J. Lowe [143], F. Lu [32a], J. Lu [2], L. Lu [39], H.J. Lubatti [138], C. Luci [132a,132b], A. Lucotte [55], A. Ludwig [43], D. Ludwig [41], I. Ludwig [48], J. Ludwig [48], F. Luehring [61], G. Luijckx [105], D. Lumb [48], L. Luminari [132a], E. Lund [117], B. Lund-Jensen [147], B. Lundberg [79], J. Lundberg [146a,146b], J. Lundquist [35], M. Lungwitz [81], A. Lupi [122a,122b], G. Lutz [99], D. Lynn [24], J. Lys [14], E. Lytken [79], H. Ma [24], L.L. Ma [172], J.A. Macana Goia [93], G. Maccarrone [47], A. Macchiolo [99], B. Maček [74], J. Machado Miguens [124a,b], D. Macina [49], R. Mackeprang [35], R.J. Madaras [14], W.F. Mader [43], R. Maenner [58c], T. Maeno [24], P. Mättig [174], S. Mättig [41], P.J. Magalhaes Martins [124a,f], L. Magnoni [29], E. Magradze [51], C.A. Magrath [104], Y. Mahalalel [153], K. Mahboubi [48], G. Mahout [17], C. Maiani [132a,132b], C. Maidantchik [23a], A. Maio [124a,l], S. Majewski [24], Y. Makida [66], N. Makovec [115], P. Mal [6], Pa. Malecki [38], P. Malecki [38], V.P. Maleev [121], F. Malek [55], U. Mallik [63], D. Malon [5], S. Maltezos [9],

V. Malyshev [107], S. Malyukov [65], R. Mameghani [98], J. Mamuzic [12b], A. Manabe [66], L. Mandelli [89a], I. Mandić [74], R. Mandrysch [15], J. Maneira [124a], P.S. Mangeard [88], I.D. Manjavidze [65], A. Mann [54], P.M. Manning [137], A. Manousakis-Katsikakis [8], B. Mansoulie [136], A. Manz [99], A. Mapelli [29], L. Mapelli [29], L. March [80], J.F. Marchand [29], F. Marchese [133a,133b], M. Marchesotti [29], G. Marchiori [78], M. Marcisovsky [125], A. Marin [21,*], C.P. Marino [61], F. Marroquim [23a], R. Marshall [82], Z. Marshall [34,m], F.K. Martens [158], S. Marti-Garcia [167], A.J. Martin [175], B. Martin [29], B. Martin [88], F.F. Martin [120], J.P. Martin [93], Ph. Martin [55], T.A. Martin [17], B. Martin dit Latour [49], M. Martinez [11], V. Martinez Outschoorn [57], A.C. Martyniuk [82], M. Marx [82], F. Marzano [132a], A. Marzin [111], L. Masetti [81], T. Mashimo [155], R. Mashinistov [94], J. Masik [82], A.L. Maslennikov [107], M. Maß [42], I. Massa [19a,19b], G. Massaro [105], N. Massol [4], A. Mastroberardino [36a,36b], T. Masubuchi [155], M. Mathes [20], P. Matricon [115], H. Matsumoto [155], H. Matsunaga [155], T. Matsushita [67], C. Mattravers [118,u], J.M. Maugain [29], S.J. Maxfield [73], E.N. May [5], A. Mayne [139], R. Mazini [151], M. Mazur [20], M. Mazzanti [89a], E. Mazzoni [122a,122b], S.P. Mc Kee [87], A. McCarn [165], R.L. McCarthy [148], T.G. McCarthy [28], N.A. McCubbin [129], K.W. McFarlane [56], J.A. Mcfayden [139], H. McGlone [53], G. Mchedlidze [51], R.A. McLaren [29], T. Mclaughlan [17], S.J. McMahon [129], T.J. McMahon [17], R.A. McPherson [169,h], A. Meade [84], J. Mechnich [105], M. Mechtel [174], M. Medinnis [41], R. Meera-Lebbai [111], T. Meguro [116], R. Mehdiyev [93], S. Mehlhase [41], A. Mehta [73], K. Meier [58a], J. Meinhardt [48], B. Meirose [79], C. Melachrinos [30], B.R. Mellado Garcia [172], L. Mendoza Navas [162], Z. Meng [151,t], A. Mengarelli [19a,19b], S. Menke [99], C. Menot [29], E. Meoni [11], D. Merkl [98], P. Mermod [118], L. Merola [102a,102b], C. Meroni [89a], F.S. Merritt [30], A. Messina [29], J. Metcalfe [103], A.S. Mete [64], S. Meuser [20], C. Meyer [81], J.-P. Meyer [136], J. Meyer [173], J. Meyer [54], T.C. Meyer [29], W.T. Meyer [64], J. Miao [32d], S. Michal [29], L. Micu [25a], R.P. Middleton [129], P. Miele [29], S. Migas [73], L. Mijović [41], G. Mikenberg [171], M. Mikestikova [125], B. Mikulec [49], M. Mikuž [74], D.W. Miller [143], R.J. Miller [88], W.J. Mills [168], C. Mills [57], A. Milov [171], D.A. Milstead [146a,146b], D. Milstein [171], A.A. Minaenko [128], M. Miñano [167], I.A. Minashvili [65], A.I. Mincer [108], B. Mindur [37], M. Mineev [65], Y. Ming [130], L.M. Mir [11], G. Mirabelli [132a], L. Miralles Verge [11], A. Misiejuk [76], A. Mitra [118], J. Mitrevski [137], G.Y. Mitrofanov [128], V.A. Mitsou [167], S. Mitsui [66], P.S. Miyagawa [82], K. Miyazaki [67], J.U. Mjörnmark [79], T. Moa [146a,146b], P. Mockett [138], S. Moed [57], V. Moeller [27], K. Mönig [41], N. Möser [20], S. Mohapatra [148], B. Mohn [13], W. Mohr [48], S. Mohrdieck-Möck [99], A.M. Moisseev [128,*], R. Moles-Valls [167], J. Molina-Perez [29], L. Moneta [49], J. Monk [77], E. Monnier [83], S. Montesano [89a,89b], F. Monticelli [70], S. Monzani [19a,19b], R.W. Moore [2], G.F. Moorhead [86], C. Mora Herrera [49], A. Moraes [53], A. Morais [124a,b], N. Morange [136], J. Morel [54], G. Morello [36a,36b], D. Moreno [81], M. Moreno Llácer [167], P. Morettini [50a], M. Morii [57], J. Morin [75], Y. Morita [66], A.K. Morley [29], G. Mornacchi [29], M.-C. Morone [49], J.D. Morris [75], H.G. Moser [99], M. Mosidze [51], J. Moss [109], R. Mount [143], E. Mountricha [9], S.V. Mouraviev [94], E.J.W. Moyse [84], M. Mudrinic [12b], F. Mueller [58a], J. Mueller [123], K. Mueller [20], T.A. Müller [98], D. Muenstermann [42], A. Muijs [105], A. Muir [168], Y. Munwes [153], K. Murakami [66], W.J. Murray [129], I. Mussche [105], E. Musto [102a,102b], A.G. Myagkov [128], M. Myska [125], J. Nadal [11], K. Nagai [160], K. Nagano [66], Y. Nagasaka [60], A.M. Nairz [29], Y. Nakahama [115], K. Nakamura [155], I. Nakano [110], G. Nanava [20], A. Napier [161], M. Nash [77,u], N.R. Nation [21], T. Nattermann [20], T. Naumann [41], G. Navarro [162], H.A. Neal [87], E. Nebot [80], P.Yu. Nechaeva [94], A. Negri [119a,119b], G. Negri [29], S. Nektarijevic [49], A. Nelson [64], S. Nelson [143], T.K. Nelson [143], S. Nemecek [125], P. Nemethy [108], A.A. Nepomuceno [23a], M. Nessi [29], S.Y. Nesterov [121], M.S. Neubauer [165], A. Neusiedl [81], R.M. Neves [108], P. Nevski [24], P.R. Newman [17], R.B. Nickerson [118], R. Nicolaidou [136], L. Nicolas [139], B. Nicquevert [29], F. Niedercorn [115], J. Nielsen [137], T. Niinikoski [29], A. Nikiforov [15], V. Nikolaenko [128], K. Nikolaev [65], I. Nikolic-Audit [78], K. Nikolopoulos [24], H. Nilsen [48], P. Nilsson [7], Y. Ninomiya [155], A. Nisati [132a], T. Nishiyama [67], R. Nisius [99], L. Nodulman [5], M. Nomachi [116], I. Nomidis [154], H. Nomoto [155], M. Nordberg [29], B. Nordkvist [146a,146b], P.R. Norton [129], J. Novakova [126], M. Nozaki [66], M. Nožička [41], I.M. Nugent [159a], A.-E. Nuncio-Quiroz [20], G. Nunes Hanninger [20], T. Nunnemann [98], E. Nurse [77], T. Nyman [29], B.J. O'Brien [45], S.W. O'Neale [17,*], D.C. O'Neil [142], V. O'Shea [53], F.G. Oakham [28,d], H. Oberlack [99], J. Ocariz [78], A. Ochi [67], S. Oda [155], S. Odaka [66], J. Odier [83], G.A. Odino [50a,50b], H. Ogren [61], A. Oh [82], S.H. Oh [44], C.C. Ohm [146a,146b], T. Ohshima [101], H. Ohshita [140], T.K. Ohska [66], T. Ohsugi [59], S. Okada [67], H. Okawa [163], Y. Okumura [101], T. Okuyama [155], M. Olcese [50a], A.G. Olchevski [65], M. Oliveira [124a,f], D. Oliveira Damazio [24], E. Oliver Garcia [167], D. Olivito [120], A. Olszewski [38], J. Olszowska [38], C. Omachi [67], A. Onofre [124a,v], P.U.E. Onyisi [30], C.J. Oram [159a], G. Ordonez [104], M.J. Oreglia [30], F. Orellana [49], Y. Oren [153], D. Orestano [134a,134b], I. Orlov [107], C. Oropeza Barrera [53], R.S. Orr [158], E.O. Ortega [130], B. Osculati [50a,50b],

R. Ospanov [120], C. Osuna [11], G. Otero y Garzon [26], J.P. Ottersbach [105], M. Ouchrif [135c], F. Ould-Saada [117], A. Ouraou [136], Q. Ouyang [32a], M. Owen [82], S. Owen [139], A. Oyarzun [31b], O.K. Øye [13], V.E. Ozcan [77], N. Ozturk [7], A. Pacheco Pages [11], C. Padilla Aranda [11], E. Paganis [139], F. Paige [24], K. Pajchel [117], S. Palestini [29], D. Pallin [33], A. Palma [124a,b], J.D. Palmer [17], Y.B. Pan [172], E. Panagiotopoulou [9], B. Panes [31a], N. Panikashvili [87], S. Panitkin [24], D. Pantea [25a], M. Panuskova [125], V. Paolone [123], A. Paoloni [133a,133b], A. Papadelis [146a], Th.D. Papadopoulou [9], A. Paramonov [5], W. Park [24,w], M.A. Parker [27], F. Parodi [50a,50b], J.A. Parsons [34], U. Parzefall [48], E. Pasqualucci [132a], A. Passeri [134a], F. Pastore [134a,134b], Fr. Pastore [29], G. Pásztor [49,x], S. Pataraia [172], N. Patel [150], J.R. Pater [82], S. Patricelli [102a,102b], T. Pauly [29], M. Pecsy [144a], M.I. Pedraza Morales [172], S.V. Peleganchuk [107], H. Peng [172], R. Pengo [29], A. Penson [34], J. Penwell [61], M. Perantoni [23a], K. Perez [34,m], T. Perez Cavalcanti [41], E. Perez Codina [11], M.T. Pérez García-Estañ [167], V. Perez Reale [34], I. Peric [20], L. Perini [89a,89b], H. Pernegger [29], R. Perrino [72a], P. Perrodo [4], S. Persembe [3a], A. Perus [115], V.D. Peshekhonov [65], O. Peters [105], B.A. Petersen [29], J. Petersen [29], T.C. Petersen [35], E. Petit [83], A. Petridis [154], C. Petridou [154], E. Petrolo [132a], F. Petrucci [134a,134b], D. Petschull [41], M. Petteni [142], R. Pezoa [31b], A. Phan [86], A.W. Phillips [27], P.W. Phillips [129], G. Piacquadio [29], E. Piccaro [75], M. Piccinini [19a,19b], A. Pickford [53], S.M. Piec [41], R. Piegaia [26], J.E. Pilcher [30], A.D. Pilkington [82], J. Pina [124a,l], M. Pinamonti [164a,164c], A. Pinder [118], J.L. Pinfold [2], J. Ping [32c], B. Pinto [124a,b], O. Pirotte [29], C. Pizio [89a,89b], R. Placakyte [41], M. Plamondon [169], W.G. Plano [82], M.-A. Pleier [24], A.V. Pleskach [128], A. Poblaguev [24], S. Poddar [58a], F. Podlyski [33], L. Poggioli [115], T. Poghosyan [20], M. Pohl [49], F. Polci [55], G. Polesello [119a], A. Policicchio [138], A. Polini [19a], J. Poll [75], V. Polychronakos [24], D.M. Pomarede [136], D. Pomeroy [22], K. Pommès [29], L. Pontecorvo [132a], B.G. Pope [88], G.A. Popeneciu [25a], D.S. Popovic [12a], A. Poppleton [29], X. Portell Bueso [48], R. Porter [163], C. Posch [21], G.E. Pospelov [99], S. Pospisil [127], I.N. Potrap [99], C.J. Potter [149], C.T. Potter [85], G. Poulard [29], J. Poveda [172], R. Prabhu [77], P. Pralavorio [83], S. Prasad [57], R. Pravahan [7], S. Prell [64], K. Pretzl [16], L. Pribyl [29], D. Price [61], L.E. Price [5], M.J. Price [29], P.M. Prichard [73], D. Prieur [123], M. Primavera [72a], K. Prokofiev [108], F. Prokoshin [31b], S. Protopopescu [24], J. Proudfoot [5], X. Prudent [43], H. Przysiezniak [4], S. Psoroulas [20], E. Ptacek [114], J. Purdham [87], M. Purohit [24,w], P. Puzo [115], Y. Pylypchenko [117], J. Qian [87], Z. Qian [83], Z. Qin [41], A. Quadt [54], D.R. Quarrie [14], W.B. Quayle [172], F. Quinonez [31a], M. Raas [104], V. Radescu [58b], B. Radics [20], T. Rador [18a], F. Ragusa [89a,89b], G. Rahal [177], A.M. Rahimi [109], S. Rajagopalan [24], S. Rajek [42], M. Rammensee [48], M. Rammes [141], M. Ramstedt [146a,146b], K. Randrianarivony [28], P.N. Ratoff [71], F. Rauscher [98], E. Rauter [99], M. Raymond [29], A.L. Read [117], D.M. Rebuzzi [119a,119b], A. Redelbach [173], G. Redlinger [24], R. Reece [120], K. Reeves [40], A. Reichold [105], E. Reinherz-Aronis [153], A. Reinsch [114], I. Reisinger [42], D. Reljic [12a], C. Rembser [29], Z.L. Ren [151], A. Renaud [115], P. Renkel [39], B. Rensch [35], M. Rescigno [132a], S. Resconi [89a], B. Resende [136], P. Reznicek [98], R. Rezvani [158], A. Richards [77], R. Richter [99], E. Richter-Was [38,y], M. Ridel [78], S. Rieke [81], M. Rijpstra [105], M. Rijssenbeek [148], A. Rimoldi [119a,119b], L. Rinaldi [19a], R.R. Rios [39], I. Riu [11], G. Rivoltella [89a,89b], F. Rizatdinova [112], E. Rizvi [75], S.H. Robertson [85,h], A. Robichaud-Veronneau [49], D. Robinson [27], J.E.M. Robinson [77], M. Robinson [114], A. Robson [53], J.G. Rocha de Lima [106], C. Roda [122a,122b], D. Roda Dos Santos [29], S. Rodier [80], D. Rodriguez [162], Y. Rodriguez Garcia [15], A. Roe [54], S. Roe [29], O. Røhne [117], V. Rojo [1], S. Rolli [161], A. Romaniouk [96], V.M. Romanov [65], G. Romeo [26], D. Romero Maltrana [31a], L. Roos [78], E. Ros [167], S. Rosati [138], M. Rose [76], G.A. Rosenbaum [158], E.I. Rosenberg [64], P.L. Rosendahl [13], L. Rosselet [49], V. Rossetti [11], E. Rossi [102a,102b], L.P. Rossi [50a], L. Rossi [89a,89b], M. Rotaru [25a], I. Roth [171], J. Rothberg [138], I. Rottländer [20], D. Rousseau [115], C.R. Royon [136], A. Rozanov [83], Y. Rozen [152], X. Ruan [115], I. Rubinskiy [41], B. Ruckert [98], N. Ruckstuhl [105], V.I. Rud [97], G. Rudolph [62], F. Rühr [6], A. Ruiz-Martinez [64], E. Rulikowska-Zarebska [37], V. Rumiantsev [91,*], L. Rumyantsev [65], K. Runge [48], O. Runolfsson [20], Z. Rurikova [48], N.A. Rusakovich [65], D.R. Rust [61], J.P. Rutherfoord [6], C. Ruwiedel [14], P. Ruzicka [125], Y.F. Ryabov [121], V. Ryadovikov [128], P. Ryan [88], M. Rybar [126], G. Rybkin [115], N.C. Ryder [118], S. Rzaeva [10], A.F. Saavedra [150], I. Sadeh [153], H.F.-W. Sadrozinski [137], R. Sadykov [65], F. Safai Tehrani [132a,132b], H. Sakamoto [155], G. Salamanna [105], A. Salamon [133a], M. Saleem [111], D. Salihagic [99], A. Salnikov [143], J. Salt [167], B.M. Salvachua Ferrando [5], D. Salvatore [36a,36b], F. Salvatore [149], A. Salzburger [29], D. Sampsonidis [154], B.H. Samset [117], H. Sandaker [13], H.G. Sander [81], M.P. Sanders [98], M. Sandhoff [174], P. Sandhu [158], T. Sandoval [27], R. Sandstroem [105], S. Sandvoss [174], D.P.C. Sankey [129], A. Sansoni [47], C. Santamarina Rios [85], C. Santoni [33],

R. Santonico [133a,133b], H. Santos [124a], J.G. Saraiva [124a,l], T. Sarangi [172], E. Sarkisyan-Grinbaum [7], F. Sarri [122a,122b], G. Sartisohn [174], O. Sasaki [66], T. Sasaki [66], N. Sasao [68], I. Satsounkevitch [90], G. Sauvage [4], J.B. Sauvan [115], P. Savard [158,d], V. Savinov [123], D.O. Savu [29], P. Savva [9], L. Sawyer [24,i], D.H. Saxon [53], L.P. Says [33], C. Sbarra [19a,19b], A. Sbrizzi [19a,19b], O. Scallon [93], D.A. Scannicchio [163], J. Schaarschmidt [115], P. Schacht [99], U. Schäfer [81], S. Schaetzel [58b], A.C. Schaffer [115], D. Schaile [98], R.D. Schamberger [148], A.G. Schamov [107], V. Scharf [58a], V.A. Schegelsky [121], D. Scheirich [87], M.I. Scherzer [14], C. Schiavi [50a,50b], J. Schieck [98], M. Schioppa [36a,36b], S. Schlenker [29], J.L. Schlereth [5], E. Schmidt [48], M.P. Schmidt [175,*], K. Schmieden [20], C. Schmitt [81], M. Schmitz [20], A. Schöning [58b], M. Schott [29], D. Schouten [142], J. Schovancova [125], M. Schram [85], C. Schroeder [81], N. Schroer [58c], S. Schuh [29], G. Schuler [29], J. Schultes [174], H.-C. Schultz-Coulon [58a], H. Schulz [15], J.W. Schumacher [20], M. Schumacher [48], B.A. Schumm [137], Ph. Schune [136], C. Schwanenberger [82], A. Schwartzman [143], Ph. Schwemling [78], R. Schwienhorst [88], R. Schwierz [43], J. Schwindling [136], W.G. Scott [129], J. Searcy [114], E. Sedykh [121], E. Segura [11], S.C. Seidel [103], A. Seiden [137], F. Seifert [43], J.M. Seixas [23a], G. Sekhniaidze [102a], D.M. Seliverstov [121], B. Sellden [146a], G. Sellers [73], M. Seman [144b], N. Semprini-Cesari [19a,19b], C. Serfon [98], L. Serin [115], R. Seuster [99], H. Severini [111], M.E. Sevior [86], A. Sfyrla [29], E. Shabalina [54], M. Shamim [114], L.Y. Shan [32a], J.T. Shank [21], Q.T. Shao [86], M. Shapiro [14], P.B. Shatalov [95], L. Shaver [6], C. Shaw [53], K. Shaw [164a,164c], D. Sherman [175], P. Sherwood [77], A. Shibata [108], S. Shimizu [29], M. Shimojima [100], T. Shin [56], A. Shmeleva [94], M.J. Shochet [30], D. Short [118], M.A. Shupe [6], P. Sicho [125], A. Sidoti [15], A. Siebel [174], F. Siegert [48], J. Siegrist [14], Dj. Sijacki [12a], O. Silbert [171], J. Silva [124a,z], Y. Silver [153], D. Silverstein [143], S.B. Silverstein [146a], V. Simak [127], O. Simard [136], Lj. Simic [12a], S. Simion [115], B. Simmons [77], M. Simonyan [35], P. Sinervo [158], N.B. Sinev [114], V. Sipica [141], G. Siragusa [81], A.N. Sisakyan [65], S.Yu. Sivoklokov [97], J. Sjölin [146a,146b], T.B. Sjursen [13], L.A. Skinnari [14], K. Skovpen [107], P. Skubic [111], N. Skvorodnev [22], M. Slater [17], T. Slavicek [127], K. Sliwa [161], T.J. Sloan [71], J. Sloper [29], V. Smakhtin [171], S.Yu. Smirnov [96], L.N. Smirnova [97], O. Smirnova [79], B.C. Smith [57], D. Smith [143], K.M. Smith [53], M. Smizanska [71], K. Smolek [127], A.A. Snesarev [94], S.W. Snow [82], J. Snow [111], J. Snuverink [105], S. Snyder [24], M. Soares [124a], R. Sobie [169,h], J. Sodomka [127], A. Soffer [153], C.A. Solans [167], M. Solar [127], J. Solc [127], U. Soldevila [167], E. Solfaroli Camillocci [132a,132b], A.A. Solodkov [128], O.V. Solovyanov [128], J. Sondericker [24], N. Soni [2], V. Sopko [127], B. Sopko [127], M. Sorbi [89a,89b], M. Sosebee [7], A. Soukharev [107], S. Spagnolo [72a,72b], F. Spanò [34], R. Spighi [19a], G. Spigo [29], F. Spila [132a,132b], E. Spiriti [134a], R. Spiwoks [29], M. Spousta [126], T. Spreitzer [158], B. Spurlock [7], R.D.St. Denis [53], T. Stahl [141], J. Stahlman [120], R. Stamen [58a], E. Stanecka [29], R.W. Stanek [5], C. Stanescu [134a], S. Stapnes [117], E.A. Starchenko [128], J. Stark [55], P. Staroba [125], P. Starovoitov [91], A. Staude [98], P. Stavina [144a], G. Stavropoulos [14], G. Steele [53], P. Steinbach [43], P. Steinberg [24], I. Stekl [127], B. Stelzer [142], H.J. Stelzer [41], O. Stelzer-Chilton [159a], H. Stenzel [52], K. Stevenson [75], G.A. Stewart [53], J.A. Stillings [20], T. Stockmanns [20], M.C. Stockton [29], K. Stoerig [48], G. Stoicea [25a], S. Stonjek [99], P. Strachota [126], A.R. Stradling [7], A. Straessner [43], J. Strandberg [87], S. Strandberg [146a,146b], A. Strandlie [117], M. Strang [109], E. Strauss [143], M. Strauss [111], P. Strizenec [144b], R. Ströhmer [173], D.M. Strom [114], J.A. Strong [76,*], R. Stroynowski [39], J. Strube [129], B. Stugu [13], I. Stumer [24,*], J. Stupak [148], P. Sturm [174], D.A. Soh [151,r], D. Su [143], S. Subramania [2], Y. Sugaya [116], T. Sugimoto [101], C. Suhr [106], K. Suita [67], M. Suk [126], V.V. Sulin [94], S. Sultansoy [3d], T. Sumida [29], X. Sun [55], J.E. Sundermann [48], K. Suruliz [164a,164b], S. Sushkov [11], G. Susinno [36a,36b], M.R. Sutton [139], Y. Suzuki [66], Yu.M. Sviridov [128], S. Swedish [168], I. Sykora [144a], T. Sykora [126], B. Szeless [29], J. Sánchez [167], D. Ta [105], K. Tackmann [29], A. Taffard [163], R. Tafirout [159a], A. Taga [117], N. Taiblum [153], Y. Takahashi [101], H. Takai [24], R. Takashima [69], H. Takeda [67], T. Takeshita [140], M. Talby [83], A. Talyshev [107], M.C. Tamsett [24], J. Tanaka [155], R. Tanaka [115], S. Tanaka [131], S. Tanaka [66], Y. Tanaka [100], K. Tani [67], N. Tannoury [83], G.P. Tappern [29], S. Tapprogge [81], D. Tardif [158], S. Tarem [152], F. Tarrade [24], G.F. Tartarelli [89a], P. Tas [126], M. Tasevsky [125], E. Tassi [36a,36b], M. Tatarkhanov [14], C. Taylor [77], F.E. Taylor [92], G. Taylor [137], G.N. Taylor [86], W. Taylor [159b], M. Teixeira Dias Castanheira [75], P. Teixeira-Dias [76], K.K. Temming [48], H. Ten Kate [29], P.K. Teng [151], Y.D. Tennenbaum-Katan [152], S. Terada [66], K. Terashi [155], J. Terron [80], M. Terwort [41,p], M. Testa [47], R.J. Teuscher [158,h], C.M. Tevlin [82], J. Thadome [174], J. Therhaag [20], T. Theveneaux-Pelzer [78], M. Thioye [175], S. Thoma [48], J.P. Thomas [17], E.N. Thompson [84], P.D. Thompson [17], P.D. Thompson [158], A.S. Thompson [53], E. Thomson [120], M. Thomson [27], R.P. Thun [87], T. Tic [125], V.O. Tikhomirov [94], Y.A. Tikhonov [107], C.J.W.P. Timmermans [104], P. Tipton [175], F.J. Tique Aires Viegas [29], S. Tisserant [83], J. Tobias [48], B. Toczek [37],

T. Todorov [4], S. Todorova-Nova [161], B. Toggerson [163], J. Tojo [66], S. Tokár [144a], K. Tokunaga [67], K. Tokushuku [66], K. Tollefson [88], M. Tomoto [101], L. Tompkins [14], K. Toms [103], A. Tonazzo [134a,134b], G. Tong [32a], A. Tonoyan [13], C. Topfel [16], N.D. Topilin [65], I. Torchiani [29], E. Torrence [114], E. Torró Pastor [167], J. Toth [83,x], F. Touchard [83], D.R. Tovey [139], D. Traynor [75], T. Trefzger [173], J. Treis [20], L. Tremblet [29], A. Tricoli [29], I.M. Trigger [159a], S. Trincaz-Duvoid [78], T.N. Trinh [78], M.F. Tripiana [70], N. Triplett [64], W. Trischuk [158], A. Trivedi [24,w], B. Trocmé [55], C. Troncon [89a], M. Trottier-McDonald [142], A. Trzupek [38], C. Tsarouchas [29], J.C.-L. Tseng [118], M. Tsiakiris [105], P.V. Tsiareshka [90], D. Tsionou [4], G. Tsipolitis [9], V. Tsiskaridze [48], E.G. Tskhadadze [51], I.I. Tsukerman [95], V. Tsulaia [123], J.-W. Tsung [20], S. Tsuno [66], D. Tsybychev [148], A. Tua [139], J.M. Tuggle [30], M. Turala [38], D. Turecek [127], I. Turk Cakir [3e], E. Turlay [105], P.M. Tuts [34], A. Tykhonov [74], M. Tylmad [146a,146b], M. Tyndel [129], D. Typaldos [17], H. Tyrvainen [29], G. Tzanakos [8], K. Uchida [20], I. Ueda [155], R. Ueno [28], M. Ugland [13], M. Uhlenbrock [20], M. Uhrmacher [54], F. Ukegawa [160], G. Unal [29], D.G. Underwood [5], A. Undrus [24], G. Unel [163], Y. Unno [66], D. Urbaniec [34], E. Urkovsky [153], P. Urquijo [49], P. Urrejola [31a], G. Usai [7], M. Uslenghi [119a,119b], L. Vacavant [83], V. Vacek [127], B. Vachon [85], S. Vahsen [14], C. Valderanis [99], J. Valenta [125], P. Valente [132a], S. Valentinetti [19a,19b], S. Valkar [126], E. Valladolid Gallego [167], S. Vallecorsa [152], J.A. Valls Ferrer [167], H. van der Graaf [105], E. van der Kraaij [105], E. van der Poel [105], D. van der Ster [29], B. Van Eijk [105], N. van Eldik [84], P. van Gemmeren [5], Z. van Kesteren [105], I. van Vulpen [105], W. Vandelli [29], G. Vandoni [29], A. Vaniachine [5], P. Vankov [41], F. Vannucci [78], F. Varela Rodriguez [29], R. Vari [132a], E.W. Varnes [6], D. Varouchas [14], A. Vartapetian [7], K.E. Varvell [150], V.I. Vassilakopoulos [56], F. Vazeille [33], G. Vegni [89a,89b], J.J. Veillet [115], C. Vellidis [8], F. Veloso [124a], R. Veness [29], S. Veneziano [132a], A. Ventura [72a,72b], D. Ventura [138], M. Venturi [48], N. Venturi [16], V. Vercesi [119a], M. Verducci [138], W. Verkerke [105], J.C. Vermeulen [105], A. Vest [43], M.C. Vetterli [142,d], I. Vichou [165], T. Vickey [145b,aa], G.H.A. Viehhauser [118], S. Viel [168], M. Villa [19a,19b], M. Villaplana Perez [167], E. Vilucchi [47], M.G. Vincter [28], E. Vinek [29], V.B. Vinogradov [65], M. Virchaux [136,*], S. Viret [33], J. Virzi [14], A. Vitale [19a,19b], O. Vitells [171], I. Vivarelli [48], F. Vives Vaque [11], S. Vlachos [9], M. Vlasak [127], N. Vlasov [20], A. Vogel [20], P. Vokac [127], M. Volpi [11], G. Volpini [89a], H. von der Schmitt [99], J. von Loeben [99], H. von Radziewski [48], E. von Toerne [20], V. Vorobel [126], A.P. Vorobiev [128], V. Vorwerk [11], M. Vos [167], R. Voss [29], T.T. Voss [174], J.H. Vossebeld [73], A.S. Vovenko [128], N. Vranjes [12a], M. Vranjes Milosavljevic [12a], V. Vrba [125], M. Vreeswijk [105], T. Vu Anh [81], R. Vuillermet [29], I. Vukotic [115], W. Wagner [174], P. Wagner [120], H. Wahlen [174], J. Wakabayashi [101], J. Walbersloh [42], S. Walch [87], J. Walder [71], R. Walker [98], W. Walkowiak [141], R. Wall [175], P. Waller [73], C. Wang [44], H. Wang [172], J. Wang [151], J. Wang [32d], J.C. Wang [138], R. Wang [103], S.M. Wang [151], A. Warburton [85], C.P. Ward [27], M. Warsinsky [48], P.M. Watkins [17], A.T. Watson [17], M.F. Watson [17], G. Watts [138], S. Watts [82], A.T. Waugh [150], B.M. Waugh [77], J. Weber [42], M. Weber [129], M.S. Weber [16], P. Weber [54], A.R. Weidberg [118], J. Weingarten [54], C. Weiser [48], H. Wellenstein [22], P.S. Wells [29], M. Wen [47], T. Wenaus [24], S. Wendler [123], Z. Weng [151,r], T. Wengler [29], S. Wenig [29], N. Wermes [20], M. Werner [48], P. Werner [29], M. Werth [163], M. Wessels [58a], K. Whalen [28], S.J. Wheeler-Ellis [163], S.P. Whitaker [21], A. White [7], M.J. White [86], S. White [24], S.R. Whitehead [118], D. Whiteson [163], D. Whittington [61], F. Wicek [115], D. Wicke [174], F.J. Wickens [129], W. Wiedenmann [172], M. Wielers [129], P. Wienemann [20], C. Wiglesworth [73], L.A.M. Wiik [48], A. Wildauer [167], M.A. Wildt [41,p], I. Wilhelm [126], H.G. Wilkens [29], J.Z. Will [98], E. Williams [34], H.H. Williams [120], W. Willis [34], S. Willocq [84], J.A. Wilson [17], M.G. Wilson [143], A. Wilson [87], I. Wingerter-Seez [4], S. Winkelmann [48], F. Winklmeier [29], M. Wittgen [143], M.W. Wolter [38], H. Wolters [124a,f], G. Wooden [118], B.K. Wosiek [38], J. Wotschack [29], M.J. Woudstra [84], K. Wraight [53], C. Wright [53], B. Wrona [73], S.L. Wu [172], X. Wu [49], Y. Wu [32b], E. Wulf [34], R. Wunstorf [42], B.M. Wynne [45], L. Xaplanteris [9], S. Xella [35], S. Xie [48], Y. Xie [32a], C. Xu [32b], D. Xu [139], G. Xu [32a], B. Yabsley [150], M. Yamada [66], A. Yamamoto [66], K. Yamamoto [64], S. Yamamoto [155], T. Yamamura [155], J. Yamaoka [44], T. Yamazaki [155], Y. Yamazaki [67], Z. Yan [21], H. Yang [87], U.K. Yang [82], Y. Yang [61], Y. Yang [32a], Z. Yang [146a,146b], S. Yanush [91], W.-M. Yao [14], Y. Yao [14], Y. Yasu [66], J. Ye [39], S. Ye [24], M. Yilmaz [3c], R. Yoosoofmiya [123], K. Yorita [170], R. Yoshida [5], C. Young [143], S. Youssef [21], D. Yu [24], J. Yu [7], J. Yu [32c,ab], L. Yuan [32a,ac], A. Yurkewicz [148], V.G. Zaets [128], R. Zaidan [63], A.M. Zaitsev [128], Z. Zajacova [29], Yo.K. Zalite [121], L. Zanello [132a,132b], P. Zarzhitsky [39], A. Zaytsev [107], C. Zeitnitz [174], M. Zeller [175], P.F. Zema [29], A. Zemla [38], C. Zendler [20], A.V. Zenin [128], O. Zenin [128], T. Ženiš [144a], Z. Zenonos [122a,122b], S. Zenz [14], D. Zerwas [115], G. Zevi della Porta [57], Z. Zhan [32d], D. Zhang [32b],

H. Zhang [88], J. Zhang [5], X. Zhang [32d], Z. Zhang [115], L. Zhao [108], T. Zhao [138], Z. Zhao [32b], A. Zhemchugov [65], S. Zheng [32a], J. Zhong [151,ad], B. Zhou [87], N. Zhou [163], Y. Zhou [151], C.G. Zhu [32d], H. Zhu [41], Y. Zhu [172], X. Zhuang [98], V. Zhuravlov [99], D. Zieminska [61], B. Zilka [144a], R. Zimmermann [20], S. Zimmermann [20], S. Zimmermann [48], M. Ziolkowski [141], R. Zitoun [4], L. Živković [34], V.V. Zmouchko [128,*], G. Zobernig [172], A. Zoccoli [19a,19b], Y. Zolnierowski [4], A. Zsenei [29], M. zur Nedden [15], V. Zutshi [106], L. Zwalinski [29]

[1] *University at Albany, 1400 Washington Ave, Albany, NY 12222, United States*
[2] *University of Alberta, Department of Physics, Centre for Particle Physics, Edmonton, AB T6G 2G7, Canada*
[3] *Ankara University[(a)], Faculty of Sciences, Department of Physics, TR-061000 Tandogan, Ankara; Dumlupinar University[(b)], Faculty of Arts and Sciences, Department of Physics, Kutahya; Gazi University[(c)], Faculty of Arts and Sciences, Department of Physics, 06500 Teknikokullar, Ankara; TOBB University of Economics and Technology[(d)], Faculty of Arts and Sciences, Division of Physics, 06560 Sogutozu, Ankara; Turkish Atomic Energy Authority[(e)], 06530 Lodumlu, Ankara, Turkey*
[4] *LAPP, Université de Savoie, CNRS/IN2P3, Annecy-le-Vieux, France*
[5] *Argonne National Laboratory, High Energy Physics Division, 9700 S. Cass Avenue, Argonne, IL 60439, United States*
[6] *University of Arizona, Department of Physics, Tucson, AZ 85721, United States*
[7] *The University of Texas at Arlington, Department of Physics, Box 19059, Arlington, TX 76019, United States*
[8] *University of Athens, Nuclear & Particle Physics, Department of Physics, Panepistimiopouli, Zografou, GR-15771 Athens, Greece*
[9] *National Technical University of Athens, Physics Department, 9-Iroon Polytechniou, GR-15780 Zografou, Greece*
[10] *Institute of Physics, Azerbaijan Academy of Sciences, H. Javid Avenue 33, AZ 143 Baku, Azerbaijan*
[11] *Institut de Física d'Altes Energies, IFAE, Edifici Cn, Universitat Autònoma de Barcelona, ES-08193 Bellaterra (Barcelona), Spain*
[12] *University of Belgrade[(a)], Institute of Physics, P.O. Box 57, 11001 Belgrade; Vinca Institute of Nuclear Sciences[(b)], M. Petrovica Alasa 12-14, 11001 Belgrade, Serbia*
[13] *University of Bergen, Department for Physics and Technology, Allegaten 55, NO-5007 Bergen, Norway*
[14] *Lawrence Berkeley National Laboratory and University of California, Physics Division, MS50B-6227, 1 Cyclotron Road, Berkeley, CA 94720, United States*
[15] *Humboldt University, Institute of Physics, Berlin, Newtonstr. 15, D-12489 Berlin, Germany*
[16] *University of Bern, Albert Einstein Center for Fundamental Physics, Laboratory for High Energy Physics, Sidlerstrasse 5, CH-3012 Bern, Switzerland*
[17] *University of Birmingham, School of Physics and Astronomy, Edgbaston, Birmingham B15 2TT, United Kingdom*
[18] *Bogazici University[(a)], Faculty of Sciences, Department of Physics, TR-80815 Bebek-Istanbul; Dogus University[(b)], Faculty of Arts and Sciences, Department of Physics, 34722 Kadikoy, Istanbul; Gaziantep University[(c)], Faculty of Engineering, Department of Physics Engineering, 27310 Sehitkamil, Gaziantep; Istanbul Technical University[(d)], Faculty of Arts and Sciences, Department of Physics, 34469 Maslak, Istanbul, Turkey*
[19] *INFN Sezione di Bologna[(a)]; Università di Bologna, Dipartimento di Fisica[(a)], viale C. Berti Pichat, 6/2, IT-40127 Bologna, Italy*
[20] *University of Bonn, Physikalisches Institut, Nussallee 12, D-53115 Bonn, Germany*
[21] *Boston University, Department of Physics, 590 Commonwealth Avenue, Boston, MA 02215, United States*
[22] *Brandeis University, Department of Physics, MS057, 415 South Street, Waltham, MA 02454, United States*
[23] *Universidade Federal do Rio De Janeiro, COPPE/EE/IF[(a)], Caixa Postal 68528, Ilha do Fundao, BR-21945-970 Rio de Janeiro; Universidade de Sao Paulo[(b)], Instituto de Fisica, R.do Matao Trav. R.187, Sao Paulo, SP 05508-900, Brazil*
[24] *Brookhaven National Laboratory, Physics Department, Bldg. 510A, Upton, NY 11973, United States*
[25] *National Institute of Physics and Nuclear Engineering[(a)], Bucharest-Magurele, Str. Atomistilor 407, P.O. Box MG-6, R-077125; University Politehnica Bucharest[(b)], Rectorat, AN 001, 313 Splaiul Independentei, sector 6, 060042 Bucuresti; West University[(c)] in Timisoara, Bd. Vasile Parvan 4, Timisoara, Romania*
[26] *Universidad de Buenos Aires, FCEyN, Dto. Fisica, Pab I, C. Universitaria, 1428 Buenos Aires, Argentina*
[27] *University of Cambridge, Cavendish Laboratory, J.J. Thomson Avenue, Cambridge CB3 0HE, United Kingdom*
[28] *Carleton University, Department of Physics, 1125 Colonel By Drive, Ottawa ON K1S 5B6, Canada*
[29] *CERN, CH-1211 Geneva 23, Switzerland*
[30] *University of Chicago, Enrico Fermi Institute, 5640 S. Ellis Avenue, Chicago, IL 60637, United States*
[31] *Pontificia Universidad Católica de Chile, Facultad de Fisica, Departamento de Fisica[(a)], Avda. Vicuna Mackenna 4860, San Joaquin, Santiago; Universidad Técnica Federico Santa María, Departamento de Física[(b)], Avda. Espãna 1680, Casilla 110-V, Valparaíso, Chile*
[32] *Institute of High Energy Physics, Chinese Academy of Sciences[(a)], P.O. Box 918, 19 Yuquan Road, Shijing Shan District, CN, Beijing 100049; University of Science & Technology of China (USTC), Department of Modern Physics[(b)], Hefei, CN, Anhui 230026; Nanjing University, Department of Physics[(c)], Nanjing, CN, Jiangsu 210093; Shandong University, High Energy Physics Group[(d)], Jinan, CN, Shandong 250100, China*
[33] *Laboratoire de Physique Corpusculaire, Clermont Université, Université Blaise Pascal, CNRS/IN2P3, FR-63177 Aubiere Cedex, France*
[34] *Columbia University, Nevis Laboratory, 136 So. Broadway, Irvington, NY 10533, United States*
[35] *University of Copenhagen, Niels Bohr Institute, Blegdamsvej 17, DK-2100 Kobenhavn 0, Denmark*
[36] *INFN Gruppo Collegato di Cosenza[(a)]; Università della Calabria, Dipartimento di Fisica[(b)], IT-87036 Arcavacata di Rende, Italy*
[37] *Faculty of Physics and Applied Computer Science of the AGH–University of Science and Technology (FPACS, AGH–UST), al. Mickiewicza 30, PL-30059 Cracow, Poland*
[38] *The Henryk Niewodniczanski Institute of Nuclear Physics, Polish Academy of Sciences, ul. Radzikowskiego 152, PL-31342 Cracow, Poland*
[39] *Southern Methodist University, Physics Department, 106 Fondren Science Building, Dallas, TX 75275-0175, United States*
[40] *University of Texas at Dallas, 800 West Campbell Road, Richardson, TX 75080-3021, United States*
[41] *DESY, Notkestr. 85, D-22603 Hamburg and Platanenallee 6, D-15738 Zeuthen, Germany*
[42] *TU Dortmund, Experimentelle Physik IV, DE-44221 Dortmund, Germany*
[43] *Technical University Dresden, Institut für Kern- und Teilchenphysik, Zellescher Weg 19, D-01069 Dresden, Germany*
[44] *Duke University, Department of Physics, Durham, NC 27708, United States*
[45] *University of Edinburgh, School of Physics & Astronomy, James Clerk Maxwell Building, The Kings Buildings, Mayfield Road, Edinburgh EH9 3JZ, United Kingdom*
[46] *Fachhochschule Wiener Neustadt; Johannes Gutenbergstrasse 3, AT-2700 Wiener Neustadt, Austria*
[47] *INFN Laboratori Nazionali di Frascati, via Enrico Fermi 40, IT-00044 Frascati, Italy*
[48] *Albert-Ludwigs-Universität, Fakultät für Mathematik und Physik, Hermann-Herder Str. 3, D-79104 Freiburg i.Br., Germany*
[49] *Université de Genève, Section de Physique, 24 rue Ernest Ansermet, CH-1211 Geneve 4, Switzerland*
[50] *INFN Sezione di Genova[(a)]; Università di Genova, Dipartimento di Fisica[(b)], via Dodecaneso 33, IT-16146 Genova, Italy*
[51] *Institute of Physics of the Georgian Academy of Sciences, 6 Tamarashvili St., GE-380077 Tbilisi; Tbilisi State University, HEP Institute, University St. 9, GE-380086 Tbilisi, Georgia*
[52] *Justus-Liebig-Universität Giessen, II Physikalisches Institut, Heinrich-Buff Ring 16, D-35392 Giessen, Germany*
[53] *University of Glasgow, Department of Physics and Astronomy, Glasgow G12 8QQ, United Kingdom*
[54] *Georg-August-Universität, II Physikalisches Institut, Friedrich-Hund Platz 1, D-37077 Göttingen, Germany*
[55] *Laboratoire de Physique Subatomique et de Cosmologie, Université Joseph Fourier, CNRS–IN2P3, INPG, Grenoble, France*
[56] *Hampton University, Department of Physics, Hampton, VA 23668, United States*
[57] *Harvard University, Laboratory for Particle Physics and Cosmology, 18 Hammond Street, Cambridge, MA 02138, United States*
[58] *Ruprecht-Karls-Universität Heidelberg: Kirchhoff-Institut für Physik[(a)], Im Neuenheimer Feld 227, D-69120 Heidelberg; Physikalisches Institut[(b)], Philosophenweg 12, D-69120 Heidelberg; ZITI Ruprecht-Karls-University Heidelberg[(c)], Lehrstuhl für Informatik V, B6, 23-29, D-68131 Mannheim, Germany*
[59] *Hiroshima University, Faculty of Science, 1-3-1 Kagamiyama, Higashihiroshima-shi, JP, Hiroshima 739-8526, Japan*
[60] *Hiroshima Institute of Technology, Faculty of Applied Information Science, 2-1-1 Miyake Saeki-ku, Hiroshima-shi, JP, Hiroshima 731-5193, Japan*
[61] *Indiana University, Department of Physics, Swain Hall West 117, Bloomington, IN 47405-7105, United States*

[62] Institut für Astro- und Teilchenphysik, Technikerstrasse 25, A-6020 Innsbruck, Austria
[63] University of Iowa, 203 Van Allen Hall, Iowa City, IA 52242-1479, United States
[64] Iowa State University, Department of Physics and Astronomy, Ames High Energy Physics Group, Ames, IA 50011-3160, United States
[65] Joint Institute for Nuclear Research, JINR Dubna, RU-141980 Moscow Region, Russia
[66] KEK, High Energy Accelerator Research Organization, 1-1 Oho, Tsukuba-shi, Ibaraki-ken 305-0801, Japan
[67] Kobe University, Graduate School of Science, 1-1 Rokkodai-cho, Nada-ku, JP, Kobe 657-8501, Japan
[68] Kyoto University, Faculty of Science, Oiwake-cho, Kitashirakawa, Sakyou-ku, Kyoto-shi, JP Kyoto 606-8502, Japan
[69] Kyoto University of Education, 1 Fukakusa, Fujimori, Fushimi-ku, Kyoto-shi, JP, Kyoto 612-8522, Japan
[70] Universidad Nacional de La Plata, FCE, Departamento de Física, IFLP (CONICET–UNLP), C.C. 67, 1900 La Plata, Argentina
[71] Lancaster University, Physics Department, Lancaster LA1 4YB, United Kingdom
[72] INFN Sezione di Lecce[(a)]; Università del Salento, Dipartimento di Fisica[(b)], Via Arnesano, IT-73100 Lecce, Italy
[73] University of Liverpool, Oliver Lodge Laboratory, P.O. Box 147, Oxford Street, Liverpool L69 3BX, United Kingdom
[74] Jožef Stefan Institute and University of Ljubljana, Department of Physics, SI-1000 Ljubljana, Slovenia
[75] Queen Mary University of London, Department of Physics, Mile End Road, London E1 4NS, United Kingdom
[76] Royal Holloway, University of London, Department of Physics, Egham Hill, Egham, Surrey TW20 0EX, United Kingdom
[77] University College London, Department of Physics and Astronomy, Gower Street, London WC1E 6BT, United Kingdom
[78] Laboratoire de Physique Nucléaire et de Hautes Energies, UPMC, Université Paris Diderot, CNRS/IN2P3, 4 place Jussieu, FR-75252 Paris Cedex 05, France
[79] Fysiska Institutionen, Lunds Universitet, Box 118, SE-221 00 Lund, Sweden
[80] Universidad Autonoma de Madrid, Facultad de Ciencias, Departamento de Fisica Teorica, ES-28049 Madrid, Spain
[81] Universität Mainz, Institut für Physik, Staudinger Weg 7, DE-55099 Mainz, Germany
[82] University of Manchester, School of Physics and Astronomy, Manchester M13 9PL, United Kingdom
[83] CPPM, Aix-Marseille Université, CNRS/IN2P3, Marseille, France
[84] University of Massachusetts, Department of Physics, 710 North Pleasant Street, Amherst, MA 01003, United States
[85] McGill University, High Energy Physics Group, 3600 University Street, Montreal, Quebec H3A 2T8, Canada
[86] University of Melbourne, School of Physics, AU, Parkville, Victoria 3010, Australia
[87] The University of Michigan, Department of Physics, 2477 Randall Laboratory, 500 East University, Ann Arbor, MI 48109-1120, United States
[88] Michigan State University, Department of Physics and Astronomy, High Energy Physics Group, East Lansing, MI 48824-2320, United States
[89] INFN Sezione di Milano[(a)]; Università di Milano, Dipartimento di Fisica[(b)], via Celoria 16, IT-20133 Milano, Italy
[90] B.I. Stepanov Institute of Physics, National Academy of Sciences of Belarus, Independence Avenue 68, Minsk 220072, Belarus
[91] National Scientific & Educational Centre for Particle & High Energy Physics, NC PHEP BSU, M. Bogdanovich St. 153, Minsk 220040, Belarus
[92] Massachusetts Institute of Technology, Department of Physics, Room 24-516, Cambridge, MA 02139, United States
[93] University of Montreal, Group of Particle Physics, C.P. 6128, Succursale Centre-Ville, Montreal, Quebec, H3C 3J7, Canada
[94] P.N. Lebedev Institute of Physics, Academy of Sciences, Leninsky pr. 53, RU-117 924 Moscow, Russia
[95] Institute for Theoretical and Experimental Physics (ITEP), B. Cheremushkinskaya ul. 25, RU-117 218 Moscow, Russia
[96] Moscow Engineering & Physics Institute (MEPhI), Kashirskoe Shosse 31, RU-115409 Moscow, Russia
[97] Lomonosov Moscow State University, Skobeltsyn Institute of Nuclear Physics (MSU SINP), 1(2), Leninskie gory, GSP-1, Moscow 119991 Russian Federation, Russia
[98] Ludwig-Maximilians-Universität München, Fakultät für Physik, Am Coulombwall 1, DE-85748 Garching, Germany
[99] Max-Planck-Institut für Physik (Werner-Heisenberg-Institut), Föhringer Ring 6, 80805 München, Germany
[100] Nagasaki Institute of Applied Science, 536 Aba-machi, JP, Nagasaki 851-0193, Japan
[101] Nagoya University, Graduate School of Science, Furo-Cho, Chikusa-ku, Nagoya, 464-8602, Japan
[102] INFN Sezione di Napoli[(a)]; Università di Napoli, Dipartimento di Scienze Fisiche[(b)], Complesso Universitario di Monte Sant'Angelo, via Cinthia, IT-80126 Napoli, Italy
[103] University of New Mexico, Department of Physics and Astronomy, MSC07 4220, Albuquerque, NM 87131, United States
[104] Radboud University Nijmegen/NIKHEF, Department of Experimental High Energy Physics, Heyendaalseweg 135, NL-6525 AJ, Nijmegen, Netherlands
[105] Nikhef National Institute for Subatomic Physics, and University of Amsterdam, Science Park 105, 1098 XG Amsterdam, Netherlands
[106] Department of Physics, Northern Illinois University, LaTourette Hall Normal Road, DeKalb, IL 60115, United States
[107] Budker Institute of Nuclear Physics (BINP), RU, Novosibirsk 630 090, Russia
[108] New York University, Department of Physics, 4 Washington Place, New York, NY 10003, United States
[109] Ohio State University, 191 West Woodruff Ave, Columbus, OH 43210-1117, United States
[110] Okayama University, Faculty of Science, Tsushimanaka 3-1-1, Okayama 700-8530, Japan
[111] University of Oklahoma, Homer L. Dodge Department of Physics and Astronomy, 440 West Brooks, Room 100, Norman, OK 73019-0225, United States
[112] Oklahoma State University, Department of Physics, 145 Physical Sciences Building, Stillwater, OK 74078-3072, United States
[113] Palacký University, 17. listopadu 50a, 772 07 Olomouc, Czech Republic
[114] University of Oregon, Center for High Energy Physics, Eugene, OR 97403-1274, United States
[115] LAL, Univ. Paris-Sud, IN2P3/CNRS, Orsay, France
[116] Osaka University, Graduate School of Science, Machikaneyama-machi 1-1, Toyonaka, Osaka 560-0043, Japan
[117] University of Oslo, Department of Physics, P.O. Box 1048, Blindern, NO-0316 Oslo 3, Norway
[118] Oxford University, Department of Physics, Denys Wilkinson Building, Keble Road, Oxford OX1 3RH, United Kingdom
[119] INFN Sezione di Pavia[(a)]; Università di Pavia, Dipartimento di Fisica Nucleare e Teorica[(b)], Via Bassi 6, IT-27100 Pavia, Italy
[120] University of Pennsylvania, Department of Physics, High Energy Physics Group, 209 S. 33rd Street, Philadelphia, PA 19104, United States
[121] Petersburg Nuclear Physics Institute, RU-188 300 Gatchina, Russia
[122] INFN Sezione di Pisa[(a)]; Università di Pisa, Dipartimento di Fisica E. Fermi[(b)], Largo B. Pontecorvo 3, IT-56127 Pisa, Italy
[123] University of Pittsburgh, Department of Physics and Astronomy, 3941 O'Hara Street, Pittsburgh, PA 15260, United States
[124] Laboratorio de Instrumentacao e Fisica Experimental de Particulas – LIP[(a)], Avenida Elias Garcia 14-1, PT-1000-149 Lisboa; Universidad de Granada, Departamento de Fisica Teorica y del Cosmos and CAFPE[(b)], E-18071 Granada, Spain
[125] Institute of Physics, Academy of Sciences of the Czech Republic, Na Slovance 2, CZ-18221 Praha 8, Czech Republic
[126] Charles University in Prague, Faculty of Mathematics and Physics, Institute of Particle and Nuclear Physics, V Holesovickach 2, CZ-18000 Praha 8, Czech Republic
[127] Czech Technical University in Prague, Zikova 4, CZ-166 35 Praha 6, Czech Republic
[128] State Research Center Institute for High Energy Physics, Moscow Region, 142281, Protvino, Pobeda street, 1, Russia
[129] Rutherford Appleton Laboratory, Science and Technology Facilities Council, Harwell Science and Innovation Campus, Didcot OX11 0QX, United Kingdom
[130] University of Regina, Physics Department, Canada
[131] Ritsumeikan University, Noji Higashi 1 chome 1-1, JP, Kusatsu, Shiga 525-8577, Japan
[132] INFN Sezione di Roma I[(a)]; Università La Sapienza, Dipartimento di Fisica[(b)], Piazzale A. Moro 2, IT-00185 Roma, Italy
[133] INFN Sezione di Roma Tor Vergata[(a)]; Università di Roma Tor Vergata, Dipartimento di Fisica[(b)], via della Ricerca Scientifica, IT-00133 Roma, Italy
[134] INFN Sezione di Roma Tre[(a)]; Università Roma Tre, Dipartimento di Fisica[(b)], via della Vasca Navale 84, IT-00146 Roma, Italy
[135] Réseau Universitaire de Physique des Hautes Energies (RUPHE): Université Hassan II, Faculté des Sciences Ain Chock[(a)], B.P. 5366, MA, Casablanca; Centre National de l'Energie des Sciences Techniques Nucleaires (CNESTEN)[(b)], B.P. 1382 R.P. 10001 Rabat 10001; Université Mohamed Premier[(c)], LPTPM, Faculté des Sciences, B.P. 717. Bd. Mohamed VI, 60000 Oujda; Université Mohammed V, Faculté des Sciences[(d)], 4 Avenue Ibn Battouta, B.P. 1014 R.P., 10000 Rabat, Morocco
[136] CEA, DSM/IRFU, Centre d'Etudes de Saclay, FR-91191 Gif-sur-Yvette, France
[137] University of California Santa Cruz, Santa Cruz Institute for Particle Physics (SCIPP), Santa Cruz, CA 95064, United States

[138] University of Washington, Seattle, Department of Physics, Box 351560, Seattle, WA 98195-1560, United States
[139] University of Sheffield, Department of Physics & Astronomy, Hounsfield Road, Sheffield S3 7RH, United Kingdom
[140] Shinshu University, Department of Physics, Faculty of Science, 3-1-1 Asahi, Matsumoto-shi, JP, Nagano 390-8621, Japan
[141] Universität Siegen, Fachbereich Physik, D 57068 Siegen, Germany
[142] Simon Fraser University, Department of Physics, 8888 University Drive, CA, Burnaby, BC V5A 1S6, Canada
[143] SLAC National Accelerator Laboratory, Stanford, California 94309, United States
[144] Comenius University, Faculty of Mathematics, Physics & Informatics[(a)], Mlynska dolina F2, SK-84248 Bratislava; Institute of Experimental Physics of the Slovak Academy of Sciences, Dept. of Subnuclear Physics[(b)], Watsonova 47, SK-04353 Kosice, Slovak Republic
[145] University of Johannesburg, Department of Physics[(a)], P.O. Box 524, Auckland Park, Johannesburg 2006; School of Physics, University of the Witwatersrand[(b)], Private Bag 3, Wits 2050, Johannesburg, South Africa
[146] Stockholm University, Department of Physics[(a)]; The Oskar Klein Centre[(b)], AlbaNova, SE-106 91 Stockholm, Sweden
[147] Royal Institute of Technology (KTH), Physics Department, SE-106 91 Stockholm, Sweden
[148] Stony Brook University, Department of Physics and Astronomy, Nicolls Road, Stony Brook, NY 11794-3800, United States
[149] University of Sussex, Department of Physics and Astronomy Pevensey 2 Building, Falmer, Brighton BN1 9QH, United Kingdom
[150] University of Sydney, School of Physics, AU, Sydney NSW 2006, Australia
[151] Insitute of Physics, Academia Sinica, TW, Taipei 11529, Taiwan
[152] Technion, Israel Inst. of Technology, Department of Physics, Technion City, IL, Haifa 32000, Israel
[153] Tel Aviv University, Raymond and Beverly Sackler School of Physics and Astronomy, Ramat Aviv, IL, Tel Aviv 69978, Israel
[154] Aristotle University of Thessaloniki, Faculty of Science, Department of Physics, Division of Nuclear & Particle Physics, University Campus, GR-54124, Thessaloniki, Greece
[155] The University of Tokyo, International Center for Elementary Particle Physics and Department of Physics, 7-3-1 Hongo, Bunkyo-ku, JP, Tokyo 113-0033, Japan
[156] Tokyo Metropolitan University, Graduate School of Science and Technology, 1-1 Minami-Osawa, Hachioji, Tokyo 192-0397, Japan
[157] Tokyo Institute of Technology, Department of Physics, 2-12-1 O-Okayama, Meguro, Tokyo 152-8551, Japan
[158] University of Toronto, Department of Physics, 60 Saint George Street, Toronto M5S 1A7, Ontario, Canada
[159] TRIUMF[(a)], 4004 Wesbrook Mall, Vancouver, B.C. V6T 2A3; York University[(b)], Department of Physics and Astronomy, 4700 Keele St., Toronto, Ontario, M3J 1P3, Canada
[160] University of Tsukuba, Institute of Pure and Applied Sciences, 1-1-1 Tennoudai, Tsukuba-shi, JP, Ibaraki 305-8571, Japan
[161] Tufts University, Science & Technology Center, 4 Colby Street, Medford, MA 02155, United States
[162] Universidad Antonio Narino, Centro de Investigaciones, Cra 3 Este No.47A-15, Bogota, Colombia
[163] University of California, Irvine, Department of Physics & Astronomy, CA 92697-4575, United States
[164] INFN Gruppo Collegato di Udine[(a)]; ICTP[(b)], Strada Costiera 11, IT-34014 Trieste; Università di Udine, Dipartimento di Fisica[(c)], via delle Scienze 208, IT-33100 Udine, Italy
[165] University of Illinois, Department of Physics, 1110 West Green Street, Urbana, Illinois 61801, United States
[166] University of Uppsala, Department of Physics and Astronomy, P.O. Box 516, SE-751 20 Uppsala, Sweden
[167] Instituto de Física Corpuscular (IFIC), Centro Mixto UVEG-CSIC, Apdo. 22085 ES-46071 Valencia, Dept. Física At. Mol. y Nuclear; Dept. Ing. Electrónica; Univ. of Valencia, and Inst. de Microelectrónica de Barcelona (IMB-CNM-CSIC), 08193 Bellaterra, Spain
[168] University of British Columbia, Department of Physics, 6224 Agricultural Road, CA, Vancouver, B.C. V6T 1Z1, Canada
[169] University of Victoria, Department of Physics and Astronomy, P.O. Box 3055, Victoria B.C., V8W 3P6, Canada
[170] Waseda University, WISE, 3-4-1 Okubo, Shinjuku-ku, Tokyo, 169-8555, Japan
[171] The Weizmann Institute of Science, Department of Particle Physics, P.O. Box 26, IL-76100 Rehovot, Israel
[172] University of Wisconsin, Department of Physics, 1150 University Avenue, WI 53706 Madison, Wisconsin, United States
[173] Julius-Maximilians-University of Würzburg, Physikalisches Institute, Am Hubland, 97074 Würzburg, Germany
[174] Bergische Universität, Fachbereich C, Physik, Postfach 100127, Gauss-Strasse 20, D-42097 Wuppertal, Germany
[175] Yale University, Department of Physics, PO Box 208121, New Haven CT, 06520-8121, United States
[176] Yerevan Physics Institute, Alikhanian Brothers Street 2, AM-375036 Yerevan, Armenia
[177] Centre de Calcul CNRS/IN2P3, Domaine scientifique de la Doua, 27 bd du 11 Novembre 1918, 69622 Villeurbanne Cedex, France

[a] Also at LIP, Portugal.
[b] Also at Faculdade de Ciencias, Universidade de Lisboa, Lisboa, Portugal.
[c] Also at CPPM, Marseille, France.
[d] Also at TRIUMF, Vancouver, Canada.
[e] Also at FPACS, AGH–UST, Cracow, Poland.
[f] Also at Department of Physics, University of Coimbra, Coimbra, Portugal.
[g] Also at Università di Napoli Parthenope, Napoli, Italy.
[h] Also at Institute of Particle Physics (IPP), Canada.
[i] Also at Louisiana Tech University, Ruston, United States.
[j] Also at Universidade de Lisboa, Lisboa, Portugal.
[k] At California State University, Fresno, United States.
[l] Also at Faculdade de Ciencias, Universidade de Lisboa and at Centro de Fisica Nuclear da Universidade de Lisboa, Lisboa, Portugal.
[m] Also at California Institute of Technology, Pasadena, United States.
[n] Also at University of Montreal, Montreal, Canada.
[o] Also at Baku Institute of Physics, Baku, Azerbaijan.
[p] Also at Institut für Experimentalphysik, Universität Hamburg, Hamburg, Germany.
[q] Also at Manhattan College, New York, United States.
[r] Also at School of Physics and Engineering, Sun Yat-sen University, Guangzhou, China.
[s] Also at Taiwan Tier-1, ASGC, Academia Sinica, Taipei, Taiwan.
[t] Also at School of Physics, Shandong University, Jinan, China.
[u] Also at Rutherford Appleton Laboratory, Didcot, UK.
[v] Also at Departamento de Fisica, Universidade de Minho, Braga, Portugal.
[w] Also at Department of Physics and Astronomy, University of South Carolina, Columbia, United States.
[x] Also at KFKI Research Institute for Particle and Nuclear Physics, Budapest, Hungary.
[y] Also at Institute of Physics, Jagiellonian University, Cracow, Poland.
[z] Also at Centro de Fisica Nuclear da Universidade de Lisboa, Lisboa, Portugal.
[aa] Also at Department of Physics, Oxford University, Oxford, UK.
[ab] Also at CEA, Gif sur Yvette, France.
[ac] Also at LPNHE, Paris, France.
[ad] Also at Nanjing University, Nanjing Jiangsu, China.
[*] Deceased.

Nuclear Instruments and Methods in Physics Research A 623 (2010) 558–560

Contents lists available at ScienceDirect

Nuclear Instruments and Methods in Physics Research A

journal homepage: www.elsevier.com/locate/nima

# The ATLAS beam pick-up based timing system

C. Ohm [a,*], T. Pauly [b]

[a] Stockholm University, Department of Physics, 106 91 Stockholm, Sweden
[b] European Organization for Nuclear Research, 1211 Genève, Switzerland

ARTICLE INFO

Available online 10 March 2010

*Keywords:*
ATLAS
Beam monitoring
Level-1 trigger
BPTX
LHC
LHC timing signals

ABSTRACT

The ATLAS BPTX stations are composed of electrostatic button pick-up detectors, located 175 m away along the beam pipe on both sides of ATLAS. The pick-ups are installed as a part of the LHC beam instrumentation and used by ATLAS for timing purposes.

The usage of the BPTX signals in ATLAS is twofold: they are used both in the trigger system and for LHC beam monitoring. The BPTX signals are discriminated with a constant-fraction discriminator to provide a Level-1 trigger when a bunch passes through ATLAS. Furthermore, the BPTX detectors are used by a stand-alone monitoring system for the LHC bunches and timing signals. The BPTX monitoring system measures the phase between collisions and clock with a precision better than 100 ps in order to guarantee a stable phase relationship for optimal signal sampling in the sub-detector front-end electronics. In addition to monitoring this phase, the properties of the individual bunches are measured and the structure of the beams is determined.

On September 10, 2008, the first LHC beams reached the ATLAS experiment. During this period with beam, the ATLAS BPTX system was used extensively to time in the read-out of the sub-detectors. In this paper, we present the performance of the BPTX system and its measurements of the first LHC beams.


## 1. Introduction

The ATLAS experiment [1] at the Large Hadron Collider (LHC) [2] must be synchronized to the collisions to ensure the quality of the event data recorded by its sub-detectors. In order to facilitate this, the LHC provides beam related timing signals to the experiments via optical fibers that are several kilometers long [3]. The phase of these clock signals can drift, e.g. due to temperature fluctuations, causing front-end electronics to sample at non-optimal working point. On both sides of ATLAS, 175 m upstream from the interaction point, beam pick-up detectors are installed along the LHC beam pipe. This paper describes how these detectors are used:

- to monitor the phase between the collisions and the LHC clock signals that drive the ATLAS electronics;
- to monitor the structure and uniformity of the LHC beams;
- as input to the trigger system.

## 2. The BPTX detectors

The BPTX stations are beam position monitors provided by the LHC machine, but operated by experiments for timing purposes. They are composed of four electrostatic button pick-up detectors, arranged symmetrically in the transverse plane around the LHC beam pipe. Since the signal from a passing charge distribution is linearly proportional to distance to first order, the signals from all four pick-ups are summed to cancel out potential beam position deviations. The resulting signal is then transmitted to the underground counting room *USA15* via a 220 m low-loss cable. Fig. 1 shows the installed BPTX station for beam 2 on the C-side of ATLAS. At the bottom of the photograph, the cables from the four button pick-ups are visible.

## 3. Usage of the beam pick-up signals

The BPTX signals are used for two separate purposes within ATLAS, by the trigger system and by a monitoring system for the LHC beams and timing signals. Fig. 2 shows the BPTX system and how it interacts with the related systems [4,5]. The optical timing signals from the LHC arrive in the underground counting room to a receiver module, the `RF2TTC`. This module converts the optical signals to *TTC*[1] signals and can also manipulate their phase,

* Corresponding author. Tel.: +41 79 771 2149; fax: +41 22 767 1126.
*E-mail address:* christian.ohm@cern.ch (C. Ohm).

[1] TTC is the standard hardware system used across the LHC experiments for distribution of fast Timing, Trigger and Control signals.

0168-9002/$ - see front matter © 2010 Elsevier B.V. All rights reserved.
doi:10.1016/j.nima.2010.03.069

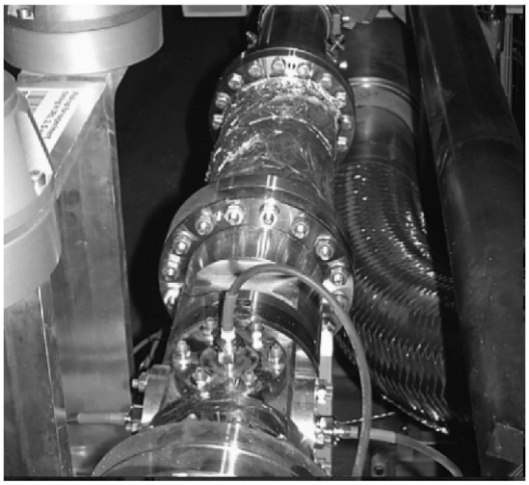

**Fig. 1.** A photograph of one of the two ATLAS BPTX stations.

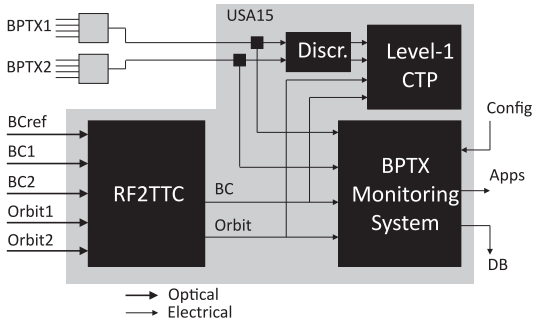


**Fig. 2.** Diagram showing the BPTX system and how it interacts with the related systems in ATLAS.

duration, etc. if needed. The electrical signals are then transmitted to the ATLAS sub-detectors via the *Central Trigger Processor* (CTP) of the Level-1 trigger system and to the BPTX monitoring system.

### 3.1. Level-1 trigger

The ATLAS trigger system is designed in three levels, each level sequentially refining the selection of events to be saved for further offine analysis. The Level-1 trigger is implemented in custom electronics and performs a first selection of events within 2.5 μs, based primarily on reduced-granularity data from the calorimeters and the muon spectrometer. The selected events are processed further by the *High Level Trigger* system which is implemented in software. The signals from the BPTX stations are discriminated with a constant-fraction discriminator to provide ATLAS with an accurate and reliable timing reference in the form of a standard NIM pulse. This pulse is fed into the Level-1 *Central Trigger Processor* where it serves as a trigger condition indicating a bunch passing through ATLAS.

### 3.2. Monitoring of the LHC beams and timing signals

Furthermore, the BPTX detectors are used by a stand-alone monitoring system for the LHC bunches and timing signals. The BPTX and LHC timing signals are digitized by a deep-memory, high sampling rate (5 GHz) oscilloscope[2] and transferred to a computer running Linux for analysis. The features of the scope enables capturing

[2] *WaveRunner 64 Xi* from LeCroy [6].

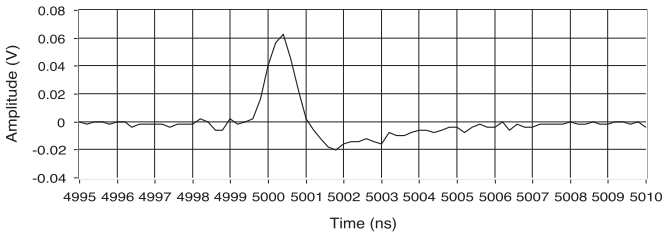


**Fig. 3.** The first LHC bunch on its way to ATLAS.

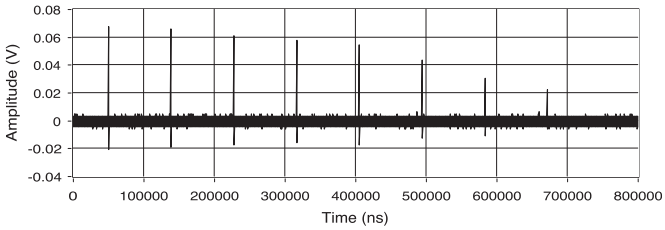


**Fig. 4.** A bunch passing ATLAS in eight consecutive turns.

a full LHC turn in one acquisition while retaining enough detail to get about 5 measurement points on the sharp falling edge of each BPTX pulse (see e.g. Fig. 3). Since most of the high-frequency content of the BPTX signals is attenuated by the long transmission line, the frequency spectrum of the signals arriving in ATLAS peaks around 400 MHz, making an analog bandwidth of 600 MHz sufficient for the oscilloscope used for digitization. By making fits to the identified bunch pulses and clock edges, the BPTX monitoring system measures the phase between each bunch and the clock signal with high accuracy. Monitoring these quantities is crucial to guarantee a stable phase relationship for optimal signal sampling in the sub-detector front-end electronics. In addition to monitoring this phase, the intensity and longitudinal length of the individual bunches are measured and the structure of the beams is determined. Using the BPTX monitoring applications, the shifter in the control room can verify that the timing signals are synchronized to the collisions, and also look for so-called *satellite bunches*, out-of-time bunches that would cause off-center collisions in ATLAS.

The monitoring system is running independently from the ATLAS online data acquisition infrastructure, enabling monitoring of the LHC machine in the control room even when ATLAS is not taking data. Summary data from the BPTX monitoring system, e.g. mean bunch intensity and phase, are published to the ATLAS *Detector Control System* [7] and ultimately saved to the conditions database.

## 4. Results from the first LHC beams

### 4.1. The first proton bunches in ATLAS

On September 10, 2008, the first LHC proton bunch reached ATLAS. Fig. 3 shows the pulse recorded by the BPTX monitoring system.

A few hours later, a bunch was successfully circulated 8 turns around the accelerator and seen by ATLAS as depicted in Fig. 4. The pulses are separated by 89 μs, corresponding to the time it takes for an LHC bunch to circulate around the 27 km long ring. The pulse amplitude, which is proportional to the bunch intensity, is degrading from turn to turn, which is consistent with the beam loss and debunching expected for a beam not yet captured by the LHC RF system.

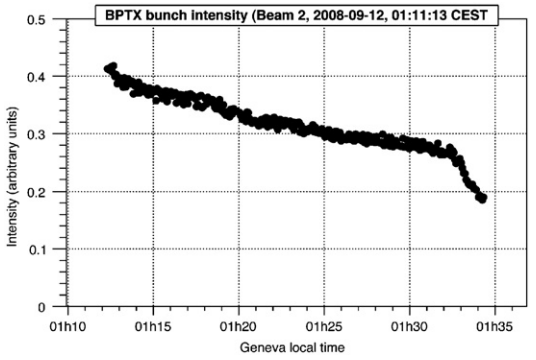


**Fig. 5.** Intensity measured by the BPTX monitoring system during 20 min of circulating beam.

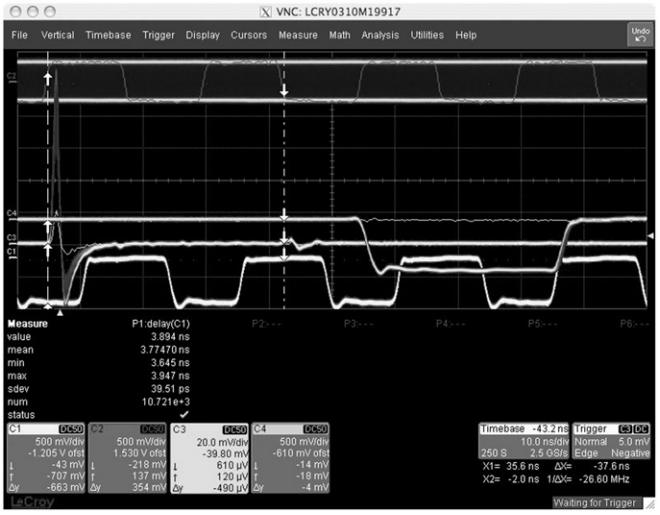


**Fig. 6.** Oscilloscope traces from 20 min of circulating beam with persistency.

### 4.2. Monitoring of a longer LHC run

Around 1 AM on September 12, 2008, a single bunch was circulated around the LHC for about 20 min after being captured by the RF system. The BPTX monitoring system measured the intensity during this period, and the resulting plot is shown in Fig. 5. It should be noted that this is a relative but not yet normalized intensity measurement. The scattering of the data points suggests that the precision is around 10%.

Fig. 6 shows an oscilloscope picture recorded in persistency mode during the same time period. The falling edge of the analog BPTX signal for beam 2 (the scope channel with bipolar pulses to the left) is used as scope trigger and can be seen together with the discriminated BPTX signal used as Level-1 trigger input (with longer NIM pulse to the right). The clock related to beam 2 (bottom) is stable within an RMS of 40 ps with respect to the beam, indicating RF capture. The reference clock signal (top), corresponding to the bunch frequency at a higher energy, has a different frequency.

## 5. Conclusions

In the first period of beam in the LHC, the BPTX system was used extensively as a trigger to time in the read-out windows of the sub-detectors of the ATLAS experiment. The BPTX monitoring system was able to record the very first LHC bunch approaching ATLAS, and provided detailed information about the beams during these first days of data taking.

## Acknowledgments

The authors would like to thank the ATLAS Collaboration and its Level-1 Central Trigger group in which most of this work was carried out. We would also like to express our deepest gratitude to the LHC community, both for the support and for providing the BPTX detectors.

## References

[1] The ATLAS Collaboration, J. Instr. 3 (2008) S08003.
[2] L. Evans, P. Bryant, J. Instr. 3 (2008) S08001.
[3] S. Baron, TTC challenges and upgrade for the LHC, in: Proceedings of the 11th Workshop on Electronics for LHC and Future Experiments, Heidelberg, 2005, pp. 125–129.
[4] T. Pauly, et al., ATLAS level-1 trigger timing-in strategies, in: Proceedings of the 11th Workshop on Electronics for LHC and Future Experiments, Heidelberg, 2005, pp. 274–278.
[5] C. Ohm, Phase and intensity monitoring of the particle beams at the ATLAS experiment, M.Sc. Thesis, Linköping University, Sweden, LITH-IFM-EX–07/1808–SE, 2007.
[6] LeCroy Corporation, WaveRunner Xi Series (datasheet), 2007 〈http://www.lecroy.com/tm/products/Scopes/WaveRunner_Xi/WRXi_datasheet.pdf〉.
[7] A. Barriuso Poy, H. Boterenbrood, H.J. Burckhart, J. Cook, V. Filimonov, S. Franz, O. Gutzwiller, B. Hallgren, V. Khomutnikov, S. Schlenker, F. Varela, J. Instr. 3 (2008) P05006.

Journal of Physics: Conference Series **219** (2010) 022040 doi:10.1088/1742-6596/219/2/022040

# The software of the ATLAS beam pick-up based LHC monitoring system

**C Ohm[1] and T Pauly[2]**

[1]Department of Physics, Stockholm University, 106 09 Stockholm, Sweden
[2]European Organization for Nuclear Research, 1211 Genève, Switzerland

E-mail: christian.ohm@cern.ch, thilo.pauly@cern.ch

**Abstract.** The ATLAS BPTX stations are comprised of electrostatic button pick-up detectors, located 175 m away along the beam pipe on both sides of ATLAS. The pick-ups are installed as a part of the LHC beam instrumentation and used by ATLAS for timing purposes. The signals from the ATLAS BPTX detectors are used both in the trigger system and for a stand-alone monitoring system for the LHC beams and timing signals. The monitoring software measures the phase between collisions and clock with high accuracy in order to guarantee a stable phase relationship for optimal signal sampling in the sub-detector front-end electronics. It also measures the properties of the individual bunches and the structure of the beams. In this paper, the BPTX monitoring software is described, its algorithms explained and a few example monitoring displays shown. In addition, results from the monitoring system during the first period of single beam running in September 2008 are presented.

## 1. Introduction

The ATLAS experiment [1] at the Large Hadron Collider (LHC) [2] must be synchronized to the proton-proton collisions to ensure the quality of the event data recorded by its sub-detectors. In order to facilitate the synchronization, ATLAS receives timing signals from the LHC machine and has two beam pick-up detectors at its disposal, installed upstream from the interaction point. The signals from these so-called *BPTX* detectors serve two purposes in ATLAS:

- The BPTX signals are used in a stand-alone monitoring system for the LHC beams and timing signals. The system monitors the phase between the collisions and the LHC clock signals that drive the ATLAS electronics in order to discover potential drifts. This system also measures the structure and uniformity of the LHC beams, and properties of their individual bunches.
- By discriminating the signals from the BPTX detectors and compensating for the lengths of the transmission lines, the BPTX system provides Level-1 trigger input signals synchronous to bunches passing through ATLAS. These trigger signals serve as an absolute time reference and are particularly useful when timing in the triggers based on real physics signals.

A concise description of the ATLAS BPTX system can be found in [3] and the concepts are described in more detail in [4, 5]. This paper describes the software of the beam pick-up based monitoring system for the LHC beams and timing signals, and presents a few results from the first period of single beam running in September 2008.

### *1.1. LHC timing signals*

In order to allow the LHC experiments to be synchronized to the collisions, the accelerator provides them with timing signals related to its beams, transmitted through several kilometers of optical fibers[6]. Temperature changes that affect the properties of the fibers or other unforeseen problems with the transmission can introduce phase shifts in the clock signals and cause the ATLAS on-detector electronics to sample the detector signals at a non-optimal working point. In turn, this will jeopardize the quality of the data for the recorded events and the efficiency of the trigger system. Figure 1 shows how the timing signals are distributed from the RF center of the LHC machine to the experiments.

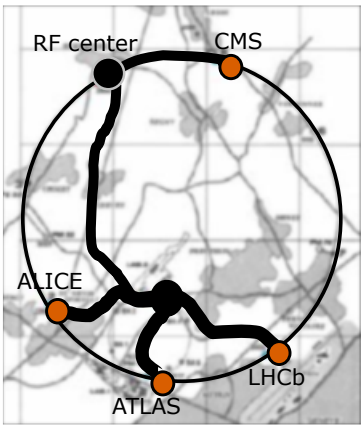


Figure 1: An illustration of how the LHC timing signals are transmitted from the RF center to the four major LHC experiments.

The LHC provides one reference clock signal, *BCref*, corresponding to the frequency at maximum beam energy and two clock signals that are synchronous to the accelerating beams, *BC1* and *BC2*. In addition, two orbit signals *Orbit1* and *Orbit2* with $f_{\mathrm{Orbit}i} = f_{\mathrm{BC}i}/3564$ are provided to mark every LHC turn, synchronized to their respective beams.

### *1.2. The ATLAS BPTX detectors*

On both sides of ATLAS, 175 m upstream from the interaction point, beam pick-up detectors are installed along the LHC beam pipe. These so-called *BPTX stations* are beam position monitors provided by the LHC machine, but operated by the experiments for timing purposes. They are comprised of four electrostatic button pick-up detectors each, arranged symmetrically in the transverse plane around the beam pipe.

Figure 2 shows the ATLAS BPTX station for beam 2, installed in the accelerator tunnel on the C-side of ATLAS. At the bottom of the photograph, the cables from three of the four button pick-ups are visible. The signals are combined and transmitted to the underground counting room *USA15* via a ∼220 m low-loss cable.

### *1.3. Usage of the BPTX signals in ATLAS*

As briefly mentioned in the Introduction, the ATLAS BPTX system serves two purposes. Figure 3 shows how the BPTX signals are used both in the trigger system and for the BPTX monitoring system which will be described in more detail in the following sections. The signals from the four pick-ups are combined to eliminate potential effects of the beam position in the transverse plane[1] before they are transmitted to the underground counting room *USA15*. The signals are split and fed into a constant-fraction discriminator to form a beam-related Level-1 trigger input, and into the BPTX monitoring system. The LHC timing signals enter the counting room as optical signals and are converted by the `RF2TTC` timing receiver. The `RF2TTC` module controls what signals are passed through to ATLAS and allows the manipulation of certain parameters, e.g. their phase, pulse duration and polarity.

[1] To first order, the signal amplitude from an individual pick-up is proportional to its closest distance to the passing charge. Since the BPTX stations are installed for timing purposes, the signals from all four pick-ups are summed which effectively cancels out any offset along an axis in the transverse plane.

Figure 2: A photograph of one of the two ATLAS BPTX stations.

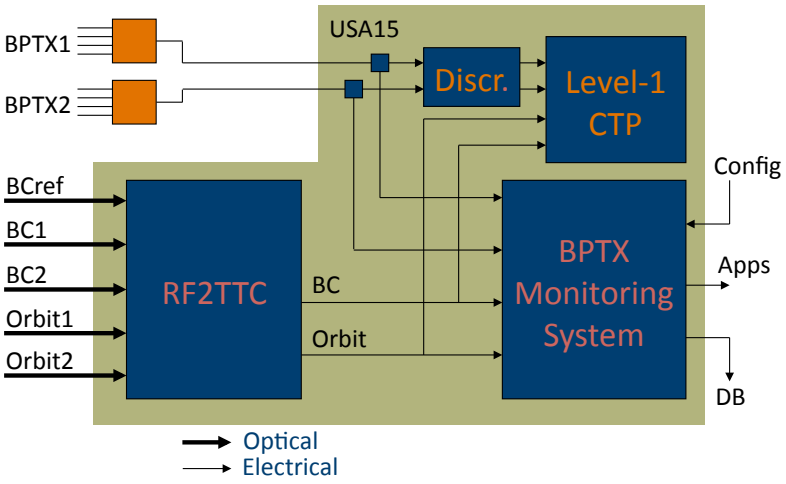


Figure 3: The usage of the BPTX signals in ATLAS.

## 2. Overview of the BPTX monitoring system software

For the monitoring of the LHC beams and timing signals in ATLAS, a flexible software solution was chosen. The BPTX and LHC timing signals are captured and digitized by a deep-memory, high sampling rate oscilloscope[2]. By default, 100 $\mu$s are captured, digitized and transferred to a rack-mounted Linux computer installed in *USA15*. Since it takes 89 $\mu$s for a bunch to travel around the LHC, this guarantees capturing all bunches in the accelerator at least once per acquisition, allowing measurements on a bunch-by-bunch basis. By frequently ($\sim$0.5 Hz) analyzing these signals together, phase drifts or other problems in the beams or timing signals will be discovered. The analysis is done completely in software and allows measuring and

[2] LeCroy WaveRunner 64 Xi. This oscilloscope has an analog bandwidth of 600 MHz and a sampling rate of 5 GS/s.

monitoring

- the average phase between the timing signals and the collisions
- the beam structure and detection of out-of-time bunches, including in the abort gap
- individual bunch properties, e.g. intensity, phase and longitudinal length

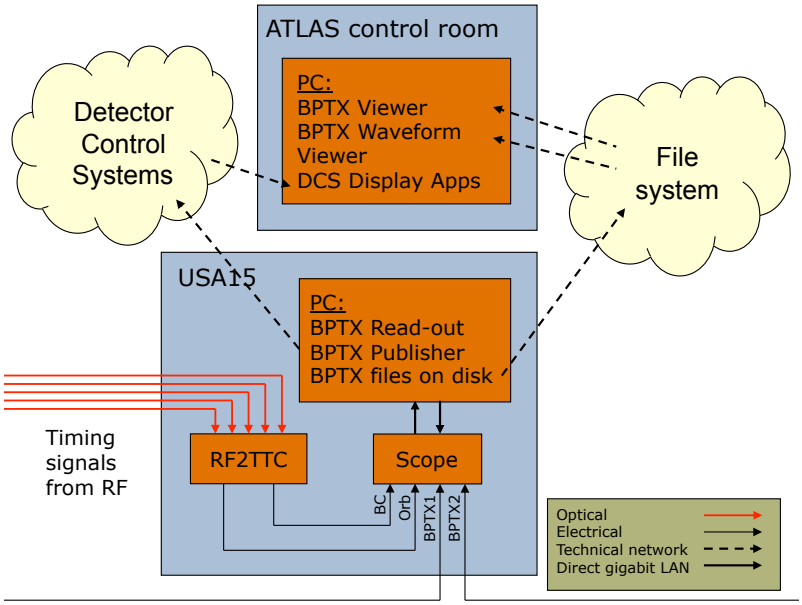


Figure 4: Diagram showing the components of the BPTX monitoring system and how they interact.

The software of the BPTX monitoring system is divided into several applications (see Figure 4) that perform separate, well-defined tasks:

- *BPTX Read-out* is the heart of the monitoring software, processes the digitized waveforms, and extracts parameters describing the identified bunches and clock edges. It then combines the condensed information to assign a phase and *Bunch Crossing Identifier* (BCID) to each bunch. The output is saved on disk where it can be read by other components in the monitoring system.
- *BPTX Viewer* gives the control room shifter an overview of the LHC beams and timing signals, and offers the possibility to track changes over time and identify oddly behaving bunches.
- *BPTX Waveform Viewer* lets the control room shifter inspect saved waveforms to investigate.
- *BPTX Publisher* communicates with other parts of the ATLAS software framework and transmits summary data to make it available to other online services and permanently saved in the ATLAS conditions database.

The three first components are described in the following sections. For information about the file formats, implementation details and the mathematical model of the signal from the BPTX detectors, the reader is referred to [5].

## 3. BPTX Read-out: signal processing and analysis

### *3.1. Signal processing*

This section describes the algorithms that extract the locations of the timing signal pulses and the parameters that describe the LHC bunches. The information extracted from the waveforms are saved in a condensed, lightweight representation called *waveform descriptors*, which are used internally for the rest of the processing, written to disk and read by other applications of the monitoring system. By combining the descriptors for the BPTX and timing signals, each bunch can be assigned a BCID and a phase.

*3.1.1. Clock and orbit signal processing* Clock signals coming from the RF2TTC module during ATLAS data taking exhibit a rise-time of about 1 ns which agrees with test measurements [6]. With a sampling rate of 5 GS/s, the edge in the digitized signal will therefore consist of about 5 samples, which allows performing a fit in order to determine the threshold crossing with high precision. During the design phase of the BPTX monitoring system, three methods were considered for determining the exact locations of the clock edges.

(i) Linear interpolation between the two sample points around the threshold crossing
(ii) Linear fit based on 5 samples points around the threshold crossing
(iii) Third order polynomial fit based on 5 samples points around the threshold crossing

All three methods were tested on simulated clock signals exhibiting noise and cycle-to-cycle jitter characteristic of the output signals of the `RF2TTC` module. All three algorithms had sub-picosecond precision. The linear interpolation is used as the default method as it is the computationally least demanding.

*3.1.2. BPTX signal processing* An LHC bunch can be described by three parameters, its arrival time, its intensity (number of protons) and its longitudinal length. During the development phase of the BPTX monitoring system, several ways of measuring these parameters were considered and tested with simulations.

When a bunch passes through a BPTX station, it gives rise to a fast bipolar pulse with a frequency spectrum peaking at around 400 MHz and tails reaching a few GHz. The long transmission line and the limited analog bandwidth of the oscilloscope attenuate the high-frequency content and shape the signal accordingly. After quantifying the couplings between different properties of the bipolar pulse and the bunch parameters in a simulation study, the waveform features in Figure 5 were chosen.

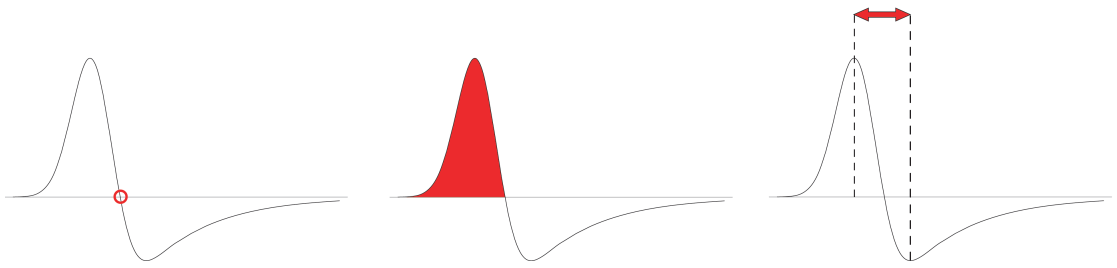

Figure 5: The waveform features measured to determine the bunch arrival time (left) and intensity (middle). The distance between the peak and the valley of the bipolar pulse correlates well with the longitudinal length of the bunch and is therefore used to measure this parameter.

The zero-crossing is a sharp vertical edge and thus a well-suited region to pick off the time of the pulse. Moreover, it is stationary with varying bunch intensity. The location of the

zero-crossing is determined by solving where the function resulting from a linear interpolation between the last positive and first negative samples crosses zero. Simulations suggest that the location of the zero-crossing relative to the actual arrival time depends slightly on the bunch length, which degrades the resolution of the arrival time measurement if the beams contain bunches of varying length. However, as soon as the mathematical model that the simulations rely upon has been tuned to data, this correlation can be determined and compensated for at the signal processing stage.

The value of the integral under the peak of the pulse is proportional to the number of protons in the bunch and is therefore chosen for the intensity measurement. This is implemented by performing numerical integration of the the peak if it passes a programmable threshold voltage.

The peak-to-valley distance scales with the longitudinal length of the bunch, and is relatively easy to measure. By fitting a second order polynomial to three sample points around maximum (minimum), a more accurate determination of the peak (valley) location is achieved, enhancing the the resolution of this measurement considerably.

These three measurements can be done with relatively low computational costs and perform well for our purposes. For more detailed motivations on the chosen waveform features, see [5].

### *3.2. Bunch phase and BCID association*

When the individual signals have been processed and their extracted features saved in waveform descriptors, the arrival time of each bunch can be matched with a clock edge. The time difference between the bunch arrival time and the clock edge defines the phase of the bunch and the number of clock ticks since the orbit pulse determines the BCID. The BCID association can also be done by matching the identified bunches to a reference LHC fill pattern, which could be useful in the unlikely event that the orbit signal is unavailable.

## 4. BPTX Viewer: visualization of monitoring data

The objective of the BPTX monitoring system is to monitor the LHC beams and timing signals during ATLAS data taking. It is therefore important that the measurements are presented in a way that provides both overview and detail. The BPTX Viewer application provides an interactive graphical user interface for displaying monitoring data recorded with the BPTX Read-out program. Figure 6 shows a typical monitoring display in BPTX Viewer. The panel on the left allows the user to browser through the data sets currently accessible on disk or to automatically display the most recent data. The bottom panel shows measured bunch quantities vs. BCID. In this case, the individual bunch intensity of beam 1 (blue) and beam 2 (red) is plotted for a simulated data set, and visualizes the fill structure and uniformity of both beams. The main panel shows summary histograms for the clock signal period time and distributions of the measured bunch phase, intensity and length for both beams.

The main panel has several tabs, and the second one, labeled "Outliers", offers an interface for finding deviating bunches. By defining a set of cuts on the measured bunch parameters, e.g. bunches with low intensity can be found easily and their information displayed in the table (see Figure 7). For example, displaying the bunches that have a phase that deviates from the mean value could reveal low-intensity, out-of-time bunches, so-called *satellite bunches* or *ghost bunches*. Although the signal model is yet to be tuned to data, simulations show that even two bunches in consecutive RF buckets[3] can be distinguished and identified correctly by the software as long as they have comparable intensity.

The third tab displays the current log file of the BPTX Read-out application for easy inspection in case the control room shifter suspects there are problems in the read-out or signal

[3] In the LHC, the RF frequency is 400 MHz, resulting in a temporal distance of 2.5 ns between the so-called RF buckets where the bunches can be situated.


Figure 6: Screen shot of the BPTX Viewer application displaying measurements of simulated beam data.

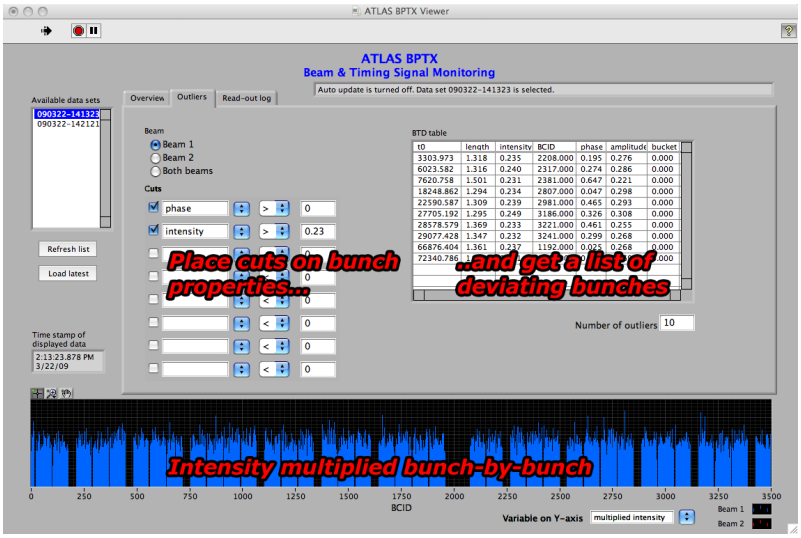


Figure 7: The Outliers tab in BPTX Viewer allows the shifter to identify deviating LHC bunches by placing cuts on their measured properties.

processing in the BPTX monitoring system.

## 5. BPTX Waveform Viewer: a waveform display tool

If the shifter in the ATLAS control room suspects that there is a problem with the timing signals or one of the beams, the waveforms available on disk can be inspected with the BPTX Waveform Viewer. Figure 8 shows an example view of simulated BPTX signals for both LHC beams.

## 6. Integration with the ATLAS online infrastructure and permanent storage

The BPTX Publisher application runs in parallel to the BPTX Read-out program on the rack-PC in USA15, and is responsible for shipping summary data from the BPTX monitoring system to the ATLAS *Detector Control System* (DCS)[7]. By publishing the data to DCS, it

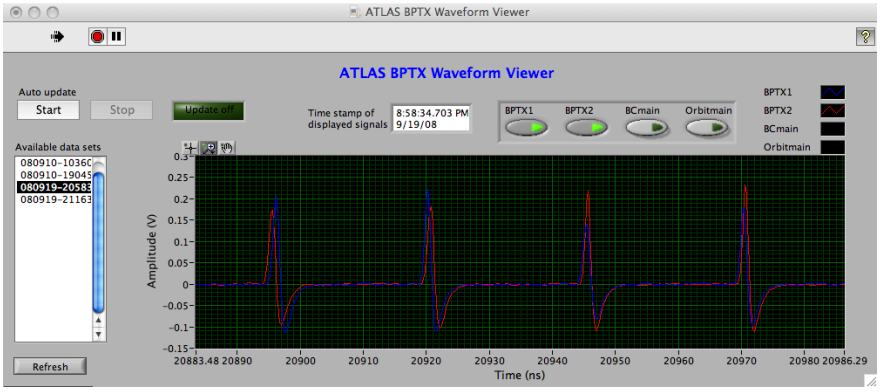


Figure 8: A screen shot from BPTX Waveform Viewer showing simulated BPTX signal waveforms.

is automatically made available to other ATLAS online services and recorded in the conditions database for permanent storage.

## 7. Results from the first LHC beams

At 10:18 AM on September 10, 2008, the LHC successfully circulated the first proton bunch. During the following week the BPTX system was used extensively to time in the ATLAS trigger system, and the BPTX monitoring system gave real-time information about the LHC beams to the shifters in the ATLAS control room. This section contains some plots from the monitoring system and presents a few preliminary results that indicate the resolution of its measurements.

### *7.1. First LHC bunches in ATLAS*

Figure 9 shows the first low-intensity LHC bunch on its way to ATLAS, as seen by the BPTX station 175 m in front of ATLAS, before it hit the collimators and produced the first so-called *splash event*. The amplitude of the pulse is consistent with a reported bunch intensity of $2 \times 10^8$ protons per bunch. For the nominal bunch intensity of $1.15 \times 10^{11}$ protons per bunch, the pulse amplitude is expected to increase by a factor of ∼500.

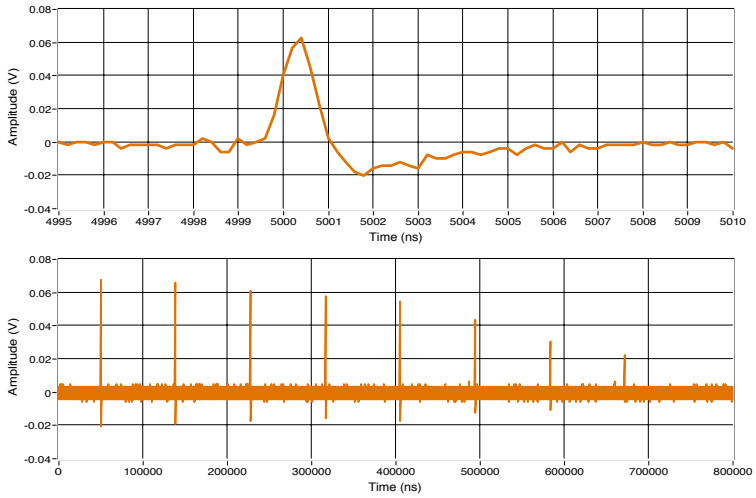


Figure 9: Top: The very first proton bunch approaching ATLAS as seen by the BPTX monitoring system on September 10, 2008. Bottom: A proton bunch recorded when circulating eight turns around the LHC.

A few hours later, the LHC managed to circulate a single bunch eight turns around the LHC. Since the beam was not yet captured by the RF system, the pulse amplitude was reduced from turn to turn as can be seen in the bottom plot of Figure 9. This can be explained by the debunching that is expected when the beam is not constrained longitudinally by an electric field.

### *7.2. Longer injection*

A few days later, the LHC managed to capture a bunch with its RF system and circulate it for a longer period. Figure 10 shows the beam intensity measured over time by the BPTX monitoring system for the longest LHC fill so far, with a total duration of about 20 minutes. The scatter of data points indicates that the resolution of this measurement is around 10 percent.

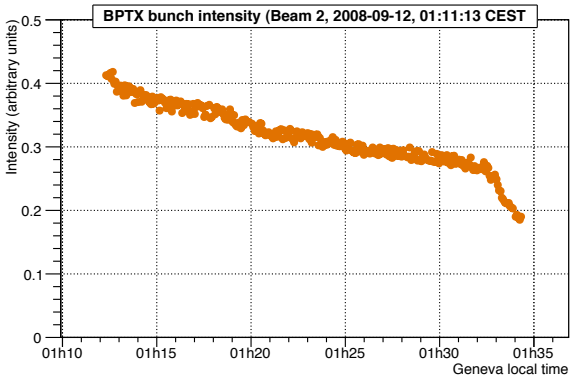


Figure 10: Beam intensity varying over a ∼20 min fill as measured by the BPTX monitoring system.

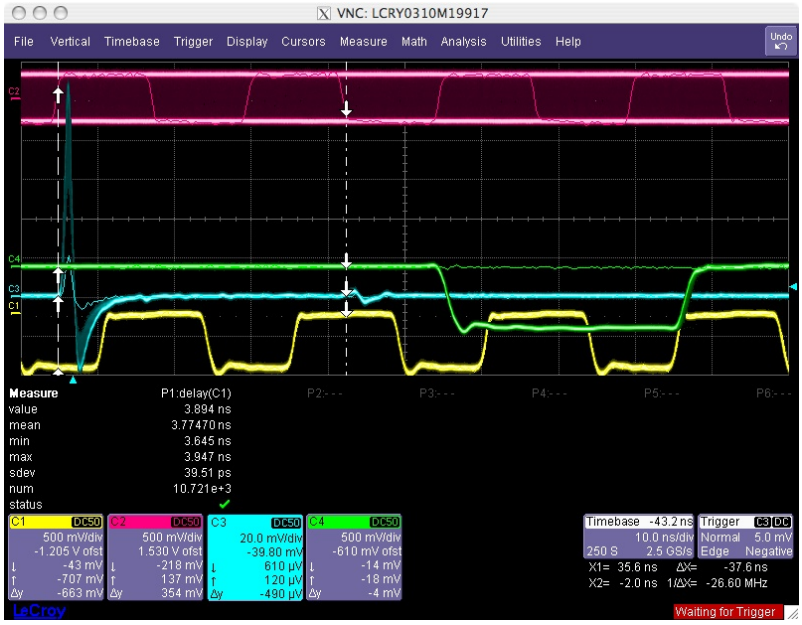


Figure 11: Oscilloscope trace taken in persistency mode during a long LHC fill.

*7.3. Bunch phase resolution*
During the fill mentioned in Section 7.2, the phase between the bunch and the closest edge of the clock signal was measured with a precision of 40 ps. This number includes not only the accuracy of the phase measurement, but also the clock jitter and possibly varying bunch arrival times. Figure 11 illustrates this phase stability with a picture from an oscilloscope that was running in persistency mode. Since all measurements were performed on the same bunch, potential effects on the arrival time determination due to varying bunch length are not included.

*7.4. BPTX signal noise*
The period of single beam running offered the first possibility to measure the noise of the BPTX signals during operation with beam. By analyzing waveforms captured during this time, the standard deviation of the sample values in regions without bunch pulses was measured to be 1.7 mV. On September 10, the LHC reported a bunch intensity of $2 \times 10^9$ protons, for which the measured BPTX pulse amplitude was 0.06 V. Since the pulse amplitude varies linearly with bunch intensity, setting the threshold level to $5\sigma_{noise} = 8.5$ mV the lowest possible bunch intensity that the BPTX system is sensitive to would be $3 \times 10^8$, corresponding to 0.26% of the nominal LHC bunch intensity. As can be seen in Figure 11, a small reflection of the bunch pulse was discovered in the recorded BPTX waveforms. The reflection is caused by impedance variations in the components that combine the signals from the four pick-ups, and is likely to scale with pulse amplitude. This feature could limit the sensitivity to detect satellite bunches in LHC fills with high bunch intensities, however there are plans to implement an appropriate filter to correct for it at the signal processing level.

## 8. Conclusions
The BPTX monitoring system in ATLAS is designed to monitor the relation between the LHC beams and timing signals to ensure the quality of the recorded event data. In addition, the structure of the beams and properties of the individual bunches can be measured and displayed with the BPTX application suite. During the first period of LHC running the BPTX signals were successfully used in the trigger system and the monitoring system measured both bunch intensity and phase with satisfactory performance, however, further calibration studies are needed to reach optimal performance.

## Acknowledgments
The authors would like to thank the ATLAS Collaboration and its Level-1 Central Trigger group in which most of this work was carried out. We would also like to express our gratitude to the LHC machine groups.

## References
[1] The ATLAS Collaboration 2008 "The ATLAS Experiment at the CERN Large Hadron Collider" *JINST* **3** (2008) S08003.
[2] L. Evans and P. Bryant (editors) 2008 "LHC Machine" *JINST* **3** (2008) S08001.
[3] C. Ohm, T. Pauly 2009 "The ATLAS beam pick-up based timing system" To appear in *Proc. 1st Int. Conf. on Technology and Instrumentation in Particle Physics (Tsukuba) Preprint* hep-ex/0905.3648
[4] T. Pauly et al. 2005 "ATLAS Level-1 Trigger Timing-In Strategies" *Proc. 11th Workshop on Electronics for LHC and Future Experiments (Heidelberg)* pp 274-278.
[5] C. Ohm 2007 *Phase and Intensity Monitoring of the Particle Beams at the ATLAS Experiment* M.Sc. thesis, Linköping University, Sweden, LITH-IFM-EX–07/1808–SE.
[6] S. Baron 2005 "TTC challenges and upgrade for the LHC" *Proc. 11th Workshop on Electronics for LHC and Future Experiments (Heidelberg)* pp 125-129.
[7] A. Barriuso Poy, H. Boterenbrood, H. J. Burckhart, J. Cook, V. Filimonov, S. Franz, O. Gutzwiller, B. Hallgren, V. Khomutnikov, S. Schlenker and F. Varela 2008 "The detector control system of the ATLAS experiment". *JINST* **3** (2008) P05006.